



**Deliverable 2.6:**  
**Modelling of the steel-clay interface - approaches,  
first results and model refinements**  
Work Package 2

The project leading to this application has received funding from the European Union's Horizon 2020 research and innovation programme under grant agreement No 847593.



## Document information

Project Acronym	<b>EURAD</b>
Project Title	<b>European Joint Programme on Radioactive Waste Management</b>
Project Type	<b>European Joint Programme (EJP)</b>
EC grant agreement No.	<b>847593</b>
Project starting / end date	<b>1<sup>st</sup> June 2019 – 30 May 2024</b>
Work Package No.	<b>2</b>
Work Package Title	<b><u>A</u>ssessment of <u>C</u>hemical <u>E</u>volution of ILW and HLW <u>D</u>isposal Cells</b>
Work Package Acronym	<b>ACED</b>
Deliverable No.	<b>D2.6</b>
Deliverable Title	<b>Modelling of the steel-clay interface - approaches, first results and model refinements</b>
Lead Beneficiary	<b>NAGRA</b>
Contractual Delivery Date	<b>August 2020</b>
Actual Delivery Date	<b>February 2021</b>
Type	<b>Report</b>
Dissemination level	<b>PU</b>
Authors	<b>Vaclava Havlova (UJV), Mirjam Kiczka (U. Bern), Angela Mendoza Miranda (UJV), Martin Klajmon (UJV), Paul Wersin (U. Bern), Marek Pekala (U.Bern), Andreas Jenni (U. Bern), Jebiril Hadi (U.Bern), J. Samper (UDC), L. Montenegro (UDC), A. Mon (UDC), Margit Fabian (MTA), Janos Osan (MTA), Alexandre Dauzères (IRSN), Diederik Jacques (SCK CEN).</b>

### To be cited as:

Havlova V., Kiczka M., Mendoza Miranda A., Klajmon M., Wersin P., Pekala M. Jenni A., Hadi J., Samper J., Montenegro L., Mon A., Fabian M, Osan J., A. Dauzeres, D. Jacques (2020): Modelling of the steel-clay interface – approaches, first results and model refinements. Final version as of 28 08 2020 of deliverable D2.6 of the HORIZON 2020 project EURAD. EC Grant agreement no: 847593.

### Disclaimer

All information in this document is provided "as is" and no guarantee or warranty is given that the information is fit for any particular purpose. The user, therefore, uses the information at its sole risk and liability. For the avoidance of all doubts, the European Commission has no liability in respect of this document, which is merely representing the authors' view.

### Acknowledgement

This document is a deliverable of the European Joint Programme on Radioactive Waste Management (EURAD). EURAD has received funding from the European Union's Horizon 2020 research and innovation programme under grant agreement No 847593.

Status of deliverable		
	By	Date
Delivered (Lead Beneficiary)	Mirjam Kiczka (UniBern) Vaclava Havlova (UJV)	09/07/2020
Verified (WP Leader)	Diederik Jacques (SCK CEN)	26/07/2020
Reviewed (Reviewers)	SCK CEN	27/09/2020
Verified (PMO)	Bernd Grambow (IMT Atlantique)	08/11/2020
Approved (PMO)	Bernd Grambow IMT Atlantique)	18/02/2021
Submitted to EC (Coordinator)	Andra	18/02/2021

## Executive Summary

The general objective of Task 2 in work package “Assessment of Chemical Evolution of ILW and HLW Disposal Cells”, short ACED, is to provide geochemical and coupled reactive transport models for assessing the geochemical evolution at steel/clay material and steel/cement material interfaces in terms of corrosion rates, geochemical alterations and physical alterations. Task 2.1 focusses on the steel-clay interface and follows a combined modeling-experimental approach in order to increased confidence and decreased uncertainty of model simulations. Existing experiments to be modelled include the long-term in-situ experiments FEBEX and MaCoTe as well as new lab experiments performed at ÚJV and the Fe/Bentonite interface cells experiments (FBexperiments) run by CIEMAT. New laboratory experiments are looking at the effect of Fe(II) on smectite of Uni Bern and on steel interaction with claystone of MTA. The deliverable is summing the activities performed in the first period of the project.

ÚJV Rez based development of models for the interface of canister material (carbon steel) and bentonite on data from already existing experiments, both laboratory and in-situ (Grimsel test site), observing behaviour of the system under differing temperatures (lab up to 70°C). Data has been selected, sorted and categorised in each of the considered experiments (CoPr, MaCoTe, UOS) in order to be used for the development of the model using the PHREEQC geochemical software code. The very first modelling step, based on evaluation of available data has been made in order to characterize the bentonite pore solution, in contact with either iron powder or carbon steel powder.

On the basis of comparing simulated bentonite pore waters (BPWs) and the initial groundwaters, it can be clearly seen that the initial solution composition and temperature had generally minor effects on BPWs composition, whereas the initial bentonite composition has the dominant effect. This also explains differing CZ BaM bentonite and MX-80-based BPWs. Different pore water compositions might be reflected in varying composition of corrosion products in the system iron/steel-bentonite-water.

Uni Bern presents in Chapter 3 scoping calculations for a new Fe(II) diffusion cell experiment currently under development, which aims at a better understanding of the Fe(II)-montmorillonite interaction. The scoping calculations are used for the design optimization, evaluating the expected evolution of the Fe-sorption front depending on initial Fe and Na concentrations. Furthermore, the impact of uncertainties in diffusion and sorption parameters on the calculated temporal evolution of Fe and Na reservoir concentrations was assessed.

Preliminary model results are presented by UDC in Chapter 4 for the coupled thermo-hydro-mechanical and chemical (THMC) reactive transport model of the long-term laboratory corrosion tests. This THMC model is based on the reactive transport model of the FB3 corrosion test (Mon, 2017) and has been extended to the timeframe of the FB4 corrosion test (7 years). As expected, experimental data from the FB4 corrosion test are not yet available for model calibration. The model considers a constant steel corrosion rate and the precipitation of magnetite, goethite, siderite and Fe(OH)<sub>2</sub>. Several sensitivity runs have been performed to evaluate the uncertainties in steel corrosion rate and the kinetics of magnetite precipitation.

A corrosion model for the steel-bentonite interactions in the FEBEX in situ experiment has been postulated by UDC in Chapter 5. The model is based on a previous THMC model of the FEBEX in-situ test (Samper et al., 2018b). This model will be the starting point for modelling the interactions of corrosion products and bentonite at several locations of the FEBEX in situ test. The model will be updated during the second year of the ACED WP by considering the inputs from the SOTA of ACED Task 1 and the conceptual model of steel corrosion and Fe diffusion proposed by Hadi et al. (2019).

Uni Bern developed a new THC model of the FEBEX in situ test using the computer code PFLOTTRAN. Preliminary results on thermo-hydro-chemical evolution for a heated section are presented in Chapter 6. Aerobic and anaerobic corrosion of the steel liner are implemented with a first order kinetic rate law and constant corrosion rate, respectively. The corrosion model further considers precipitation of goethite and magnetite as well as sorption of Fe on montmorillonite. For the next year an improved parameterization of presently included processes as well as the consideration of additional mineral

phases (i.e.  $\text{Fe}(\text{OH})_2$ , or siderite) and the implementation of the conceptual Fe(II)-montmorillonite interaction model of Hadi et al. (2019) are foreseen.

Finally, the set-up of MTA experimental cells designed to study the interaction of steel and Boda Claystone Formation (BCF) is presented in Chapter 7. First parameterization of transport and mineralogy of the BCF as well as the initial porewater composition to be used in the model are defined.

## Table of content

Executive Summary.....	4
Table of content.....	6
List of Figures.....	10
List of Tables.....	15
Glossary.....	17
1. Introduction and context.....	19
2. Interaction of Fe/steel with Ca-Mg bentonite (ÚJV).....	22
2.1 Laboratory experiments with Corrosion products CoPr (Fe powder/carbon steel/bentonite)	22
2.1.1 Materials.....	22
2.1.2 Conditions.....	26
2.1.3 Results.....	27
2.2 In situ experiment MaCoTe (carbon steel/bentonite).....	34
2.2.1 Materials.....	34
2.2.2 Conditions.....	36
2.2.3 Results.....	37
2.3 Laboratory experiment with canister material (carbon steel/bentonite, UOS).....	41
2.3.1 Materials.....	41
2.3.2 Conditions.....	42
2.3.3 Results.....	44
2.4 Proposed modelling approach.....	46
2.5 Conceptual Model.....	46
2.5.1 Modelling concept.....	46
2.5.2 Processes to be modelled.....	46
2.5.3 Initial conditions and input parameters.....	47
2.6 Modelling tools applied.....	51
2.7 First results and discussion – Modelling of bentonite pore water (BPW) composition.....	51
3. Interaction of Fe(II) with montmorillonite (UniBern).....	57
3.1 Fe(II) diffusion cell experiments.....	57
3.1.1 Dimensions.....	57
3.1.2 Materials.....	58
3.1.3 Conditions.....	58
3.2 Proposed modelling approach.....	58
3.3 Conceptual Model.....	58
3.3.1 Objectives of the Model.....	58

3.3.2	Processes to be modelled .....	59
3.3.3	Important assumptions, simplifications, limitations.....	59
3.3.4	Boundary Conditions .....	59
3.3.5	Initial conditions / parameters.....	59
3.4	Numerical model.....	60
3.4.1	Spatial and temporal discretization.....	60
3.4.2	Sensitivity analyses .....	61
3.4.3	Model calibration.....	61
3.5	First results and discussion .....	61
4.	Numerical modelling of the FB lab experiments of CIEMAT on the interactions of FEBEX bentonite and steel corrosion products (UDC) .....	65
4.1	FB laboratory corrosion experiments.....	65
4.1.1	Dimensions .....	66
4.1.2	Materials .....	67
4.1.3	Conditions .....	67
4.2	Proposed modelling approach.....	69
4.3	Conceptual Model.....	70
4.3.1	Objectives of the model .....	70
4.3.2	Processes to be modelled .....	70
4.3.3	Important assumptions, simplifications and limitations.....	71
4.3.4	Boundary Conditions .....	71
4.3.5	Initial conditions / parameters.....	72
4.4	Numerical model.....	77
4.4.1	Spatial and temporal discretization.....	77
4.4.2	Sensitivity analyses .....	77
4.4.3	Model calibration.....	83
4.5	First results and discussion .....	83
4.5.1	Thermo-hydro-mechanical results .....	83
4.5.2	Chemical results .....	86
5.	Corrosion model of the steel bentonite interactions in the FEBEX in situ experiment – UDC Approach .....	97
5.1	The FEBEX in situ experiment .....	97
5.1.1	Dimensions .....	97
5.1.2	Materials .....	98
5.1.3	Conditions.....	99
5.1.4	Previous models of the FEBEX in situ test.....	99
5.2	Proposed modelling approach.....	103

5.3	Conceptual Model.....	104
5.3.1	Objectives of the Model .....	104
5.3.2	Processes to be modelled .....	104
5.3.3	Important assumptions, simplifications, limitations.....	106
5.3.4	Boundary Conditions .....	107
5.3.5	Initial conditions / parameters.....	107
5.4	Numerical model.....	110
5.4.1	Spatial and temporal discretization.....	110
5.4.2	Sensitivity analyses .....	110
5.4.3	Model calibration.....	113
5.5	First results and discussion .....	113
6.	Corrosion model of the steel bentonite interaction in the FEBEX in-situ experiment – UniBern approach.....	118
6.1	The FEBEX in-situ experiment .....	118
6.2	Proposed modelling approach.....	118
6.3	Conceptual Model.....	118
6.3.1	Objectives of the Model .....	118
6.3.2	Processes to be modelled .....	118
6.3.3	Important assumptions, simplifications, limitations.....	119
6.3.4	Boundary Conditions .....	120
6.3.5	Initial conditions / parameters.....	120
6.4	Numerical model.....	123
6.4.1	Spatial and temporal discretization.....	123
6.4.2	Sensitivity analyses .....	124
6.4.3	Model calibration.....	124
6.5	First results and discussion .....	124
7.	Steel – claystone interaction (MTA/SCK) .....	129
7.1	The MTA experiment .....	129
7.1.1	Experimental set up.....	130
7.1.2	Materials .....	132
7.1.3	Conditions.....	132
7.2	Proposed modelling approach.....	132
8.	Summary and Way forward .....	133
8.1	Summary .....	133
8.2	Planned continuation, improvements .....	133
8.3	Missing data validation .....	136
9.	Conclusions .....	137

**EURAD** Deliverable 2.6 – Modelling of the steel-clay interface

Appendix A. Supporting Information to Chapter 2 – Interaction of Fe/steel with Ca-Mg bentonite . 137

Appendix B. Supporting Information to Chapter 6 – Corrosion model of the FEBEX in-situ experiment by UniBern 138

References ..... 142

## List of Figures

Figure 1-1 – Overall scope of the ACED project with its (sub)tasks and required information exchange between the different tasks. The red rectangle highlights the subtask dealt with in this report (source: WP proposal) .....	19
Figure 1-2 – Scheme of the subtask 2.1 organization with rectangles in dotted line representing interactions between partners in the modelling group (source: WP proposal).....	20
Figure 2-1 – X-ray diffraction pattern of source bentonite BaM (lot 2014-1). (Gondolli et al. 2018b) ...	24
Figure 2-2 – View of the iron powder particle structure, magnification x1020. (Gondolli et al. 2018b) .	25
Figure 2-3 – Schematic cross-section of experimental cell. 1-body made of plastic composite, with a water inlet, 2-metal bottom, 3-porous stone, 4-seals, 5-compacted bentonite, 6-iron powder, 7-steel disc .....	26
Figure 2-4 – Fully operating experimental setup inside a glove box. A pressure exchanger with synthetic groundwater is shown on the right, a water saturation system with pressure monitor is shown in front and two heating devices with temperature regulators are shown at the back .....	26
Figure 2-5 – Middle part of experimental cell (40 °C, duration 487 days) after separation of the steel disc; the grey layer is a mixture of iron powder with corrosion products attached to compacted bentonite .....	27
Figure 2-6 – Detailed view of a steel disc with attached layer of iron powder with corrosion products (40 °C, duration 487 days).....	27
Figure 2-7 – Compacted bentonite with partly separated layer of a mixture of iron powder with corrosion products (laboratory temperature, duration 189 days) .....	27
Figure 2-8 – Compacted “porous disc” of a mixture of iron powder with corrosion products (70 °C, duration 340 days); dark green lines and spots are corrosion/alteration products .....	27
Figure 2-9 – X-ray diffraction pattern obtained for the bentonite sample taken from the experimental cell after 189 days at 70 °C .....	28
Figure 2-10 – Graphical presentation of CEC <sub>Cu</sub> values of bentonite BaM taken from the bentonite-iron interface for three different temperatures (laboratory, 40 and 70 °C) and durations of the experiment (from 97 to 487 days), in comparison to unaltered bentonite BaM. The x-axis shows the total duration of each set of samples in days; the sample set of 188 days is a replication of a previous half-year set. (Gondolli et al. 2018b) .....	29
Figure 2-11 – Raman spectra obtained for “porous disc” of iron powder taken from the experimental cell after 340 days at 70 °C, the side of the contact with a steel disc analyzed. The Raman shift marked at 1070 cm <sup>-1</sup> belongs to carbonate, the Raman shift marked at 671 cm <sup>-1</sup> belongs to magnetite. Reference magnetite spectrum (RRUFF database, www.rruff.info) shown for comparison .....	33
Figure 2-12 – Carbon steel sample .....	35
Figure 2-13 – Modules with bentonite BaM (left) and MX-80 (right). Dobrev et al. (2018) .....	36
Figure 2-14 – The corrosion testing apparatus installed in the natural granitic environment of the GTS (photo Nagra).....	37
Figure 2-15 – Mean carbon steel corrosion rates in bentonite BaM and in bentonite MX-80 (Dobrev et al., 2020). Time (in days) on x axis; corrosion rate (µm/year) on y axis. ....	38
Figure 2-16 – Illustrative diffraction trace for carbon steel in bentonite in the 1-year experiment. (Dobrev et al., 2018).....	39

Figure 2-17 – Schematic representation of the experimental cell for compacted bentonite experiment. 1 - plastic parts of the corrosion cell, 2 - metal part of the corrosion cell, 3 - frit, 4 - bentonite BaM, 5 – steel metal plate (sample). Dobrev et al. (2017b) .....	42
Figure 2-18 – Illustration of corrosion cells outside glove box Dobrev et al. (2017b) .....	43
Figure 2-19 – Bentonite (side in contact with steel sample) and steel sample with bentonite residues. Dobrev et al. (2017) .....	43
Figure 2-20 – 422707.9 steel surface with bentonite BaM residues after a one-year test displayed by secondary electrons (SE) on the left and back-scattered electrons (BSE) on the right, including relevant elemental analyses of different parts of the sample surface. (Dobrev et al. 2017b) .....	46
Figure 2-21 – Calculated chemical compositions of the considered BPWs. ....	53
Figure 2-22 – Comparison of the initial solutions and the calculated BPWs by means of a Piper diagram. ....	55
Figure 3-1 – Schematic and dimensions of the Fe(II)-diffusion experiment. ....	57
Figure 3-2 – Evolution of Fe and non-reactive Tracer concentrations in the bottom (left) and top (right) reservoirs depending on $D_e$ (top) and parameterization of CEC (bottom) in the montmorillonite disc. Note the logarithmic scale of the right panels. ....	62
Figure 3-3 – Prediction of Fe sorption front for the Base Case and Variant cases with different Fe and Na concentrations. ....	63
Figure 3-4 – Fe sorption front and distribution of Fe on different sorption sites for the BC (left), with Eh dependency of the $\equiv\text{Ss}/\text{w}1\text{OFe}^{2+}$ complex formation and in the variant case (right), with a fixed logK corresponding to the experimental conditions of Soltermann et al. (2014). ....	64
Figure 4-1 – Picture and scheme of the FB corrosion tests (Turrero et al., 2011). ....	66
Figure 4-2 – Sketch of the FB corrosion tests cells (Turrero et al., 2011). ....	66
Figure 4-3 – General sampling of the FB cells and detailed sampling at the interface iron-bentonite of the FB3 cell (Turrero et al., 2011). ....	68
Figure 4-4 – Summary of the corrosion products found in the FB1, FB2 and FB 3 cells (Torres et al., 2013). ....	69
Figure 4-5 – One dimensional finite element mesh for the numerical model of the FB corrosion tests. ....	77
Figure 4-6 – Sketch of the SC corrosion tests on small cells (Torres et al., 2008). ....	78
Figure 4-7 – Spatial distribution of the measured (symbol) and the computed (lines) saturation degree at the end of the SC-a3 corrosion test (6 months) at 100°C for the base run and the sensitivity run to the bentonite permeability. ....	79
Figure 4-8 – Sensitivity of the computed cumulative precipitation of magnetite at the end of the SC-a3 corrosion test (6 months) at 100°C to changes in the bentonite permeability. ....	79
Figure 4-9 – Measured (symbol) and computed (line) weight of iron at the end of the SC-a3 corrosion test (6 months) at 100°C to changes in the bentonite permeability. ....	79
Figure 4-10 – Spatial distribution of the measured (symbol) and the computed (lines) saturation degree at the end of the SC-a3 corrosion test (6 months) at 100°C for the base run and the sensitivity run to the vapor tortuosity factor. ....	80
Figure 4-11 – Sensitivity of the computed cumulative precipitation of magnetite at the end of the SC-a3 corrosion test (6 months) at 100°C for the base run and the sensitivity run to the vapor tortuosity factor. ....	80

Figure 4-12 – Measured (symbol) and computed (line) weight of iron at the end of the SC-a3 corrosion test (6 months) at 100°C for the base run and the sensitivity run to the vapor tortuosity factor. .... 81

Figure 4-13 – Sensitivity of the computed cumulative precipitation of magnetite at the end of the SC-a3 corrosion test (6 months) at 100°C to magnetite precipitation at equilibrium (sensitivity run) and kinetically controlled (base run). .... 81

Figure 4-14 – Measured (symbol) and computed (line) weight of iron at the end of the SC-a3 corrosion test (6 months) at 100°C to magnetite precipitation at equilibrium (sensitivity run) and kinetically controlled (base run). .... 82

Figure 4-15 – Sensitivity of the computed cumulative precipitation of magnetite at the end of the SC-a3 corrosion test (6 months) at 100°C to changes in the steel corrosion rate. .... 82

Figure 4-16 – Measured (symbol) and computed (line) weight of iron at the end of the SC-a3 corrosion test (6 months) at 100°C to changes in the steel corrosion rate. .... 83

Figure 4-17 – Time evolution of the water intake of the FB corrosion tests. .... 84

Figure 4-18 – Spatial distribution of the measured (symbols) volumetric water content at the end of the FB3 corrosion test and the computed (line) volumetric water contents at selected times in FB corrosion tests. .... 84

Figure 4-19 – Spatial distribution of the measured (symbols) porosity at the end of the FB3 corrosion test and the computed (line) porosities at the end of the FB3 and FB4 corrosion tests which fully coincide. .... 85

Figure 4-20 – Spatial distribution of the measured (symbols) temperature at the end of the FB3 corrosion test and the computed (line) temperature at the end of the FB3 and FB4 corrosion tests which fully coincide. .... 85

Figure 4-21 – Spatial distribution of the measured (symbols) relative humidity at the end of the FB3 corrosion test and the computed (line) relative humidity at the end of the FB3 and FB4 corrosion tests which fully coincide. .... 85

Figure 4-22 – Time evolution of the computed (lines) and the measured (symbols) temperature in the sensors T2 (18 mm from the heater) and T1 (74 mm from the heater) of the medium-size corrosion test on FB3 corrosion test. .... 86

Figure 4-23 – Time evolution of the computed (lines) and the measured (symbols) relative humidity in the sensors RH2 (18 mm from the heater) and RH1 (74 mm from the heater) of the medium-size corrosion test on FB3 corrosion test. .... 86

Figure 4-24 – Spatial distribution of the computed concentration of dissolved Cl<sup>-</sup> at selected times in the medium-size corrosion test on the FB corrosion tests. .... 87

Figure 4-25 – Spatial distribution of the computed concentration of dissolved Na<sup>+</sup>, K<sup>+</sup>, Mg<sup>2+</sup>, Ca<sup>2+</sup>, SO<sub>4</sub><sup>2-</sup>, HCO<sub>3</sub><sup>-</sup>, and SiO<sub>2</sub>(aq) at selected times in the FB corrosion tests. .... 88

Figure 4-26 – Spatial distribution of the computed concentration of dissolved Fe<sup>2+</sup> at selected times in the FB corrosion tests. .... 89

Figure 4-27 – Spatial distribution of the computed volume fraction of Fe(s) corrosion at selected times in the FB corrosion tests. .... 90

Figure 4-28 – Spatial distribution of the computed volume fraction of magnetite on at selected times in the FB corrosion tests. .... 90

Figure 4-29 – Spatial distribution of the computed volume fraction of calcite at selected times in the FB corrosion tests. .... 90

Figure 4-30 – Zoom of the spatial distribution of the computed volume fraction of calcite at selected times in the FB corrosion tests. ....	91
Figure 4-31 – Spatial distribution of the computed volume fraction of gypsum at selected times in the in the FB corrosion tests.....	91
Figure 4-32 – Spatial distribution of the computed volume fraction of anhydrite at selected times in the FB corrosion tests.....	91
Figure 4-33 – Spatial distribution of the computed volume fraction of quartz at selected times in the FB corrosion tests. ....	92
Figure 4-34 – Spatial distribution of the computed pH at selected times in the FB corrosion tests. ....	92
Figure 4-35 – Spatial distribution of the computed Eh at selected times in the FB corrosion tests. ....	92
Figure 4-36 – Spatial distribution of the computed (lines) and measured (symbols) concentrations of the exchanged cations at the end of the FB4 corrosion test. ....	93
Figure 4-37 – Spatial distribution of the computed concentration of exchanged $Fe^{2+}$ at the end of the FB corrosion tests. ....	93
Figure 4-38 – Spatial distribution of the computed concentration of sorbed species on strong, weak #1 and weak #2 sorption sites at the end of the FB4 corrosion test. ....	94
Figure 4-39 – Spatial distribution of the computed $Cl^-$ concentration at the end of the FB4 corrosion test before and after the cooling phase. ....	95
Figure 4-40 – Spatial distribution of the computed $HCO_3^-$ concentration at the end of the FB4 corrosion test before and after the cooling phase. ....	95
Figure 4-41 – Spatial distribution of the computed $SiO_2(aq)$ concentration at the end of the FB4 corrosion test before and after the cooling phase. ....	95
Figure 4-42 – Spatial distribution of the computed dissolved $Fe^{2+}$ concentration at the end of the FB4 corrosion test before and after the cooling phase. ....	96
Figure 4-43 – Spatial distribution of the computed exchanged $Fe^{2+}$ concentration at the end of the FB4 corrosion test before and after the cooling phase. ....	96
Figure 4-44 – Spatial distribution of the computed pH at the end of the FB4 corrosion test before and after the cooling phase. ....	96
Figure 5-1 – General layout of the FEBEX in situ test for the 1 <sup>st</sup> operation period, indicating the instrumented and sampling sections used by Samper et al., 2018b. The x coordinates of the sections are referred to the concrete plug on the left. ....	98
Figure 5-2 – General layout of the FEBEX in situ test for the 2 <sup>nd</sup> operation period. ....	98
Figure 5-3 – Concentric and coloured (red, orange, blue) halos observed at a bentonite block in contact with the steel liner in (d) a heater area and (e, f) the studied bentonite blocks BM-B-41-1 and BM-B-41-2 (Hadi et al., 2019). ....	101
Figure 5-4 – Proposed Fe diffusion mechanism at the steel–bentonite interface (Hadi et al., 2019). ....	102
Figure 5-5 – Schematic representation of the samples analysed by Kaufhold et al. (2019). ....	103
Figure 5-6 – Time evolution of the concentrations (lines) of dissolved $Cl^-$ and $SO_4^{2-}$ in the granite at a distance of 0.20 m from the bentonite/granite interface computed with revisited model with solute back-diffusion. The measured concentrations of dissolved $Cl^-$ and $SO_4^{2-}$ in sections FU1-3 and FU1-4 of the FU1 borehole after 2009 (symbols) were taken from Buil et al. (2010) and Garralón et al. (2018). ...	111
Figure 5-7 – Radial distribution of the computed concentration of dissolved $Ca^{2+}$ at the end of the 1st operation period of the FEBEX in situ experiment for the base run of the model with and without solute	

back-diffusion. The pore water concentration data inferred from aqueous extracts in sections 29 and 19 were taken from Zheng et al. (2011). ..... 112

Figure 5-8 – Radial distribution of: 1) The concentrations of dissolved  $\text{Cl}^-$  at the end of the 1<sup>st</sup> operation period (5 y) computed with the revisited model and the previous model of Zheng et al. (2011) and the pore water concentration data inferred from aqueous extracts in sections 19 (squares) and 29 (circles) from Zheng et al. (2011); and 2) The concentrations of dissolved  $\text{Cl}^-$  at the end of the 2<sup>nd</sup> operation period (18 y) computed with the revisited model without and with solute back-diffusion and the pore water concentration data inferred from aqueous extracts in sections 47 (diamonds) and 53 (crosses) from Fernández et al. (2018). ..... 114

Figure 5-9 – Radial distribution of the computed concentrations of dissolved  $\text{Ca}^{2+}$  and  $\text{Mg}^{2+}$  (left axis) and  $\text{K}^+$  (right axis) at the end of the 1<sup>st</sup> (2002) (continuous lines) and 2<sup>nd</sup> operation period (2015) (discontinuous lines). The pore water concentration data inferred from aqueous extracts in sections 19 (squares) and 29 (circles) were taken from Zheng et al. (2011). The concentrations of dissolved  $\text{Ca}^{2+}$  at the end of the 2<sup>nd</sup> operation period were computed with the revisited model without and with solute back-diffusion. .... 114

Figure 5-10 – Radial distribution of the computed concentrations of dissolved  $\text{Na}^+$  and  $\text{SO}_4^{2-}$  (left axis) and  $\text{HCO}_3^-$  (right axis), the end of the 1<sup>st</sup> (2002) (continuous lines) and 2<sup>nd</sup> operation periods (2015) (discontinuous lines). The pore water concentration data inferred from aqueous extracts in sections 19 (squares) and 29 (circles) were taken from Zheng et al. (2011). ..... 115

Figure 5-11 – Radial distribution of: 1) The computed cumulative dissolution/precipitation of calcite and pH at the end of the 1<sup>st</sup> (2002) and 2<sup>nd</sup> operation periods (2015) (top plot); and 2) The computed cumulative dissolution/precipitation of anhydrite and gypsum at the end of the 1<sup>st</sup> (2002) and 2<sup>nd</sup> operation periods (2015) (bottom plot). Positive for mineral precipitation and negative for mineral dissolution. 116

Figure 6-1 –  $\text{Ca}^{2+}$  concentration profiles in FEBEX and granite as computed for different times of the experiment (BASE CASE) ..... 125

Figure 6-2 – Fe corrosion rates over time in the Base Case and Variant Case 1 and 2. .... 126

Figure 6-3 – Stages of steel corrosion and Fe diffusion as calculated for the present Base Case model. Note that the kinetics and control of goethite and magnetite precipitation are still under development. .... 127

Figure 6-4 – Fe front after 0.5 years (aerobic corrosion phase) in case of a ~100 times faster goethite precipitation rate (left) or ten times slower aerobic corrosion rate (right) compared to the Base Case presented in Figure 6-3. .... 127

Figure 6-5 – Comparison of Fe fronts in the Base CASE and the three variant cases as calculated for  $t=18$  years. Solid lines indicate total Fe added for the cases indicated in the legend, dashed lines Fe in goethite only in the respective calculation case. The right figure is a blown up of the Fe-front marked by the rectangle in the left plot. .... 128

Figure 7-1 – Cross-section view of experimental setup with sign of different materials (top), detailed drawing with dimensions (middle) and materials in reality (bottom) of the MTA experiment ..... 132

Figure 8-1 – Contour plots of computed temperatures at the end of the 1<sup>st</sup> and 2<sup>nd</sup> operation periods of the FEBEX in situ test in 2002 and 2015, respectively. Also shown the location of Section 41 where most of the corrosion data were collected. .... 135

Figure 8-2 – Contour plots of computed saturation degrees at the end of the 1<sup>st</sup> and 2<sup>nd</sup> operation periods of the FEBEX in situ test in 2002 and 2015, respectively. Also shown the location of Section 41 where most of the corrosion data were collected. .... 136

## List of Tables

Table 2-1 – Bulk chemical analysis of Czech BaM bentonite (Červinka and Gondolli, 2015) .....	23
Table 2-2 – BaM bentonite semiquantitative X-ray powder diffraction results (Červinka and Gondolli, 2015).....	23
Table 2-3 – Results of specific surface and volume of micropores for iron powder (lot 51400) and bentonite BaM (lot 2014-1). Specific surface was determined using the BET method, and the DFT calculation was also applied to the iron powder (because of its microporous structure) (Gondolli et al. 2018b).....	25
Table 2-4 – Chemical composition of carbon steel 12050 .....	25
Table 2-5 – Composition of synthetic ground water used for bentonite saturation. (Červinka a Gondolli, 2015).....	25
Table 2-6 – Crystalline phases of corrosion / alteration products identified <b>in bentonite</b> samples by X-ray diffraction. “+” means positive detection.....	28
Table 2-7 – Cation exchange capacity values of bentonite samples from the bentonite / iron powder interface determined by the Cu-triene method, CECCu values calculated from the difference in copper concentration, CECSum values calculated from the sum of exchanged majority ions (Na, K, Ca, Mg). All CEC values corrected for natural / residual moisture of bentonite and a blank sample of Cu-triene (chemical composition). (Gondolli et al. 2018b) .....	30
Table 2-8 – Crystalline phases identified on <b>steel discs</b> by X-ray diffraction. “+” means positive detection, “++” means that the given phase predominates (semi-quantitative determination). LAB = laboratory temperature .....	31
Table 2-9 – Crystalline phases identified in <b>iron powder samples</b> by X-ray diffraction. “+” positive detection, “++” phase predominates (semi-quantitative determination), “?” unidentified phases have been detected. LAB = laboratory temperature. ....	32
Table 2-10 – Silicate analysis of bentonite MX-80 and bentonite BaM used in experiments (Dobrev et al. 2018).....	34
Table 2-11 – Semiquantitative X-ray powder diffraction results of MX-80 (Rueedi et al. 2013) .....	34
Table 2-12 – Chemical composition of carbon steel 12022 according to the standard, according to the manufacturer and obtained by analysis. Dobrev et al. (2018).....	35
Table 2-13 – Composition of Grimsel ground water (GGW) used for bentonite saturation. (Dobrev et al. 2017a).....	36
Table 2-14 – Corrosion products identified on the metal samples after 1 year, borehole 15.001. (Dobrev et al. 2018).....	39
Table 2-15 – Corrosion products identified on the metal samples after 2 years, borehole 15.002. (Dobrev et al. 2018).....	40
Table 2-16 – Corrosion products identified on the metal samples after 3 years, borehole 15.004. (Dobrev et al. 2020).....	41
Table 2-17 – Average values of cation exchange capacity of bentonite samples after contact with corroding steel for the indicated corrosion duration (BaMkor). CEC values for selected reference samples (BaM <sub>refer</sub> , bentonite reference materials SAz-1 and SWy-2) are shown for comparison. ....	44
Table 2-18 – Determined corrosion products of metal samples.....	45
Table 2-19 – Chemical composition and other parameters of the initial aqueous solutions. ....	48
Table 2-20 – Mineralogical composition and other parameters of the BaM and MX-80 bentonites. ....	49

Table 2-21 – Cation exchange characteristics of the considered bentonites.....	50
Table 2-22 – Surface complexation characteristics of the considered bentonites. ....	51
Table 2-23 – List of BPW models developed in this stage of work. ....	52
Table 2-24 – Calculated chemical compositions of the considered BPWs and the resulting bentonite mineralogical compositions, exchanger compositions, and surface edge site compositions. ....	53
Table 3-1 – Parameterization of site types, site capacities, protolysis constants and sorption parameters as considered in the Base Case.....	60
Table 3-2 – Initial composition of reservoir solution and montmorillonite porewater as considered in the Base Case .....	60
Table 3-3 – Summary of variant cases.....	61
Table 4-1 Mineralogical composition of the FEBEX bentonite (Fernández et al., 2001). ....	67
Table 4-2 – Water flow parameters (ENRESA, 2006a; Zheng et al., 2010). ....	72
Table 4-3 – Thermal parameters (ENRESA, 2006a; Zheng et al., 2010). ....	73
Table 4-4 – Solute transport parameters (ENRESA, 2006a; Zheng et al., 2010). ....	73
Table 4-5 – Mechanical parameters (ENRESA, 2006a; Zheng et al., 2010). ....	73
Table 4-6 – Chemical reactions and equilibrium constants for aqueous complexes and minerals (Wolery, 1992), protolysis constants for surface complexation reactions (Bradbury and Baeyens, 1997; 1998; 2003) and selectivity coefficients for cation exchange reactions (ENRESA, 2006b) at 25°C. ....	74
Table 4-7 – Chemical composition (in mol/L) of the bentonite initial porewater (Fernández et al., 2001) and the Grimsel hydration boundary water (Turrero et al., 2001). ....	76
Table 5-1 – Reactions and equilibrium constants for aqueous species and mineral dissolution/precipitation at 25 °C (Wolery, 1992); protolysis constants for surface complexation reactions for a triple-site sorption model (Bradbury and Baeyens, 2005); and selectivity constants for cation exchange reactions (ENRESA, 2006a). ....	105
Table 5-2. Thermal, hydrodynamic and mechanical parameters of the bentonite and granite (Zheng and Samper 2008; Zheng et al., 2011, based on ENRESA 2006a).....	108
Table 5-3 – Thermal, hydrodynamic and mechanical parameters (Zheng and Samper, 2008, based on ENRESA, 2006a).....	108
Table 5-4 – Initial pore water composition (Fernández et al., 2001; Samper et al., 2008a), initial mineral volume fractions (Samper et al., 2008a), initial concentrations of exchanged ions (Fernández et al., 2004) and total concentrations of surface complexation sites (Bradbury and Bayens, 1997, 2003). .	109
Table 5-5 – Effective diffusion coefficients in the bentonite and granite for the base run of the revisited model with and without solute back-diffusion from the bentonite into the granite.....	110
Table 6-1 – Initial conditions of FEBEX and granite porewaters, mineralogy and exchanger composition as used in the model. ....	121
Table 6-2 – Hydrodynamic and thermal parameters of steel, bentonite and granite .....	122
Table 6-3 – Parameterization of site types, site capacities, protolysis constants and sorption parameters as considered in the Base Case.....	123
Table 6-4 – Spatial discretization of the FEBEX model. Thick black lines indicate the active model domain boundaries. The regions HEATER_INERT and STEEL_INERT are inactive, the EDZ has the same initial conditions and parameterization as the rock.....	124

## Glossary

AAS	Atomic absorption spectroscopy
ABM1, ABM2	Alternative Buffer Material Tests performed at Äspö Hard Rock Laboratory (S)
ACED	<u>A</u> ssessment of <u>C</u> hemical <u>E</u> volution of ILW and HLW <u>D</u> isposal Cells
BaM	Commercial name of Czech bentonite (Bentonite and Montmorillonite)
BC	Base Case
BCF	Boda Claystone Formation
BO-ADUS	Name of borehole at Grimsel test site
BPW	Bentonite Porewater
CEC	Cation exchange capacity
CIEMAT	Centro de Investigaciones Energéticas, Medioambientales y Tecnológicas, Spain
CoPr	Corrosion Products (Abbreviation for experiments performed at ÚJV)
ČSN	Czech technical standard
DGR	Deep Geological Repository
EBS	Engineered Barrier System
EURAD	European Joint Programme on Radioactive Waste Management
FB experiment	Fe/Bentonite interface cells
FEBEX	Full-scale Engineered Barriers Experiment
GGW	Grimsel groundwater
GTS	Grimsel test site
HLW	High Level Waste
ICP	Inductive coupled plasma
IF	Interface
ILW	Intermediate Level Waste
LAB	Laboratory
MTA	Hungarian Academy of Sciences Centre for Energy Research
MaCoTe	Material Corrosion Test (Experiment at Grimsel test site)
MX-80	Bentonite of Wyoming

## EURAD Deliverable 2.6 – Modelling of the steel-clay interface

NRG	Nuclear Research and Consultancy Group, Netherlands
PEBS	Long-term performance of Engineered Barrier Systems EU project
SCK-CEN	Belgian nuclear research centre in Mol, Belgium
SEM/TEM	Scanning electron microscopy / Transmission electron microscopy
SGW	Synthetic ground water (based on Červinka and Gondolli 2015)
SNF	Spent nuclear fuel
SURAO	Radioactive Waste Repository Authority of Czech Republic
SWy-2 / SWy-3	Na-montmorillonites (Wyoming) from source clay repository
THCM model	Thermo-hydro-chemical-mechanical model
UAM	Autonomous University of Madrid, Spain
UDC	University of A Coruña, Spain
ÚJV	Nuclear Research Institute, Czech Republic
UOS	Disposal container project (Abbreviation for experiments performed at ÚJV)
X, N-CT	X-ray, neutron-computed tomography
XRD	X-ray diffraction
XRF	X-ray fluorescence
WP	Work package

## 1. Introduction and context

The work presented in this report is part of the EURAD work package “**A**ssessment of **C**hemical **E**volution of ILW and HLW **D**isposal **C**ells”, short ACED. The broader scope of this work package is the assessment of the chemical evolution at the disposal cell scale involving interacting components/materials and thermal, hydraulic and/or chemical gradients by considering ILW and HLW disposal concepts representative for different concepts throughout Europe. The main objective is to improve methodologies to obtain multi-scale quantitative models for the chemical model at cell disposal scale based on existing and new experimental data and process knowledge and to improve the description of the most relevant processes driving the chemical evolution into robust mathematical frameworks.

An important basis for the work package is state-of-the-art scientific knowledge and experimental evidence on chemical processes acting at the interface of 2 materials. The investigation of the interface processes is dealt with in Task 2 of the ACED WP (Figure 1-1). **The general objective of this task is to provide geochemical and coupled reactive transport models for assessing the geochemical evolution at steel/clay material and steel/cement material interfaces in terms of corrosion rates, geochemical alterations and physical alterations.** These models will provide the bases of the up-scaling to waste package (Task 3) and disposal cell (Task 4) modelling (see Figure 1-1).

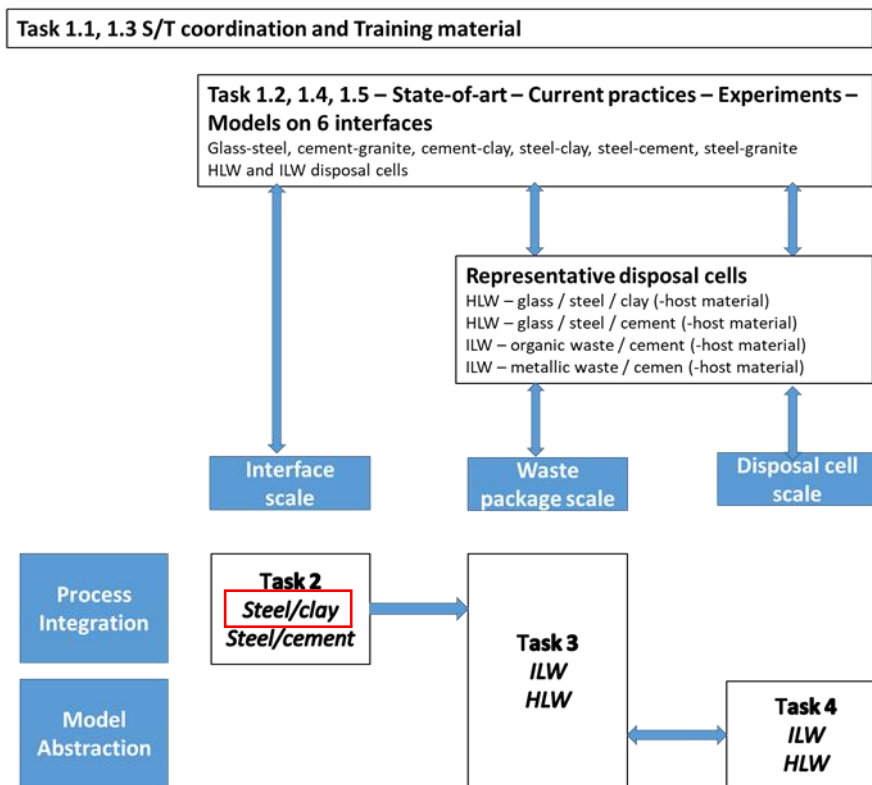


Figure 1-1 – Overall scope of the ACED project with its (sub)tasks and required information exchange between the different tasks. The red rectangle highlights the subtask dealt with in this report (source: WP proposal)

Task 2.1 focusses on the steel-clay interface and follows a combined modeling-experimental approach in order to increased confidence and decreased uncertainty of model simulations. Key factors and parameters for the conceptual description of steel/material interactions in reactive transport models and for model validation such as corrosion rates, physicochemical evolution and mineralogical evolution are determined in existing experiments and new experimental studies:

- Existing experiments to be modelled include the long-term in-situ experiments FEBEX (chapters 5 and 6) and MaCoTe (chapter 2) as well as lab experiments performed at ÚJV (impact of steel corrosion on the chemistry of Ca-Mg bentonite at different temperatures, chapter 2) and the FB lab experiments of CIEMAT (Interactions of FEBEX bentonite and steel corrosion products, chapter 4).
- New laboratory experiments are looking at the effect of Fe(II) on smectite (chapter 3) and on steel interaction with claystone (chapter 7.1). Figure 1-2 provides an overview of the Task 2.1 experiments and numerical modelling with the interactions between project partners as defined in the proposal.

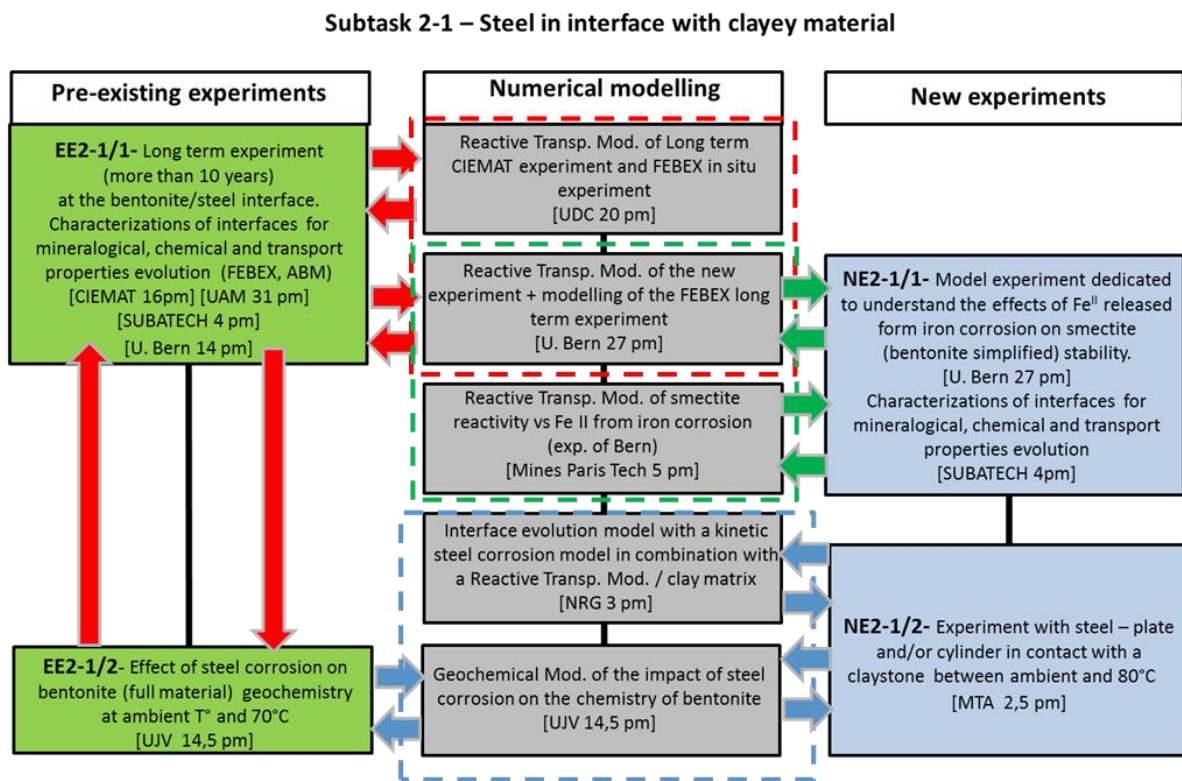


Figure 1-2 – Scheme of the subtask 2.1 organization with rectangles in dotted line representing interactions between partners in the modelling group (source: WP proposal)<sup>1</sup>

This report presents the development of models for the steel/clay material interface reactivity. First modelling results and refinement of the modelling approach are provided and missing data for model validation defined. **Progress in experimental work of Task 2.1 is only addressed with respect to its impact on model development.**

The report is structured as following:

Chapter 2 presents the work of ÚJC investigating the interaction of Fe/steel with Ca-Mg bentonite. It deals with three different sets of experiments, the laboratory experiments studying the interaction of corrosion products with Czech BaM bentonite (chapter 2.1), an in-situ experiments at Grimsel Test site

<sup>1</sup> The NRG contribution (Interface evolution model with a kinetic steel corrosion model in combination with a reactive transport model) is taken over by SCK CEN.

done in the framework of MaCoTe (Material Corrosion Test) (chapter 2.2) and laboratory experiments interacting different canister materials with BaM bentonite (chapter 2.3). Chapter 2.4 to 2.6 present the approach, conceptual model and modelling tools, which will be used to elaborate a concise model of the corrosion and interaction of corrosion products with Ca-Mg bentonites based on the knowledge gained from the three experiments. First results of modelling of the bentonite pore waters are shown in chapter 2.7

Chapter 3 presents the Fe(II)-montmorillonite interaction experiment of University of Bern. This diffusion cell experiment is designed to elucidate the effect of Fe(II) on montmorillonite and provide a basis for the development of a model for redox changes in bentonite induced by Fe(II) from corrosion diffusing into the bentonite. Scoping calculations are presented, which are used for the final design of the experiment.

Chapter 4 presents the numerical models of the FB laboratory experiments developed by UDC. These experiments were performed by CIEMAT with the support of UAM for the characterization of the interactions of steel corrosion products and compacted FEBEX bentonite. The model developed for these tests specifically focusses on the operational and the early post-closure transient phases of the repository before achieving full saturation of the EBS.

Chapter 5 presents the numerical model of the FEBEX in-situ test developed by UDC. It provides results for the general thermo-hydraulic-chemical evolution during the test and presents the conceptual model and proposed implementation of the steel corrosion model into the existing numerical model.

Chapter 6 presents the approach and first results of the numerical model of the FEBEX in-situ test developed by UniBern. A special focus on this model will be the integration of the insights from the laboratory experiments as described in Chapter 3 to the full-scale FEBEX model.

Chapter 7 summarizes the planned experiments of steel-claystone interaction of MTA and SCK CEN.

Chapter 8 provides a summary of the status of the model development within Task 2.1 of ACED and gives an outlook on the planned work and aspired model improvements. Missing data for validation of the different models is summarized.

## 2. Interaction of Fe/steel with Ca-Mg bentonite (ÚJV)

The ÚJV experiments were focused on studying carbon steel/iron corrosion, including corrosion product formation, under increased temperature and conditions as close to deep geological repository (DGR) conditions as possible (anaerobic box; underground laboratory). The chapter describes

- accelerated corrosion product formation experiment CoPr (laboratory, iron powder + steel discs + Ca\_Mg bentonite; ambient temperatures, 40 °C and 70 °C; anaerobic box);
- in situ heated corrosion test MaCoTe (Grimsel test site, carbon steel + Ca\_Mg bentonite + MX80; 70 °C; anaerobic conditions in the borehole);
- laboratory corrosion test UOS (laboratory; Mn steel + Ca\_Mg bentonite; 70 °C; anaerobic box);

### 2.1 Laboratory experiments with Corrosion products CoPr (Fe powder/carbon steel/bentonite)

Corrosion products (CoPr) experiment was aimed to conduct experiment that simulated a situation of the intensive exposure of bentonite to iron ions produced due to corrosion. This was achieved through the use of powdered iron with a large reaction surface and an enhanced iron/bentonite ratio compared to the use of solid metal samples that are generally used in such corrosion tests. With the exception of temperature (laboratory, 40°C and 70°C) and time (the duration of the experiments ranged from 97 to 487 days), the other parameters were fixed (i.e. the amount of iron and bentonite in the reaction system (bentonite/Fe ratio = 3.5:1), the saturation liquid composition and pressure (synthetic groundwater, 5 MPa) and anaerobic conditions (the experiments were conducted in a glovebox).

The experiments tried to accelerate formation of corrosion products as those are usually formed in small amounts within conventional corrosion experiments. The experiments were conducted under SURAO funded project and were summarised and presented in Gondolli et al. (2018b).

#### 2.1.1 Materials

##### 2.1.1.1 Bentonite

The type of bentonite used in these experiments was **BaM** (commercial name “Bentonite and Montmorillonite”, produced by KERAMOST a.s. (Czech Republic)). This type of bentonite was also used for the experiments described in chapter 2.3. Bentonite composition is described in Červinka and Gondolli (2015) (Table 2-1 and Table 2-2). The X-ray diffraction pattern of the BaM bentonite is presented in Figure 2-1 and its specific surface in Table 2-3.

Table 2-1 – Bulk chemical analysis of Czech BaM bentonite (Červinka and Gondolli, 2015)

Component	% dry wt.
SiO <sub>2</sub>	49.99
Al <sub>2</sub> O <sub>3</sub>	14.56
Fe <sub>2</sub> O <sub>3</sub>	12.22
TiO <sub>2</sub>	3.10
CaO	3.11
MgO	3.16
Na <sub>2</sub> O	0.19
K <sub>2</sub> O	0.90
P <sub>2</sub> O <sub>5</sub>	0.70
MnO	0.120
SO <sub>3</sub> total.	0.10
SO <sub>3</sub> sulfate.	0.08
FeO	4.79
CO <sub>2</sub>	4.53

Table 2-2 – BaM bentonite semiquantitative X-ray powder diffraction results (Červinka and Gondolli, 2015)

Component	% dry wt.
Smectite (montmorillonite)	88
Quartz	5
Anatase	4
Siderite (Ca, Mg)	3

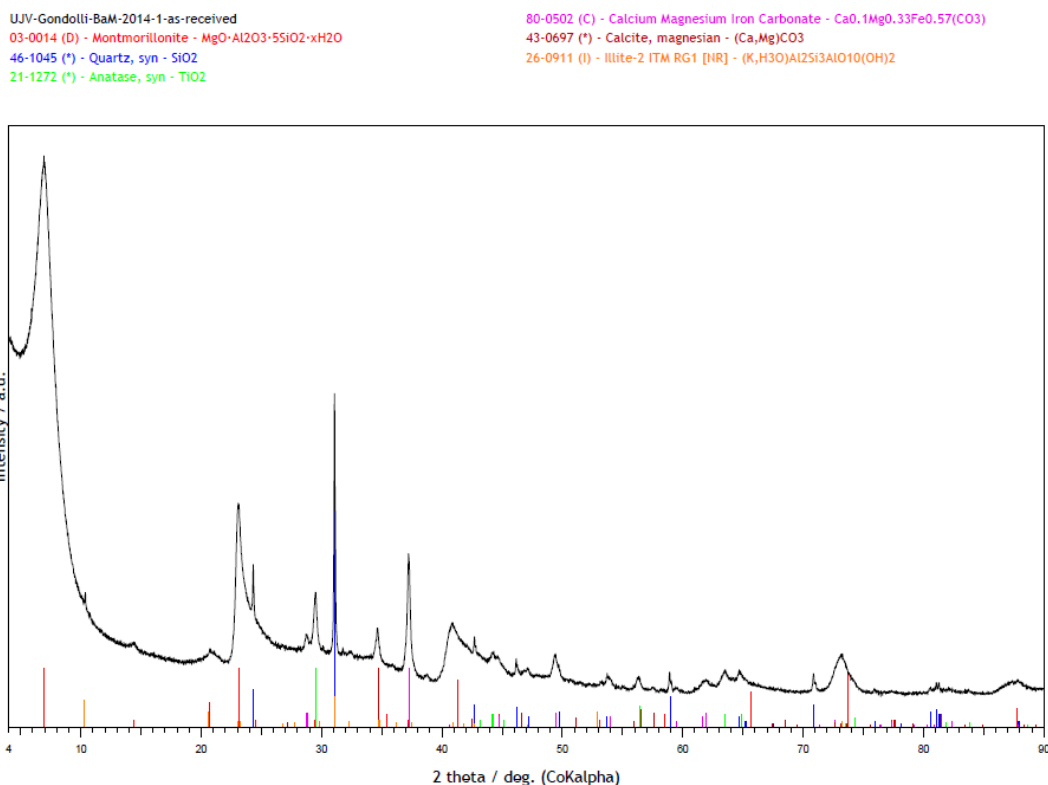


Figure 2-1 – X-ray diffraction pattern of source bentonite BaM (lot 2014-1). (Gondolli et al. 2018b)

#### 2.1.1.2 Metal samples

The metal samples used in this work were iron powder (high purity iron, Riedel-de Haën (Germany)) and **steel No. 12050**.

Due to the fact that a powder sample of suitable carbon steel was not available on the market and its laboratory preparation would be complicated and would not necessarily lead to a homogeneous material for all experiments, it was decided to use iron powder. Iron powder samples were prepared from commercially available material produced by Riedel-de Haën (Germany; product code 12310, batch 51400, declared grain size  $<212 \mu m$ ). The iron powder was not treated in any way before being placed in the corrosion cells (Gondolli et al. 2018a).

The specific surface of the iron powder is presented in the Table 2-3 and a view of the structure in *Figure 2-2*.

The supporting steel discs were made from carbon steel 12050 (Table 2-4) and were used as provided; only degreasing was applied prior to their installation. Their surface was not modified in any way and before the experiment their condition was only visually checked before being weighed on analytical scales (Gongolli et al. 2018a).

Table 2-3 – Results of specific surface and volume of micropores for iron powder (lot 51400) and bentonite BaM (lot 2014-1). Specific surface was determined using the BET method, and the DFT calculation was also applied to the iron powder (because of its microporous structure) (Gondolli et al. 2018b)

Replication	Iron powder $S_{BET}$ [ $m^2 g^{-1}$ ]	Iron powder $S_{DFT}$ [ $m^2 g^{-1}$ ]	Iron powder $V_{micro(DFT)}$ [ $cm^3 g^{-1}$ ]	Bentonite BaM $S_{BET}$ [ $m^2 g^{-1}$ ]
1	18.447	6.554	0.016	125.701
2	32.010	11.028	0.027	121.702
3	42.068	14.825	0.036	121.919

Table 2-4 – Chemical composition of carbon steel 12050

Component	C	Si	Mn	P	S	Cr	Ni	Mo
[%]	0.435	0.253	0.560	0.007	0.001	0.18	0.13	0.030

### 2.1.1.3 Solution for the saturation of bentonite samples

For bentonite saturation, synthetic granitic water SGW was used, with composition (Table 2-5) and parameters described in Červinka and Gondolli (2015) and Gondolli et al. (2018a).

Table 2-5 – Composition of synthetic ground water used for bentonite saturation. (Červinka a Gondolli, 2015)

Component	Na <sup>+</sup>	K <sup>+</sup>	Ca <sup>2+</sup>	Mg <sup>2+</sup>	Cl <sup>-</sup>	SO <sub>4</sub> <sup>2-</sup>	HCO <sub>3</sub> <sup>-</sup>
[mg dm <sup>-3</sup> ]	10.4	1.8	19	7	33.6	27.7	30.4

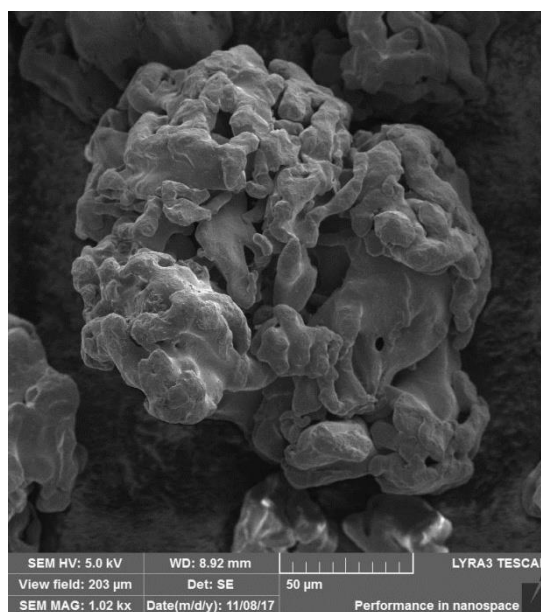


Figure 2-2 – View of the iron powder particle structure, magnification x1020. (Gondolli et al. 2018b)

### 2.1.2 Conditions

The experiment was performed in anaerobic conditions, in special cells at ambient temperatures, 40 °C and 70 °C. In order to remove the additional oxygen from the experimental cells, they were placed inside a glove box MB 200B (MBRAUN GmbH, Germany;  $c(O_2) < 0.1$  ppm) for a period of 14 days before the start of the saturation process and kept in the glove box until the end of the corrosion experiment.

The initial pressure applied during the saturation period of the cells with granitic grater, was near atmospheric values, and then it was gradually increased up to 5 MPa. After four days of saturation, heating devices were switched on for selected cells. In the following series of cells, these two steps were initiated simultaneously.

An illustrative figure of operating experimental equipment is presented in Figure 2-3 and Figure 2-4 (Gondolli et al. 2018b). A steel disc (35 mm x 1 mm) was inserted into the experimental cell and a determined amount of iron powder was evenly distributed over its surface. Then, a force of 10 kN was applied to the powder for a short time to form a cohesive layer. Later, a determined amount of bentonite was placed in the cell and compacted to a dry density of  $1600 \text{ kg m}^{-3}$  using a hydraulic press.

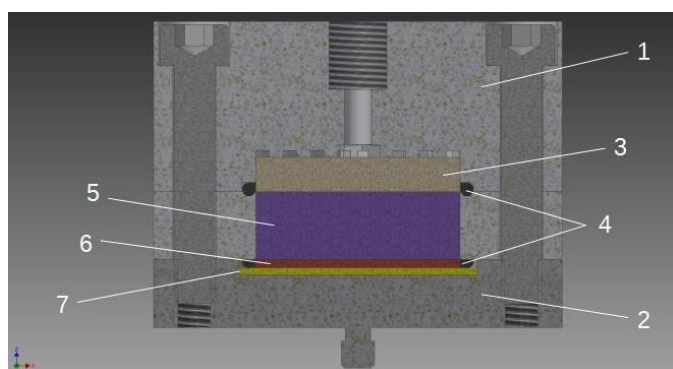


Figure 2-3 – Schematic cross-section of experimental cell. 1-body made of plastic composite, with a water inlet, 2-metal bottom, 3-porous stone, 4-seals, 5-compacted bentonite, 6-iron powder, 7-steel disc



Figure 2-4 – Fully operating experimental setup inside a glove box. A pressure exchanger with synthetic groundwater is shown on the right, a water saturation system with pressure monitor is shown in front and two heating devices with temperature regulators are shown at the back

Sample sets for each temperature were prepared for four different durations of each set: 0.25, 0.5, 1 and 1.5 years. Replications of short time sets were prepared only for 0.5-year and 1-year sets. The real duration of the experiments was 97, 188, 189, 340, 377 and 487 days.

Once the experiment was finished, the cells were disconnected from the granitic water saturation and the heating devices and left to cool to laboratory temperature. Afterwards, cells were dismantled and experimental materials, steel discs, iron powder with corrosion products and compacted bentonite were removed, photographed and left inside the glove box to dry (Figure 2-5 and Figure 2-6). Examples of dried samples are presented in Figure 2-7 and Figure 2-8 (Gondolli et al. 2018b). The iron powder samples were transported in gas-tight vials for further analyses.



Figure 2-5 – Middle part of experimental cell (40 °C, duration 487 days) after separation of the steel disc; the grey layer is a mixture of iron powder with corrosion products attached to compacted bentonite



Figure 2-6 – Detailed view of a steel disc with attached layer of iron powder with corrosion products (40 °C, duration 487 days)



Figure 2-7 – Compacted bentonite with partly separated layer of a mixture of iron powder with corrosion products (laboratory temperature, duration 189 days)

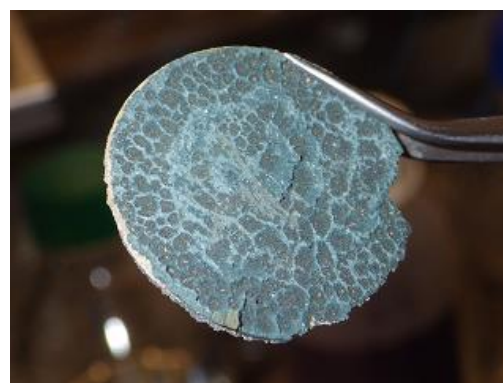


Figure 2-8 – Compacted “porous disc” of a mixture of iron powder with corrosion products (70 °C, duration 340 days); dark green lines and spots are corrosion/alteration products

## 2.1.3 Results

### 2.1.3.1 Bentonite

According to the results of the X-ray diffraction technique, apparently the corrosion processes did not have an impact on bentonite sampled from the iron-bentonite alteration interfaces, since no crystalline corrosion products were identified in this material. However, it is important to note, that the visual state of the bentonite may indicate the presence of some corrosion/alteration products, but since a significant amount of them were not crystalline, the X-ray diffraction method was unable to identify them, see Figure 2-9 and Table 2-6 (Gondolli et al. 2018b).

UJV Gondoli 3 bent  
 03-0014 (D) - Montmorillonite - MgO·Al<sub>2</sub>O<sub>3</sub>·5SiO<sub>2</sub>·xH<sub>2</sub>O  
 46-1045 (\*) - Quartz, syn - SiO<sub>2</sub>  
 21-1272 (\*) - Anatase, syn - TiO<sub>2</sub>  
 80-0502 (C) - Calcium Magnesium Iron Carbonate - Ca<sub>0.1</sub>Mg<sub>0.33</sub>Fe<sub>0.57</sub>(CO<sub>3</sub>)  
 06-0696 (\*) - Iron, syn - Fe  
 26-0911 (I) - Illite-2 ITM RG1 [HR] - (K,H<sub>3</sub>O)Al<sub>2</sub>Si<sub>3</sub>AlO<sub>10</sub>(OH)<sub>2</sub>  
 36-0426 (\*) - Dolomite - CaMg(CO<sub>3</sub>)<sub>2</sub>

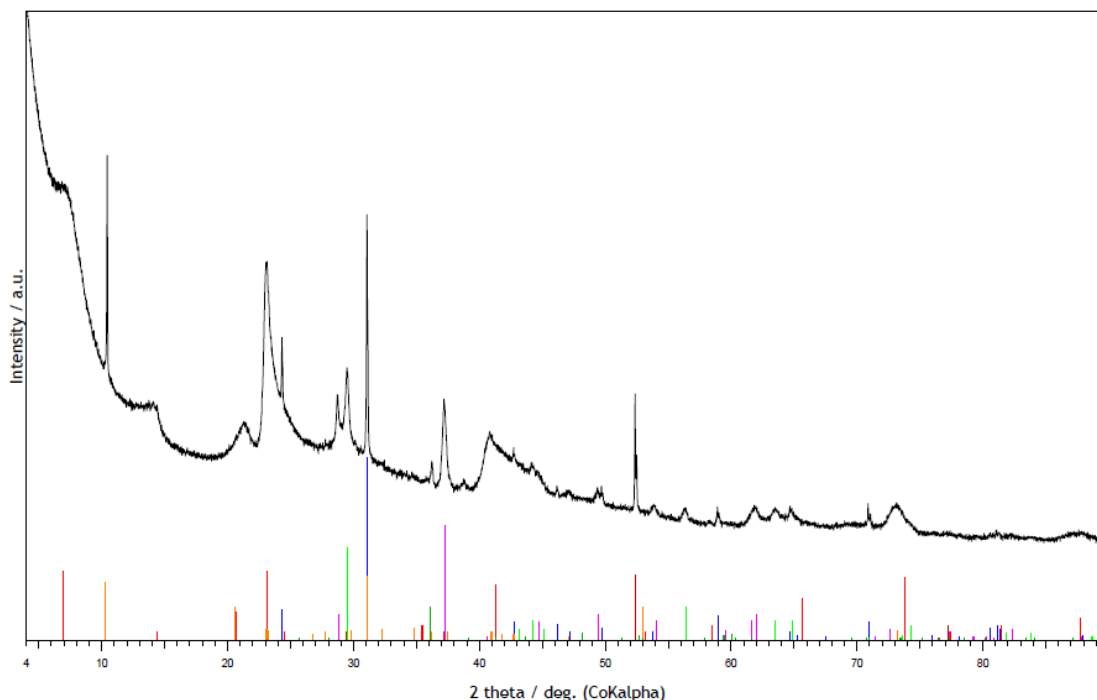


Figure 2-9 – X-ray diffraction pattern obtained for the bentonite sample taken from the experimental cell after 189 days at 70 °C

Table 2-6 – Crystalline phases of corrosion / alteration products identified **in bentonite** samples by X-ray diffraction. “+” means positive detection

Sample from cell.	Temperature	Iron	Magnetite	Carbonates, another phase
189 days series (replica)				
	LAB	-	-	Mixed Ca,Mg,Fe
	40 °C	+	-	Mixed Ca,Mg,Fe
	70 °C	-	-	Mixed Ca,Mg,Fe
340 days series				
	LAB	+	-	Mixed Ca,Mg,Fe; calcite
	40 °C	+	-	Mixed Ca,Mg,Fe
	70 °C	+	-	Mixed Ca,Mg,Fe
377 days series				
	LAB	+	-	Mixed Ca,Mg,Fe
	40 °C	+	-	Mixed Ca,Mg,Fe
	70 °C	-	-	Mixed Ca,Mg,Fe

Sample from cell.	Temperature	Iron	Magnetite	Carbonates, another phase
487 days series				
	LAB	+	-	Mixed Ca,Mg,Fe; illite, calcite
	40 °C	+	-	Mixed Ca,Mg,Fe
	70 °C	+	-	Mixed Ca,Mg,Fe

The cation exchange capacity (CEC) of bentonite samples from the iron-bentonite alteration interfaces was found to be significantly lower in comparison to source bentonite BaM (Figure 2-10 and Table 2-7). The method used for CEC determination cannot distinguish whether such a CEC decrease is caused by a montmorillonite alteration or the contribution of the presence of newly formed phases (corrosion or alteration products) with very low CEC.

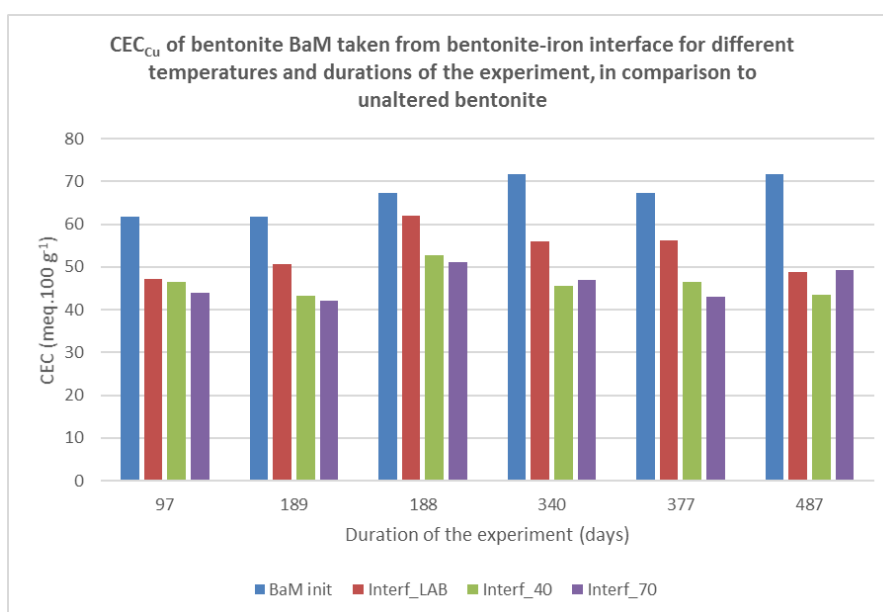


Figure 2-10 – Graphical presentation of CEC<sub>Cu</sub> values of bentonite BaM taken from the bentonite-iron interface for three different temperatures (laboratory, 40 and 70 °C) and durations of the experiment (from 97 to 487 days), in comparison to unaltered bentonite BaM. The x-axis shows the total duration of each set of samples in days; the sample set of 188 days is a replication of a previous half-year set. (Gondolli et al. 2018b)

Table 2-7 – Cation exchange capacity values of bentonite samples from the bentonite / iron powder interface determined by the Cu-triene method,  $CECCu$  values calculated from the difference in copper concentration,  $CEC_{Sum}$  values calculated from the sum of exchanged majority ions (Na, K, Ca, Mg). All CEC values corrected for natural / residual moisture of bentonite and a blank sample of Cu-triene (chemical composition). (Gondolli et al. 2018b)

Bentonite sample from cell no.	Temperature	$CEC_{Cu}$ [meq.100 g <sup>-1</sup> ]	$CEC_{Sum}$ [meq.100 g <sup>-1</sup> ]	Note
189 days series (replica.)				
	LAB	62,1	65,5	Single value
	40 °C	52,8	56,0	Single value
	70 °C	51,1	51,5	Single value
340 days series				
	LAB	55,9	58,2	Single value
	40 °C	45,5	43,3	Single value
	70 °C	47,0	47,5	Single value
377 days series				
	LAB	56,2	59,3	Single value
	40 °C	46,6	47,2	Single value
	70 °C	43,0	42,3	Single value
487 days series				
	LAB	48,7	47,3	Single value
	40 °C	43,6	39,2	Single value
	70 °C	49,4	48,1	Single value
Reference sample				
Initial BaM	-	67,4	70,4	Average values
Reference sample				
Initial BaM	-	71,8	74,4	Average values

For all bentonite samples taken from the iron-bentonite alteration interfaces, changes in the fraction of exchangeable magnesium and calcium were also found – the fraction of exchangeable magnesium decreased, and that of exchangeable calcium increased, with rising temperature. On the other hand, the fraction of exchangeable iron was very low.

#### 2.1.3.2 Metal samples

After cells dismantling, it was observed that most of the iron powder remained unreacted. A solid compact layer of iron powder was formed at 70 °C. In cells at 40 °C, a solid layer was formed in long-term experiments (≥188 days).

Analytical techniques (X-ray diffraction and Raman spectroscopy) were used in order to detect the corrosion products. In the case of steel discs, firstly, the samples were analysed with a corrosion product layer and afterwards, this layer was removed and analysed separately. In the case of the mixture of iron powder and corrosion product samples taken from the cells at 70 °C, both sides of each “porous disc” were analysed separately when possible.

The corrosion products were found mostly on the steel discs’ surface or in the mixture of iron powder with corrosion products. Magnetite was observed in cells at 70 °C and iron carbonates i.e.: chukanovite, and to a lesser extent siderite in cells at 40 °C. The corrosion products on steel discs are shown in Table 2-8, and in iron powder in Table 2-9 (Gondolli et al., 2018b).

*Table 2-8 – Crystalline phases identified on **steel discs** by X-ray diffraction. “+” means positive detection, “++” means that the given phase predominates (semi-quantitative determination). LAB = laboratory temperature*

Disc no.	Temperature	Magnetite	Chukanovite
189 days series (replica)	LAB	-	+
	40 °C	-	+
	70 °C	+	-
340 days series	LAB	-	+
	40 °C	-	+
	70 °C	+	+
377 days series	LAB	-	+
	40 °C	-	+
	70 °C	+	+
487 days series	LAB	-	+
	40 °C	-	+
	70 °C	+	+

Table 2-9 – Crystalline phases identified in **iron powder samples** by X-ray diffraction. “+” positive detection, “++” phase predominates (semi-quantitative determination), “?” unidentified phases have been detected. LAB = laboratory temperature.

Temperature (°C)	Type of sample	Period of experiment (days)	Iron	Magnetite	Chukanovite	Another phase
Laboratory	Iron powder	189	++	-	-	n.d.
Laboratory	Iron powder	340	++	-	-	-
Laboratory	Iron powder	377	++	-	-	n.d.
Laboratory	Iron powder	487	++	-	-	-
40 °C	Iron powder in contact with the steel disk	189	++	-	-	n.d.
40 °C	Iron powder in contact with the bentonite	189	++	-	-	n.d.
40 °C	Iron powder in contact with the steel disk	340	++	-	-	-
40 °C	Iron powder in contact with the bentonite	340	++	-	-	-
40 °C	Iron powder in contact with the steel disk	377	++	-	-	-
40 °C	Iron powder in contact with the bentonite	377	++	-	+	-
40 °C	Iron powder in contact with the steel disk	487	++	-	+	-
40 °C	Iron powder in contact with the bentonite	487	++	-	-	-
70 °C	Iron powder in contact with the steel disk	188	++	+	+	
70 °C	Iron powder in contact with the bentonite	188	++	-	-	siderite
70 °C	Iron powder in contact with the steel disk	189	+	+	+	-

Temperature (°C)	Type of sample	Period of experiment (days)	Iron	Magnetite	Chukanovite	Another phase
70 °C	Iron powder in contact with the bentonite	189	+	-	-	Rests of bentonite
70 °C	Iron powder in contact with the steel disk	340	++	+	+	
70 °C	Iron powder in contact with the bentonite	340	++	-	-	Rests of bentonite
70 °C	Iron powder in contact with the steel disk	377	++	++	+	-
70 °C	Iron powder in contact with the bentonite	377	++	-	-	siderite, rests of bentonite
70 °C	Iron powder in contact with the bentonite	487	++	-	-	rests of bentonite

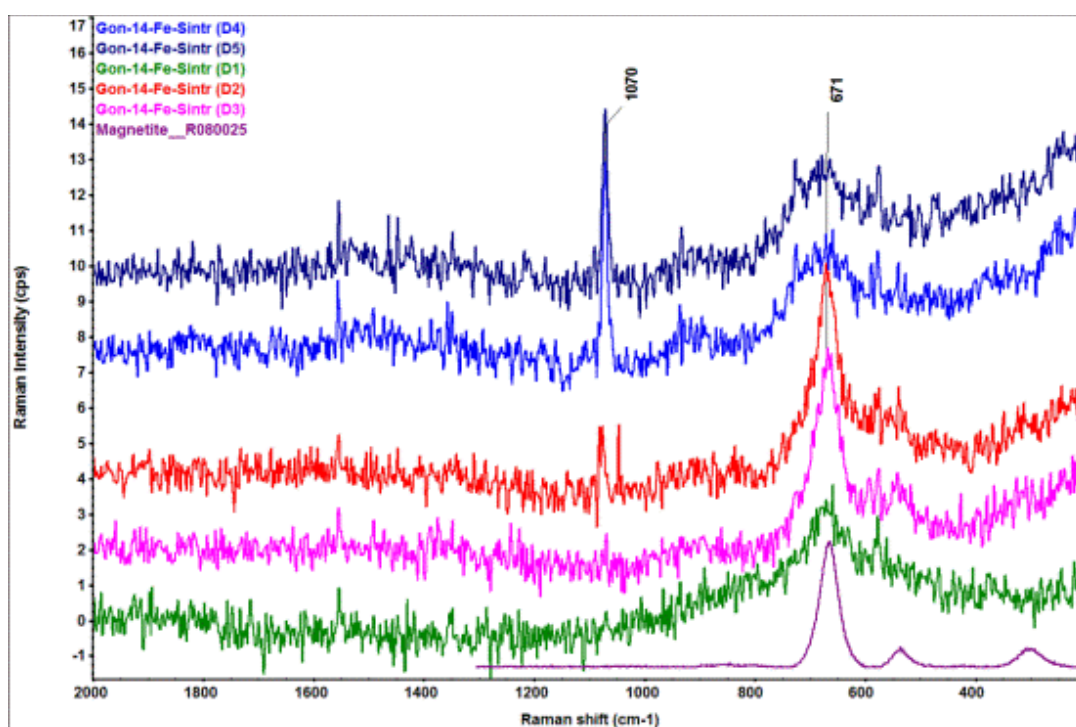


Figure 2-11 – Raman spectra obtained for “porous disc” of iron powder taken from the experimental cell after 340 days at 70 °C, the side of the contact with a steel disc analyzed. The Raman shift marked at 1070 cm<sup>-1</sup> belongs to carbonate, the Raman shift marked at 671 cm<sup>-1</sup> belongs to magnetite. Reference magnetite spectrum (RRUFF database, [www.ruff.info](http://www.ruff.info)) shown for comparison

## 2.2 In situ experiment MaCoTe (carbon steel/bentonite)

The Material Corrosion Test (MaCoTe) in the Grimsel test site (<https://www.grimsel.com/gts-phase-vi/macote-the-material-corrosion-test/macote-introduction>) consists of non-heated and heated experiments to study in-situ corrosion of candidate canister materials embedded in bentonite.

Two broad aims of the project are as follows:

- Provide confirmation of the long-term anaerobic corrosion rate of carbon steel, stainless steel and copper in compacted bentonite under repository-relevant environmental conditions,
- Provide experimental evidence of the inhibiting effect of the bentonite buffer on microbial activity and microbially-influenced corrosion.

The part, included into the WP ACED, exploits results of the heated experiment, studying a gradual temperature induced contact of carbon steel samples with two types of bentonites, CZ Ca-Mg bentonite and Na bentonite under real conditions of granitic rock massive in Grimsel test site (Dobrev et al, 2018). The project has been conducted under SURAO funding and represents the only experiment with Czech Ca-Mg bentonite being held under real in-situ conditions of real granitic host rock massive.

### 2.2.1 Materials

#### 2.2.1.1 Bentonite

Two types of bentonites were used. One of them was Czech bentonite (BaM) known as Bentonite and Montmorillonite (KERAMOST a.s., Czech Republic) and the other was MX-80 from Swiss NAGRA. The dry bulk density of both bentonites used in the experiment was  $1.5 \text{ g cm}^{-3}$ .

The bentonites were pressed into rings of 50 mm high, 50 mm inner diameter. and 72.4 mm outer diameter. The silicate analysis of both types of bentonite is shown in Table 2-10. Results of semiquantitative X-ray powder diffraction for bentonite BaM were presented in chapter 2.1.1, whereas in the case of bentonite MX-80 this information was taken from Ruedi et al. (2013) since these measurements were not carried out in the MaCoTe project (Table 2-11).

Table 2-10 – Silicate analysis of bentonite MX-80 and bentonite BaM used in experiments (Dobrev et al. 2018).

	<b>MX-80</b> [% (w/w dry matter)]	<b>BaM</b> [% (w/w dry matter)]
Annealing loss (1000°C)	11.62	16.53
SiO <sub>2</sub>	55.81	44.76
Al <sub>2</sub> O <sub>3</sub>	17.76	15.85
Fe <sub>2</sub> O <sub>3</sub> total	3.88	9.01
TiO <sub>2</sub>	0.15	0.79
CaO	2.34	1.87
MgO	1.30	2.39
Na <sub>2</sub> O	1.25	0.35
K <sub>2</sub> O	0.56	2.47
MnO	0.026	0.092
P <sub>2</sub> O <sub>5</sub>	0.23	0.43
SO <sub>3</sub> sulphate	0.18	0.02
CO <sub>2</sub>	0.43	2.51
FeO	0.68	1.35

Table 2-11 – Semiquantitative X-ray powder diffraction results of MX-80 (Ruedi et al. 2013)

Component	w/w %.
Smectite (montmorillonite)	84.9
Muscovite	4.8
Quartz	3.7
Feldspar	5.2
Calcite	1.3

### 2.2.1.2 Metal samples

Carbon steel 12022 (Železiarne Podbrezová, Slovakia) was used to prepare the metal samples with the next measurements: 18 mm high, 50 mm o.d.. The terminal samples were 24 and 21 mm high for the larger and smaller modules, respectively. (Dobrev et al., 2017a)



Figure 2-12 – Carbon steel sample

Table 2-12 shows the chemical composition of carbon steel 12022. Here it is possible to see the results of an independent analysis performed with a FOUNDRY-MASTER Xline optical emission spectrometer (Oxford Instruments, UK), the chemical composition according to the standard and the data of melt No. 30875 (Certificate 13978/1/2013, Železiarne Podbrezová, Slovakia) provided by the manufacturer. The table demonstrates a very good agreement between the observed data and those reported by the manufacturer.

Table 2-12 – Chemical composition of carbon steel 12022 according to the standard, according to the manufacturer and obtained by analysis. Dobrev et al. (2018)

	C [%]	Mn [%]	Si [%]	P [%]	S [%]	Cu [%]	Cr [%]	Ni [%]	Fe [%]
Standard	0.15-0.22	0.5-0.8	0.17-0.37	0.04	0.04	0.25	0.25	0.25	Up to 100%
Melt No. 30875	0.16	0.53	0.23	0.009	0.008	0.14	0.03	0.06	Up to 100%
Analysis	0.18	0.51	0.21	0.009	0.006	0.15	0.03	0.05	Up to 100%

The microstructure of carbon steel was ferritic pearlitic and contained carbide and sulphide inclusions. The results were consistent with ČSN 41 2022.

### 2.2.1.3 Solution for the saturation of bentonite samples

Anoxic groundwater from the Grimsel Test Site (GTS) was used for saturation of the bentonite samples. It had been delivered from the site in 4 closed plastic containers under Ar gas. The required groundwater quantity (2 plastic containers) was transferred into the argon-filled glove box. The pH, Eh and O<sub>2</sub> content

were measured. The following data were obtained in the 2 containers: pH = 9.24 and 9.26, respectively, oxidation-reduction potential converted to the standard hydrogen electrode  $E_h = 203,7$  mV and 201,5 mV, respectively,  $cO_2 < 0,1$  mg/l. Dobrev et al. (2017a) measured the cation and anion concentrations in the groundwater used to pre-saturate the modules by atomic absorption spectroscopy (AAS) on a Savant AA instrument (GBC, Australia), the results are shown in Table 2-13. Once the saturation process was over, the oxygen content in the water was below  $0.01$  mg l<sup>-1</sup>.

Table 2-13 – Composition of Grimsel ground water (GGW) used for bentonite saturation. (Dobrev et al. 2017a)

Component	Na <sup>+</sup>	K <sup>+</sup>	Ca <sup>2+</sup>	Mg <sup>2+</sup>	Fe	Cl <sup>-</sup>	F <sup>-</sup>	NO <sub>3</sub> <sup>-</sup>	SO <sub>4</sub> <sup>2-</sup>	Total alkalinity
[mg dm <sup>-3</sup> ]	8.3	0.2	7.5	0.009	< 0,1	0.9	3.9	Not detected	5.64	18.1

### 2.2.2 Conditions

Two types of modules were assembled, larger modules carried 10 carbon steel samples, the shorter modules, 5 carbon steel samples (Figure 2-13). Bentonite BaM was used for the larger modules, bentonite MX-80 for the shorter modules.



Figure 2-13 – Modules with bentonite BaM (left) and MX-80 (right). Dobrev et al. (2018)

In order to attain anaerobic conditions for the experiment, the assembled modules were placed in an MB 200B glove box (MBRAUN GmbH, Germany) prior to saturation with ground water from the Grimsel Test Site (GTS).

A temperature of 70 °C was selected for the experiment based on calculation of the disposal canister surface temperature.

A total of five boreholes (15.001, 15.002, 15.003, 15.004, 15.005) were installed in the Grimsel Test Site see Figure 2-14.



Figure 2-14 – The corrosion testing apparatus installed in the natural granitic environment of the GTS (photo Nagra)

Once the experiment was finished (after 1, 2 and 3 years) the apparatus was taken from the boreholes no. 15.001, 15.002 and 15.004, together with samples of groundwater from the GTS for microbiological analyses.

Inside the glove box, two bentonite samples were taken from each module: from the top cap area and from the bottom cap area. The humidity inside the glove box is very low and so partial sample drying could not be avoided. This introduces an uncertainty into the evaluation, which must be taken into account when evaluating the results.

## 2.2.3 Results

### 2.2.3.1 Bentonite BaM and MX-80

Dobrev et al. (2018) point out that the moisture content of the bentonites at dry bulk density  $1,5 \text{ g.cm}^{-3}$  is about 35% (both in the 1-year, 2-years and 3-years corrosion tests).

### 2.2.3.2 Metal samples

The mean corrosion rates of carbon steel in the environment of bentonite BaM and of bentonite MX-80 (measured in 1 year of the experiment) are similar. A similar situation is observed after 2 and 3 years (Figure 2-15). Since a smaller number of samples is available for the evaluation of the corrosion rate from the bentonite MX-80 compared to the BaM bentonite, the variance of the corrosion rate is much greater specially in the 2-years experiment.

Dobrev et al. (2018, 2020) point out that final conclusions can be made when the results from the remaining modules will be available. Non-uniform corrosion was observed in all the carbon steel samples.

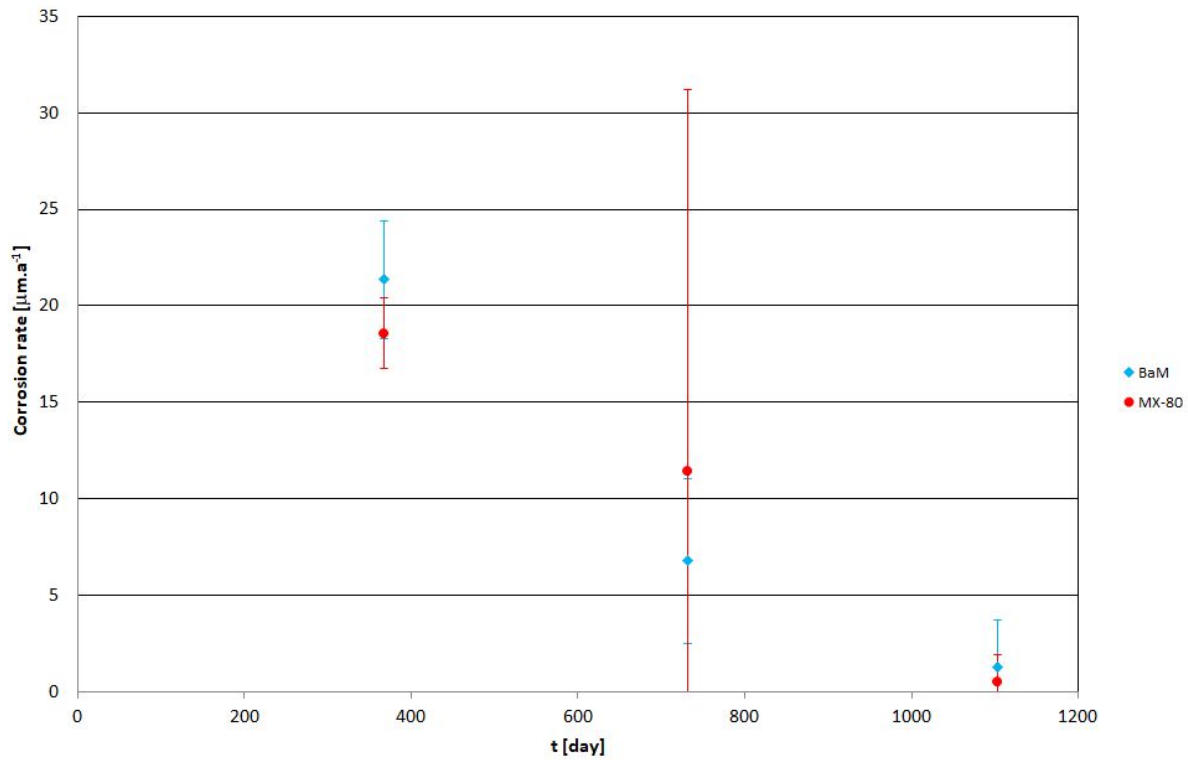


Figure 2-15 – Mean carbon steel corrosion rates in bentonite BaM and in bentonite MX-80 (Dobrev et al., 2020). Time (in days) on x axis; corrosion rate (μm/year) on y axis.

Corrosion products identified by X-ray diffraction analysis (PANalytical, B. V., Almelo, The Netherlands, Co cathode, 40 kV, 30 mA) on the carbon steel samples in the bentonite BaM environment after 1 and 2 years of experiments were chukanovite and siderite (Figure 2-16). Only chukanovite was detected after the 3-years experiment. In the bentonite MX-80 environment, only siderite was identified on the carbon steel samples (Table 2-14, Table 2-15, Table 2-16).

MaCoTe\_AN\_BaM\_Fe\_1\_01  
 06-0696 (\*) - Iron, syn - Fe  
 60-0353 (I) - Chukanovite - Fe2(CO3)(OH)2  
 46-1045 (\*) - Quartz, syn - SiO2  
 03-0014 (D) - Montmorillonite - MgO·Al2O3·5SiO2·xH2O  
 26-0911 (I) - Illite-2 ITM RG1 [NR] - (K,H3O)Al2Si3AlO10  
 86-2336 (C) - Calcite magnesian - (Mg<sub>12</sub>Ca<sub>8</sub>71)(CO<sub>3</sub>)<sub>10</sub>  
 29-0696 (\*) - Siderite - FeCO<sub>3</sub>  
 80-0885 (C) - Kaolinite 1 ITA RG - Al<sub>2</sub>(Si<sub>2</sub>O<sub>5</sub>)(OH)<sub>4</sub>

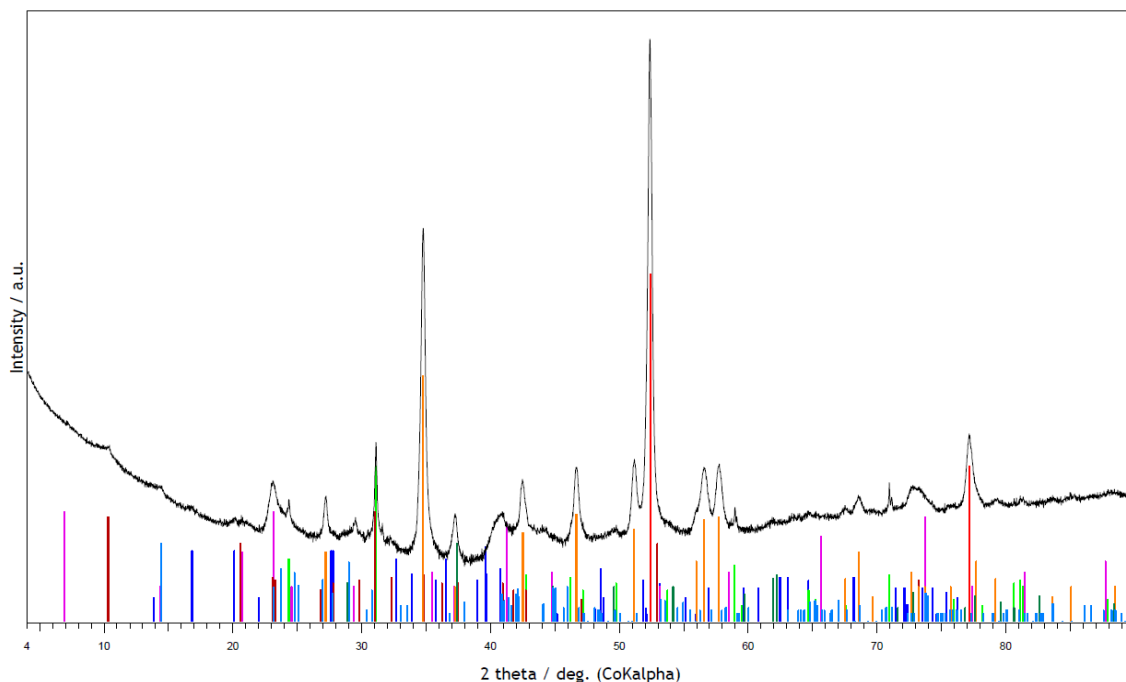


Figure 2-16 – Illustrative diffraction trace for carbon steel in bentonite in the 1-year experiment. (Dobrev et al., 2018)

Raman spectra (DXR Smart Raman instrument, Thermo Scientific, USA), exhibited a weak signal of carbonate on some of the steel samples. Whether it was siderite or chukanovite could not be determined. No corrosion products were found by Raman spectroscopy on the remaining carbon steel samples. Both carbon steel sample types exhibit non-uniform corrosion and the corrosion rates are similar. Any other corrosion products could not be identified by the methods used (quantity below the detection limits, amorphous phase, etc.).

Table 2-14 – Corrosion products identified on the metal samples after 1 year, borehole 15.001. (Dobrev et al. 2018)

Sample	Bentonite	X-ray diffraction analysis	Raman spectroscopy
1	BaM	Siderite Chukanovite	Carbonate
2	BaM	Siderite	Not detected
3	BaM	Siderite	Not detected
4	BaM	Not detected	Not detected
5	BaM	Siderite Chukanovite	Not detected
6	BaM	Siderite Chukanovite	Carbonate
7	BaM	Siderite Chukanovite	Carbonate

Sample	Bentonite	X-ray diffraction analysis	Raman spectroscopy
8	BaM	Siderite Chukanovite	Not detected
9	BaM	Siderite Chukanovite	Not detected
10	BaM	Siderite	Carbonate
1	MX-80	Siderite	Carbonate
2	MX-80	Siderite	Carbonate
3	MX-80	Siderite	Not detected
4	MX-80	Siderite	Carbonate
5	MX-80	Siderite	Carbonate

Table 2-15 – Corrosion products identified on the metal samples after 2 years, borehole 15.002. (Dobrev et al. 2018)

Sample	Bentonite	X-ray diffraction analysis	Raman spectroscopy
1	BaM	Chukanovite	Carbonate
2	BaM	Chukanovite	Carbonate
3	BaM	Chukanovite	Carbonate
4	BaM	Chukanovite	Carbonate
5	BaM	Chukanovite	Not detected
6	BaM	Chukanovite	Carbonate
7	BaM	Chukanovite	Carbonate
8	BaM	Chukanovite	Carbonate
9	BaM	Chukanovite	Not detected
10	BaM	Chukanovite	Carbonate
1	MX-80	Siderite	Carbonate
2	MX-80	Siderite	Not detected
3	MX-80	Siderite	Carbonate
4	MX-80	Siderite	Carbonate
5	MX-80	Siderite	Carbonate

Table 2-16 – Corrosion products identified on the metal samples after 3 years, borehole 15.004. (Dobrev et al. 2020)

Sample	Bentonite	X-ray diffraction analysis	Raman spectroscopy
1	BaM	Chukanovite	Not detected
2	BaM	Chukanovite	Not detected
3	BaM	Chukanovite	Not detected
4	BaM	Chukanovite	Not detected
5	BaM	Chukanovite	Not detected
6	BaM	Chukanovite	Not detected
7	BaM	Chukanovite	Not detected
8	BaM	Chukanovite	Not detected
9	BaM	Chukanovite	Carbonate
10	BaM	Chukanovite	Not detected
1	MX-80	Siderite	Not detected
2	MX-80	Siderite	Carbonate
3	MX-80	Siderite	Not detected
4	MX-80	Siderite	Carbonate
5	MX-80	Siderite	Not detected

The authors note that these are only preliminary results and it is necessary to wait for the results from the remaining boreholes.

## 2.3 Laboratory experiment with canister material (carbon steel/bentonite, UOS)

The UOS experiment was focused on a laboratory survey of anaerobic corrosion of a potential disposal canister material in contact with CZ Ca-Mg bentonite. The results used here in WP ACED include the heated (70 °C) experiment with manganese steel 422707.9 under anaerobic conditions in a glove box. The experiment tries to simulate DGR conditions in the heated period not long after SNF disposal.

### 2.3.1 Materials

#### 2.3.1.1 Bentonite

Experiments were carried out in the context of a SURAO funded project and were analyzed and reported by Dobrev et al. (2017b).

In this work, bentonite "Bentonite and Montmorillonite" (BaM) commercially produced by KERAMOST a.s. was used. More detailed information on "BaM" bentonite can be found in the report Červinka and Gondolli, (2015) and in Table 2-1 and Table 2-2 of this report.

#### 2.3.1.2 Metal samples

Corrosion tests were conducted with five types of metallic materials designed to be potentially suitable for the design of storage packaging assemblies (UOS). Carbon steel, titanium alloy and copper for the outer shell and austenitic stainless steel, two-phase stainless steel and carbon steel have been designed

for the inner shell.. Even though different types of metallic samples were tested, this report focuses on manganese steel 422707.9 (ČSN 422707) used instead of steel 12022 due to the unavailability 12022 at that moment. The similar chemical composition was taken into account.

### 2.3.1.3 Solution for the saturation of bentonite samples

Synthetic granitic water (SGW) was used to saturate the bentonite in the compacted bentonite tests – see Table 4.

## 2.3.2 Conditions

The metal samples (diameter of 35 mm and thickness of 1 mm) were degreased in ethanol and weighed prior to the corrosion test.

The bentonite BaM ( $1600 \text{ kg}\cdot\text{m}^{-3}$ ) was pressed directly into corrosion cells and its dimensions were 30 mm diameter and 11 mm height. The natural water content of bentonite BaM (9.93% by weight) was taken from the results of the silicate bentonite analysis performed by Gematest spol. s r.o.

The bentonite in the corrosion cells was saturated with SGW (synthetic granitic water), which was previously deoxygenated in a glove box MB 200B (MBRAUN GmbH, Germany) with an argon atmosphere (Linde Gas as, Czech Republic).

The arrangement in the corrosion cell (*Figure 2-17*) was as follows: a sample of metallic material was placed in the lower metal part of the corrosion cell. The central plastic part of the cell was then placed on the lower metal part together with a o-ring and pressed into it using a MEGA 11-300 DM1S hydraulic press (Form + Test Seidner + Co GmbH, Germany) to obtain the required amount of bentonite corresponding to the dry bulk density requirement mentioned above. After the bentonite was pressed into the central part, an upper plastic part with a bentonite sample saturation system and a frit was attached to the corrosion cell and the entire corrosion cell was closed. Afterwards the assembled cells were evacuated ( $-0,1 \text{ MPa}$ ) and placed in an argon atmosphere glove box to remove as much oxygen as possible from the corrosion system (especially from the bentonite).

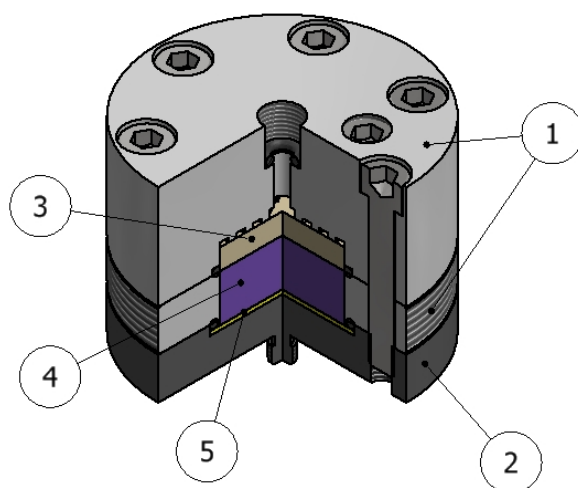


*Figure 2-17 – Schematic representation of the experimental cell for compacted bentonite experiment. 1 - plastic parts of the corrosion cell, 2 - metal part of the corrosion cell, 3 - frit, 4 - bentonite BaM, 5 – steel metal plate (sample). Dobrev et al. (2017b)*

After 21 days in an anaerobic atmosphere, the corrosion cells were placed in the heating mantles (that at the time was still turned off). Then the corrosion cells were connected to hoses and MINIMESS valves in order to connect them to the water saturation system. All these operations were performed in a glove

box in the absence of oxygen. Later the cells and the heating mantles were removed from the glove box and were connected to the heating switchboard (MKsystem, Czech Republic) with a built-in temperature controller OMRON E5CS (OMRON Japan) and a resistance temperature sensor PT100 (Sensit s.r.o Czech Republic) that kept the temperature of the corrosion system constant throughout the test. Once the cells were heated up to 70 °C the saturation process was initiated. The cells were saturated with deoxygenated water (SCW) contained in a hermetic container through a hose previously flushed with argon. The saturation pressure was increased gradually until reaching 5 MPa. The pressure and temperature were kept constant and measured during the corrosion test. (Figure 2-18).

The corrosion tests were performed in four series with steel 422707.9 (12 metal samples per series) The time series for the corrosion test was 0.25; 0.5; 1 and 1.5 years.



Figure 2-18 – Illustration of corrosion cells outside glove box Dobrev et al. (2017b)

At the end of the corrosion test, cells were placed in the glove box. During the disassembly, the bentonite sample was separated from the metal sample (bentonite remains on the metal sample), see Figure 2-19. The bentonite in the middle of the cell was immediately weighed inside the glove box to determine its water content. Both the metal samples and the bentonite samples were left in the glove box both to remove residual water from the metal sample and to dry the bentonite to prevent iron oxidation in the bentonite after being removed from the glove box. The minimum time in the glove box was one week. The samples were then processed for individual analyzes.

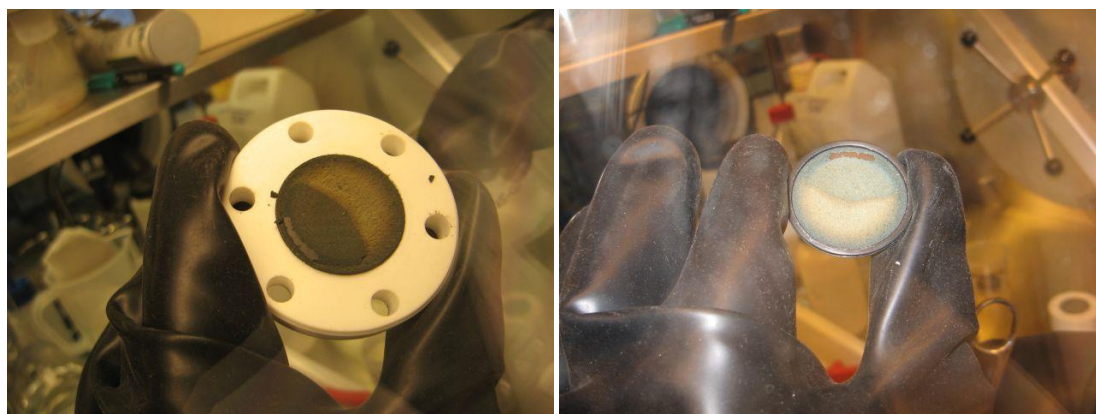


Figure 2-19 – Bentonite (side in contact with steel sample) and steel sample with bentonite residues. Dobrev et al. (2017)

### 2.3.3 Results

#### 2.3.3.1 Bentonite

The aim was to determine the cation exchange capacity (CEC) of bentonite potentially altered by corrosive steel products – and the ion exchange smectite complex. Any remains of bentonite stuck on the surface of the metal sample after opening the cell (metal-bentonite contact) was used for the determination of CEC. After drying this layer was spontaneously separated from the metal. Later, the bentonite sample was processed according to a certified methodology, or with modifications reflecting the character of the sample (with respect to the amount of material obtained).

The Table 2-17 shows the mean CEC values of bentonite samples after the corrosion tests, respectively, their development over time as a function of the length of the test, as compared to the bentonite reference samples from each determination: BaM bentonite used for the preparation of the samples, Clay Mineral Society “SAz-1” (basically a Ca-montmorillonite standard) and SWy-2 (standard Na-Ca bentonite) (Dobrev *et al.*, 2017b).

*Table 2-17 – Average values of cation exchange capacity of bentonite samples after contact with corroding steel for the indicated corrosion duration (BaM<sub>kor</sub>). CEC values for selected reference samples (BaM<sub>refer</sub>, bentonite reference materials SAZ-1 and SWy-2) are shown for comparison.*

3-months test		6-months test		1-year test		1,5-year test	
Sample	CEC [meq/100g]	sample	CEC [meq/100 g]	sample	CEC [meq/100g]	sample	CEC [meq/100 g]
BaM <sub>kor</sub>	62.9 ± 1.2	BaM <sub>kor</sub>	57.4 ± 0.7	BaM <sub>kor</sub>	53.9 ± 1.0	BaM <sub>kor</sub>	50.3 ± 2.0
BaM <sub>refer</sub>	67.9 ± 0.2	BaM <sub>refer</sub>	68.6 ± 0.6	BaM <sub>refer</sub>	62.1 ± 1.6	BaM <sub>refer</sub>	59.0 ± 0.8
SAz-1	133.9 ± 0.4	SAz-1	134.8 ± 1.9	SAz-1	124.1 ± 3.8	SAz-1	112.3 ± 2.3
SWy-2	78.4 ± 0.6	SWy-2	77.9 ± 0.2	SWy-2	73.0 ± 0.8	SWy-2	69.5 ± 0.7

The results show a decrease of CEC depending on the time of contact with the corroding steel sample. However, this trend is also clearly identifiable for reference materials (especially SAz-1 and SWy-2) (Dobrev *et al.*, 2017b). Comparing bentonite samples from corrosion tests (BaM<sub>kor</sub>) and reference bentonite BaM (BaM<sub>refer</sub>), it is possible to see a significant decrease in mean CEC in BaM<sub>kor</sub> over time (see Table 2-17), which may indicate that the corrosion process and the corrosion products may have affected the bentonite. However, it should be noted that this is not necessarily the only effect on smectite as a major carrier of CEC, but the decrease in CEC may be due to a combination of several factors, including the presence of corrosion / alteration products with very low CEC. This is due to the fact the used method is not capable of identify the individual mineral phases, the resulting CEC is always determined for the whole solid material sample. For samples from the 1 year and 1,5 year corrosion tests, much less metal sample material was obtained than the samples from the 0,25 and 0,5 year tests, where a significant amount of bentonite was obtained. In some cases (especially in the 1 and a 1,5 tests), the steel sample was almost completely separated from the bentonite and thus insufficient bentonite was obtained for CEC analysis.

It was observed that the cation exchange capacity of bentonite was affected by the corrosion experiments, however it was not possible to distinguish if the decrease was caused by the formation of new phases (corrosion/alteration products).

#### 2.3.3.2 Metal samples

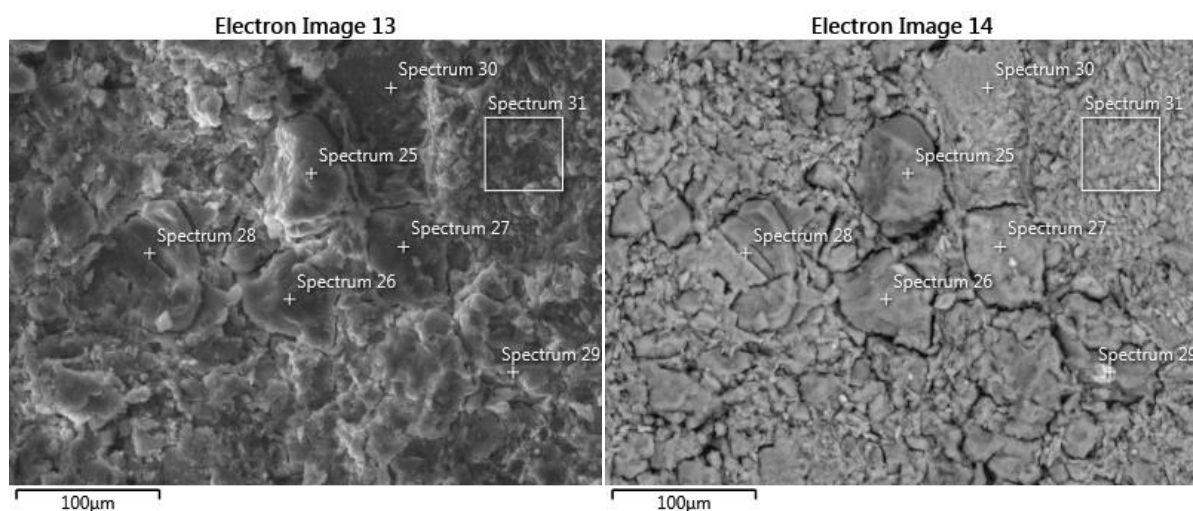
Determination of the corrosion rate of carbon steel was carried out according to the ISO 8407. A new sample of carbon steel of the same size was used as a reference sample for the pickling process and was pre-weighed and degreased in the same manner as for the sample preparation for the experiment. Inside the glove box, bentonite residues were removed from the metal specimens prior to immersion to determine cation exchange capacity. Prior to decontamination of the carbon steel samples, the diameter

of the corroded surface was also determined. These values were used to calculate the sample area in contact with the compacted bentonite (Dobrev et al. 2017b).

The corrosion products on the metal samples were determined by Raman spectroscopy and X-ray diffraction analysis. The chemical composition of the surface layers was measured on a scanning electron microscope (SEM). Due to the thin layers of corrosion products on the surface of metal samples, only a qualitative analysis was possible in most measurements to determine the corrosion products. Table 2-18 presents the detected corrosion products. Siderite and chukanovite were detected on the steel surface of 422707.9. In addition to the corrosion products themselves, bentonite minerals that were expected on the sample surface were identified. The elemental surface mapping and the sample cross-section analysis performed on a Vega TS 5130 XM Scanning Electron Microscope (Tescan, Czech Republic) are consistent with the demonstrated presence of bentonite on their surface (Figure 2-20).

Table 2-18 – Determined corrosion products of metal samples.

Sample	Time [year]	X-ray diffraction analysis	Raman spectroscopy
Steel 422707.9	0,25	FeCO <sub>3</sub> (10% rel.)	Below detection limit
Steel 422707.9	0,5	FeCO <sub>3</sub> (5% rel.) Fe <sub>2</sub> CO <sub>3</sub> (OH) <sub>2</sub>	FeCO <sub>3</sub>
Steel 422707.9	1	FeCO <sub>3</sub> Fe <sub>2</sub> CO <sub>3</sub> (OH) <sub>2</sub>	Below detection limit
Steel 422707.9	1,5	FeCO <sub>3</sub> Fe <sub>2</sub> CO <sub>3</sub> (OH) <sub>2</sub>	Below detection limit



Analysis of one specific parts of the sample	O [%rel]	Mg [%rel]	Al [%rel]	Si [%rel]	P [%rel]	K [%rel]	Ca [%rel]	Ti [%rel]	Mn [%rel]	Fe [%rel]
25	53.3	3.0	10.2	24.9	-	0.6	0.5	0.3	-	7.2
26	48.8	3.0	9.7	25.1	-	0.8	0.8	0.4	-	11.5
27	44.0	3.9	7.2	25.3	-	0.6	1.0	2.0	-	16.2
28	35.7	3.1	6.9	23.8	-	0.7	9.3	0.1	-	20.4
29	32.4	1.2	2.4	5.7	0.1	0.1	0.8	3.2	0,6	53.5
30	38.7	0.2	0.5	1.1	-	-	58.1	-	-	1.4
31	55.6	0.7	1.4	4.0	-	0.2	36.1	0.2	-	1.8

*Figure 2-20 – 422707.9 steel surface with bentonite BaM residues after a one-year test displayed by secondary electrons (SE) on the left and back-scattered electrons (BSE) on the right, including relevant elemental analyses of different parts of the sample surface. (Dobrev et al. 2017b)*

## 2.4 Proposed modelling approach

The aim of modelling the experiments presented in chapters 2.1, 2.2 and 2.3, is to assess the chemical evolution at the steel – bentonite interface under increased temperature conditions. Moreover, development and transfer of corrosion products, evolving under such conditions, will be also simulated.

## 2.5 Conceptual Model

UJV aim in this case is to describe the conceptual view, identify the geochemical disturbances during the long-term evolution of disposal cell, prepare relevant input data-sets, develop individual geochemical models and finally carry out 1D reactive-transport modelling calculations for the existing laboratory experiments.

### 2.5.1 Modelling concept

The geochemical modelling approach applied is based on a three-step procedure.

- Identification of the most important processes in the system carbon steel – bentonite
- At first, a simple equilibrium model of the iron-bentonite-water systems will be constructed to identify the main chemical driving processes in the systems within a long-term scale.
- Secondly, a kinetic model will be developed to include also kinetic effects and thereby time-dependence of the geochemical processes.
- The one-dimensional (1D) reactive-transport models will include not only kinetic but also transport phenomena in order to understand more realistically the temporal as well as spatial development of the steel corrosion and corrosion products formation, in the iron/steel-bentonite-water systems. This three-stage modelling workflow is similar to the workflow that was applied and established in the earlier UJV project Corrosion Products (Gondolli et al., 2018b,c).
- Finally, evaluation of result transfer into the large scale representation of disposal cell.

### 2.5.2 Processes to be modelled

The geochemical processes studied are:

- dissolution/precipitation of the bentonite primary minerals,
- dissolution of the solid iron,
- changes in the aqueous solution composition
- precipitation of secondary solid phases, including corrosion as well as bentonite alteration products.

Within the kinetic and reactive-transport model, the temporal and spatial evolution of these processes, respectively, will also be computationally investigated.

Prior to the above modelling work, some preliminary geochemical calculations were needed to be carried out; in particular, to model of the bentonite pore waters (BPWs) that are assumed to be in equilibrium with bentonite materials before adding the iron material into the system. The results of the BPW modelling are presented in this deliverable as obtained first step. Results of the equilibrium, kinetic, and reactive-transport models will be presented and discussed in the final outcome of this project.

To model the BPW, following processes are included: thermodynamic equilibrium between the aqueous solution, bentonite primary minerals, bentonite well-soluble salts, and selected secondary minerals, reaction between species in the aqueous phase, cation exchange reactions and surface complexation reactions. More detailed information about the modelled processes can be found in Sections 2.5.3 and 2.6.

### 2.5.3 Initial conditions and input parameters

In this section, the characterization and properties of the initial aqueous solutions and bentonite materials used in the three earlier UJV projects are summarized (see also Chapters 2.1- 2.3). These data were also used as input to the geochemical modeling calculations carried out in this study (see further).

#### 2.5.3.1 Initial aqueous solutions

Chemical composition and other parameters of the initial aqueous solutions (groundwaters) considered to saturate bentonite materials, i.e., the synthetic groundwater (SGW) and Grimsel groundwater (GGW), are shown in Table 2-19.

Table 2-19 – Chemical composition and other parameters of the initial aqueous solutions.

Aqueous solution	SGW <sup>a</sup> (Table 2-5)		GGW <sup>b</sup> (Table 2-13)	
Project(s)	CoPr, UOS		MaCoTe	
Ion/Concentration	mg kgw <sup>-1</sup>	mol kgw <sup>-1</sup>	mg kgw <sup>-1</sup>	mol kgw <sup>-1</sup>
Na <sup>+</sup>	10.4	4.46E-04 <sup>c</sup>	8.30	3.11E-04 <sup>c</sup>
K <sup>+</sup>	1.8	4.60E-05	0.20	5.12E-06
Ca <sup>2+</sup>	19.0	4.74E-04	7.50	1.87E-04
Mg <sup>2+</sup>	7.0	2.88E-04	0.01	4.11E-07
Cl <sup>-</sup>	33.6	9.48E-04	0.90	2.54E-05
SO <sub>4</sub> <sup>2-</sup>	27.7	2.88E-04	5.64	5.87E-05
HCO <sub>3</sub> <sup>-</sup>	30.4	4.98E-04	18.10	2.97E-04
Al <sup>3+</sup>	0.1	3.71E-06	0	0
Si	10.1	1.68E-04	0	0
Fe <sup>2+</sup>	0.1	1.79E-06	0.1	1.79E-06
F <sup>-</sup>	0	0	3.90	2.05E-04
pH	7.90		9.25	
E <sub>h</sub> (V)	0.181		0.203	
pe <sup>d</sup>	3.06		3.43	
I (mol kgw <sup>-1</sup> ) <sup>e</sup>	2.97E-03		9.38E-04	
log P <sub>CO2</sub> (atm) <sup>f</sup>	-3.43		-5.02	
<sup>a</sup> The composition was taken from Gondolli et al. (2018b,c). <sup>b</sup> The composition was taken from Dobrev et al. 2018. <sup>c</sup> Adjusted to achieve charge balance of the solution. <sup>d</sup> pe = E <sub>h</sub> /0.05917. <sup>e</sup> Ionic strength. <sup>f</sup> Calculated from the solution composition.				

### 2.5.3.2 Bentonite materials

Mineralogical composition and other parameters of the bentonite materials, i.e., the BaM and MX-80 bentonites, are shown in Table 2-20.

Regarding the well soluble salts, their contents (in mol kg<sup>-1</sup>) are: 5.10E-04 of halite, 8.70E-04 of gypsum, 4.10E-04 of Mg(NO<sub>3</sub>)<sub>2</sub>, and 4.00E-02 of nahcolite for BaM (Červinka and Gondolli 2015), and 1.35E-03 of halite for MX-80 (Bradbury and Baeyens 2002).

Table 2-20 – Mineralogical composition and other parameters of the BaM and MX-80 bentonites.

Parameter	$M$ (g mol <sup>-1</sup> )	$\rho$ (g cm <sup>-3</sup> ) <sup>a</sup>	BaM (Table 2-2)		MX-80 (Table 2-11)	
			$w$	$n$ (mol d m <sup>-3</sup> ) <sup>a</sup>	$w$	$n$ (mol d m <sup>-3</sup> ) <sup>a</sup>
Mineral						
Montmorillonite <sup>b</sup>	366.21/376.7 2 <sup>c</sup>	2.69/2.63 <sup>c</sup>	0.877	9.2492	0.850	7.8919
Quartz (SiO <sub>2</sub> )	60.08	2.62	0.053	3.4071	0.037	2.1541
Anatase (TiO <sub>2</sub> )	79.88	3.90	0.039	1.8856	-	-
CaMg-Siderite (Ca <sub>0.1</sub> Mg <sub>0.33</sub> Fe <sub>0.57</sub> CO <sub>3</sub> )	103.86	3.55	0.031	1.1528	-	-
Calcite (CaCO <sub>3</sub> )	100.09	2.71	-	-	0.013	0.4543
Muscovite (KAl <sub>2</sub> AlSi <sub>3</sub> O <sub>10</sub> (OH) <sub>2</sub> )	398.31	2.82	-	-	0.048	0.4215
Feldspar (Albite; NaAlSi <sub>3</sub> O <sub>8</sub> )	262.22	2.62	-	-	0.052	0.6936
Porosity			0.415		0.430	
$V_{\text{water}}$ (dm <sup>-3</sup> )			1		1	
$m_{\text{bentonite}}$ (kg)			3.86		3.50	
S/L ratio (kg dm <sup>-3</sup> )			3.86		3.50	
$\rho_{\text{mineralogical}}$ (g cm <sup>-3</sup> )			2.74		2.64	
$\rho_{\text{dry}}$ (g cm <sup>-3</sup> )			1.60		1.50	
$\rho_{\text{saturated}}$ (g cm <sup>-3</sup> )			2.02		1.93	
<sup>a</sup> Mineral density values ( $\rho$ ) were taken from <a href="http://webmineral.com">http://webmineral.com</a> . Mole numbers of minerals ( $n$ ) are per dm <sup>3</sup> of the aqueous solution (porewater) assuming the given S/L ratio.						
<sup>b</sup> Different montmorillonites occur in BaM and MX-80. The mean chemical compositions are Ca <sub>0.17</sub> Mg <sub>0.34</sub> Al <sub>1.66</sub> Si <sub>4</sub> O <sub>10</sub> (OH) <sub>2</sub> and Na <sub>0.409</sub> K <sub>0.024</sub> Ca <sub>0.009</sub> (Si <sub>3.738</sub> Al <sub>0.262</sub> )(Al <sub>1.598</sub> Mg <sub>0.214</sub> Fe <sub>0.208</sub> )O <sub>10</sub> (OH) <sub>2</sub> for montmorillonites in BaM and MX-80, respectively. The chemical formula for the MX-80 montmorillonite was taken from the Thermoddem database (Blanc et al., 2012).						
<sup>c</sup> Values for BaM montmorillonite/MX-80 montmorillonite.						

### 2.5.3.2 Cation exchange

The cation exchange reactions on the montmorillonite interlayer sites were considered for the cations Na<sup>+</sup>, K<sup>+</sup>, Ca<sup>2+</sup>, Mg<sup>2+</sup>, and Fe<sup>2+</sup> using the Gaines-Thomas convention (Gaines and Thomas 1953). The equilibrium constants (log  $K$ ) of the exchange reactions were taken from the PHREEQC.DAT database distributed with PHREEQC (Parkhurst and Appelo 2013) and are shown in Table 2-21. These log  $K$  values correspond very well with those reported for the MX-80 bentonite (Bradbury and Baeyens 2002) and were also used in our previous modeling studies on bentonite and iron–bentonite systems (Gondoli et al. 2018a, Červinka et al. 2018)., Table 2-20 also includes the cation exchange capacity (CEC) characteristics and the initial composition of the respective exchangeable sites for the BaM and MX-80 bentonites.

Table 2-21 – Cation exchange characteristics of the considered bentonites.

Cation exchange reaction <sup>a</sup>	log <i>K</i> <sup>b</sup>	Initial composition (eq kg <sup>-1</sup> ) <sup>c</sup>	
		BaM	MX-80
Na <sup>+</sup> + X <sup>-</sup> = NaX	0	0.039	0.524
K <sup>+</sup> + X <sup>-</sup> = KX	0.700	0.034	0.014
Ca <sup>2+</sup> + 2 X <sup>-</sup> = CaX <sub>2</sub>	0.800	0.117	0
Mg <sup>2+</sup> + 2 X <sup>-</sup> = MgX <sub>2</sub>	0.602	0.357	0.132
Fe <sup>2+</sup> + 2 X <sup>-</sup> = FeX <sub>2</sub>	0.444	0	0
CEC <sub>sum</sub>		0.547	0.670

<sup>a</sup> The symbol X denotes montmorillonite exchangeable sites.  
<sup>b</sup> From the PHREEQC.DAT database (Parkhurst and Appelo 2013).  
<sup>c</sup> The data were taken from Červinka and Gondolli (2015) and Mendoza and Havlová (2020) for BaM and MX-80, respectively

### 2.5.3.3 Surface complexation

The surface complexation reactions included protonation and deprotonation reactions of the specific surface edge sites (i.e., surface hydroxyl groups ≡SOH) of montmorillonite minerals.

For the MX-80 bentonite, the surface complexation site types, their equilibrium constants and capacity were all taken from Bradbury and Baeyens (2002) and are shown in Table 2-22.

For the BaM bentonite, surface complexation characteristics were unknown. In an earlier study of Červinka and Hanuláková (2013), however, these characteristics were determined for the B-75 bentonite, which can be seen analogous to BaM. We therefore assumed that BaM had identical surface complexation characteristics as B-75. These are shown in Table 2-22 too. It should be noted that Červinka and Hanuláková (2013) used a somewhat large surface sites capacity value of 0.151 mol kg<sup>-1</sup>, which corresponds to approx. 28% of total CEC of BaM (it is usually only about 10-15% of CEC (e.g., Bradbury and Baeyens, 2002)). Therefore, in the BPW models for BaM, we used a decreased value of 0.082 mol kg<sup>-1</sup>, corresponding to 15% of the CEC of BaM (Table 2-22). For both bentonites, a surface area value of 30 m<sup>2</sup> g<sup>-1</sup> was estimated to be available for the surface complexation reactions (Bradbury and Baeyens 2002). The initial composition of the surface edge sites was calculated in PHREEQC according to the simple protocol proposed by Bradbury and Baeyens (2002), which is based on the equilibration of the surface sites with a 0.001 mol kgw<sup>-1</sup> NaCl solution at pH = 8, and atmospheric O<sub>2</sub> (log *P*<sub>O<sub>2</sub>/atm</sub> = -0.68), and CO<sub>2</sub> (log *P*<sub>CO<sub>2</sub>/atm</sub> = -3.40). Results are shown in Table 2-22. Finally, it should be noted that in the PHREEQC modeling of the surface complexations, the electrical diffuse layer was not considered, corresponding to the approach applied by Červinka and Hanuláková (2013).

Table 2-22 – Surface complexation characteristics of the considered bentonites.

BaM			MX-80		
Surface complexation reaction <sup>a</sup>	log K <sup>a</sup>	Initial composition (mol) <sup>b</sup>	Surface complexation reaction <sup>c</sup>	log K <sup>c</sup>	Initial composition (mol) <sup>d</sup>
$\equiv\text{SOH} + \text{H}^+ = \equiv\text{SOH}_2^+$	4.15	4.462e-05	$\equiv\text{S}^{\text{A}}\text{OH} + \text{H}^+ = \equiv\text{S}^{\text{A}}\text{OH}_2^+$	4.50	1.960e-05
$\equiv\text{SOH} = \equiv\text{SOH}$	0	3.159e-01	$\equiv\text{S}^{\text{A}}\text{OH} = \equiv\text{S}^{\text{A}}\text{OH}$	0	6.197e-02
$\equiv\text{SOH} = \equiv\text{SO}^- + \text{H}^+$	-10.48	1.046e-03	$\equiv\text{S}^{\text{A}}\text{OH} = \equiv\text{S}^{\text{A}}\text{O}^- + \text{H}^+$	-7.90	7.801e-02
			$\equiv\text{S}^{\text{B}}\text{OH} + \text{H}^+ = \equiv\text{S}^{\text{B}}\text{OH}_2^+$	6.00	1.382e-03
			$\equiv\text{S}^{\text{B}}\text{OH} = \equiv\text{S}^{\text{B}}\text{OH}$	0	1.382e-01
			$\equiv\text{S}^{\text{B}}\text{OH} = \equiv\text{S}^{\text{B}}\text{O}^- + \text{H}^+$	-10.50	4.370e-04

<sup>a</sup> Taken from Červinka and Hanuláková (2013). For BaM, only one type of weak complexation types was considered.

<sup>b</sup> Per 3.86 kg of BaM. Calculated with PHREEQC.

<sup>c</sup> Taken from Bradbury and Baeyens (2002). For MX-80, two types of weak complexation sites (A and B) were considered.

<sup>d</sup> Per 3.50 kg of MX-80. Calculated with PHREEQC.

## 2.6 Modelling tools applied

For all geochemical calculations carried out in this work, the PHREEQC hydrochemical modeling code version 3.6.3 (Parkhurst and Appelo 2013) was used, together with the Thermoddem thermodynamic database version V1.10 (Blanc et al. 2012; <https://thermoddem.brgm.fr/>). PHREEQC is a freeware modeling tool developed by USGS suitable for modeling aqueous solutions, both equilibrium and kinetic reaction modeling, and 1D reactive-transport. To capture the non-ideality of the aqueous phase, the activity coefficients of ionic species were modeled in PHREEQC using the Lawrence Livermore National Laboratory (LLNL) aqueous model (Parkhurst and Appelo 2013), given by:

$$\log \gamma_i = \frac{A_\gamma z_i^2 \sqrt{I}}{1 + a_i^\circ B_\gamma \sqrt{I}} + \dot{B}I$$

where  $\gamma_i$ ,  $z_i$  and  $a_i^\circ$  are the activity coefficient, charge number and diameter of ionic species  $i$ , respectively,  $I$  is the ionic strength and  $A_\gamma$ ,  $B_\gamma$  and  $\dot{B}$  are temperature-dependent Debye-Hückel parameters. The LLNL model is expected to give reasonable estimation of the activity coefficients up to an ionic strength value of 1 mol kg<sup>-1</sup>. This range covers all the aqueous solutions considered in this work.

## 2.7 First results and discussion – Modelling of bentonite pore water (BPW) composition

Prior to modeling of the bentonite-iron-water systems, calculations of the initial porewaters composition of the bentonite materials were needed to be carried out to produce input solutions for the subsequent equilibrium, kinetic and reactive-transport modeling calculations.

The modelling of bentonite porewater is a nontrivial geochemical modelling task, which includes a number of various phenomena that need to be described adequately. More information on this topic can be found, for example, in Bradbury and Baeyens (2002), Wersin (2003), Wersin et al. (2004), and Curti et al. (2011).

In principle, the estimation of a BPW composition is based on the thermodynamic equilibration of an initial solution with bentonite minerals and well-soluble salts, cation exchange and surface edge sites of montmorillonite minerals, and selected gases (Bradbury and Baeyens 2002, Červinka et al. 2018). BPW composition is then influenced mainly by the bentonite mineralogical composition, initial solution composition, gas phase composition, bentonite compaction, and diffusion of dissolved species through bentonite (Červinka and Gondolli 2015, Červinka et al. 2018).

In this section, the considerations, parameters, and other details on the equilibrium bentonite porewater (BPW) models developed in this work are given, followed by the presentation and discussion of the calculated BPW compositions.

In this work, the BPW models were constructed in line with earlier equilibrium BPW models developed at UJV in the last decade (Červinka and Hanuláková 2013; Červinka and Gondolli 2015; Červinka et al. 2018; Gondolli et al. 2018b,c). In principle, all these models can be seen as modifications of the conventional approach proposed by Bradbury and Baeyens (2002). The BPW models developed were successfully validated against data calculated by other BPW models available in literature (Bradbury and Baeyens 2002; Červinka and Hanuláková 2013); for details, see Červinka et al. (2017).

A total of 6 different BPW compositions has been introduced in order to reflect (i) the different combinations of bentonite materials and initial aqueous solutions used in the earlier UJV experiments, and (ii) the different temperatures considered (i.e., 25 and 70 °C). These 6 BPWs are, for the sake of clarity, listed in Table 2-23. From now on, the BPW model identifiers shown in Table 2-23 will be used to refer to the respective BPWs.

Table 2-23 – List of BPW models developed in this stage of work.

#	Bentonite	Initial solution	Project(s)	t (°C)	BPW model identifier
1	BaM	SGW	CoPr, UOS	25	BPW-BAM-SGW-25
2				70	BPW-BAM-SGW-70
3	BaM	GGW	MaCoTe	25	BPW-BAM-GGW-25
4				70	BPW-BAM-GGW-70
5	MX-80	GGW	MaCoTe	25	BPW-MX80-GGW-25
6				70	BPW-MX80-GGW-70

The BPW models contained the following features to capture the real chemical processes between a bentonite material and an aqueous solution:

- Equilibrium with the aqueous solution, bentonite primary minerals (except montmorillonite and anatase (see Table 2-20)), bentonite well-soluble salts, and the following secondary minerals: calcite (CaCO<sub>3</sub>), dolomite (CaMg(CO<sub>3</sub>)<sub>2</sub>), goethite (FeO(OH)), and kaolinite (Al<sub>2</sub>Si<sub>2</sub>O<sub>5</sub>(OH)<sub>4</sub>);
- Reaction between species in the aqueous phase (e.g., acid-base and complexation reactions);
- Cation exchange reactions on interlayer sites of montmorillonite minerals. This included exchange reactions for the cations Na<sup>+</sup>, K<sup>+</sup>, Ca<sup>2+</sup>, Mg<sup>2+</sup>, and Fe<sup>2+</sup>;

- Surface complexation reactions (i.e., protonation/deprotonation) on surface edge sites of montmorillonite minerals;
- Anoxic conditions with a constant CO<sub>2</sub> partial pressure of 3.98 · 10<sup>-4</sup> atm.

In the presented modelling approach, the equilibration of the aqueous solution with bentonite materials including all the relevant processes listed above was considered a quick equilibrium process, with neither temporal nor spatial effects considered. This is a common simplification applied in BPW modelling studies (Bradbury and Baeyens 2002; Gondolli et al. 2018a).

The BPW model developed and used in this work containing all necessary PHREEQC scripts will be provided on request.

Using the BPW model developed, the chemical compositions for the BPWs listed in Table 2-19 were calculated. The resulting BPW compositions and other related data are shown in Table 2-24 and illustrated graphically in Figure 2-21 and, by means of a Piper diagram, in Figure 2-22.

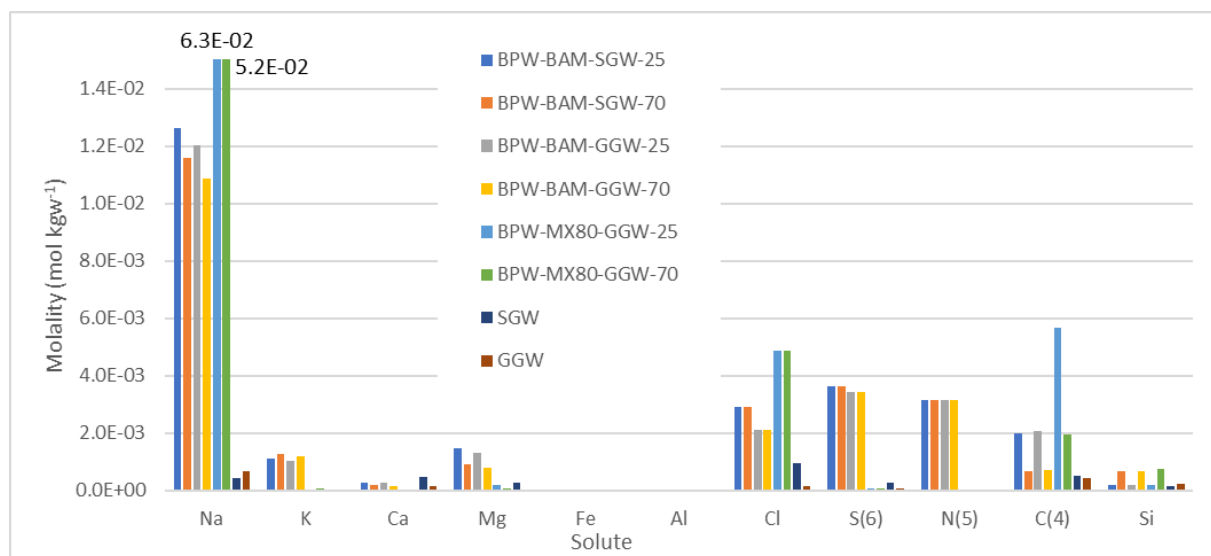


Figure 2-21 – Calculated chemical compositions of the considered BPWs.

It can be seen from Table 2-24 that the resulting calculated pH values were between 8.3 and 8.9, with the MX-80-based BPWs having slightly higher pH values than those of BaM. With regard to the differences between the calculated BPWs and the initial solutions (SGW and GGW), Table 2-7 and Figure 2-21 show that all the calculated BPWs contained more Na<sup>+</sup>, Mg<sup>2+</sup>, chlorides, and carbonates than the respective initial solutions. The calculated BaM-based BPWs had all very similar composition; moreover, it can be clearly seen in the Piper diagram in Figure 2-22 that, in general, the initial solution composition and temperature had rather minor effects, whereas the bentonite composition had the dominant effect on the resulting chemical composition of the BPWs. This explains the differences between the BaM- and MX-80-based BPWs. The apparent charge imbalance of the calculated BPWs reported in Table 2-24 was due to the presence of charged surface complexation sites; the whole bentonite-water systems were, however, charge balanced and electroneutral.

Table 2-24 – Calculated chemical compositions of the considered BPWs and the resulting bentonite mineralogical compositions, exchanger compositions, and surface edge site compositions.

Parameter/BPW	BPW-BAM-SGW-25	BPW-BAM-SGW-70	BPW-BAM-GGW-25	BPW-BAM-GGW-70	BPW-MX80-GGW-25	BPW-MX80-GGW-70
pH	8.44	8.27	8.46	8.29	8.85	8.68
pe	-4.04	-6.22	-4.06	-5.97	-2.65	-4.30

Parameter/BPW	BPW-BAM-SGW-25	BPW-BAM-SGW-70	BPW-BAM-GGW-25	BPW-BAM-GGW-70	BPW-MX80-GGW-25	BPW-MX80-GGW-70
$T$ (°C)	25	70	25	70	25	70
$\log P_{\text{CO}_2}$ (atm)	-3.40	-3.40	-3.40	-3.40	-3.40	-3.40
$I$ (mol kg <sup>-1</sup> )	0.020	0.018	0.019	0.017	0.037	0.030
Charge imbalance (%)	5.9	3.3	6.8	4.0	70.5	75.6
<b>Concentration (mol kg<sup>-1</sup>)</b>						
Na	1.264E-02	1.161E-02	1.203E-02	1.089E-02	6.227E-02	5.193E-02
K	1.110E-03	1.280E-03	1.053E-03	1.196E-03	7.082E-07	8.788E-05
Ca	2.822E-04	1.736E-04	2.537E-04	1.513E-04	5.239E-05	5.116E-05
Mg	1.464E-03	9.087E-04	1.317E-03	7.918E-04	1.988E-04	6.113E-05
Fe	6.929E-08	8.556E-08	6.640E-08	7.884E-08	6.430E-11	3.346E-11
Al	4.043E-08	1.305E-06	4.211E-08	1.378E-06	5.074E-08	3.281E-07
Cl	2.914E-03	2.914E-03	2.127E-03	2.127E-03	4.882E-03	4.881E-03
S(6)	3.642E-03	3.643E-03	3.416E-03	3.416E-03	6.103E-05	6.102E-05
N(5)	3.155E-03	3.155E-03	3.155E-03	3.155E-03	0.000E+00	0.000E+00
C(4)	1.999E-03	6.607E-04	2.081E-03	6.971E-04	5.664E-03	1.945E-03
Si	1.918E-04	6.563E-04	1.922E-04	6.601E-04	2.062E-04	7.698E-04
<b>Minerals (mol)</b>						
Quartz	3.407	3.407	3.407	3.407	2.447	2.370
CaMg-siderite	1.153	1.153	1.153	1.153	-	-
Muscovite	-	-	-	-	0.471	0.458
Albite	-	-	-	-	0.547	0.586
Calcite	0	0	0	0	3.14E-01	1.98E-01
Dolomite	0.038	0.038	0.038	0.038	0.080	0.134
Kaolinite	0	0	0	0	0	0
Goethite	2.47E-12	0	1.48E-12	3.46E-08	0	0
<b>Exchanger (mol)</b>						
NaX	2.948E-01	2.958E-01	2.955E-01	2.970E-01	1.923E+00	1.895E+00
KX	1.299E-01	1.298E-01	1.300E-01	1.298E-01	1.100E-04	1.282E-02
CaX <sub>2</sub>	1.919E-01	1.914E-01	1.916E-01	1.911E-01	6.012E-02	1.215E-01
MgX <sub>2</sub>	6.517E-01	6.517E-01	6.516E-01	6.515E-01	1.505E-01	9.659E-02
FeX <sub>2</sub>	7.772E-06	1.168E-05	7.766E-06	1.166E-05	2.936E-09	2.967E-09
<b>Surface sites (mol)</b>						
≡SOH <sub>2</sub> <sup>+</sup>	1.620E-05	2.397E-05	1.547E-05	2.258E-05	-	-
≡SOH	3.141E-01	3.150E-01	3.140E-01	3.149E-01	-	-
≡SO <sup>-</sup>	2.850E-03	1.936E-03	2.980E-03	2.054E-03	-	-
≡S <sup>A</sup> OH <sub>2</sub> <sup>+</sup>	-	-	-	-	6.380E-07	1.321E-06
≡S <sup>A</sup> OH	-	-	-	-	1.420E-02	1.996E-02
≡S <sup>A</sup> O <sup>-</sup>	-	-	-	-	1.258E-01	1.200E-01
≡S <sup>B</sup> OH <sub>2</sub> <sup>+</sup>	-	-	-	-	1.943E-04	2.881E-04

Parameter/BPW	BPW-BAM-SGW-25	BPW-BAM-SGW-70	BPW-BAM-GGW-25	BPW-BAM-GGW-70	BPW-MX80-GGW-25	BPW-MX80-GGW-70
$\equiv\text{S}^{\text{BOH}}$	-	-	-	-	1.368E-01	1.376E-01
$\equiv\text{S}^{\text{BO}^-}$	-	-	-	-	3.044E-03	2.079E-03

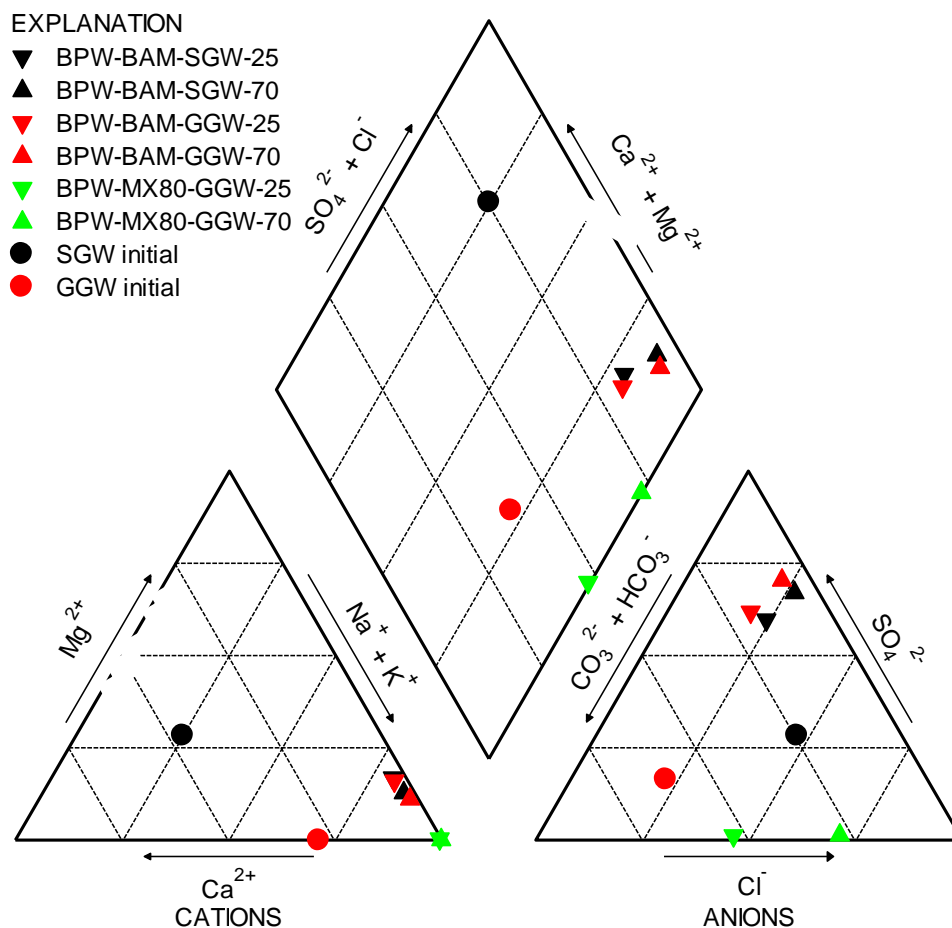


Figure 2-22 – Comparison of the initial solutions and the calculated BPWs by means of a Piper diagram.

It should be noted that in all calculations of the BPWs shown in Table 2.6, the pH of the resulting BPWs was controlled by the fixed  $\text{CO}_2$  partial pressure and the equilibrium with calcite and not by the involved surface complexation reactions (Bradbury and Baeyens 2002). In a closed system without fixed  $\text{CO}_2$  partial pressure, however, pH would be determined by the surface reactions. Since the laboratory experiments within the UOS (chapter 2.3) and Corrosion Products (chapter 2.1) projects were carried out under a 5 MPa pressure in a closed cell placed in a glove box, we also performed a test BPW calculation without the assumption of a fixed  $\text{CO}_2$  pressure to examine the effect of such an approach on the modeling results. The BPW-BAM-SGW-25 was chosen for this purpose. It was found that calculations without constant  $\text{CO}_2$  pressure resulted in an unreasonable BPW composition with  $\text{pH} = 6.3$  and a total  $\text{C}^{\text{IV}}$  molality around  $0.1 \text{ mol kg}^{-1}$ , which corresponded to a very high  $\text{CO}_2$  partial pressure value of 1.4 atm. The reason for such a strange behavior is the presence of the mineral nahcolite ( $\text{NaHCO}_3$ ) in the ensemble of well soluble salts of BaM, which is an enormous donor of inorganic carbon into the system. The dissolved carbon has no mineral carbonate to precipitate (the Ca and Mg concentrations are not high enough for calcite or dolomite to precipitate) and, thus, remains in the solution. The only possibility to avoid this problem is the suppression of nahcolite dissolution, which leads to a reasonable pH value of 8.1 (controlled by the surface edge sites) and a  $\text{C}^{\text{IV}}$  molality of

$6.8E-04 \text{ mol kg}^{-1}$ . However, such an approach would not correspond to the reality since the presence of nahcolite in BaM was undoubtedly verified (Červinka and Gondolli 2015). Therefore, for the subsequent modeling calculations in this project, the BPWs the pH of which was controlled by the fixed  $\text{CO}_2$  pressure (Table 2-7) were considered. It should be noted that the issue described above is only seen for the BaM-based BPWs since MX-80 only contains no other well-soluble salt than NaCl.

### 3. Interaction of Fe(II) with montmorillonite (UniBern)

The Fe(II) diffusion cell experiment studies the interaction of Fe(II) released from the corroding steel canister with the bentonite. This so-far poorly understood interaction may involve complex sorption coupled with redox reactions between Fe(II) released from the corrosion process and the structural iron in the clay. The experimental and thus modelling focus is set on the interaction of Fe with montmorillonite during Fe transport through compacted, fully saturated clay in the absence of oxygen, conditions which are expected to prevail after closure of the repository and consumption of all oxygen, thus leaving out the complicating effects of the initial oxic stage. The objective of this experiment is to better understand the effects of Fe corrosion on bentonite stability for the long-term anaerobic phase. Reactive transport modelling during and after the experiment will provide an important basis for the long-term predictions on degradation processes in bentonite. The Fe(II)-montmorillonite interaction model to be developed in this part of Task 2.1 of ACED will be integrated in the coupled steel-corrosion-bentonite interaction model, which will be developed by UniBern considering findings from in-situ test (Chapter 6).

Chapter 3.1 describes the planned Fe(II) diffusion cell experiment. Chapter 3.2 and chapter 3.3 present the proposed modelling approach and the conceptual model, respectively. Chapter 3.4 provides the numerical model as used for the scoping calculations performed for design optimization. The results of the scoping calculations are presented in chapter 3.5.

#### 3.1 Fe(II) diffusion cell experiments

The cell experiment is currently in the preparation and optimisation stage and has not started yet. The presented experimental details thus reflect the status at the time the scoping calculations were performed and might be still subject to change.

##### 3.1.1 Dimensions

Figure 3-1 shows the set-up of the Fe(II) diffusion experiment with its dimensions.

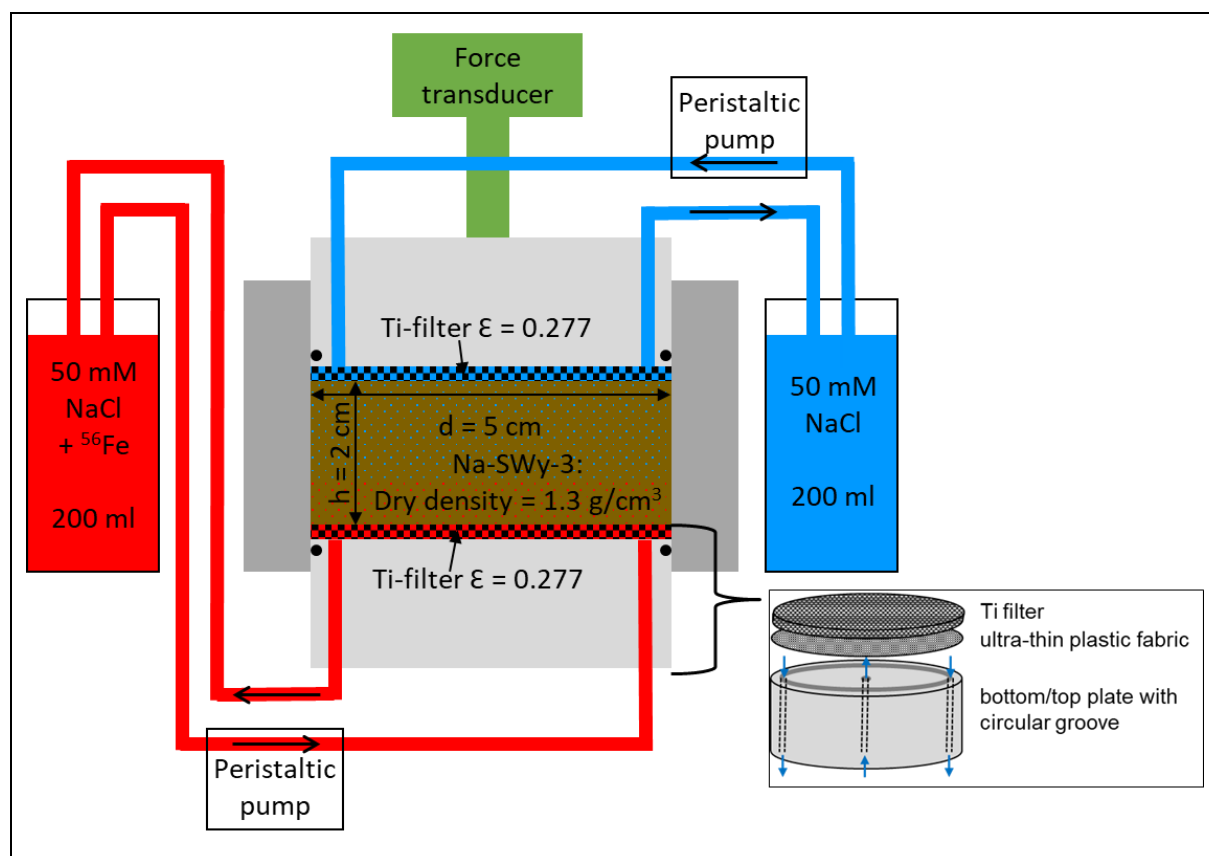


Figure 3-1 – Schematic and dimensions of the Fe(II)-diffusion experiment.

### 3.1.2 Materials

The diffusion cell will be prepared with purified SWy-3 (elutriation), which is comparable to SWy-2. SWy-2 and SWy-3 are the same as SWy-1. SWy-2 and SWy-3 were collected from the same mine from where SWy-1 was collected at two later occasions ([http://www.clays.org/sourceclays\\_data.html](http://www.clays.org/sourceclays_data.html)). Purification was required as bulk SWy-3 analyses indicated the presence of approximately 3% of the Fe to be present as Fe<sup>3+</sup> impurities (lepidocrocite). The initial reduction level of structural Fe is 17%, which is assumed to be isolated in illitic layers. Characterization of purified material has not been performed. The montmorillonite SWy-3 in the diffusion cell will be compacted to a dry density of 1.3 g/cm<sup>3</sup>, fully saturated and equilibrated with anaerobic 50 mM NaCl solution.

Top and bottom reservoir will contain 200 ml of 50 mM NaCl solution. <sup>56</sup>Fe solution will be added to the bottom reservoir; the final Fe target concentration therein is not yet decided.

### 3.1.3 Conditions

The entire experiment will be performed under anoxic conditions in a glovebag with continuous oxygen scrubbing (Pd catalyst beads; 3-6% H<sub>2</sub> in glovebag atmosphere). Still, traces of oxygen (<2 ppm) are likely continuously present in the glovebag. The experiment itself will be further confined from the glovebag atmosphere as the reservoirs will be tight closed and the tubing connection sealed. Solution sampling will be done through a septum present on the reservoir neck. Any ultimate traces of O<sub>2</sub> potentially present in the reservoir headspace are expected to be scrubbed by the Fe(II) solution (pH >6) present in the reservoir and tubes, and thus have very low chances to enter the core.

Clay powder is dried, compacted, and saturated under anoxic conditions. The montmorillonite will be fully saturated. The solution in the reservoirs and filters will be circulated continuously. There will be no hydraulic gradient and flow in the diffusion cell.

## 3.2 Proposed modelling approach

A reactive transport model is used for the simulation of the Fe diffusion and sorption in the diffusion cell. The powerful simulator PFLOTRAN ([www.pflotran.org](http://www.pflotran.org)), an open source, massively parallelised subsurface flow and reactive transport code, will be used for numerical implementation.

The ANDRA/Thermochimie Database v9.b (Giffaut et al., 2014; Grivé et al., 2015) is used for the calculation of aqueous reactions.

## 3.3 Conceptual Model

### 3.3.1 Objectives of the Model

The objective of this migration experiment is to understand the effects of Fe corrosion on bentonite stability for the long-term anaerobic phase. The focus is on the interaction of Fe(II) with smectite without complicating factors from the transient phase (e.g. variable saturation, variable redox conditions such as encountered in the FEBEX experiment). Main focus is the understanding and quantification of the electron transfer of sorbed Fe(II) to structural Fe(III) in the octahedral montmorillonite structure. This process model should later be incorporated in the corrosion models for e.g. the FEBEX-corrosion-model (see chapter 6).

At the present stage of the project, the model serves for scoping calculations, which should provide the following information:

- Optimum Fe concentration and Fe/Na ratio in the reservoir in order to obtain i) Fe-loading of the montmorillonite high enough for analytical detection of the expected Fe redox transitions within the montmorillonite structure and ii) development of an Fe diffusion front in the compacted montmorillonite deep enough for spatially resolved analytics within reasonable time.

- Prediction of the Fe diffusion front with time, determination of required experimental duration.
- Prediction of relative contribution of Fe sorption on edge and planar sites.

During the experiment, the development of tracer concentrations in the reservoir over time will be used for modelling the transport parameters in the experiment and thus update the predicted progress of the diffusion fronts.

### 3.3.2 Processes to be modelled

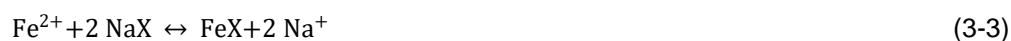
The Fe(II) experiments represent a simplified experimental system. The geochemical model is therefore constrained to the following processes:

- Aqueous chemistry of Na, Cl and Fe including the following species:  $\text{Fe}^{2+}$ ,  $\text{Fe}^{3+}$ ,  $\text{Fe}(\text{OH})_2$ ,  $\text{Fe}(\text{OH})_2^+$ ,  $\text{Fe}(\text{OH})_3$ ,  $\text{Fe}(\text{OH})_3^-$ ,  $\text{Fe}(\text{OH})_4^-$ ,  $\text{Fe}(\text{OH})_4^{2-}$ ,  $\text{FeOH}^+$ ,  $\text{FeOH}^{2+}$ ,  $\text{FeCl}^+$ ,  $\text{FeCl}^{2+}$ ,  $\text{FeCl}_2$ ,  $\text{FeCl}_2^+$ ,  $\text{FeCl}_3^-$ ,  $\text{FeCl}_3$ ,  $\text{Na}^+$ ,  $\text{NaCl}(\text{aq})$ ,  $\text{H}_2(\text{aq})$ ,  $\text{O}_2(\text{aq})$ ,  $\text{OH}^-$ ,  $\text{H}^+$
- Protonation and de-protonation reactions of the montmorillonite edge sites contributing to pH buffering, according to



where S indicates a generic surface sorption site (strong, weak1 or weak2) on montmorillonite.

- Cation exchange involving Na and Fe(II)



- Fe(II) surface complexation reactions (non-electrostatic) on strong and weak1 sites of montmorillonite without electron transfer



- Sorption of Fe(II) on montmorillonite (non-electrostatic) and transfer of an electron to the structural Fe(III) of montmorillonite. At the present stage of the modelling, the formulation of Soltermann et al. (2014) for Fe(II) surface complexation with electron release is adopted:



### 3.3.3 Important assumptions, simplifications, limitations

- The montmorillonite is initially and throughout the experiment fully water-saturated and isothermal (25°C). The initial state assumes no residual atmospheric oxygen in neither the montmorillonite nor the reservoir solutions.
- All aqueous reactions, exchange reactions, surface protonation/de-protonation and surface complexation reactions assume chemical equilibrium. No mineral dissolution and precipitation reactions are considered.
- Transport in the clay is by diffusion only. A single, full porosity is considered for transport.
- The concentrations in the filter and the reservoirs are assumed to be identical, due to continuous flushing of the filter. Thus, transport from reservoir to filter is not limited by the filter.

### 3.3.4 Boundary Conditions

The experimental system is a closed system. The outer boundaries of the reservoirs are no-flux boundaries.

### 3.3.5 Initial conditions / parameters

In the Base Case, the total (physical) porosity of the montmorillonite disc is taken to be 0.52 corresponding to a dry density of 1.3 g/cm<sup>3</sup>. An effective diffusion coefficient  $D_e$  of  $2 \cdot 10^{-11}$  m<sup>2</sup>/s is selected based on the study of Bestel et al. (2018).

The parameterization of protolysis and sorption reactions as considered in the Base Case are summarized in Table 3-1, the initial conditions considered for the reservoirs and montmorillonite porewater in Table 3-2.

Table 3-1 – Parameterization of site types, site capacities, protolysis constants and sorption parameters as considered in the Base Case

Site types	capacity	Reference
$\equiv S^s OH$	$2 \cdot 10^{-3}$ mol/kg	Bradbury and Baeyens (1997)
$\equiv S^{w1} OH$	$4 \cdot 10^{-2}$ mol/kg	
$\equiv S^{w2} OH$	$4 \cdot 10^{-2}$ mol/kg	
CEC	0.87 eq/kg	
Surface complexation reaction	log K	Reference
$\equiv S^{s/w1} OH \leftrightarrow S^{s/w1} O^- + H^+(aq)$	-7.9	Bradbury and Baeyens (1997)
$\equiv S^{s/w1} OH + H^+(aq) \leftrightarrow S^{s/w1} OH_2^+$	4.5	
$\equiv S^{w2} OH \leftrightarrow S^{w2} O^- + H^+(aq)$	-10.5	
$\equiv S^{w2} OH + H^+(aq) \leftrightarrow S^{w2} OH_2^+$	6.0	
$\equiv S^s OH + Fe^{2+} \leftrightarrow \equiv S^s OFe^+ + H^+$	1.9	Soltermann et al. (2014) for Fe rich montmorillonite (SWy-2)
$\equiv S^{w1} OH + Fe^{2+} \leftrightarrow \equiv S^{w1} OFe^+ + H^+$	-1.7	
$\equiv S^s OH + Fe^{2+} \leftrightarrow \equiv S^s OFe^{2+} + H^+ + e^-$	-1.4	
$\equiv S^{w1} OH + Fe^{2+} \leftrightarrow \equiv S^{w1} OFe^{2+} + H^+ + e^-$	-3.8	
Cation exchange reaction	log $K_{sel-GT}$	
$Fe^{2+} + 2 NaX \leftrightarrow FeX_2 + 2 Na^+$	0.8	Soltermann et al. (2014)

Table 3-2 – Initial composition of reservoir solution and montmorillonite porewater as considered in the Base Case

Parameter	Bottom Reservoir	Top Reservoir	Montmorillonite porewater
pH	5.66	7	8
pe	-2.5	-3.9	-4.9
Na [mol/L]	$5 \cdot 10^{-2}$	$5 \cdot 10^{-2}$	$5 \cdot 10^{-2}$
Cl [mol/L]	$1.5 \cdot 10^{-1}$	$1.5 \cdot 10^{-1}$	$1.5 \cdot 10^{-1}$
Fe [mol/L]	$5 \cdot 10^{-2}$	0	0
Tracer [mol/L]	$5 \cdot 10^{-2}$	$5 \cdot 10^{-2}$	$5 \cdot 10^{-2}$

### 3.4 Numerical model

#### 3.4.1 Spatial and temporal discretization

The experimental system is modelled as a 1-D structured cylindrical grid with a single cell in radial direction having a diameter of 5 cm. Top and bottom reservoir are described as single cells of 10 cm

each, the filters as single cells of 0.1 cm each. The 2 cm thick clay disc is divided into 20 x 0.1 cm thick cells.

Total calculation time is set to 10 years with a maximum time stepping of 0.01 years (3.6 days). Output is generated for time intervals of 36.5 days.

### 3.4.2 Sensitivity analyses

Several variant cases were run in order to estimate the impact of transport and sorption parameters uncertainty on the expected experimental outcome. Furthermore, NaCl-background and Fe concentrations were varied in order to evaluate optimum experimental conditions with respect to Fe-loading and diffusion front. Table 3-3 lists the different variant cases calculated so far during the scoping calculations.

Table 3-3 – Summary of variant cases

Parameter	Base Case (BC)	Variant Case
$D_e$ [m <sup>2</sup> /s]	$2 * 10^{-11}$	$5 * 10^{-12}$ / $8 * 10^{-11}$
CEC [eq/kg]	0.87	0.435 (50% BC) 1.305 (150% BC)
$\log K_{sel}$ Fe/Na	0.8	0.5 / 1.1 (uncertainty reported by Soltermann et al. (2014))
$\log K$ of $\equiv S^{s/w1}OH + Fe^{2+} \leftrightarrow \equiv S^{s/w1}OFe^{2+} + H^+ + e^-$	-Dependency of Fe(III) surface complex formation on pe included according to Soltermann et al. (2014)	Log K fixed corresponding to experimental conditions of Soltermann et al. (2014)
NaCl-Background [mmol]	50	100 / 2000
Fe in bottom reservoir [mmol]	50	2 / (5) / 20 / 200
Fe/Na ratio	1	0.0025 / 0.025 / 0.04 / 0.05 / 0.4 / 0.5 / 4 /

### 3.4.3 Model calibration

Model calibrations will be carried out when results are available.

## 3.5 First results and discussion

Figure 3-2 visualizes the expected evolution of the non-reactive tracer (e.g. HTO) and Fe in the bottom and top reservoir at Base Case Fe and Na concentrations (Fe/Na both 50 mM) for the range of expected  $D_e$  values (top graphs) and within an uncertainty range for the parameterization of the cation exchange. These indicate that at BC Fe/Na ratios, a Fe-breakthrough in the top reservoir cannot be expected within the first year of the experiment. The monitoring of tracer and Fe concentrations in the bottom reservoir over time however will allow for a determination of the  $D_e$  value during the experiment. As the evolution of Fe concentrations in the bottom reservoir is less affected by the uncertainty in sorption parameterization than in  $D_e$ , comparison of tracer and Fe depletion in the reservoir can be used for an evaluation of the applicability of the simplified single porosity model for the description of Fe diffusion in the montmorillonite disc.

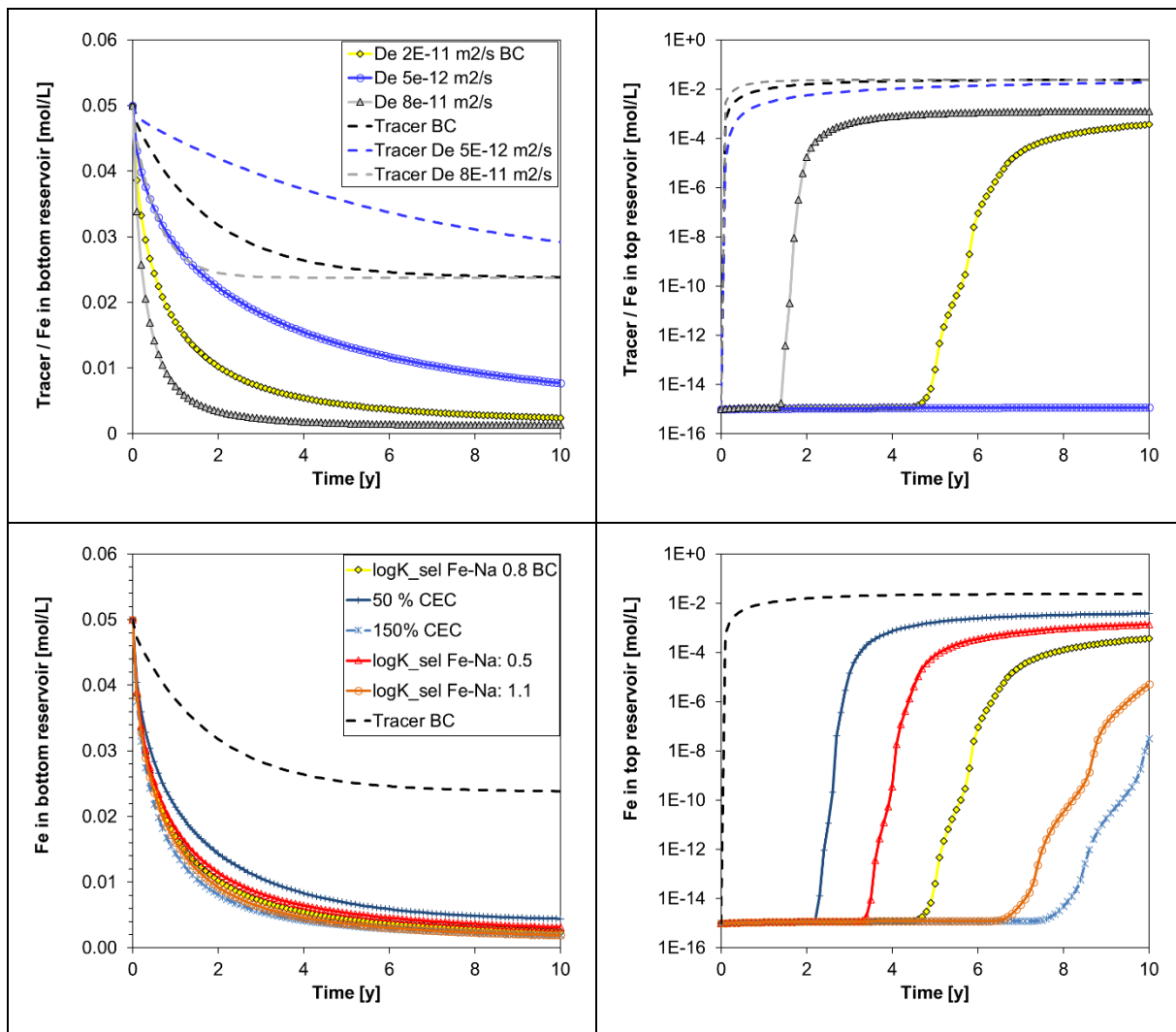


Figure 3-2 – Evolution of Fe and non-reactive Tracer concentrations in the bottom (left) and top (right) reservoirs depending on  $D_e$  (top) and parameterization of CEC (bottom) in the montmorillonite disc. Note the logarithmic scale of the right panels.

The dependence of the Fe sorption front on the selected Fe and Na concentration is visualized in Figure 3-3. At initial Fe reservoir concentrations above 20 mM and Na concentrations in the range of 50 to 100 mM, maximum Fe loadings of 0.3 to 0.4 mol/kg montmorillonite can be obtained. This equals 60 to 80 % of the structural Fe (0.5 mol per kg Na-SWy-3). At lower Fe/Na ratios, Fe sorption to the planar CE sites is decreased and total sorbed Fe will be less than the equivalent of 50% of the structural Fe. After 1 year, the model predicts a sorption front reaching between 0.5 and 1.5 cm into the bentonite for conditions meeting the above criteria. For extremely high Fe concentrations (200 mM) the Fe front might reach even further, however, given the experimental difficulties to guarantee the absence of precipitation at such high Fe concentrations, these are not considered practicable.

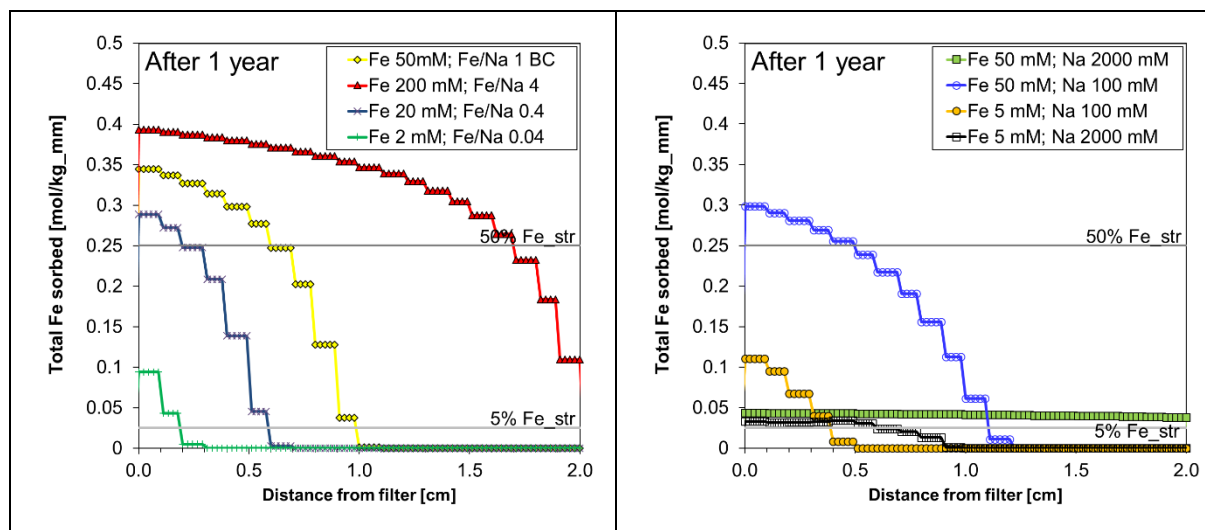


Figure 3-3 – Prediction of Fe sorption front for the Base Case and Variant cases with different Fe and Na concentrations.

Figure 3-4 (left) visualizes the distribution of Fe over the different sorption sites calculated with the sorption model of Soltermann et al. (2014). At the high Fe loadings obtained over the largest part of the sorption front, cation exchange dominates, whereas in the first 1-2 mm of the diffusion front sorption is controlled by specific sorption to the edge sites. The strong Eh dependency of the formation of Fe(III) surface complexes in the model of Soltermann results in predicted negligible formation of those Fe(III) surface complexes at the redox conditions considered for the planned experiment (pe around -4). In comparison, applying fixed complex formation constants corresponding to the anoxic conditions in the Soltermann study (Figure 3-4 right) predicts almost exclusively Fe(III) on the edge sites. The stronger Fe(III) complex in this case also results in a steeper sorption front, however, the effect of the surface complex formation constant on the overall progress of the sorption front remains in the range of 1 mm.

It should be noted, that the Soltermann model was developed for the description of the redox dependent sorption behaviour of Fe and not for the quantification of the change in structural Fe oxidation state. Thus, the negligible formation of Fe(III) surface complexes under experimental conditions does not imply that no electron transfer is predicted. Following the work of Latta et al. (2017) electron transfer from sorbed Fe(II) to structural Fe(III) is presumably not limited to Fe(II) sorbing at the edges but also occurs directly via the planar sites. They observed for Na-SWy-2 a 1:1 stoichiometry of Fe sorbed and structural Fe reduced, until around 50 % of the structural Fe in the montmorillonite was reduced. Above this value, further reduction was observed until around 80% was reduced, although it did not follow the 1:1 stoichiometry anymore. Thus, with the present knowledge we expect the extent of structural Fe(III) reduction in the cell experiment to approach the extent of Fe sorbed. However, further in-house pre-experiments and in particular the cell experiment itself target at an improved understanding and quantification of the electron transfer process. The results of these planned experiments will then provide the base for the development of a model extension, capable of describing and quantifying the changes of the montmorillonite.

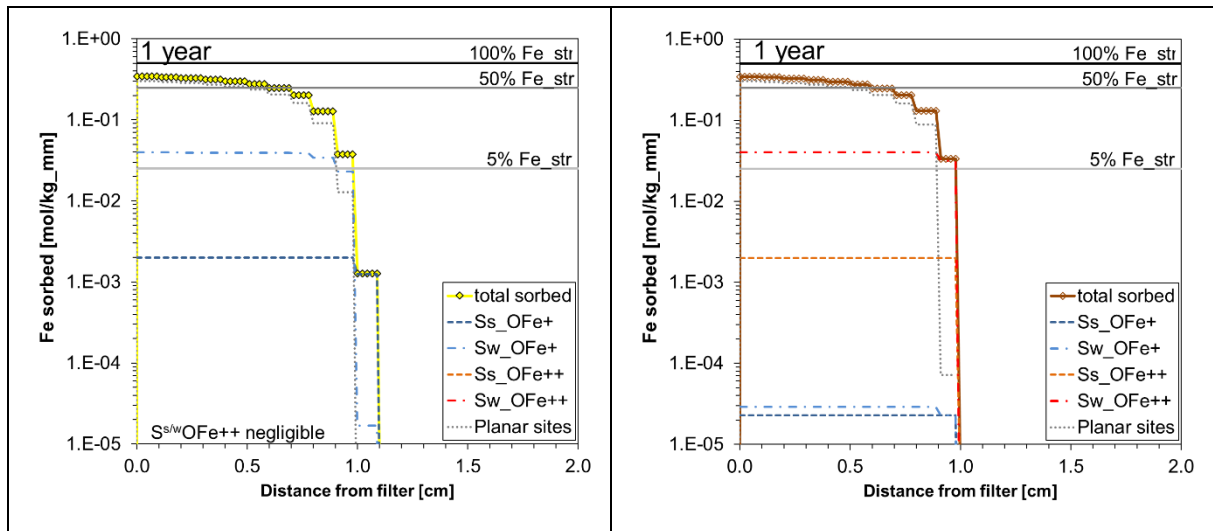


Figure 3-4 – Fe sorption front and distribution of Fe on different sorption sites for the BC (left), with Eh dependency of the  $\equiv S^{s/w1} OFe^{2+}$  complex formation and in the variant case (right), with a fixed logK corresponding to the experimental conditions of Soltermann et al. (2014).

## 4. Numerical modelling of the FB lab experiments of CIEMAT on the interactions of FEBEX bentonite and steel corrosion products (UDC)

This chapter presents the numerical models of the FB laboratory experiments developed by UDC. These experiments were performed by CIEMAT with the support of UAM for the characterization of the interactions of steel corrosion products and compacted FEBEX bentonite. The description of the numerical model includes the proposed modelling approach and the preliminary model predictions. The proposed model improvements and the identification of the missing data for model validation are summarized in chapter 8.

### 4.1 FB laboratory corrosion experiments

Six heating and hydration column tests (FB corrosion tests) were performed by CIEMAT on FEBEX bentonite samples in contact with Fe powder to: (1) Simulate the operational and the early post-closure transient phases of the repository before achieving full saturation of the EBS; and (2) Study the steel corrosion products and bentonite interactions under repository conditions and analyse how such interactions affect the bentonite properties (Turrero *et al.*, 2011).

Columns containing the Fe powder and bentonite samples were hydrated at a constant pressure at the top of the column through the bentonite while the temperature was maintained constant at 100°C at the bottom of the column where the Fe-powder was placed (Figure 4-1).

Six cells (FB1 to FB6) were mounted at the same time on August 2006. Tests were performed at anoxic conditions for durations ranging from 6 months to 13 years. All of them were mounted and run in the same way (heating and hydration), except for the FB6 cell, in which no hydration takes place. Cells were dismantled sequentially to study the evolution of the corrosion processes and evaluate how corrosion affects the properties of the bentonite. The FB1 and FB2 were dismantled during the NF-PRO project after 6 and 15 months, respectively. The FB3 and FB4 cells were dismantled after 4.5 years and 7 years of operation, respectively, within the PEBS project. Data from FB4 cell are still unpublished. FB5 and FB6 cells will be dismantled after 13 years of operation during the second half of 2020 with a delay of 4-6 months due to the COVID-19 crisis.

The FB corrosion tests were carried out on medium-size cells containing a cylinder of bentonite in contact with a cylinder of Fe-powder. The bentonite and the Fe-powder samples were emplaced into cylindrical hermetic cells with an internal diameter of 7 cm and an inner length of 10 cm (Figure 4-1). The outer cells were made of Teflon to decrease the lateral heat conduction and framed with clamps to prevent bentonite swelling. A temperature of 100°C was imposed at the bottom of the column through a plane stainless steel heater while on the top of the column a hydration system injected water at a pressure of 600 kPa through a stainless steel tank at a controlled temperature of 22°C. The tank was periodically weighed to check the water intake (Turrero *et al.*, 2011).

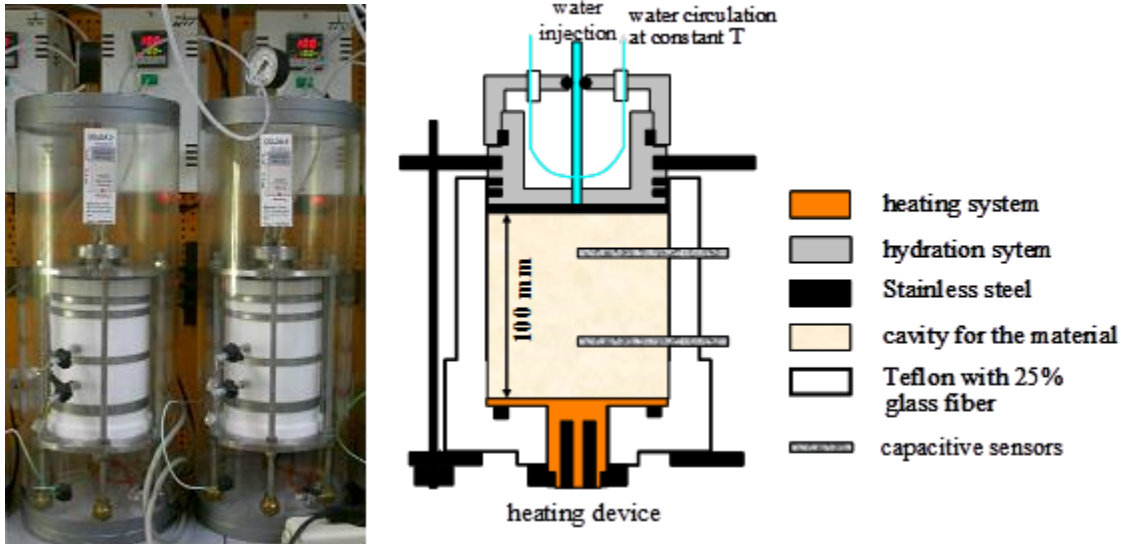


Figure 4-1 – Picture and scheme of the FB corrosion tests (Turrero et al., 2011).

The FB corrosion column tests were instrumented with two capacitive sensors to record the relative humidity and the temperature in the bentonite at 1.8 cm and 7.4 cm from the heating system (Figure 4-1). The FB corrosion column tests were dismantled at ambient temperature after the heating and hydration phase.

#### 4.1.1 Dimensions

The medium-size cells corrosion FB corrosion tests contain a cylindrical sample of compacted FEBEX bentonite with a height of 8.68 cm and a radius of 3.5 cm in contact with a cylindrical sample of Fe-powder with a height of 1.3 cm and a radius of 3.5 cm (Turrero et al., 2011). Both samples were emplaced into cylindrical hermetic cells with an internal diameter of 7 cm and an inner length of 10 cm (Figure 4-2).

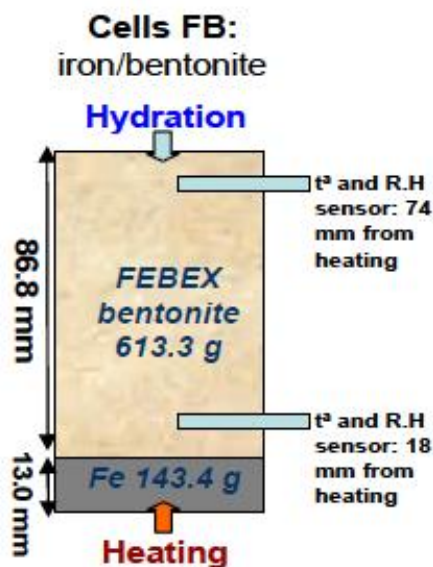


Figure 4-2 – Sketch of the FB corrosion tests cells (Turrero et al., 2011).

#### 4.1.2 Materials

Blocks of FEBEX bentonite were compacted with its hygroscopic water content (14%) at a nominal dry density of 1.65 g/cm<sup>3</sup> and placed inside the FB cells. Table 4-1 shows the FEBEX bentonite mineralogical composition (Fernández et al., 2001). The cation exchange capacity is 102±4 meq/100g, being the main exchangeable cations calcium, magnesium and sodium. The predominant soluble ions are chloride, sulfate, bicarbonate and sodium. The external specific surface area is 61 m<sup>2</sup>/g and the total specific surface area is about 725 m<sup>2</sup>/g (Turrero et al., 2011).

Table 4-1 Mineralogical composition of the FEBEX bentonite (Fernández et al., 2001).

Mineral	Content (wt.%)
Montmorillonite	92 ± 3
Plagioclase	3 ± 1
K-feldspar	traces
Quartz	2 ± 1
Calcite	1 ± 0.5
Cristobalite/Tridymite	2 ± 1

At the bottom of the cell, in contact with the heater, 143.4 g of Fe powder were placed giving rise to an iron layer thickness of 13.0 mm (Figure 4-2). The Fe powder used in the FB corrosion tests, which was used instead of carbon-steel plates to favour the corrosion process, was manufactured by Goodfellow with a particle size of 60 µm and purity higher than 99% (Turrero et al., 2011).

The FB corrosion column tests were hydrated with granitic water collected in the Grimsel Test Site from the BO-ADUS borehole (Turrero et al., 2011). The granitic water is alkaline, reduced and Na-Ca-HCO<sub>3</sub> type. The reducing character of the hydration water was preserved during hydration.

Once dismantled, three types of samples are analysed (Figure 4-3): (1) Precipitates found at the iron/bentonite interface near the Fe powder/bentonite interface; (2) Bentonite samples in three zones, hydration zone, intermediate zone, and heated zone near the Fe powder/bentonite interface, and (3) Iron samples.

#### 4.1.3 Conditions

The FB corrosion tests were performed at the following conditions:

- 1) Unsaturated bentonite
- 2) Non-isothermal conditions
- 3) Fe powder in contact with compacted bentonite. Fe powder has a specific surface area of 0.13 m<sup>2</sup>/g which is much larger than that of carbon steel.

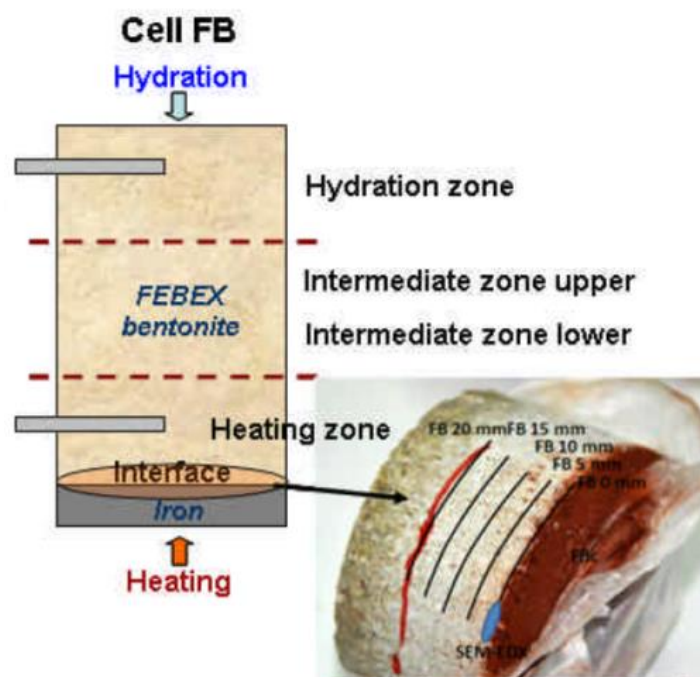


Figure 4-3 – General sampling of the FB cells and detailed sampling at the interface iron-bentonite of the FB3 cell (Turrero et al., 2011).

The chemical interactions of the bentonite and the corrosion products depend on the availability of water at the Fe powder. The bentonite relative humidity plays an important role in Fe oxidation (Torres et al., 2013). Water vapour is the oxidizing agent. High relative humidity allows the formation of different crystalline phases (Turrero et al., 2013). Goethite was detected in the 6-month test (FB1 cell). Hematite precipitated in the 15-month test (FB2 cell). On the other hand, in addition to hematite, lepidocrocite, goethite, akageneite, maghemite and magnetite were found at the bentonite-iron contact in the 52-82 months tests (FB3 and FB4 cells). Data from these cells are being re-evaluated because different characterization equipment and interpretation techniques were used. The consistency of the data from the FB4 test with the data collected from FB1, FB2 and FB3 tests is being checked by CIEMAT and UAM.

In summary, goethite precipitated at early times in the absence of water vapour in the Fe powder. Then, hematite precipitated due to the degradation of the goethite. Finally, lepidocrocite, goethite, akageneite, maghemite and magnetite were found at the bentonite-iron contact. Figure 4-4 shows a summary of the corrosion products found in the FB1, FB2 and FB 3 cells (Torres et al., 2013).

	Fe powder		
	6 months	15 months	52 months
			
<b>Date of dismantling</b>	February 2007	November 2008	December 2010
<b>Location of corrosion products</b>	At the interface	At the interface + small fraction of Fe powder	All Fe powder corroded
<b>Corrosion products</b>			
At the interface	Goethite	Goethite	Goethite
Intermediate fraction	×	Hematite	Hematite
Close to the heater	×	×	Magnetite + hydrated ferrous oxides

Figure 4-4 – Summary of the corrosion products found in the FB1, FB2 and FB 3 cells (Torres et al., 2013)

## 4.2 Proposed modelling approach

UDC performed a reactive transport model of the FB3 corrosion test (Mon, 2017). ENRESA (UDC) will perform reactive transport models of the FB4, FB5 and FB6 corrosion tests in close collaboration with CIEMAT and UAM. The FB4 corrosion test was dismantled in 2013 after 7 years of heating and hydration. Data from the FB4 corrosion test are still unpublished. CIEMAT and UAM have agreed with UDC to provide the experimental data needed to model the FB4 corrosion test by the end of June 2020.

FB5 corrosion test was dismantled in the beginning of 2020. According to CIEMAT & UAM, the dismantling and characterization of this test has been delayed due to the Covid-19 crisis. The FB6 corrosion test will be dismantled at the end of 2020. The numerical models of the FB5 and FB6 corrosion tests will be performed once all the experimental data have been collected, analyzed, processed and validated.

The coupled reactive THCM model of the FB column tests accounts for non-isothermal two-phase flow conditions, the bentonite deformation, the hydration of the sample on the top of the column and the heating at the bottom. Special emphasis will be given to the modelling of the mineralogical and structural changes in the bentonite near the Fe powder. Model results will be compared to available measured data on corrosion products and mineralogical alterations in the bentonite.

The reactive transport model of the FB3 corrosion test performed by Mon (2017) will be the starting point. The model will be extended from 1593 days (the duration of the FB3 corrosion test) to 2555 days (7 years, the duration of the FB4 corrosion test).

Later on in the ACED WP, the model will be improved by accounting for:

- 1) An early stage with aerobic corrosion and a late stage of anaerobic corrosion.
- 2) A time-varying corrosion rate depending on ambient conditions (T, pH, Eh).
- 3) Steel corrosion and Fe diffusion with the conceptual model of Hadi et al. (2019).
- 4) Kinetically-controlled magnetite precipitation and the precipitation of other corrosion products such as goethite, siderite, chukanovite and Fe-phyllsilicates.
- 5) Kinetically-controlled smectite dissolution and zeolite precipitation.

The model of the FB4, FB5 and FB6 corrosion tests will be performed with the following stages:

- 1) Analysis of available data.
- 2) Formulation of the revised conceptual geochemical model.
- 3) Definition of the model structure (spatial and time discretization; parameterization).
- 4) Sensitivity analyses prior to model calibration.
- 5) Model calibration.
- 6) Uncertainty analyses.

The main outcomes of the models of the FB4, FB5 and FB6 corrosion test include: 1) Improving the understanding of the dependence of the corrosion rate and the bentonite mineralogical alterations on thermal, hydrodynamic, solute transport and geochemical conditions; 2) Gaining confidence on reactive transport modelling of the iron-bentonite interactions; and 3) Reducing the uncertainties of reactive transport models.

## 4.3 Conceptual Model

### 4.3.1 Objectives of the model

The model of the FB4 corrosion test will be performed by ENRESA (UDC) in close collaboration with the CIEMAT and UAM teams who performed the tests. The collaboration between the modelling and the experimental groups will be most useful to identify the crucial aspects of the conceptual model of steel/clay interactions which is the fundamental basis of the reactive transport model. This active collaboration will also help to identify the experimental data that is best for model validation and testing the predictions of corrosion rates and clay alterations.

The three main objectives of the THCM reactive transport model of the FB4 corrosion tests include:

- (1) Evaluating the steel corrosion rate in contact with compacted bentonite.
- (2) Identifying the crucial aspects of the conceptual geochemical models of steel corrosion in contact with compacted bentonite and improving such conceptual model.
- (3) Identifying the critical parameters and the most informative experimental data for model discrimination.

In order to achieve these objectives, ENRESA (UDC) will perform a multicomponent geochemical reactive transport model of the FB corrosion tests. The model will account for time-varying corrosion rate depending on ambient conditions (T, pH, Eh) and will be based on the revised conceptual and mathematical model of the steel/bentonite interactions identified in ACED Task 1.

### 4.3.2 Processes to be modelled

The following processes will be considered in the coupled reactive transport model of the FB4 corrosion test:

- 1) Coupled non-isothermal single-phase (saturated conditions) and two-phase (unsaturated conditions) flow and multicomponent geochemical reactive transport.
- 2) Geochemical homogeneous reactions: aqueous complexation, acid-base and redox reactions.
- 3) Geochemical heterogeneous reactions: cation exchange, protonation/deprotonation by surface complexation reactions, iron sorption by cation exchange and surface complexation and mineral dissolution/precipitation under LEA and kinetic control.
- 4) Kinetically-controlled Fe(s) corrosion.
- 5) Constant and time-varying corrosion rates depending on ambient conditions such as temperature, pH, Eh, ionic strength and carbonate concentration .
- 6) Additional corrosion products such as Fe-phyllsilicates will be considered.
- 7) Kinetically-controlled smectite dissolution.

- 8) Changes in porosity and other parameters caused by mineral dissolution/precipitation will be taken into account.

#### 4.3.3 Important assumptions, simplifications and limitations

The thermo-osmosis permeability is derived from Zheng et al. (2010) and is equal to  $4.2 \cdot 10^{-13} \text{ m}^2/\text{K/s}$ . Similar to Zheng et al. (2010), the THCM model does not consider anion exclusion.

No vertical displacement is considered at the top of the FB4 corrosion test. The initial stress was assumed uniform and isotropic and equal to  $2.5 \cdot 10^5 \text{ Pa}$ .

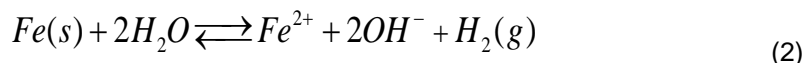
Cation exchange reactions are not considered in the Fe powder. Surface complexation reactions are assumed to occur in the bentonite and in the Fe powder to improve the convergence of the numerical solution.

All the mineral reactions considered in the reactive transport model of the FB4 corrosion test are assumed at chemical equilibrium, except for the Fe powder dissolution which is modelled with the following kinetic rate law:

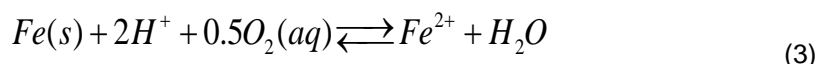
$$r_m = k_m \quad (1)$$

where  $r_m$  is the dissolution/precipitation rate ( $\text{mol}/\text{m}^2/\text{s}$ ) and  $k_m$  is the kinetic rate constant ( $\text{mol}/\text{m}^2/\text{s}$ ) at  $25^\circ\text{C}$ . The dissolution/precipitation rate in  $\text{mol}/\text{m}^2/\text{s}$ ,  $r_m$ , is multiplied by the mineral specific surface area,  $\sigma$ , to get the dissolution/precipitation rate in  $\text{mol}/\text{m}^3/\text{s}$ ,  $R_m$ . The specific surface area  $\sigma$  is defined as the surface area of the mineral per unit fluid volume. The model assumes that  $\sigma$  is constant in time.

Fe powder is treated as a porous material made of 100% metallic iron,  $\text{Fe}(s)$ . Under anaerobic conditions,  $\text{H}_2\text{O}$  is the oxidizing agent of  $\text{Fe}(s)$  ( Lu et al.,2011; Samper et al.,2016; and Mon et al., 2017). The anaerobic  $\text{Fe}(s)$  corrosion reaction is given by:



Even though corrosion takes place according to Eq. (2), the numerical model solves the following equivalent reaction, which is written in terms of dissolved oxygen:



The model considers the diffusion of dissolved  $\text{H}_2(aq)$  and disregards  $\text{H}_2(g)$  gas transport through the gaseous phase.

The  $\text{Fe}(s)$  is kinetically controlled and assumed to corrode at a constant rate. The corrosion rate,  $r_c$ , in  $\mu\text{m}/\text{year}$  is calculated as:

$$r_c = \frac{r_m M_w}{\rho} \quad (4)$$

where  $\rho$  is the density of the iron ( $7860 \text{ kg}/\text{m}^3$ ),  $M_w$  is its molecular weight ( $55.85 \text{ g}/\text{mol}$ ) and  $r_m$  is the corrosion rate per unit mineral surface ( $\text{mol}/\text{m}^2/\text{year}$ ).

#### 4.3.4 Boundary Conditions

A liquid pressure of 600 kPa and a temperature of  $22^\circ\text{C}$  are prescribed at the top of the cell. A temperature of  $100^\circ\text{C}$  is fixed at the heater.

A Neuman boundary condition is used for solute transport according to which solute flux is equal to the product of water flux times the solute concentration of inflow water.

#### 4.3.5 Initial conditions / parameters

Hydrodynamic, mechanical, thermal and solute parameters of the bentonite and the magnetite powder are listed in Table 4-2 to Table 4-5. Bentonite parameters are taken from Zheng et al. (2010) and Samper et al. (2018a). Bentonite has an initial porosity of 0.4 and an initial gravimetric water content of 0.14, which corresponds to a saturation of 57% and a suction of  $1.27 \cdot 10^5$  kPa. Fe powder parameters are taken from Mon (2017). As an educated guess, the Fe powder is assumed to have an initial porosity of 0.38 and a saturation of 31%. The initial temperature in the FB4 corrosion test is equal to 22°C. The initial gas pressure is equal to the atmospheric pressure.

We recall that the FB tests were performed under unsaturated conditions. There is a gaseous phase because the bentonite samples were always unsaturated. The tests were performed under anoxic conditions. The initial oxygen in the bentonite sample is assumed to be consumed in the early stages of the tests.

The porewater diffusion coefficients are equal to  $2 \cdot 10^{-10}$  m<sup>2</sup>/s for all chemical species, except for Cl<sup>-</sup> which has a value of  $9 \cdot 10^{-11}$  m<sup>2</sup>/s (Zheng et al., 2010). The initial effective diffusion coefficient is equal to  $9.45 \cdot 10^{-12}$  m<sup>2</sup>/s for the Cl<sup>-</sup> and  $4.2 \cdot 10^{-12}$  m<sup>2</sup>/s for the rest of the species.

Table 4-2 – Water flow parameters (ENRESA, 2006a; Zheng et al., 2010).

	Bentonite	Fe powder
Intrinsic permeability of the liquid, $k^{il}$ (m <sup>2</sup> ) as a function of porosity	$k^{il} = k_0 \frac{\phi^3}{(1-\phi)^2} \frac{(1-\phi_0)^2}{\phi_0^3}$	
	with $\phi_0=0.40$ $k_0 = 2.75 \cdot 10^{-21}$	with $\phi_0=0.38r$ $k_0 = 2.75 \cdot 10^{-19}$
Liquid relative permeability $k^{rl}$ as a function of liquid saturation $S_l$	$k_{rl} = S_l^3$	
Retention curve: liquid saturation $S_l$ as a function of suction $\Psi$ (Pa)	$S_l = \frac{(1 - 9.1 \cdot 10^{-7}\Psi)^{1.1}}{[(1 + 5 \cdot 10^{-5}\Psi)^{1.22}]^{0.18}}$	
Liquid viscosity (kg/m·s) as a function of temperature $T$ (°K)	$0.6612 \cdot (T - 229)^{-1.562}$	
Liquid density (kg/m <sup>3</sup> ) as a function of liquid pressure $p^l$ and temperature	$998.2 \cdot e^{[5 \cdot 10^{-5} \cdot (p^l - 100) - 2.1 \cdot 10^{-4} \cdot (T - T_{ref})]}$	
Reference temperature, $T_{ref}$ (°C)	22	
Gas intrinsic permeability (m <sup>2</sup> )	$5 \cdot 10^{-10}$	
Gas relative permeability $k^{rg}$	$k_{rl} = (1 - S_l)^3$	
Vapour tortuosity	0.12	0.12
Gas viscosity (kg/m·s)	$1.76 \cdot 10^{-5}$	
Solid density (kg/m <sup>3</sup> ) as a function of temperature $T$ (°C)	$2750 \cdot e^{[-2 \cdot 10^{-5} \cdot (T - T_{ref})]}$	$2785 \cdot e^{[-2 \cdot 10^{-6} \cdot (T - T_{ref})]}$
Thermo-osmotic permeability (m <sup>2</sup> /K/s)	$4.2 \cdot 10^{-13}$	

Table 4-3 – Thermal parameters (ENRESA, 2006a; Zheng et al., 2010).

	Bentonite	Fe powder
Specific heat of the liquid (J/kg·°C)	4202	
Specific heat of the air (J/kg·°C)	1000	
Specific heat of the vapor (J/kg·°C)	1620	
Specific heat of the solid (J/kg·°C)	835.5	480
Reference temperature (°C)	22	
Thermal conductivity of the liquid (W/m·°C)	0.6	
Thermal conductivity of the air (W/m·°C)	$2.6 \cdot 10^{-2}$	
Thermal conductivity of the vapor (W/m·°C)	$4.2 \cdot 10^{-2}$	
Thermal conductivity of the solid (W/m·°C)	1.23	50.16
Vaporization enthalpy (J/kg)	$2.45 \cdot 10^6$	

Table 4-4 – Solute transport parameters (ENRESA, 2006a; Zheng et al., 2010).

	Bentonite	Fe powder
Molecular diffusion coefficient in water $D_o(T)$ in m <sup>2</sup> /s as a function of $T$ (°C) and the molecular diffusion coefficient at the reference temperature $T_{ref}$ (°C), $D_o(T_{ref})$	$D_o(T) = D_o(T_{ref}) \frac{T \mu_0^l}{T_0 \mu^l}$ $D_o(T_{ref}) = 2 \cdot 10^{-10} \text{ (except Cl}^-, D_o(T_{ref}) = 9 \cdot 10^{-11}\text{)}$	
Reference temperature (°C)	22	
Longitudinal dispersivity (m)	0.001	0.01
Solute tortuosity $\tau$ as a function of volumetric water content $\theta$ and porosity $\phi$	$\tau = \frac{\theta^{7/3}}{\phi^2}$	

Table 4-5 – Mechanical parameters (ENRESA, 2006a; Zheng et al., 2010).

	Bentonite	Fe powder
Water mechanical compressibility (Pa <sup>-1</sup> )	$5 \cdot 10^{-7}$	
Water thermal expansion (K <sup>-1</sup> )	$2.1 \cdot 10^{-4}$	
Solid thermal expansion (K <sup>-1</sup> )	$2 \cdot 10^{-5}$	$2 \cdot 10^{-6}$
State surface parameters	$e = A + B \cdot \ln \sigma' + C \cdot \ln(\Psi + P^a) + D \cdot \ln \sigma' \cdot \ln(\Psi + P^a)$ $A = 0.76; B = -0.052446;$ $C = -0.0406413; D = 0.00479977$	

The conceptual geochemical model considered in the reactive transport model of the FB corrosion tests includes the following processes: 1) Iron corrosion, 2) Aqueous complexation; 3) Acid/base; 4) Redox; 5) Mineral dissolution/precipitation; 6) Cation exchange of Ca<sup>2+</sup>, Mg<sup>2+</sup>, Na<sup>+</sup> and K<sup>+</sup> and Fe<sup>2+</sup>; and 7) Surface complexation of H<sup>+</sup> and Fe<sup>2+</sup> on three types of sorption sites (strong sites, S<sup>s</sup>OH, weak #1 sites, S<sup>w1</sup>OH and weak #2 sites, S<sup>w2</sup>OH).

The geochemical system is defined in terms of 15 primary species (H<sub>2</sub>O, H<sup>+</sup>, O<sub>2</sub>(aq), Ca<sup>2+</sup>, Mg<sup>2+</sup>, Na<sup>+</sup>, K<sup>+</sup>, Fe<sup>2+</sup>, Cl<sup>-</sup>, SO<sub>4</sub><sup>2-</sup>, HCO<sub>3</sub><sup>-</sup>, SiO<sub>2</sub>(aq), S<sup>s</sup>OH, S<sup>w1</sup>OH, S<sup>w2</sup>OH), 39 secondary aqueous species identified from speciation runs performed with EQ3/6 (Wolery, 1992), 9 minerals assumed at chemical equilibrium except for the corrosion of Fe(s) which is kinetically-controlled; and 10 secondary surface complexation species. The Gaines-Thomas convention was used for cation exchange reactions (Appelo and Postma,

1993). Surface complexation reactions were modelled with the triple-site sorption model of Bradbury and Baeyens (1997; 1998; 2003). Chemical reactions and the equilibrium constants at 25°C for aqueous species and mineral dissolution/precipitation as well as the selectivity coefficients for cation exchange and the protolysis constants for surface complexation are listed in Table 4-6.

The possibility of other competitive cations for surface complexation positions and the hypothesis of no participation of iron in surface complexation reactions will be considered.

The equilibrium constants for aqueous complexes and minerals, K, depend on temperature, T, according to (Wolery, 1992):

$$\log K(T) = \frac{b_1}{T^2} + \frac{b_2}{T} + b_3 \ln T + b_4 + b_5 T \quad (5)$$

where  $b_1$  to  $b_5$  are coefficients which are derived by fitting Eq. 5 to measured log K values at 0, 25, 60, 100, 150, 200, 250 and 300°C. This expression is valid for  $0 < T < 300$  °C.

*Table 4-6 – Chemical reactions and equilibrium constants for aqueous complexes and minerals (Wolery, 1992), protolysis constants for surface complexation reactions (Bradbury and Baeyens, 1997; 1998; 2003) and selectivity coefficients for cation exchange reactions (ENRESA, 2006b) at 25°C.*

Aqueous complexes	Log K
$\text{CaCO}_3(\text{aq}) + \text{H}^+ \Leftrightarrow \text{Ca}^{2+} + \text{HCO}_3^-$	7.0017
$\text{CaHCO}_3^+ \Leftrightarrow \text{Ca}^{2+} + \text{HCO}_3^-$	-1.0467
$\text{CaSO}_4(\text{aq}) \Leftrightarrow \text{Ca}^{2+} + \text{SO}_4^{2-}$	-2.1111
$\text{CaOH}^+ + \text{H}^+ \Leftrightarrow \text{Ca}^{2+} + \text{H}_2\text{O}$	12.850
$\text{CO}_2(\text{aq}) + \text{H}_2\text{O} \Leftrightarrow \text{H}^+ + \text{HCO}_3^-$	-6.3447
$\text{CO}_3^{2-} + \text{H}^+ \Leftrightarrow \text{HCO}_3^-$	10.3288
$\text{KSO}_4^- \Leftrightarrow \text{K}^+ + \text{SO}_4^{2-}$	-0.8796
$\text{MgCO}_3(\text{aq}) \Leftrightarrow \text{Mg}^{2+} + \text{CO}_3^{2-}$	-2.9789
$\text{MgHCO}_3^+ \Leftrightarrow \text{Ca}^{2+} + \text{HCO}_3^-$	-1.0357
$\text{MgSO}_4(\text{aq}) \Leftrightarrow \text{Mg}^{2+} + \text{SO}_4^{2-}$	-2.4117
$\text{MgOH}^+ \Leftrightarrow \text{Mg}^{2+} + \text{OH}^-$	-2.2100
$\text{NaHCO}_3(\text{aq}) \Leftrightarrow \text{Na}^+ + \text{HCO}_3^-$	-0.1541
$\text{NaSO}_4^- \Leftrightarrow \text{Na}^+ + \text{SO}_4^{2-}$	-0.8200
$\text{NaCO}_3^- \Leftrightarrow \text{Na}^+ + \text{CO}_3^{2-}$	-0.5144
$\text{NaOH}(\text{aq}) + \text{H}^+ \Leftrightarrow \text{Na}^+ + \text{H}_2\text{O}$	14.180
$\text{OH}^- + \text{H}^+ \Leftrightarrow \text{H}_2\text{O}$	13.9951
$\text{H}_3\text{SiO}_4^- + \text{H}^+ \Leftrightarrow 2\text{H}_2\text{O} + \text{SiO}_2(\text{aq})$	9.8120
$\text{HSO}_4^- \Leftrightarrow \text{H}^+ + \text{SO}_4^{2-}$	1.9791
$\text{HS}^- + 2\text{O}_2(\text{aq}) \Leftrightarrow \text{H}^+ + \text{SO}_4^{2-}$	138.31
$\text{Fe}^{3+} + 0.5\text{H}_2\text{O} \Leftrightarrow \text{H}^+ + 0.25\text{O}_2 + \text{Fe}^{2+}$	-8.490
$\text{FeHCO}_3 \Leftrightarrow \text{Fe}^{2+} + \text{HCO}_3^-$	-2.050
$\text{FeCO}_3(\text{aq}) \Leftrightarrow \text{Fe}^{2+} + \text{CO}_3^{2-}$	-4.730

$\text{FeCl}^+ \Leftrightarrow \text{Fe}^{2+} + \text{Cl}^-$	0.1605
$\text{FeCl}^{2+} \Leftrightarrow \text{Fe}^{3+} + \text{Cl}^-$	0.8108
$\text{FeOH}^+ + \text{H}^+ \Leftrightarrow \text{Fe}^{2+} + \text{H}_2\text{O}$	10.895
$\text{FeOH}^{2+} + \text{H}^+ \Leftrightarrow \text{Fe}^{3+} + \text{H}_2\text{O}$	4.3815
$\text{Fe}(\text{OH})_2(\text{aq}) + 2\text{H}^+ \Leftrightarrow \text{Fe}^{2+} + 2\text{H}_2\text{O}$	20.60
$\text{Fe}(\text{OH})_3(\text{aq}) + 3\text{H}^+ \Leftrightarrow \text{Fe}^{3+} + 3\text{H}_2\text{O}$	12.172
$\text{Fe}(\text{OH})_4^- + 4\text{H}^+ \Leftrightarrow \text{Fe}^{3+} + 4\text{H}_2\text{O}$	21.60
$\text{Fe}(\text{OH})_2^+ + 2\text{H}^+ \Leftrightarrow \text{Fe}^{3+} + 2\text{H}_2\text{O}$	5.670
$\text{Fe}(\text{SO}_4)_2^- \Leftrightarrow \text{Fe}^{3+} + 2\text{SO}_4^{2-}$	-3.213
$\text{FeSO}_4(\text{aq}) \Leftrightarrow \text{Fe}^{2+} + \text{SO}_4^{2-}$	-2.20
$\text{FeHSO}_4^{2+} \Leftrightarrow \text{Fe}^{3+} + \text{H}^+ + \text{SO}_4^{2-}$	-1.540
$\text{Fe}_2(\text{OH})_2^{4+} + 2\text{H}^+ \Leftrightarrow 2\text{Fe}^{3+} + 2\text{H}_2\text{O}$	7.2826
$\text{KOH}(\text{aq}) + \text{H}^+ \Leftrightarrow \text{K}^+ + \text{H}_2\text{O}$	14.46
$\text{H}_2(\text{aq}) + 0.5\text{O}_2 \Leftrightarrow \text{H}_2\text{O}$	46.10
$\text{NaHSiO}_3(\text{aq}) + \text{H}^+ \Leftrightarrow \text{H}_2\text{O} + \text{Na}^+ + \text{SiO}_2(\text{aq})$	8.3040
$\text{HSiO}_3^- + \text{H}^+ \Leftrightarrow \text{H}_2\text{O} + \text{SiO}_2(\text{aq})$	9.9525
$\text{MgH}_3\text{SiO}_4^+ + \text{H}^+ \Leftrightarrow 2\text{H}_2\text{O} + \text{Mg}^{2+} + \text{SiO}_2(\text{aq})$	8.5416
<b>Minerals</b>	<b>LogK</b>
$\text{Calcite} + \text{H}^+ \Leftrightarrow \text{Ca}^{2+} + \text{HCO}_3^-$	1.8487
$\text{Anhydrite} \Leftrightarrow \text{Ca}^{2+} + \text{SO}_4^{2-}$	-4.3064
$\text{Gypsum} \Leftrightarrow \text{Ca}^{2+} + \text{SO}_4^{2-} + 2\text{H}_2\text{O}$	-4.4823
$\text{Quartz} \Leftrightarrow \text{SiO}_2(\text{aq})$	-3.9993
$\text{Magnetite} + 6\text{H}^+ \Leftrightarrow 3\text{Fe}^{2+} + 0.5\text{O}_2(\text{aq}) + 3\text{H}_2\text{O}$	-6.5076
$\text{Siderite} + \text{H}^+ \Leftrightarrow \text{Fe}^{2+} + \text{HCO}_3^-$	-0.1920
$\text{Goethite} + 2\text{H}^+ \Leftrightarrow \text{Fe}^{2+} + 1.5\text{H}_2\text{O} + 0.25\text{O}_2(\text{aq})$	-7.9555
$\text{Fe}(\text{OH})_2(\text{s}) + 2\text{H}^+ \Leftrightarrow \text{Fe}^{2+} + 2\text{H}_2\text{O}$	13.9045
$\text{Fe}(\text{s}) + 2\text{H}^+ \Leftrightarrow \text{Fe}^{2+} + 2\text{H}_2\text{O} + 2\text{OH}^- + \text{H}_2(\text{aq})$	-15.064
$\text{Chukanovite} + 3\text{H}^+ \Leftrightarrow 2\text{Fe}^{2+} + \text{HCO}_3^- + 2\text{H}_2\text{O}$	12.32
$\text{Berthierine} + 10\text{H}^+ \Leftrightarrow 2\text{Fe}^{2+} + 2\text{Al}^{3+} + \text{SiO}_2(\text{aq}) + 7\text{H}_2\text{O}$	25.55
$\text{Cronstedtite} + 10\text{H}^+ \Leftrightarrow 2\text{Fe}^{2+} + 2\text{Fe}^{3+} + \text{SiO}_2(\text{aq}) + 7\text{H}_2\text{O}$	16.2603
$\text{Chlorite} + 16\text{H}^+ \Leftrightarrow 5\text{Fe}^{2+} + 2\text{Al}^{3+} + 3\text{SiO}_2(\text{aq}) + 12\text{H}_2\text{O}$	55.6554
<b>Surface complexation reactions</b>	<b>LogK</b>
$\equiv\text{S}^\circ\text{OH}_2^+ \Leftrightarrow \equiv\text{S}^\circ\text{OH} + \text{H}^+$	-4.5
$\equiv\text{S}^\circ\text{O}^- + \text{H}^+ \Leftrightarrow \equiv\text{S}^\circ\text{OH}$	7.9
$\equiv\text{S}^\circ\text{OFe}^+ + \text{H}^+ \Leftrightarrow \equiv\text{S}^\circ\text{OH} + \text{Fe}^{2+}$	0.6
$\equiv\text{S}^\circ\text{OFeOH} + 2\text{H}^+ \Leftrightarrow \equiv\text{S}^\circ\text{OH} + \text{Fe}^{2+} + \text{H}_2\text{O}$	10.0
$\equiv\text{S}^\circ\text{OFe}(\text{OH})_2^- + 3\text{H}^+ \Leftrightarrow \equiv\text{S}^\circ\text{OH} + \text{Fe}^{2+} + 2\text{H}_2\text{O}$	20.0
$\equiv\text{S}^{\text{W}1}\text{OH}_2^+ \Leftrightarrow \equiv\text{S}^{\text{W}1}\text{OH} + \text{H}^+$	-4.5

$\equiv S^{W1} O^- + H^+ \rightleftharpoons \equiv S^{W1} OH$	7.9
$\equiv S^{W1} OFe^+ + H^+ \rightleftharpoons \equiv S^{W1} OH + Fe^{2+}$	3.3
$\equiv S^{W2} OH_2^+ \rightleftharpoons \equiv S^{W2} OH + H^+$	-6.0
$\equiv S^{W2} O^- + H^+ \rightleftharpoons \equiv S^{W2} OH$	10.5
<b>Cation Exchange reactions</b>	<b>K<sub>Na-cation</sub></b>
$Na^+ + X-K \rightleftharpoons K^+ + X-Na$	0.1456
$Na^+ + 0.5 X_2-Ca \rightleftharpoons 0.5 Ca^{2+} + X-Na$	0.3265
$Na^+ + 0.5 X_2-Mg \rightleftharpoons 0.5 Mg^{2+} + X-Na$	0.3766
$Na^+ + 0.5 X_2-Fe \rightleftharpoons 0.5 Fe^{2+} + X-Na$	0.5

The initial mineral volume fractions in the bentonite are: 1% of calcite, 1% of quartz, 0.08% of gypsum and 57.92% of non-reactive smectite. The initial volume fraction of the Fe powder is assumed to be 100% of iron (Samper et al., 2016). The following secondary minerals are allowed to precipitate: anhydrite, magnetite, goethite, siderite and Fe(OH)<sub>2</sub>(s). Magnetite is assumed to be the most relevant corrosion product in the FB4 corrosion test. Some of these assumptions will be revised during the second year of the ACED WP based on the available FB4 corrosion test measured data. The precipitation of hematite and maghemite will be considered during the early stages in which the Fe powder is not yet saturated. This will be consistent with stage 1 of the conceptual model of Hadi et al. (2019).

Table 4-7 – Chemical composition (in mol/L) of the bentonite initial porewater (Fernández et al., 2001) and the Grimsel hydration boundary water (Turrero et al., 2001).

	Initial bentonite porewater	Grimsel hydration water
<b>Na<sup>+</sup></b>	1.3·10 <sup>-1</sup>	3.7·10 <sup>-4</sup>
<b>Ca<sup>2+</sup></b>	2.2·10 <sup>-2</sup>	1.8·10 <sup>-4</sup>
<b>Mg<sup>2+</sup></b>	2.3·10 <sup>-2</sup>	1.6·10 <sup>-5</sup>
<b>K<sup>+</sup></b>	1.7·10 <sup>-3</sup>	2.2·10 <sup>-5</sup>
<b>SO<sub>4</sub><sup>2-</sup></b>	3.2·10 <sup>-2</sup>	6.1·10 <sup>-5</sup>
<b>Cl<sup>-</sup></b>	1.6·10 <sup>-1</sup>	2.3·10 <sup>-5</sup>
<b>SiO<sub>2</sub>(aq)</b>	1.0·10 <sup>-4</sup>	1.9·10 <sup>-4</sup>
<b>HCO<sub>3</sub><sup>-</sup></b>	5.8·10 <sup>-4</sup>	3.9·10 <sup>-4</sup>
<b>Fe<sup>2+</sup></b>	6.6·10 <sup>-5</sup>	1.8·10 <sup>-8</sup>
<b>pH</b>	7.72	9.7

The cation exchange capacity (CEC) of the bentonite is 102 meq/100g (Fernández et al., 2004). The selectivity coefficients for exchanged Ca<sup>2+</sup> Mg<sup>2+</sup> and K<sup>+</sup> were derived from ENRESA (2006b). These selectivity coefficients were calibrated to reproduce the concentrations of exchanged cations reported

by Fernández et al. (2004) for the FEBEX bentonite. The total concentration of the sorption sites in the bentonite is 0.629 mol/L (Bradbury and Baeyens, 1997). Strong sites have a strong binding affinity but a small concentration of 0.015 mol/L. The other two types are the weak #1 and #2 sites which have binding constants weaker than those of the strong sites although their concentrations (0.307 mol/L) are larger than those of the strong sites.

The initial chemical composition of the bentonite porewater at a water content of 13.3% at 25 °C was derived from Fernández et al. (2001). The chemical composition of the Grimsel hydration water was taken from Turrero et al. (2011). Both chemical compositions are listed in Table 4-7.

The kinetics parameter for Fe(s) were taken from De Windt and Torres (2009). Fe(s) corrodes with a constant kinetic rate of  $-4 \cdot 10^{-12}$  mol/m<sup>2</sup>/s which corresponds to 0.15 µ/year. The specific surface of the iron powder is  $2.15 \cdot 10^5$  m<sup>2</sup>/m<sup>3</sup>.

## 4.4 Numerical model

### 4.4.1 Spatial and temporal discretization

The numerical water flow and multicomponent reactive transport model of the FB4 corrosion tests is performed with a 1-D finite element mesh (Figure 4-5). The model includes the bentonite block (86 nodes) and the Fe powder (13 nodes). The spatial mesh discretization is uniform, the length of the elements is equal to 1 mm. The model simulates the heating and hydration of the tests. The model duration is 1593 days for the FB3 corrosion test and 7 years for the FB4 corrosion test. A cooling phase of two days was considered after the tests. During the cooling time the hydration is stopped and the temperature is switched to ambient temperature.

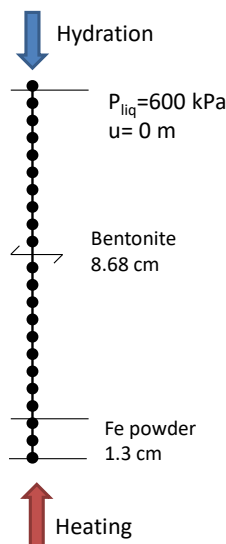


Figure 4-5 – One dimensional finite element mesh for the numerical model of the FB corrosion tests.

### 4.4.2 Sensitivity analyses

Some of the uncertainties of the reactive transport model of the FB3 and FB4 corrosion tests have been quantified with a sensitivity analysis to changes in: 1) The hydraulic conductivity of the bentonite; 2) The vapour tortuosity of the bentonite; 3) The hypothesis about magnetite precipitation (kinetic versus equilibrium); and 4) The iron corrosion rate.

This set of sensitivity runs was performed by UDC during the calibration of the reactive transport model of another type of heating and hydration corrosion tests performed by CIEMAT on FEBEX bentonite samples in contact with Fe powder. These tests are the so-called small cell corrosion tests (SC cells), with a length of 25 mm, which were designed to reproduce the repository conditions prevailing 3000 years after the emplacement of the waste when the bentonite is fully saturated (Torres et al., 2008). The THMC model of the bentonite and the Fe powder in the SC cells are the same that the FB corrosion test (Mon, 2017).

The corrosion tests on the SC cells were performed by CIEMAT in hermetic cylindrical cells which contained 21 mm of compacted bentonite and 4 mm of carbon-steel powder (Figure 4-6). The external cylindrical cell was made out of Teflon to prevent the deformation. The tests were performed with unsaturated compacted FEBEX bentonite (ENRESA 2000, 2006a) and Fe powder. The tests were performed at 25°, 50° and 100°C. The duration of the tests was of 6 and 12 months. The bentonite blocks were compacted to a dry density of 1.65 g/cm<sup>3</sup> and an initial gravimetric water content of 0.14. The hydration water was injected by a steel distribution plate at a pressure of 100 kPa. It seems that after 2 weeks the bentonite is fully saturated.

The sensitivity analysis was performed on the SC corrosion test performed at 100°C with a duration of 6 months, Fe powder and a reduced granitic Grimsel water (reduced calcium bicarbonate water) as the hydration water. This SC test is denoted as SC-a3 test.

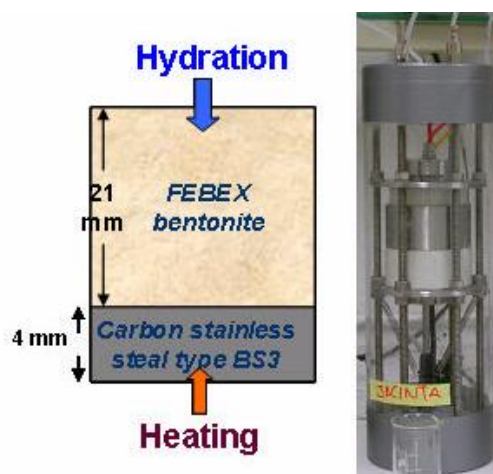


Figure 4-6 – Sketch of the SC corrosion tests on small cells (Torres et al., 2008).

#### 4.4.2.1 Sensitivity to the hydraulic conductivity of the bentonite

The intrinsic permeability of the liquid in the bentonite for the base run of the SC-a3 test is equal  $2.75 \cdot 10^{-21} \text{ m}^2$  (Table 4-2). This value coincides with that used in the reactive transport model of the FB3 and FB4 corrosion tests. The sensitivity run was performed with a permeability equal to  $3.5 \cdot 10^{-21} \text{ m}^2$ . Figure 4-7 shows the sensitivity of the computed saturation degree at the end of the test (6 months). The water saturation in the sensitivity run is slightly larger than that of the base run. The water intake of the sensitivity run is 9% larger than that of the base run. It is estimated that the bentonite samples got fully saturated after 2 weeks.

Figure 4-8 and Figure 4-9 show the sensitivity of the magnetite precipitation and the weight of iron after cooling. The precipitation of the corrosion products is slightly sensitive to the bentonite permeability. The precipitation of  $\text{Fe}(\text{OH})_2(\text{s})$  at the bentonite-iron interface in the sensitivity run is larger than that in the base run.

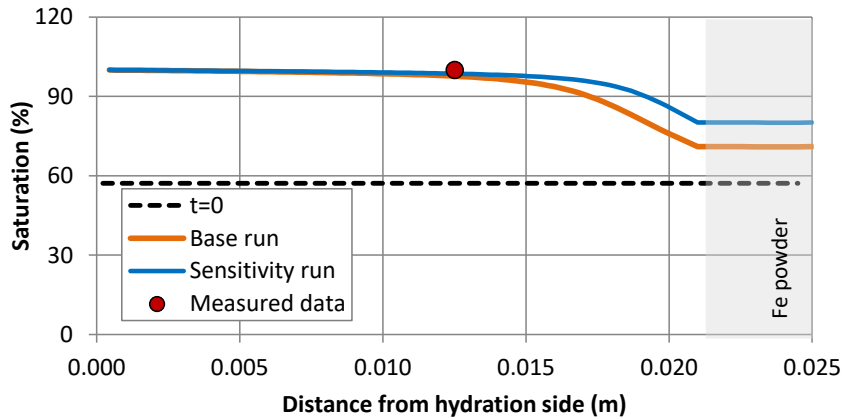


Figure 4-7 – Spatial distribution of the measured (symbol) and the computed (lines) saturation degree at the end of the SC-a3 corrosion test (6 months) at 100°C for the base run and the sensitivity run to the bentonite permeability.

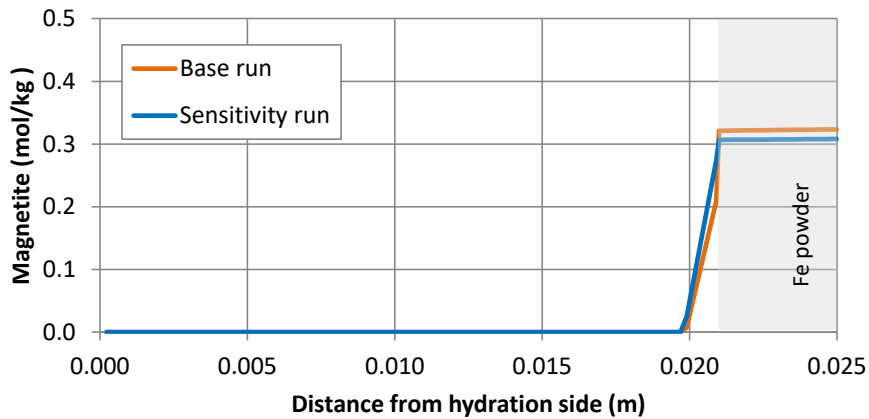


Figure 4-8 – Sensitivity of the computed cumulative precipitation of magnetite at the end of the SC-a3 corrosion test (6 months) at 100°C to changes in the bentonite permeability.

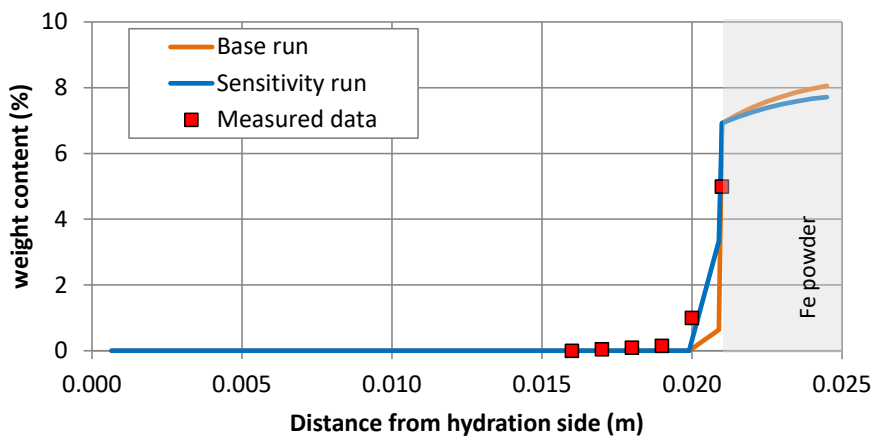


Figure 4-9 – Measured (symbol) and computed (line) weight of iron at the end of the SC-a3 corrosion test (6 months) at 100°C to changes in the bentonite permeability.

4.4.2.2 Sensitivity to the vapor tortuosity in the bentonite

The vapor tortuosity in the base run of the SC-a3 test is equal to 0.3. Sensitivity runs were performed for tortuosity factors equal to 0.2 and 0.5. Figure 4-10 shows the sensitivity of the saturation degree to changes in the tortuosity factors. The computed saturation degree increases when the vapor tortuosity factor decreases. The water intake in the sensitivity with a tortuosity factor of 0.5 decreases 10% compared to that of the base run.

Magnetite precipitation is not sensitive to changes in the tortuosity factor (Figure 4-11). Figure 4-12 shows the weight of iron for the base run and the sensitivity runs. The penetration of the corrosion products into the bentonite increases slightly when the vapor tortuosity factor decreases.

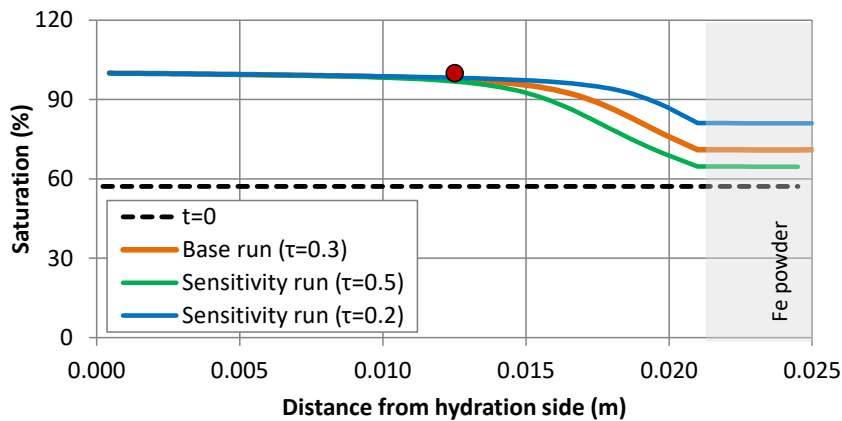


Figure 4-10 – Spatial distribution of the measured (symbol) and the computed (lines) saturation degree at the end of the SC-a3 corrosion test (6 months) at 100°C for the base run and the sensitivity run to the vapor tortuosity factor.

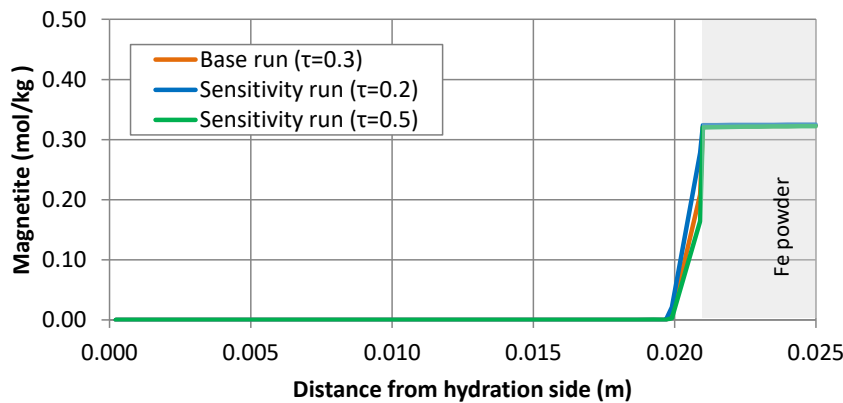


Figure 4-11 – Sensitivity of the computed cumulative precipitation of magnetite at the end of the SC-a3 corrosion test (6 months) at 100°C for the base run and the sensitivity run to the vapor tortuosity factor.

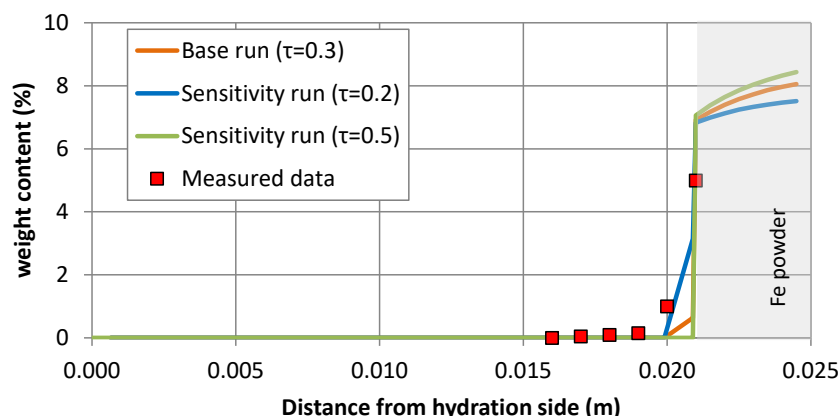


Figure 4-12 – Measured (symbol) and computed (line) weight of iron at the end of the SC-a3 corrosion test (6 months) at 100°C for the base run and the sensitivity run to the vapor tortuosity factor.

#### 4.4.2.3 Sensitivity to kinetic magnetite precipitation

A kinetic rate law taken from De Windt and Torres (2010) was used for the magnetite precipitation in the base run of the SC-a3 test. The sensitivity run accounts magnetite precipitation at chemical equilibrium as considered in the models of the FB3 and FB4 corrosion tests. Figure 4-13 shows the cumulative magnetite precipitation for the base run (kinetics) and the sensitivity run (chemical equilibrium) at 180 days and 2 days of cooling. The cumulative precipitation of magnetite at equilibrium is larger than that with a kinetic control.  $\text{Fe}(\text{OH})_2(\text{s})$  in the sensitivity run does not precipitate because the iron precipitates mostly as magnetite (Figure 4-14).

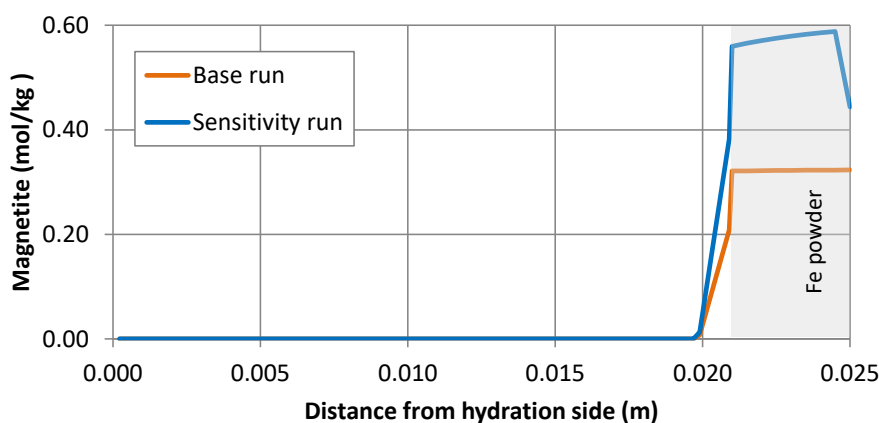


Figure 4-13 – Sensitivity of the computed cumulative precipitation of magnetite at the end of the SC-a3 corrosion test (6 months) at 100°C to magnetite precipitation at equilibrium (sensitivity run) and kinetically controlled (base run).

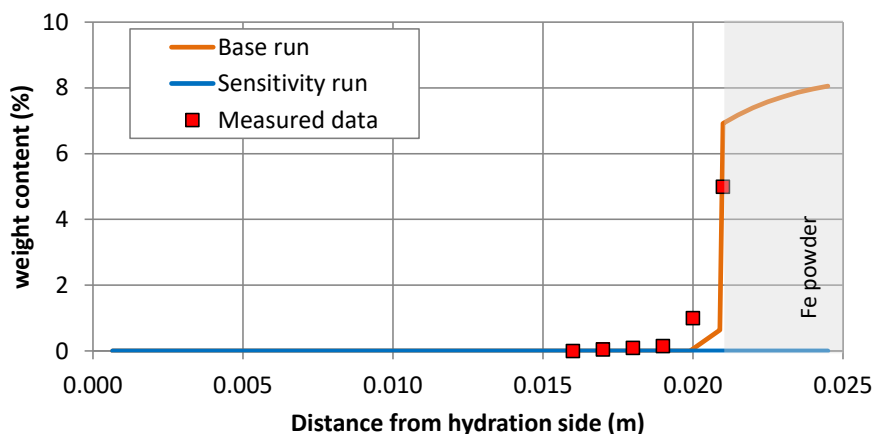


Figure 4-14 – Measured (symbol) and computed (line) weight of iron at the end of the SC-a3 corrosion test (6 months) at 100°C to magnetite precipitation at equilibrium (sensitivity run) and kinetically controlled (base run).

#### 4.4.2.4 Sensitivity to steel corrosion rate

The kinetic parameters of Fe(s) were taken from De Windt and Torres (2009). Fe(s) corrodes with a constant rate of  $-4 \cdot 10^{-12}$  mol/m<sup>2</sup>/s for the base run of the SC-a3. This value coincides with the corrosion rate used in the models of the FB3 and FB4 corrosion tests and is equal to 0.15 μ/year. The specific surface of the iron powder is  $2.15 \cdot 10^5$  m<sup>2</sup>/m<sup>3</sup>.

In the sensitivity run, the corrosion rate is 4 times smaller than that of the base run. The precipitation of magnetite in the sensitivity run is smaller than in the base run (Figure 4-15). Fe(OH)<sub>2</sub>(s) does not precipitate in the sensitivity run because the corrosion rate is too small and all the Fe<sup>2+</sup> precipitates as magnetite (Figure 4-16).

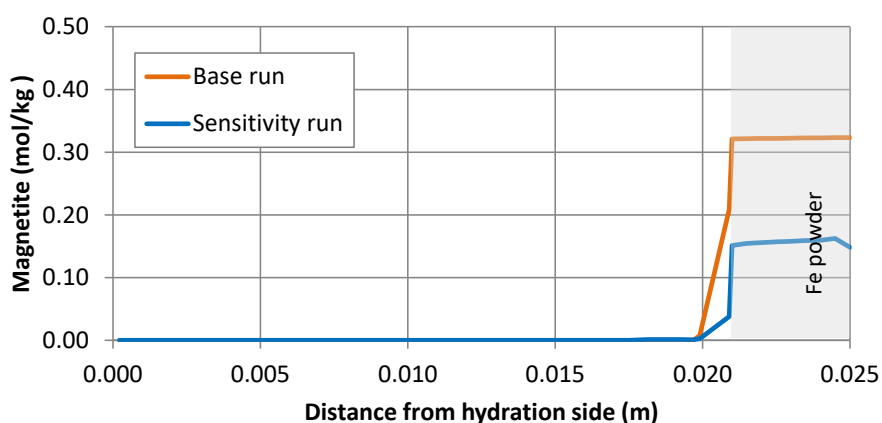


Figure 4-15 – Sensitivity of the computed cumulative precipitation of magnetite at the end of the SC-a3 corrosion test (6 months) at 100°C to changes in the steel corrosion rate.

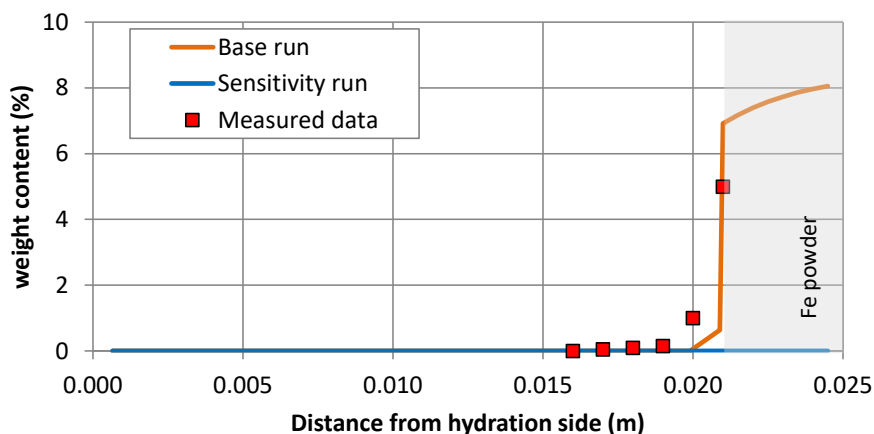


Figure 4-16 – Measured (symbol) and computed (line) weight of iron at the end of the SC-a3 corrosion test (6 months) at 100°C to changes in the steel corrosion rate.

Sensitivity analyses will be performed to quantify the main uncertainties of the reactive transport model of the FB4 corrosion cell. These uncertainties are related with: 1) Bentonite hydrodynamic and mechanical parameters; 2) The time evolution of the gas and redox conditions; 3) Other mineral phases such as Fe-phyllsilicates and chukanovite; 4) The competitive effects of other cations for surface complexation positions; and 5) The lack of relevance of iron surface complexation.

#### 4.4.3 Model calibration

The models of the FB corrosion tests will be calibrated with the following measured data:

- 1) Temperatures and relative humidities measured during the tests in the sensors.
- 2) Water content and porosity data at the end of the tests.
- 3) Aqueous extract data.
- 4) Cation exchange data.
- 5) Mineralogical observations.
- 6) Thickness and composition of the corrosion layer.
- 7) Thickness and composition of the read/orange and blue (Fe poor) zones

## 4.5 First results and discussion

This section presents the results of the thermo-hydro-mechanical and chemical model of the FB4 corrosion tests based on the model of Mon (2017) without model calibration. For comparison purposes, model results are shown also for the FB3 corrosion test.

### 4.5.1 Thermo-hydro-mechanical results

Figure 4-17 shows the time evolution of the total water intake in the FB corrosion tests. The total amount of water intake is equal to 0.083 L in 7 years. The water intake in the first year is faster than that in the later years; the 97% of the water enters during the first year.

Figure 4-18 to Figure 4-21 show the spatial distribution of the measured and the computed volumetric water content, porosity, temperature and relative humidity. Figure 4-18 shows the computed water intake at selected times and measured water content at 1593 days (FB3 corrosion test). The volumetric water content increases in the bentonite and Fe powder with time, being larger in the bentonite near the hydration side. The water content near the hydration side is larger than that near the heater because the porosity increases near the hydration zone. Water evaporates near the heater. The vapor diffuses

and condenses in colder locations. The computed volumetric water content is slightly smaller than the measured data near the hydration boundary. Near the Fe powder, however, the computed water content is larger than the measured values.

The computed porosity increases to 0.488 from the initial value (0.40) in the bentonite near the hydration side. On the other hand, computed porosity is similar to the initial value in the bentonite near the Fe powder interface. The computed porosity is smaller than the measured porosity data (Figure 4-19).

The computed relative humidity increases from 37% to 100% in the bentonite near the hydration and to 80% near the Fe powder. The computed temperature is equal to 25°C at the hydration boundary and equal to 100°C at the Fe powder. The computed temperature profile reaches in 1 day and then, it remains constant. The computed relative humidity and temperature at the end of the tests reproduce the trend of the two measured data of the FB3 corrosion test (Figure 4-20 and Figure 4-21).

Figure 4-22 shows the time evolution of the computed and measured temperatures in the sensors. The computed temperature is slightly larger than measured data in the sensors. The computed relative humidity in the sensors located near the hydration boundary reproduce the measured relative humidity data. The evolution of the computed relative humidity in the sensor near the heater does not reproduce the measured relative humidity data (Figure 4-23). This discrepancy could be due to problems in the water injection system during the tests or most probably due to vapor leakage through the sensors.

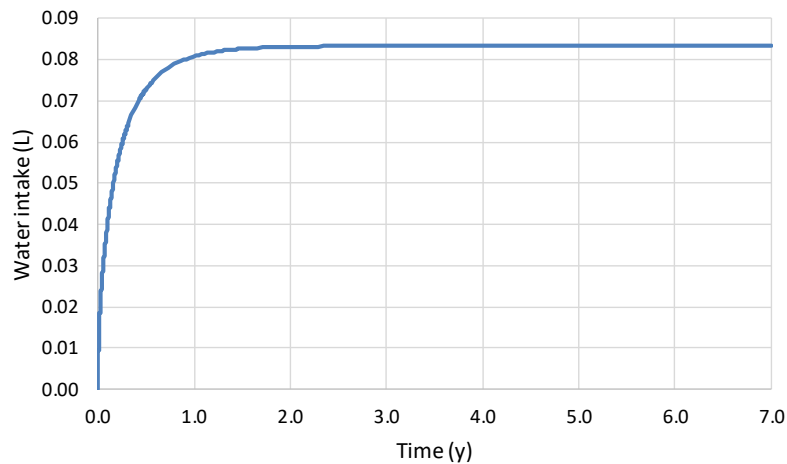


Figure 4-17 – Time evolution of the water intake of the FB corrosion tests.

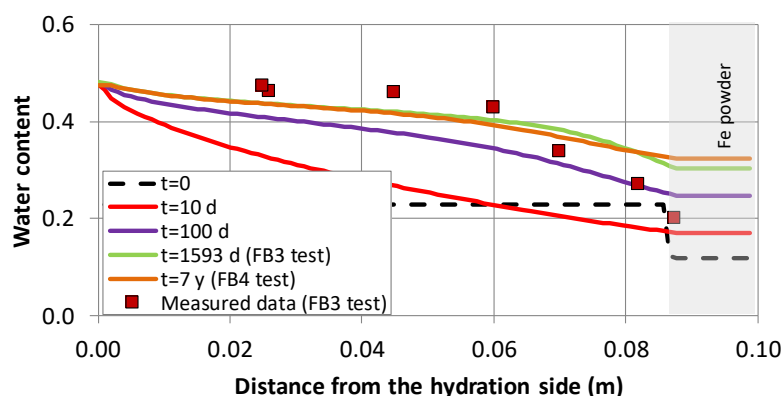


Figure 4-18 – Spatial distribution of the measured (symbols) volumetric water content at the end of the FB3 corrosion test and the computed (line) volumetric water contents at selected times in FB corrosion tests.

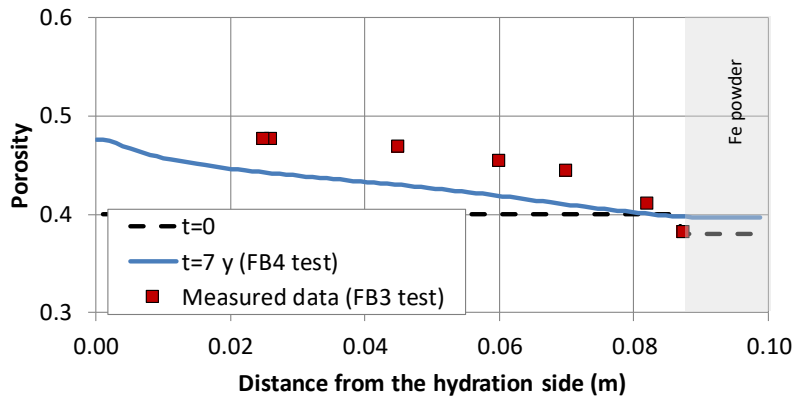


Figure 4-19 – Spatial distribution of the measured (symbols) porosity at the end of the FB3 corrosion test and the computed (line) porosities at the end of the FB3 and FB4 corrosion tests which fully coincide.

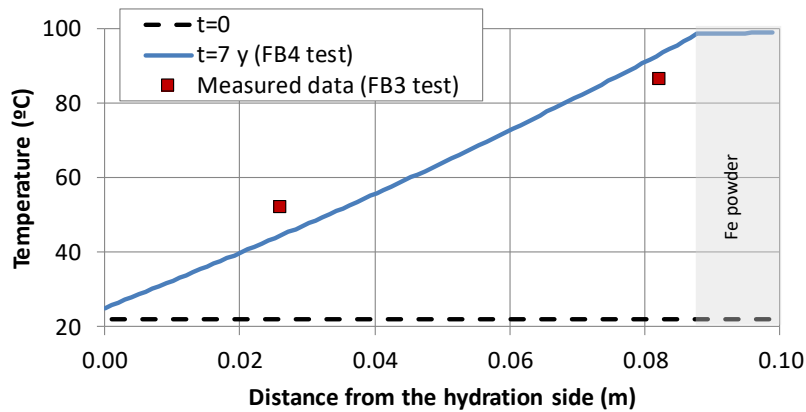


Figure 4-20 – Spatial distribution of the measured (symbols) temperature at the end of the FB3 corrosion test and the computed (line) temperature at the end of the FB3 and FB4 corrosion tests which fully coincide.

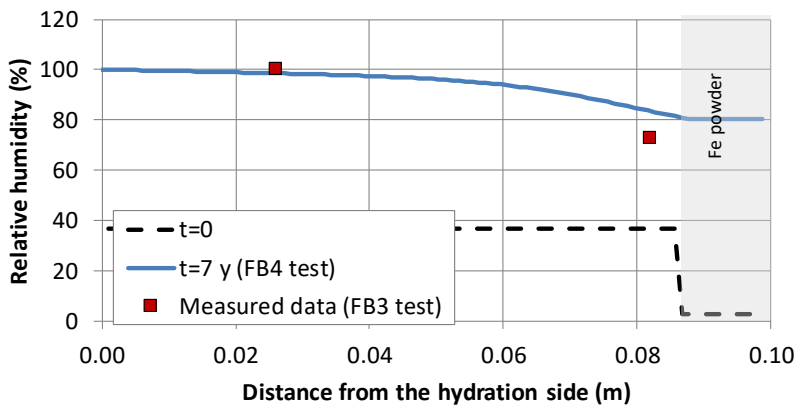


Figure 4-21 – Spatial distribution of the measured (symbols) relative humidity at the end of the FB3 corrosion test and the computed (line) relative humidity at the end of the FB3 and FB4 corrosion tests which fully coincide.

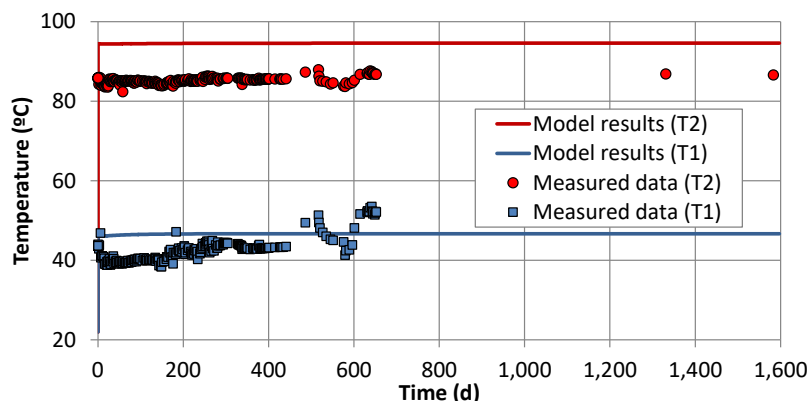


Figure 4-22 – Time evolution of the computed (lines) and the measured (symbols) temperature in the sensors T2 (18 mm from the heater) and T1 (74 mm from the heater) of the medium-size corrosion test on FB3 corrosion test.

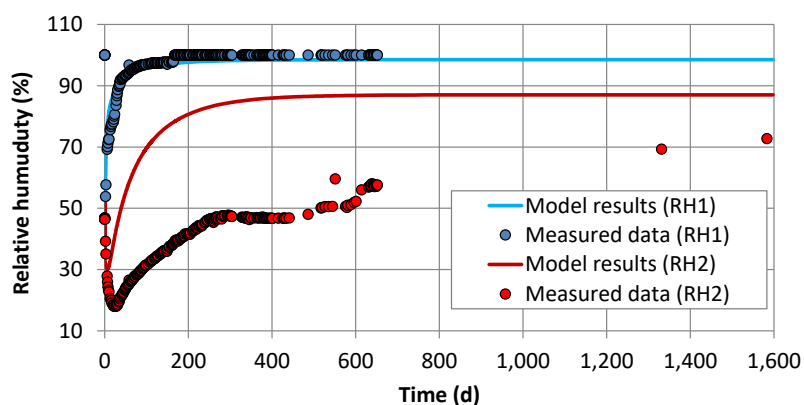


Figure 4-23 – Time evolution of the computed (lines) and the measured (symbols) relative humidity in the sensors RH2 (18 mm from the heater) and RH1 (74 mm from the heater) of the medium-size corrosion test on FB3 corrosion test.

#### 4.5.2 Chemical results

Notice that the computed model results for the FB3 and FB4 corrosion tests are shown after the cooling phase.

Figure 4-24 shows the spatial distribution of the computed  $\text{Cl}^-$  concentration at selected times. The concentration of  $\text{Cl}^-$  decreases in the bentonite because the hydration water has a  $\text{Cl}^-$  concentration smaller than that of the bentonite. Near the heater, however, it increases due to water evaporation. When the largest hydration finishes (after 1 year), the concentration increases slightly in the bentonite and it decreases in the bentonite near the Fe powder and in the Fe powder due to diffusion.

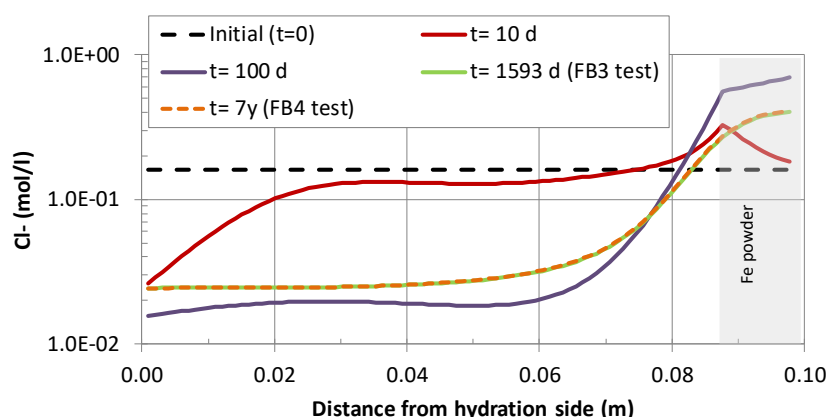


Figure 4-24 – Spatial distribution of the computed concentration of dissolved  $Cl^-$  at selected times in the medium-size corrosion test on the FB corrosion tests.

Figure 4-25 shows the computed dissolved concentration of  $Na^+$ ,  $K^+$ ,  $Mg^{2+}$ ,  $Ca^{2+}$ ,  $SO_4^{2-}$ ,  $HCO_3^-$  and  $SiO_2(aq)$  at selected times. The dissolved concentrations of  $Na^+$ ,  $K^+$ ,  $Mg^{2+}$ ,  $Ca^{2+}$  and  $SO_4^{2-}$  show patterns similar to those of  $Cl^-$  (see Figure 4-25 a, b, c and d).

The computed concentration of the dissolved sulfate is affected by the dissolution/precipitation of gypsum and anhydrite (Figure 4-25e). Computed gypsum dissolves initially in the bentonite and remains constant (Figure 4-31). Computed anhydrite precipitates in the bentonite near the heater and at 1953 days (FB3 corrosion test) and at 7 years (FB4 corrosion test) anhydrite redissolves (Figure 4-32).

The computed dissolved concentration of  $HCO_3^-$  increases near the hydration side and decreases at the bentonite Fe powder interface (Figure 4-25f) at initial times. The computed dissolved concentration of  $HCO_3^-$  in the bentonite is slightly larger than the initial value at 1593 days (FB3 corrosion test) and similar to the initial values at 7 years (FB4 corrosion test). This trend is related to the behavior of calcite. Computed calcite dissolves with time in the bentonite near the hydration side and near the Fe powder, and computed calcite precipitates at the bentonite and Fe powder interface (Figure 4-29 and Figure 4-30).

The concentration of dissolved silica increases in the bentonite and in the Fe powder (Figure 4-25g). Quartz dissolves in the bentonite near the Fe powder (Figure 4-33) and precipitates punctually at the bentonite and Fe powder interface. The dissolved  $SiO_2(aq)$  moves into the Fe powder where it accumulates. The computed silica concentration is similar to the initial concentration at 1953 days (FB3 corrosion test) and at 7 years (FB4 corrosion test).

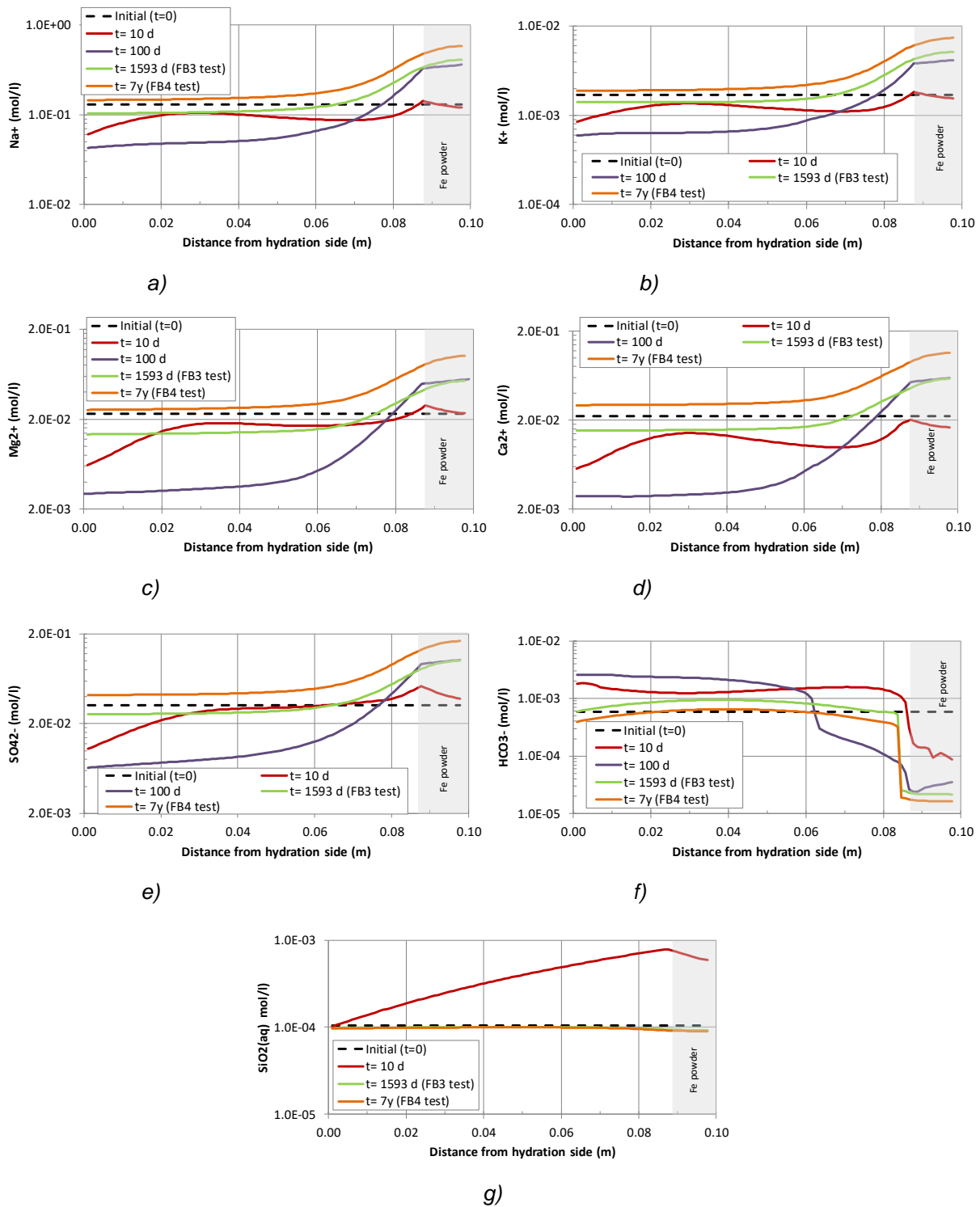


Figure 4-25 – Spatial distribution of the computed concentration of dissolved Na<sup>+</sup>, K<sup>+</sup>, Mg<sup>2+</sup>, Ca<sup>2+</sup>, SO<sub>4</sub><sup>2-</sup>, HCO<sub>3</sub><sup>-</sup>, and SiO<sub>2</sub>(aq) at selected times in the FB corrosion tests.

Figure 4-26 shows the evolution of the computed concentration of the dissolved Fe<sup>2+</sup>. The dissolved concentration of Fe<sup>2+</sup> decreases initially in the bentonite due to hydration and in the Fe powder due to magnetite precipitation. The concentration of Fe<sup>2+</sup> at the end of the test (FB3 and FB4 corrosion tests) increases due to Fe(s) corrosion.

The computed pH is equal to 7.5 after the initial chemical equilibration. It decreases in the bentonite during the first 10 days, especially near the Fe powder. Then, pH increases to become similar to the initial pH, except in the Fe powder where pH increases to 9.2 (Figure 4-34).

Figure 4-35 shows the time evolution of the computed Eh. The initial Eh is around -0.24 V after the initial chemical equilibration, and then Eh decreases to a value around -0.55 V at 1953 days (FB3 corrosion test) and at 7 years (FB4 corrosion test).

Fe(s) corrodes at a constant corrosion rate of 0.15  $\mu\text{m}/\text{year}$  in the Fe powder (Figure 4-27). Computed magnetite precipitates in the Fe powder. A small amount of magnetite precipitates 2 mm (two elements) into bentonite (Figure 4-28). The experimental observations indicates that there no magnetite penetration at the bentonite. Model results show no precipitation of siderite, goethite and  $\text{Fe}(\text{OH})_2(\text{s})$ .

Figure 4-36 shows the computed concentrations of the exchanged  $\text{Ca}^{2+}$ ,  $\text{Mg}^{2+}$ ,  $\text{Na}^+$  and  $\text{K}^+$  at the end of the FB4 corrosion test. Computed exchanged  $\text{Ca}^{2+}$  and  $\text{Mg}^{2+}$  increase slightly from the initial values in the bentonite near the hydration side and decrease near the Fe powder. On the contrary, computed exchanged  $\text{Na}^+$  decreases from the initial values near the hydration side and increases near the Fe(s). The computed concentration of the exchanged  $\text{K}^+$  show minor changes. The concentration of exchanged  $\text{Fe}^{2+}$  decreases from its initial value in the FB3 corrosion test and in the FB4 corrosion test (Figure 4-37).

Figure 4-38 shows the concentrations of the major sorbed species on strong, weak #1 and weak #2 sites at the end of the FB4 corrosion test.  $\text{Fe}^{2+}$  sorption is most important in the strong and weak #1 sites. The computed sorbed species on the strong and weak #2 sites do not show relevant changes, except for  $\text{S}^0\text{Fe}^+$ . The concentration of  $\text{S}^0\text{Fe}^+$  decreases from the initial concentration in the bentonite near the Fe powder and in the Fe powder in the FB4 corrosion test. The computed sorbed  $\text{S}^{\text{w}1}\text{OFe}^+$  increases in the bentonite and decreases in the Fe powder from the initial concentration in the FB4 corrosion test. On the other hand, computed sorbed  $\text{S}^{\text{w}1}\text{O}^-$  decreases in the bentonite and increases in the Fe powder from the initial concentration in the FB4 corrosion test.

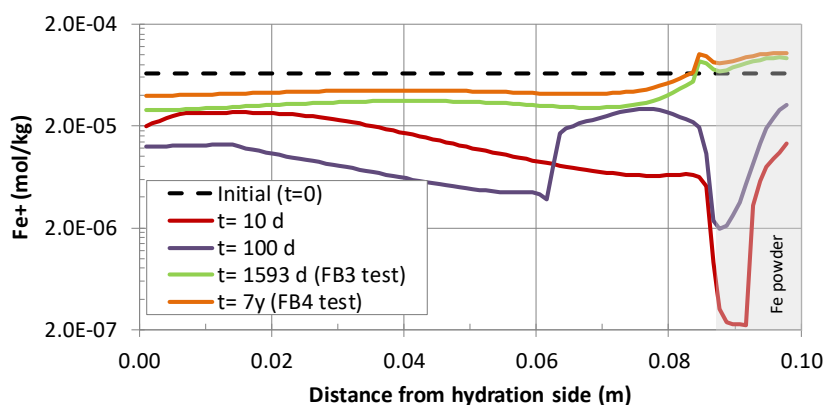


Figure 4-26 – Spatial distribution of the computed concentration of dissolved  $\text{Fe}^{2+}$  at selected times in the FB corrosion tests.

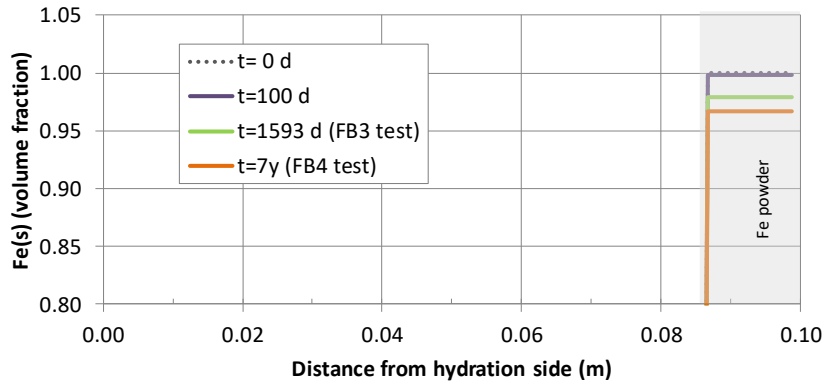


Figure 4-27 – Spatial distribution of the computed volume fraction of Fe(s) corrosion at selected times in the FB corrosion tests.

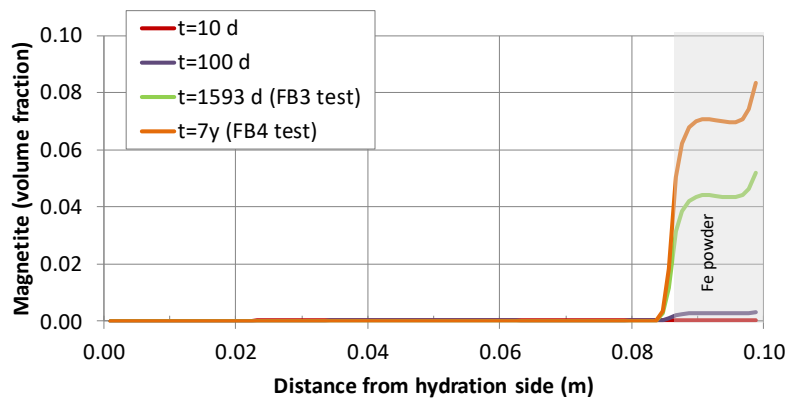


Figure 4-28 – Spatial distribution of the computed volume fraction of magnetite on at selected times in the FB corrosion tests.

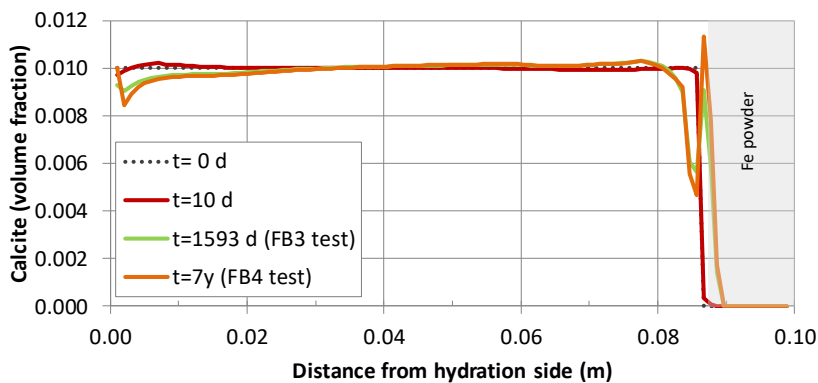


Figure 4-29 – Spatial distribution of the computed volume fraction of calcite at selected times in the FB corrosion tests.

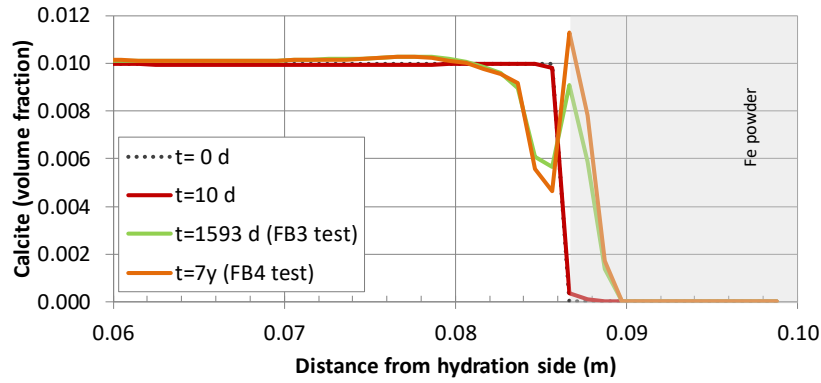


Figure 4-30 – Zoom of the spatial distribution of the computed volume fraction of calcite at selected times in the FB corrosion tests.

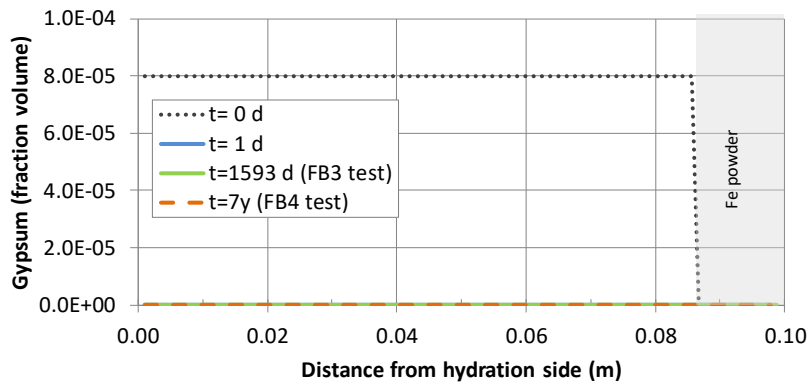


Figure 4-31 – Spatial distribution of the computed volume fraction of gypsum at selected times in the in the FB corrosion tests.

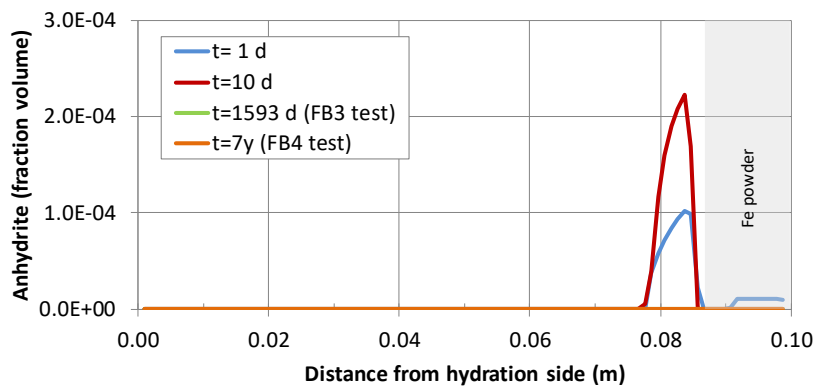


Figure 4-32 – Spatial distribution of the computed volume fraction of anhydrite at selected times in the FB corrosion tests.

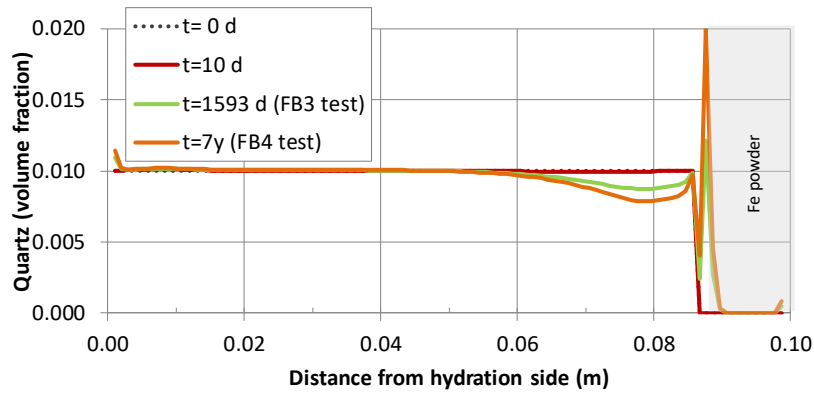


Figure 4-33 – Spatial distribution of the computed volume fraction of quartz at selected times in the FB corrosion tests.

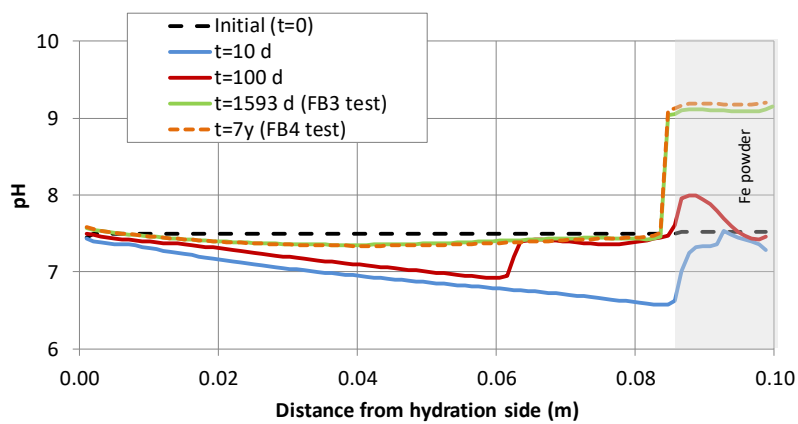


Figure 4-34 – Spatial distribution of the computed pH at selected times in the FB corrosion tests.

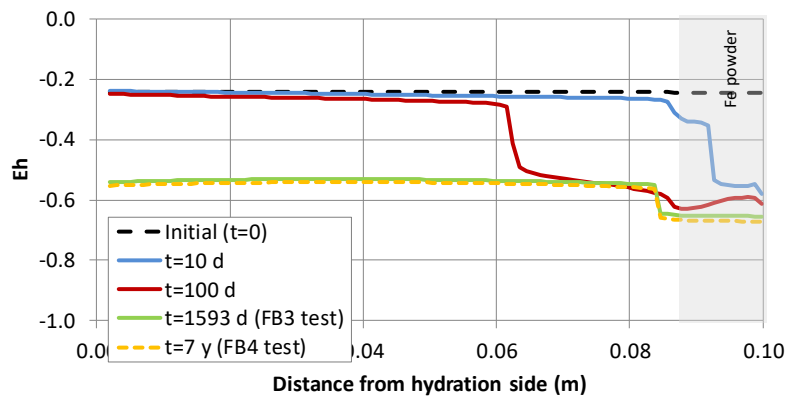


Figure 4-35 – Spatial distribution of the computed Eh at selected times in the FB corrosion tests.

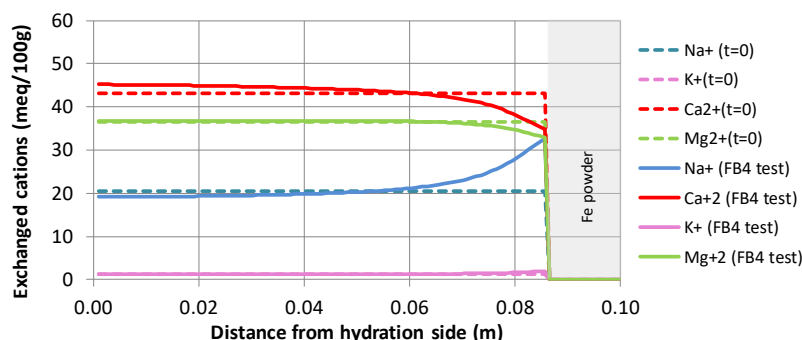


Figure 4-36 – Spatial distribution of the computed (lines) and measured (symbols) concentrations of the exchanged cations at the end of the FB4 corrosion test.

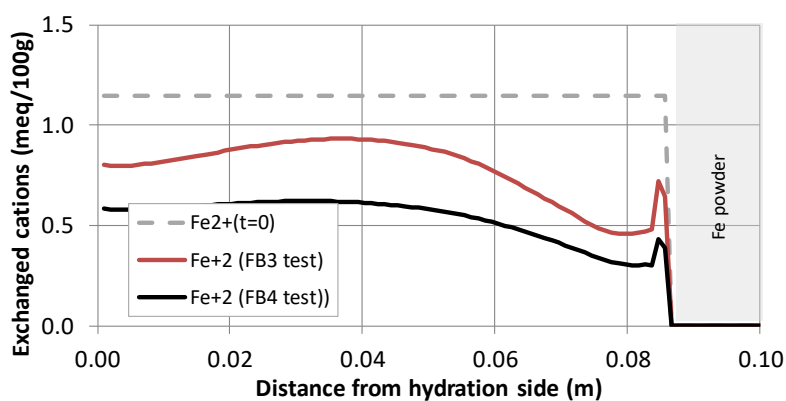


Figure 4-37 – Spatial distribution of the computed concentration of exchanged  $Fe^{2+}$  at the end of the FB corrosion tests.

Figure 4-39 to Figure 4-44 show the computed results of the dissolved concentrations of  $Cl^-$ ,  $HCO_3^-$ ,  $Fe^{2+}$  and  $SiO_2(aq)$ , the exchanged concentration of  $Fe^{2+}$  and pH at the end of the FB4 corrosion test before and after the cooling phase.

The computed dissolved concentration of  $Cl^-$  shows a slight diffusion in the bentonite and Fe powder near the interface during the cooling phase (Figure 4-39). The computed dissolved concentration of  $Na^+$ ,  $K^+$ ,  $Mg^{2+}$ ,  $Ca^{2+}$  and  $SO_4^{2-}$  show a similar to that of the  $Cl^-$  behavior during the cooling phase.

Figure 4-40 shows the concentration of  $HCO_3^-$  before and after the cooling phase of the FB4 corrosion test. The concentration of  $HCO_3^-$  increases in the bentonite due to the decreasing of the total mass of calcite during the cooling. The concentration of  $SiO_2(aq)$  decreases in the bentonite during the cooling (Figure 4-41).

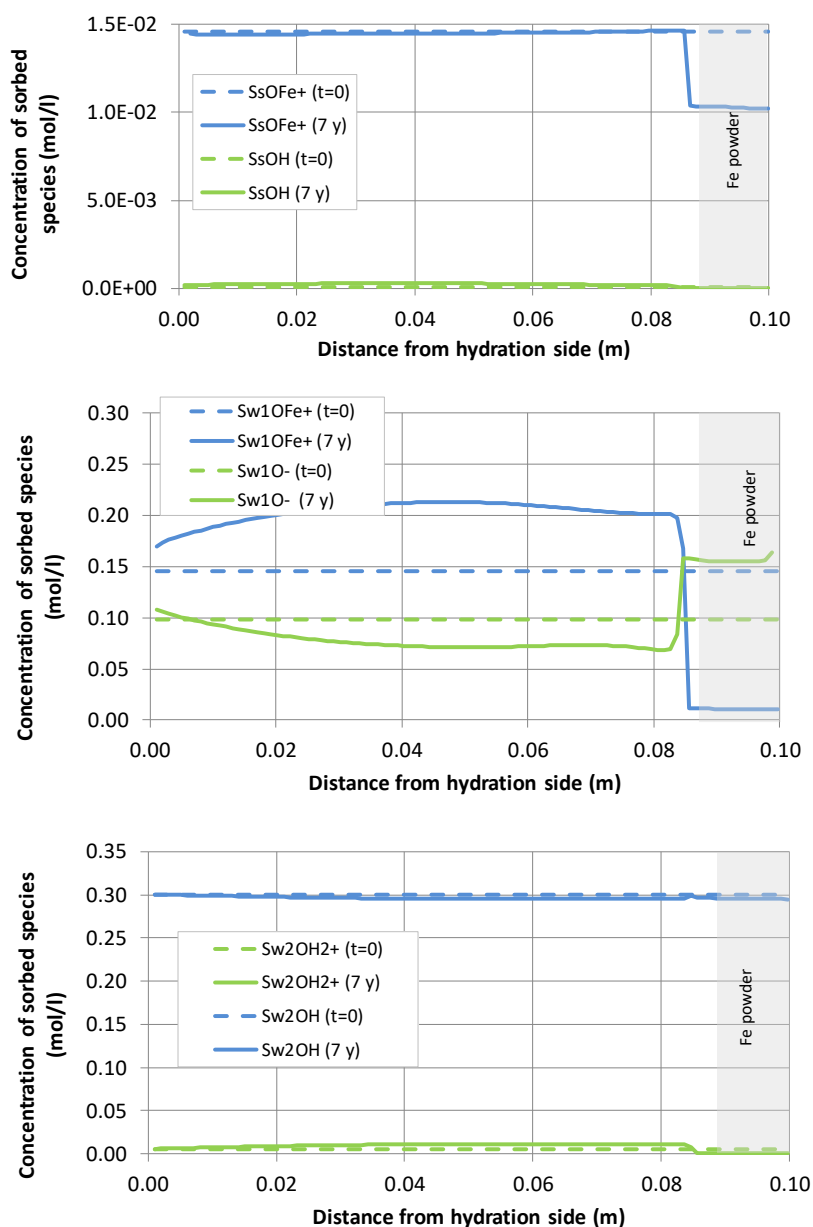


Figure 4-38 – Spatial distribution of the computed concentration of sorbed species on strong, weak #1 and weak #2 sorption sites at the end of the FB4 corrosion test.

The computed dissolved  $\text{Fe}^{2+}$  concentration increases in the Fe powder and in the bentonite near the Fe powder interface (Figure 4-42). This  $\text{Fe}^{2+}$  increasing is due to the combined effect of  $\text{Fe}(s)$  corrosion, magnetite slightly dissolution, total exchanged  $\text{Fe}^{2+}$  mass (Figure 4-43) and total sorbed  $\text{Fe}^{2+}$  mass decreasing during the cooling.

The computed pH increases to 9.2 in the Fe powder and in the bentonite near the Fe powder interface during the cooling phase (Figure 4-44). This increase in pH is caused by the change in the solubilities of calcite and magnetite with temperature.

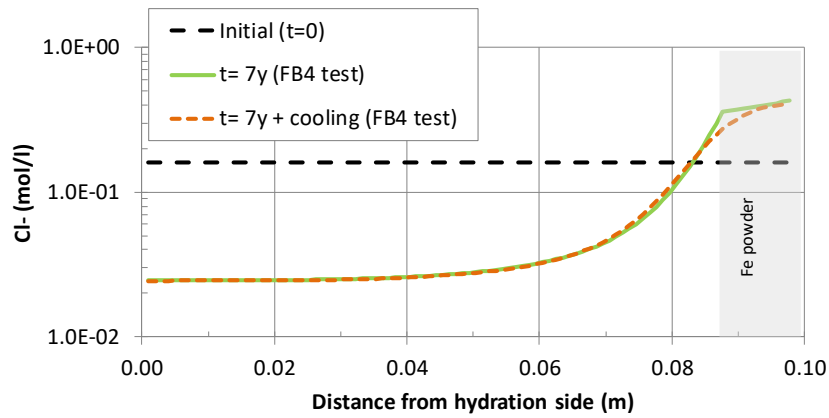


Figure 4-39 – Spatial distribution of the computed  $Cl^-$  concentration at the end of the FB4 corrosion test before and after the cooling phase.

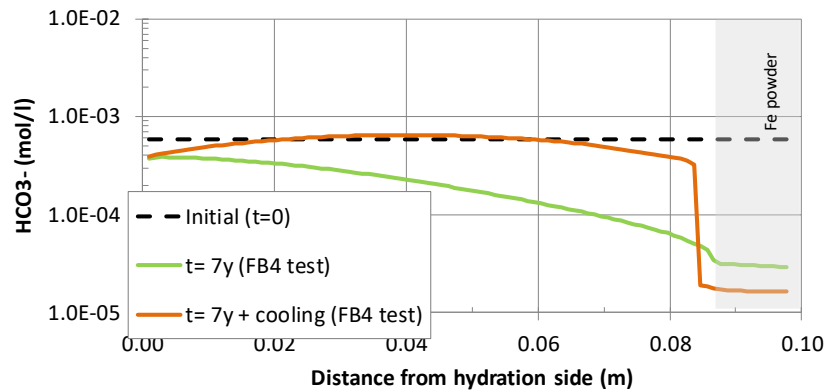


Figure 4-40 – Spatial distribution of the computed  $HCO_3^-$  concentration at the end of the FB4 corrosion test before and after the cooling phase.

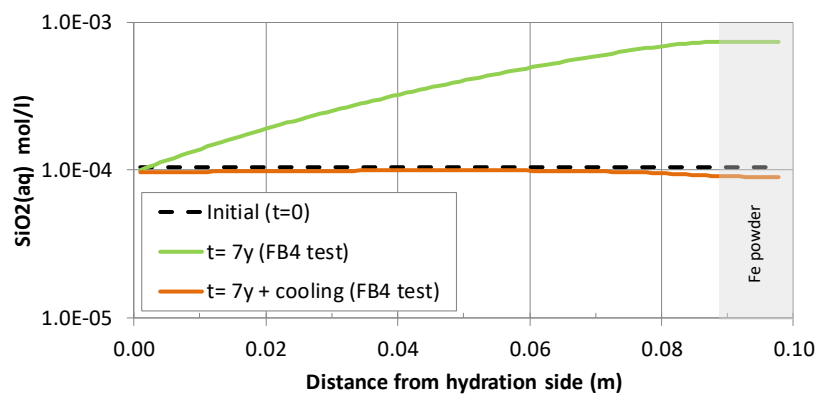


Figure 4-41 – Spatial distribution of the computed  $SiO_2(aq)$  concentration at the end of the FB4 corrosion test before and after the cooling phase.

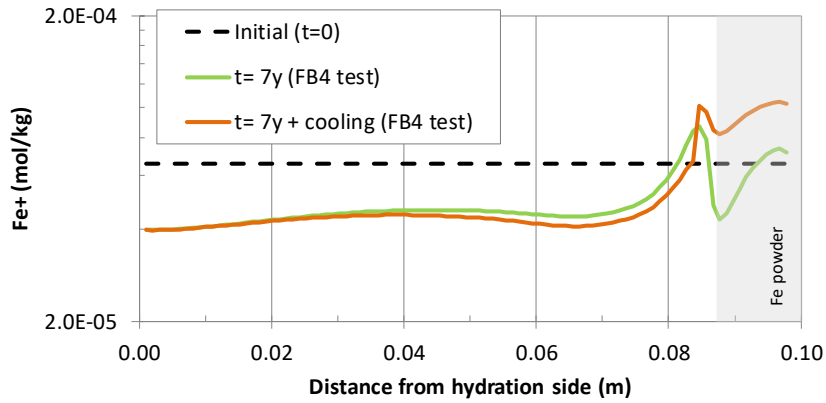


Figure 4-42 – Spatial distribution of the computed dissolved  $Fe^{2+}$  concentration at the end of the FB4 corrosion test before and after the cooling phase.

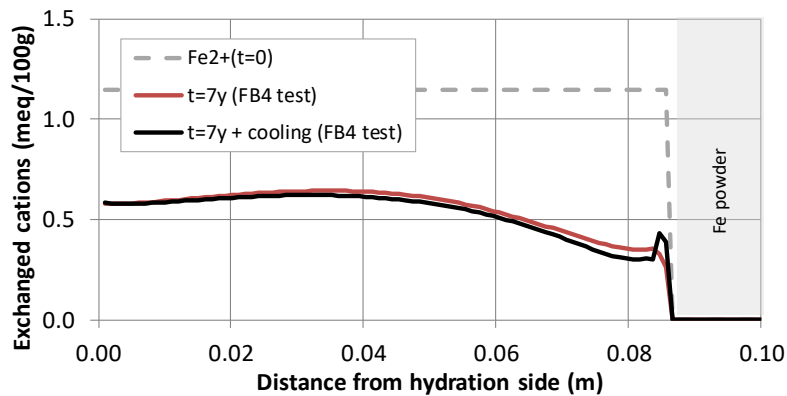


Figure 4-43 – Spatial distribution of the computed exchanged  $Fe^{2+}$  concentration at the end of the FB4 corrosion test before and after the cooling phase.

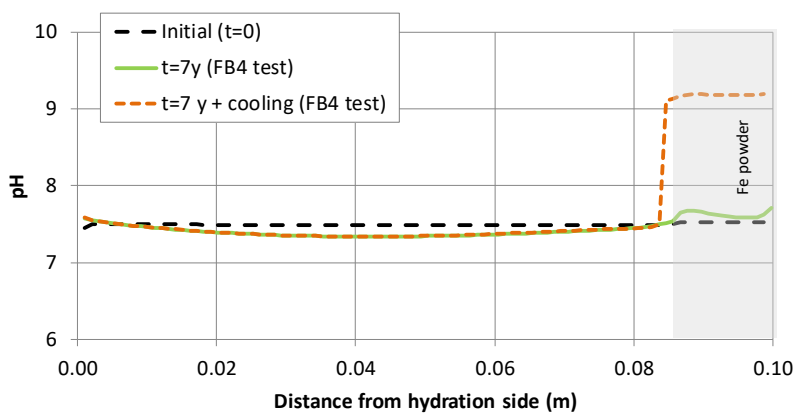


Figure 4-44 – Spatial distribution of the computed pH at the end of the FB4 corrosion test before and after the cooling phase.

## 5. Corrosion model of the steel bentonite interactions in the FEBEX in situ experiment – UDC Approach

This chapter presents the numerical model of the FEBEX in situ experiment performed by UDC at the Grimsel underground research laboratory. The description of the numerical model includes the proposed modelling approach, the preliminary model predictions of the geochemical evolution of the FEBEX in situ test which do not account yet for steel corrosion, the proposed model improvements and the identification of the missing data for model validation.

### 5.1 The FEBEX in situ experiment

FEBEX was a demonstration and research project dealing with the engineered barrier system designed for sealing and containment of a radioactive waste repository (ENRESA, 2000). FEBEX was based on the Spanish Reference Concept for the disposal of radioactive waste in crystalline rocks. Besides the laboratory experiments, FEBEX included the following two main large-scale experiments, which started in February 1997: (1) The in situ full-scale test performed at the Grimsel underground research laboratory in Switzerland (Alonso and Ledesma, 2005; ENRESA, 2000; 2006a); and (2) The mock-up test operated at the CIEMAT facilities in Spain (ENRESA, 2000; 2006a; Martín and Barcala, 2005).

The FEBEX in situ test was performed in a gallery excavated in granite in the underground research laboratory (URL) of Grimsel operated by NAGRA in Switzerland. The test began in February 1997. The 1<sup>st</sup> operation period lasted from 1997 to 2002 when heater 1 was switched off and the surrounding area was dismantled. The 2<sup>nd</sup> operation period started after the emplacement of a shotcrete plug in 2002 and ended in June 2015 when the entire bentonite barrier was fully dismantled after 18 years.

#### 5.1.1 Dimensions

The FEBEX in situ test included the heating system, the clay barrier and the instrumentation, monitoring and control system in a gallery excavated in granite in the URL of Grimsel at Switzerland. The drift was 70.4 m long and 2.27 m in diameter (ENRESA, 2000). The test zone was located in the last 17.4 m of the drift where heaters, bentonite and instrumentation were installed. The main elements of the heating system were two heaters, separated horizontally by 1 m, which simulated full-sized canisters. The heaters were placed inside a cylindrical steel liner having a diameter of 0.93 m, which had been installed concentrically with the drift. Each heater was made of carbon steel, measured 4.54 m in length and 0.90 m in diameter, had a wall thickness of 0.10 m and weighed 11 tons. The heaters were designed to maintain a maximum temperature of 100°C at the liner/bentonite interface. The bentonite barrier was made of blocks of highly compacted bentonite. The layout of the FEBEX in situ test for the 1<sup>st</sup> operation period is shown in Figure 5-1. The layout of the 2<sup>nd</sup> period is shown in Figure 5-2.

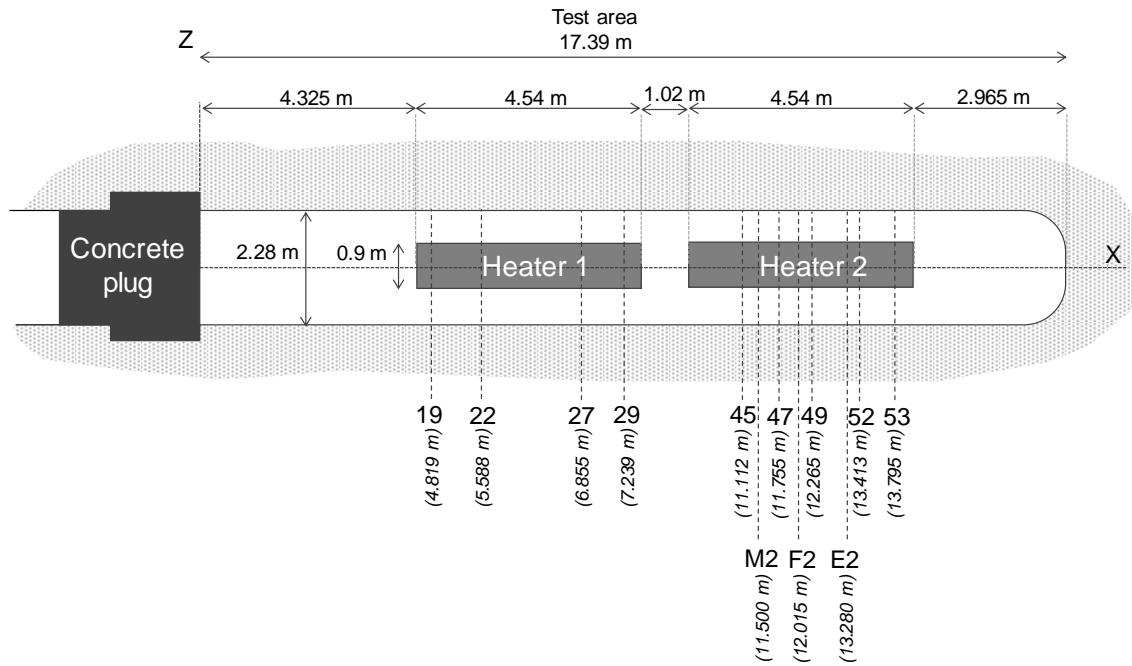


Figure 5-1 – General layout of the FEBEX in situ test for the 1<sup>st</sup> operation period, indicating the instrumented and sampling sections used by Samper et al., 2018b. The x coordinates of the sections are referred to the concrete plug on the left.

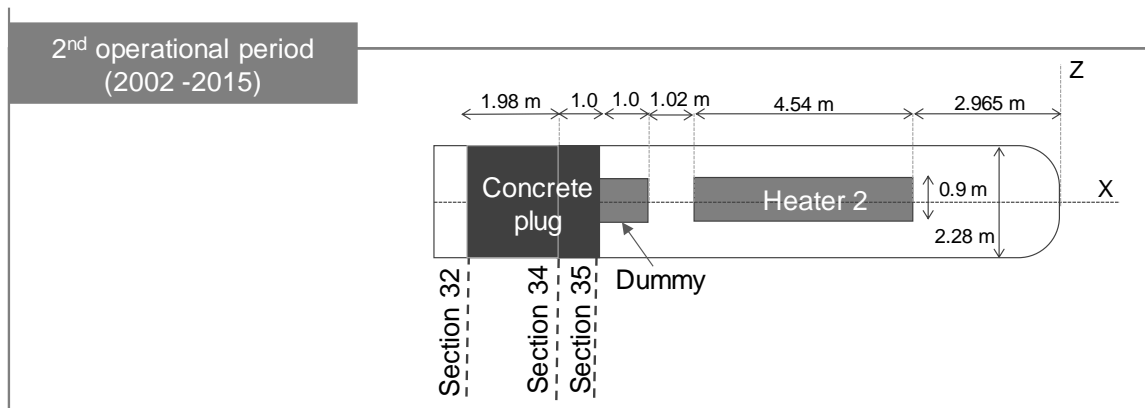


Figure 5-2 – General layout of the FEBEX in situ test for the 2<sup>nd</sup> operation period.

### 5.1.2 Materials

The clay barrier of the FEBEX in situ test was made of blocks of highly compacted bentonite, which were situated in vertical sections normal to the axis of the tunnel, with a diameter of 2.28 m (Figure 5-1). Weighted average values of initial dry density and water content of bentonite blocks were 1.7 g/cm<sup>3</sup> and 14.4%, respectively (ENRESA, 2000).

The heaters, which were made of carbon steel, were placed inside a cylindrical carbon steel liner having a diameter of 0.93 m. The liner was surrounded by the clay barrier (ENRESA, 2000). The liner had the following composition: 99.04 wt.% Fe, 0.16 wt.% C, 0.30 wt.% Si, and 0.60 wt.% Mo.

### 5.1.3 Conditions

The test began in February 1997. The 1<sup>st</sup> operation period lasted from 1997 to 2002 when heater 1 was switched off and the surrounding area was dismantled. The 2<sup>nd</sup> operation period started after the emplacement of a shotcrete plug in 2002 and ended in June 2015 when after 18 years of heating and hydration the entire bentonite barrier was fully dismantled. Once the entire bentonite barrier of the FEBEX in situ test was fully dismantled, a comprehensive post-mortem bentonite sampling and analysis program was performed to characterize the solid and liquid phases, analyse the physical and chemical changes induced by the combined effect of heating and hydration and test THM and THC model predictions (Lanyon and Gaus, 2017; Fernández et al., 2018)

### 5.1.4 Previous models of the FEBEX in situ test

Samper et al. (2008b) presented a coupled THC model of the 1<sup>st</sup> period of the FEBEX in situ test. The model achieved a good match to temperature data in the buffer and captured the general trends of the measured concentrations of dissolved Cl<sup>-</sup> and cations. However, the model failed to reproduce the measured water content data because the model did not account for swelling and the observed gradients in bentonite dry density (Villar et al., 2005). The model underestimated the measured concentrations of dissolved SO<sub>4</sub><sup>2-</sup>, probably due to uncertainties in the initial amount of gypsum in the bentonite. The model did not reproduce the pattern of the measured concentration of dissolved HCO<sub>3</sub><sup>-</sup> because the model did not account for the CO<sub>2</sub>(g) degassing from the liquid water near the heater.

Since the geochemical processes are linked and affected by thermal and hydrodynamic processes, the study, identification and modelling of the geochemical alterations require the use of coupled THCM models. Zheng et al. (2011) presented a coupled THCM model of the 1<sup>st</sup> operation period of the FEBEX in situ test with bentonite swelling and chemical and thermal osmosis. The results of this model confirmed: (1) The importance of bentonite swelling on the spatial distribution of conservative and reactive chemical species due to its effect on porosity; (2) The relevance of thermal osmosis; (3) The lack of relevance of chemical osmosis; (4) The importance of calcite dissolution/precipitation and cation exchange reactions on the concentrations of dissolved cations; and (5) The strong effect of gypsum/anhydrite dissolution/precipitation on the geochemical evolution of the bentonite barrier. Zheng et al. (2011) found that the water contents and the concentrations of the dissolved species were strongly sensitive to changes in the intrinsic permeability, the thermal osmotic permeability and the initial dissolved concentrations. Model results reproduced the measured temperatures, relative humidities, water contents and the pore water chemical data inferred from aqueous extracts. However, the model results deviated from the measured dissolved concentration data at the heater/bentonite and bentonite/granite interfaces.

Samper et al. (2018b) presented a revisited THCM model of the two operation periods of the FEBEX in situ test which extends the THCM model of Zheng et al. (2011) by improving the boundary condition at the heater/bentonite interface, refining the spatial discretization of the finite element mesh near the heater, revising the dispersivities of the bentonite and the granite and revisiting the back-diffusion of solutes from the bentonite barrier into the granite. The results of the revisited THCM model were compared to gravimetric water content data measured at the end of the 1<sup>st</sup> and 2<sup>nd</sup> operation periods and on line data of temperature and volumetric water content in the bentonite and pore water pressure in the granitic rock collected from 2002 to 2015. Samper et al. (2018b) presented the predictions of the geochemical conditions at the end of the 2<sup>nd</sup> operation period with the revisited THCM model.

Wilson (2017) presented a geochemical model of the iron-bentonite interactions at the FEBEX in situ test. They also interpreted some of the preliminary observations in the experiment and concluded that: 1) Some oxygen was likely to have been present immediately after the emplacement of the bentonite barrier; and 2) The colour zonation in some areas (Figure 5-3d) suggests a possible redox gradient with conditions going from aerobic to anaerobic from the liner/bentonite interface into the bentonite. Wilson (2017) commented that this pattern differs from most previously-published studies of iron-bentonite or iron-claystone interactions. Most simulations assume anaerobic conditions from the start ( $t = 0$ ), with

anaerobic steel corrosion and  $H_2(g)$  production. Wilson (2017) adopted a 'simple and practicable' approach focused on a good representation of the iron-bentonite geochemistry. He assumed a constant steel corrosion rate model (Wilson et al., 2015), used the reactive transport computer code QPAC (Quintessa, 2013) and considered the following processes: (1) Mineral dissolution/precipitation reactions (kinetic treatment); (2) Aqueous speciation (equilibrium); (3) Solute diffusion; and (4) Coupled porosity evolution. Wilson (2017) performed a base case with a fixed steel corrosion rate of  $1 \mu\text{m}/\text{year}$  based on Wilson et al. (2015) and 5 additional cases by considering a larger corrosion rate, a larger effective diffusion coefficient, including cation exchange processes and considering aerobic conditions at the iron-bentonite interface. Wilson (2017) concluded that the models were able to replicate essentially aerobic (Fe(III)-dominated) or anaerobic (Fe(II)-dominated) conditions, but not both. He pointed out that the observations show a heterogeneous pattern with redox gradients in some areas. He suggested that future models should account for redox gradients evolving in different regions in the presence of temperature gradients with multiphase flow. The precipitation of Fe(III)-rich minerals such as goethite requires including in the model a source of oxygen. Accounting for all these features is a complex conceptual and numerical challenge.

Hadi et al. (2019) studied experimentally the steel-iron interactions in the FEBEX in situ test and focused on the contact area between the corroding Fe source and compacted bentonite. Although the FEBEX in situ test was not specifically designed to study the steel corrosion and iron-bentonite interactions, post-mortem analyses at the end of the 1<sup>st</sup> period (2002) and especially after the 2<sup>nd</sup> period (2015) focused on this topic (Kober et al., 2017). According to Hadi et al. (2019) several steel components of the FEBEX in situ test retrieved after the 2<sup>nd</sup> operation period such as the liner, the heater, the dummy, the extensometers, the fissure-meters, the drilling rods and the cable ducts showed clear corrosion features. The impact of corrosion and the Fe migration inside the bentonite could also be observed in some zones of the bentonite surrounding the corroded objects, appearing as concentric and coloured (red, orange, blue) halos (Figure 5-3). Hadi et al. (2019) characterized the coloured interaction zones observed in two bentonite blocks, the newly formed Fe phases, and the effect of corrosion on the bentonite chemistry. These two blocks of the same section 41 were located between the two heaters during the first operation period of the experiment and after the dismantling of the heater 1 between the dummy and the heater 2. Temperatures in the range 30 to  $60^\circ\text{C}$  were likely reached in this location of the experiment (Fuentes-Cantillana and García-Siñeriz 1998). A final gravimetric water content of 26 wt.% was determined in this area of the experiment (Villar et al. 2016), showing a notable increase compared to initial water content (13 wt.% according to Fuentes-Cantillana and García-Siñeriz 1998).

According to Hadi et al. (2019), a coloured corrosion halo was observed as soon as the bentonite layer separating the dummy and the second heater was reached (Figure 5-3). This halo was asymmetric, and preferentially located on the upper left part of the liner, while the opposite side of the liner appeared almost unaffected by corrosion. In fact, a plastic sheet was placed between the granite and the lower right part of this section of the bentonite barrier during the construction of the FEBEX experiment. This sheet was inadvertently left behind and further hindered direct water ingress, and thus Fe diffusion in this area of the experiment (Villar et al. 2016). Two bentonite blocks were extracted from the bentonite backfill, one from the strongly impacted area (block BM-B-41-1, Figure 5-3e) and the other from the much less impacted area (block BM-B-41-2, Figure 5-3). These blocks were only partially exposed to the ambient atmosphere (one side was exposed and covered by a plastic sheet to limit drying and oxidation) for a few hours before they could be extracted, vacuum-packed, and transported to the laboratory.

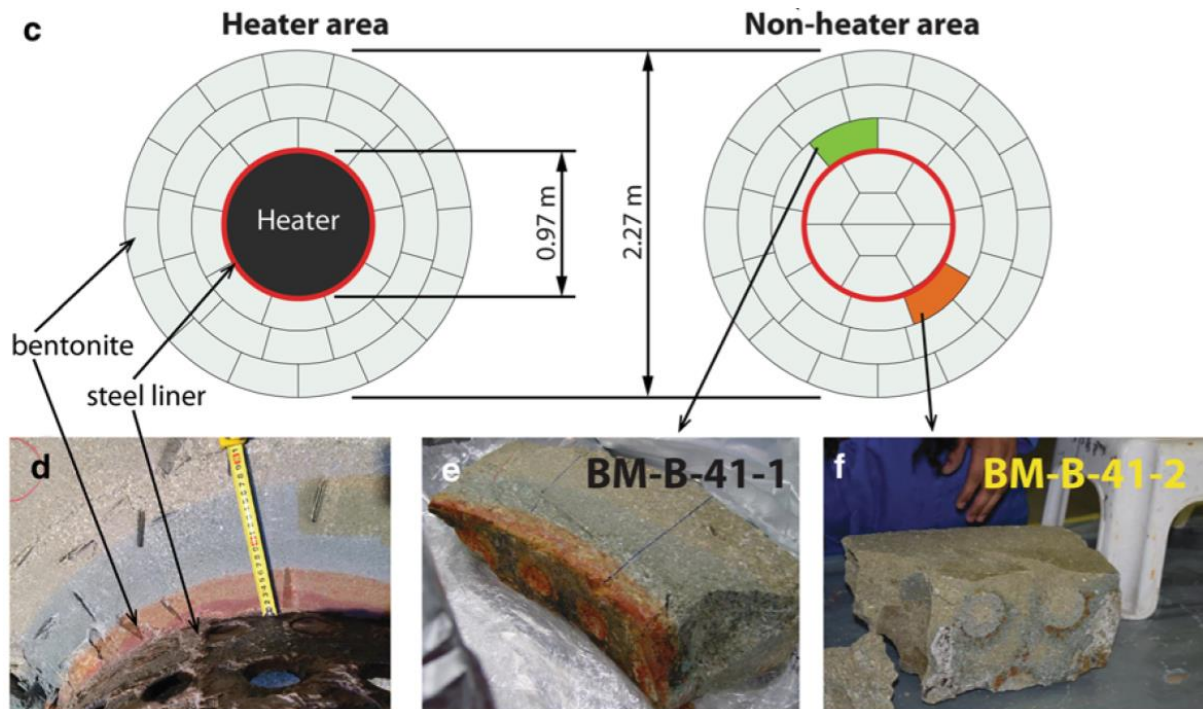


Figure 5-3 – Concentric and coloured (red, orange, blue) halos observed at a bentonite block in contact with the steel liner in (d) a heater area and (e, f) the studied bentonite blocks BM-B-41-1 and BM-B-41-2 (Hadi et al., 2019).

The combination of bulk and spatially resolved approaches employed by Hadi et al. (2019) enabled the characterization of the Fe diffusion front observed over >140 mm inside a bentonite block. Goethite was the main newly formed Fe-bearing phase present in the red-orange zone at the interface with the steel (thus only additional  $\text{Fe}^{3+}$ ), while additional  $\text{Fe}^{2+}$  was found only at the very interface (few first hundreds of micrometers) and further into the wider and Fe poorer blue zone (without additional  $\text{Fe}^{3+}$ ). The exact location and speciation of this additional  $\text{Fe}^{2+}$  is, however, still to be determined.

Hadi et al. (2019) proposed a conceptual model of Fe diffusion at the steel-bentonite interface where diffusion of  $\text{Fe}^{2+}$  occurs only when anaerobic corrosion starts occurring once  $\text{O}_2$  is depleted at the surface of the steel and sufficient water saturation conditions are met (Figure 5-4). Diffusion then proceeds in two stages. During the first stage,  $\text{Fe}^{2+}$  diffusion inside the bentonite competes with  $\text{O}_2$  diffusion toward the interface and Fe is accumulated as  $\text{Fe}^{3+}$  oxi-hydroxides (mainly goethite) near the interface. As soon as  $\text{O}_2$  is depleted inside the bentonite,  $\text{Fe}^{2+}$  diffuses into the bentonite. The understanding of the processes controlling Fe accumulation in the bentonite requires knowing the pre-existing Fe-bearing phases.

Hadi et al. (2019) emphasized that these phenomena were observed only at some specific areas and did not occur everywhere in the liner. The coloured halos were observed only along a portion of the liner located in between the two heaters, and along other steel pieces located near the granitic rock and not close to the heater. This is most likely related to varying water saturation conditions in the FEBEX in situ experiment. The bentonite near the heaters was less saturated and prevented steel corrosion. The strong contrasts in water saturation reported by Villar et al. (2016) may also explain the large differences between the two studied bentonite blocks and the resulting asymmetric corrosion halo (related to the leftover plastic sheet between the granitic host-rock and the lower part of this section of the experiment). These two blocks originated from the same section of the experiment, but the lower-most (BM-B-42-2) was almost unaffected by the corrosion of the steel liner.

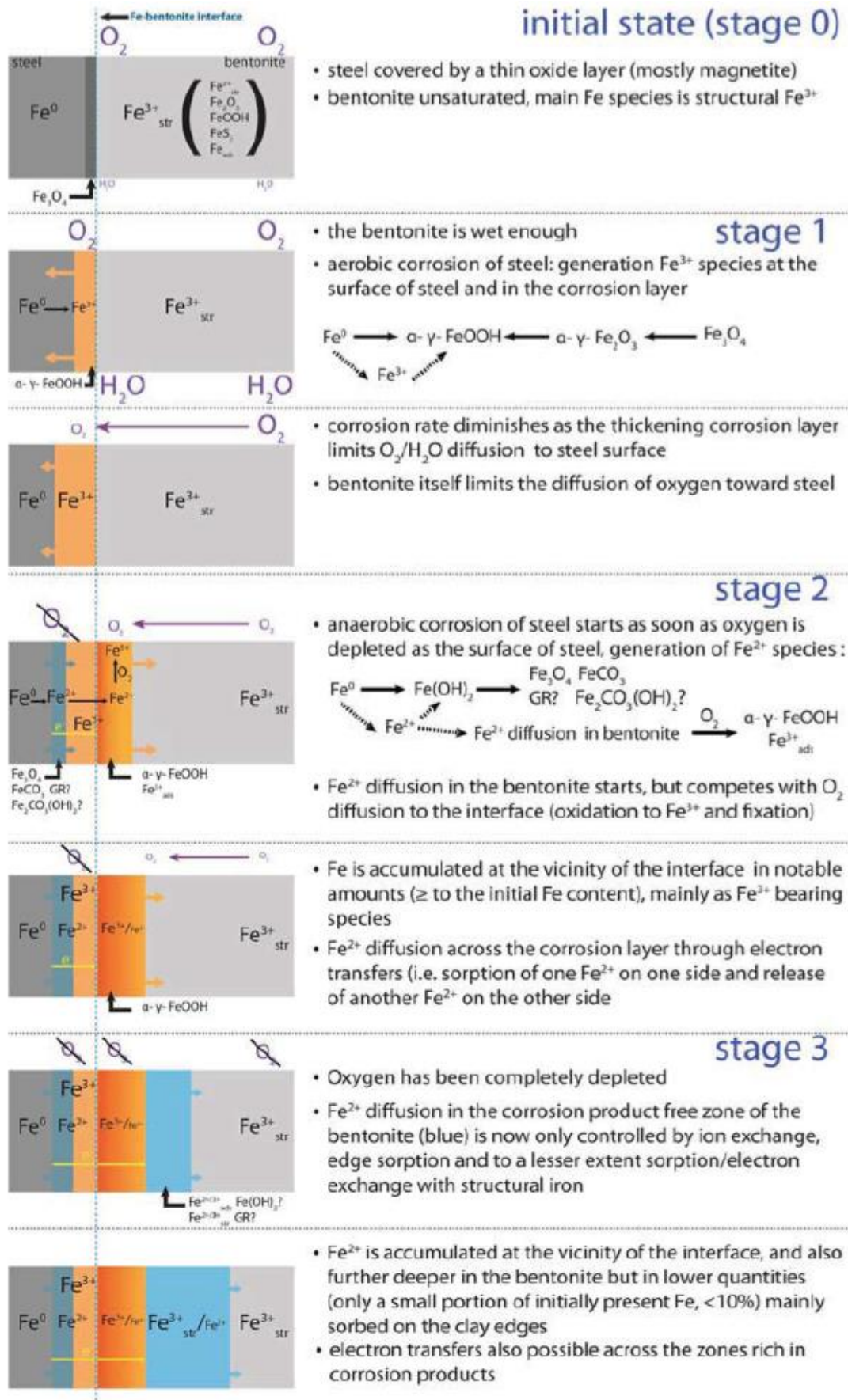


Figure 5-4 – Proposed Fe diffusion mechanism at the steel–bentonite interface (Hadi et al., 2019).

Kaufhold et al (2019) investigated the cation exchange, geochemical and mineralogical reactions taking place at the iron-bentonite interface at selected sampling sites of the FEBEX in situ test. They studied the geochemical and mineralogical alterations of the bentonite caused by the heater and inflowing water. Samples were taken at the following locations of the FEBEX in situ experiment (Figure 5-5): (1) The iron-bentonite interface in sections S36, S42 and S54; (2) Along four radial profiles in the bentonite not affected by the heater (sections S45, S50 and S53); and (3) The black material from the liner surface and the reddish clay in the holes of the liner. The contact samples taken from sections S36 (liner/dummy) and S42 (liner/heater) showed reddish colours. They concluded that bentonite samples in contact with the metal liner showed an increase in the Fe content, which was mainly present as goethite. This oxitic corrosion may be explained by the comparably large amount of air that was entrapped between the heater and the liner. Samples taken directly from the Fe surface of the liner showed an intimate intergrowth of bentonite constituents and Fe phases (even native Fe). In addition, precipitation of carbonates at the inner surface of the liner was observed. No signs of corrosion were detected at the face of the heater (section 54), where bentonite blocks were in direct contact with the heater surface. They found a marked increase in the Mg content near the heater.

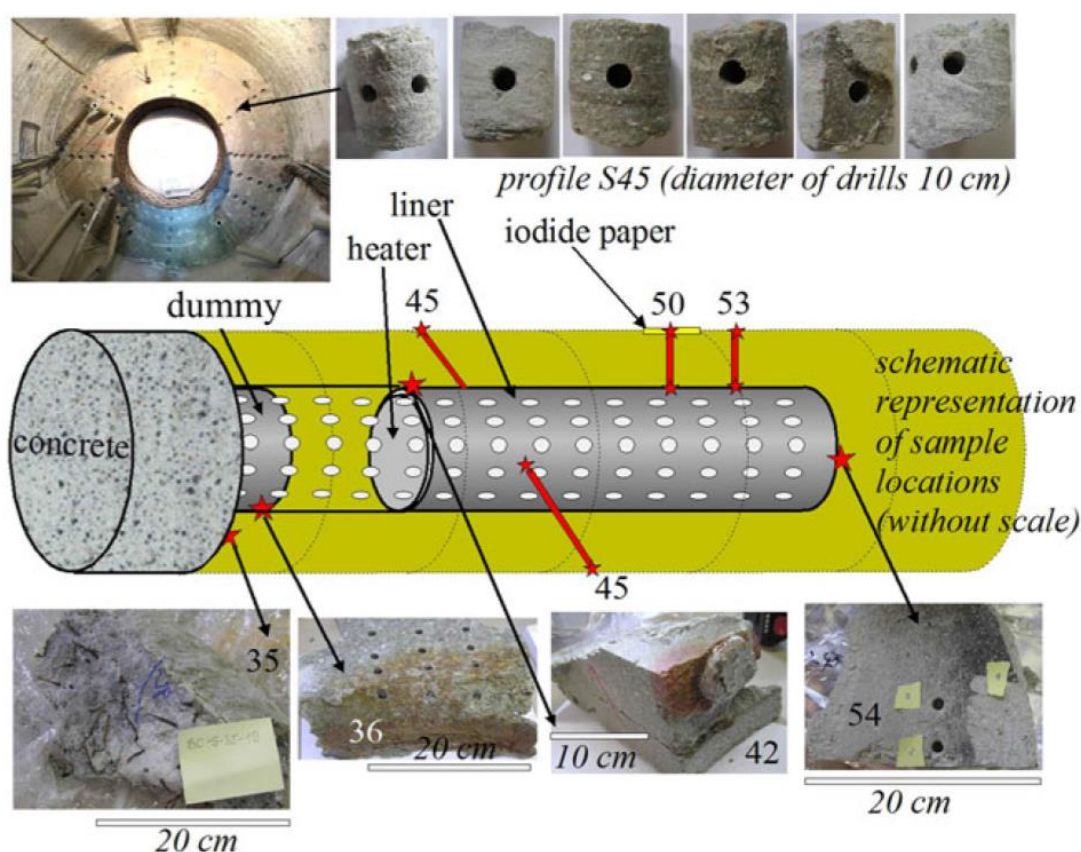


Figure 5-5 – Schematic representation of the samples analysed by Kaufhold et al. (2019).

## 5.2 Proposed modelling approach

The revisited THCM model of the FEBEX in situ test of Samper et al. (2018b) will be the starting point for modelling the interactions of corrosion products and bentonite at several locations of the FEBEX in situ test. The proposed approach for the reactive transport modelling of the FEBEX in situ test includes the following in three stages:

- 1) Updating the FEBEX in situ model developed by Samper et al. (2018b).
- 2) Improving the geochemical model by using the Fe diffusion mechanism at the steel-bentonite interface proposed by Hadi et al. (2019).
- 3) Adding the following geochemical processes: kinetically-controlled magnetite precipitation, precipitation of the corrosion products such as goethite, siderite and Fe-phyllosilicates, smectite dissolution using different kinetic laws; and zeolite precipitation.

The model will be performed with the following methodology:

- 1) Data analysis.
- 2) Formulation of the conceptual geochemical models.
- 3) Model structure (spatial and time discretization; parameterization).
- 4) Sensitivity analysis prior to model calibration.
- 5) Model calibration.
- 6) Uncertainty analysis.

## 5.3 Conceptual Model

### 5.3.1 Objectives of the Model

The main objectives of the coupled THCM model of the FEBEX in situ test proposed by ENRESA(UDC) include:

- (1) The extension of the previous THCM model of the FEBEX in situ test of Samper et al. (2018b) to account for redox processes, steel corrosion and the interactions of corrosion products and compacted FEBEX bentonite.
- (2) The testing of the conceptual geochemical model of steel corrosion in the FEBEX in situ test proposed by Hadi et al. (2019).
- (3) The improvement of the numerical model of the interactions of steel/bentonite for the FEBEX in situ test and the identification of the remaining uncertainties.

ENRESA (UDC) will perform a coupled thermo-hydro-chemical-mechanical (THCM) model of the FEBEX in situ experiment, which will account for steel corrosion and the interactions of corrosion products and bentonite. The previous THCM model of Samper et al. (2018b) will be supplemented with steel corrosion and Fe diffusion with the conceptual mechanism proposed by Hadi et al. (2019) and the inputs from the SOTA of ACED Task 1.

### 5.3.2 Processes to be modelled

The main thermo-hydrodynamic processes in the bentonite buffer of the FEBEX in situ model include:

- 1) Water flow under hydraulic, chemical and thermal gradients;
- 2) Vapour flow (advection and diffusion);
- 3) Advective and diffusive gas flow; and
- 4) Heat transport in the gas and liquid phases (convection) and in the solid phase (conduction).

The model accounts for the following solute transport processes in the aqueous phase: advection, molecular diffusion and mechanical dispersion. The geochemical model accounts for aqueous complexation and acid-base reactions, mineral dissolution/precipitation, cation exchange of  $\text{Ca}^{2+}$ ,  $\text{Mg}^{2+}$ ,  $\text{Na}^+$  and  $\text{K}^+$  and surface complexation of  $\text{H}^+$  on three types of sorption sites (strong sites,  $\text{S}^{\text{sOH}}$ , weak #1 sites,  $\text{S}^{\text{w1OH}}$  and weak #2 sites,  $\text{S}^{\text{w2OH}}$ ) according to the triple-site sorption model of Bradbury and Baeyens (1997). The geochemical system was defined in terms of 10 primary species ( $\text{H}_2\text{O}$ ,  $\text{H}^+$ ,  $\text{Cl}^-$ ,  $\text{Ca}^{2+}$ ,  $\text{Mg}^{2+}$ ,  $\text{Na}^+$ ,  $\text{K}^+$ ,  $\text{SO}_4^{2-}$ ,  $\text{HCO}_3^-$  and  $\text{SiO}_2(\text{aq})$ ), 15 secondary aqueous species identified from speciation runs performed with EQ3/6 (Wolery, 1992) and 5 minerals (calcite, gypsum, anhydrite, chalcedony and halite) assumed at chemical equilibrium. The Gaines-Thomas convention will be used for cation exchange reactions (Appelo and Postma, 1993). The chemical reactions and their equilibrium constants at 25 °C for secondary species and mineral dissolution/precipitation as well as the selectivity

coefficients for exchanged cations and the protolysis constants for the triple-site model are listed in Table 5-1.

The previous THMC models of the FEBEX in situ test performed by UDC (Samper et al., 2018b) considered neither iron corrosion nor redox reactions because the experimental evidences of steel corrosion after the dismantling of the first heater were very limited. It is planned to update the geochemical model of the FEBEX in situ test to account for a corrosion conceptual geochemical model similar to that used in the FB4 test, which is presented in Section 4 of this deliverable. The following additional species and reactions will be included: (1) Fe<sup>2+</sup> and O<sub>2</sub>(aq) as primary aqueous species; (2) Up to 15 Fe aqueous complexes; (3) Carbon steel, Fe(s), magnetite, goethite, siderite, chukanovite and Fe(OH)<sub>2</sub>(s); (4) Exchanged Fe in the cation exchange complex; and (5) 5 Fe surface complexation reactions. The chemical reactions, equilibrium constants, selectivity coefficients and the iron surface complexation constants are listed in Table 5-1.

The state surface approach taken from Lloret and Alonso (1995) is used to simulate the bentonite swelling. Additional details of the conceptual model can be found in Zheng et al. (2011).

*Table 5-1 – Reactions and equilibrium constants for aqueous species and mineral dissolution/precipitation at 25 °C (Wolery, 1992); protolysis constants for surface complexation reactions for a triple-site sorption model (Bradbury and Baeyens, 2005); and selectivity constants for cation exchange reactions (ENRESA, 2006a).*

Aqueous complexation	Log K (25°C)
CaCl <sup>+</sup> ⇌ Ca <sup>2+</sup> + Cl <sup>-</sup>	0.696
CaCO <sub>3</sub> (aq) + H <sup>+</sup> ⇌ Ca <sup>2+</sup> + HCO <sub>3</sub> <sup>-</sup>	7.002
CaHCO <sub>3</sub> <sup>+</sup> ⇌ Ca <sup>2+</sup> + HCO <sub>3</sub> <sup>-</sup>	-1.047
CaSO <sub>4</sub> (aq) ⇌ Ca <sup>2+</sup> + SO <sub>4</sub> <sup>2-</sup>	-2.111
CO <sub>2</sub> (aq) + H <sub>2</sub> O ⇌ H <sup>+</sup> + HCO <sub>3</sub> <sup>-</sup>	-6.345
CO <sub>3</sub> <sup>2-</sup> + H <sup>+</sup> ⇌ HCO <sub>3</sub> <sup>-</sup>	10.329
H <sub>3</sub> SiO <sub>4</sub> <sup>-</sup> + H <sup>+</sup> ⇌ 2 H <sub>2</sub> O + SiO <sub>2</sub> (aq)	9.812
KSO <sub>4</sub> <sup>-</sup> ⇌ K <sup>+</sup> + SO <sub>4</sub> <sup>2-</sup>	-0.879
MgCl <sup>+</sup> ⇌ Mg <sup>2+</sup> + Cl <sup>-</sup>	0.135
MgCO <sub>3</sub> (aq) ⇌ Mg <sup>2+</sup> + CO <sub>3</sub> <sup>2-</sup>	-2.979
MgHCO <sub>3</sub> <sup>+</sup> ⇌ Ca <sup>2+</sup> + HCO <sub>3</sub> <sup>-</sup>	-1.036
MgSO <sub>4</sub> (aq) ⇌ Mg <sup>2+</sup> + SO <sub>4</sub> <sup>2-</sup>	-2.412
NaHCO <sub>3</sub> (aq) ⇌ Na <sup>+</sup> + HCO <sub>3</sub> <sup>-</sup>	-0.154
NaSO <sub>4</sub> <sup>-</sup> ⇌ Na <sup>+</sup> + SO <sub>4</sub> <sup>2-</sup>	-0.820
OH <sup>-</sup> + H <sup>+</sup> ⇌ H <sub>2</sub> O	13.995
Fe <sup>3+</sup> + 0.5H <sub>2</sub> O ⇌ H <sup>+</sup> + 0.25O <sub>2</sub> + Fe <sup>2+</sup>	-8.490
FeHCO <sub>3</sub> ⇌ Fe <sup>2+</sup> + HCO <sub>3</sub> <sup>-</sup>	-2.050
FeCO <sub>3</sub> (aq) ⇌ Fe <sup>2+</sup> + CO <sub>3</sub> <sup>2-</sup>	-4.730
FeCl <sup>+</sup> ⇌ Fe <sup>2+</sup> + Cl <sup>-</sup>	0.1605
FeCl <sup>2+</sup> ⇌ Fe <sup>3+</sup> + Cl <sup>-</sup>	0.8108
FeOH <sup>+</sup> + H <sup>+</sup> ⇌ Fe <sup>2+</sup> + H <sub>2</sub> O	10.895
FeOH <sup>2+</sup> + H <sup>+</sup> ⇌ Fe <sup>3+</sup> + H <sub>2</sub> O	4.3815
Fe(OH) <sub>2</sub> (aq) + 2H <sup>+</sup> ⇌ Fe <sup>2+</sup> + 2H <sub>2</sub> O	20.60
Fe(OH) <sub>3</sub> (aq) + 3H <sup>+</sup> ⇌ Fe <sup>3+</sup> + 3H <sub>2</sub> O	12.172
Fe(OH) <sub>4</sub> <sup>-</sup> + 4H <sup>+</sup> ⇌ Fe <sup>3+</sup> + 4H <sub>2</sub> O	21.60
Fe(OH) <sub>2</sub> <sup>+</sup> + 2H <sup>+</sup> ⇌ Fe <sup>3+</sup> + 2H <sub>2</sub> O	5.670
Fe(SO <sub>4</sub> ) <sub>2</sub> <sup>-</sup> ⇌ Fe <sup>3+</sup> + 2SO <sub>4</sub> <sup>2-</sup>	-3.213

$\text{FeSO}_4(\text{aq}) \Leftrightarrow \text{Fe}^{2+} + \text{SO}_4^{2-}$	-2.20
$\text{FeHSO}_4^{2+} \Leftrightarrow \text{Fe}^{3+} + \text{H}^+ + \text{SO}_4^{2-}$	-1.540
$\text{Fe}_2(\text{OH})_2^{4+} + 2\text{H}^+ \Leftrightarrow 2\text{Fe}^{3+} + 2\text{H}_2\text{O}$	7.2826
<b>Minerals</b>	<b>Log K (25°C)</b>
$\text{Calcite} + \text{H}^+ \Leftrightarrow \text{Ca}^{2+} + \text{HCO}_3^-$	1.849
$\text{Anhydrite} \Leftrightarrow \text{Ca}^{2+} + \text{SO}_4^{2-}$	-4.306
$\text{Gypsum} \Leftrightarrow \text{Ca}^{2+} + \text{SO}_4^{2-} + 2\text{H}_2\text{O}$	-4.482
$\text{Halite} \Leftrightarrow \text{Na}^+ + \text{Cl}^-$	1.585
$\text{Chalcedony} \Leftrightarrow \text{SiO}_2(\text{aq})$	-3.728
$\text{Smectite} + 6.56\text{H}^+ \Leftrightarrow 0.135 \text{Na}^+ + 0.055 \text{K}^+ + 0.125 \text{Ca}^{2+} + 0.525 \text{Mg}^{2+} + 1.69 \text{Al}^{3+} + 3.86 \text{SiO}_2(\text{aq}) + 4.82 \text{H}_2\text{O}$	6.260
$\text{Analcime} + 4\text{H}^+ \Leftrightarrow \text{Na}^+ + \text{Al}^{3+} + 2\text{SiO}_2(\text{aq}) + 3\text{H}_2\text{O}$	6.783
$\text{Fe}(\text{s}) + 2\text{H}^+ \Leftrightarrow \text{Fe}^{2+} + 2\text{H}_2\text{O} + 2\text{OH}^- + \text{H}_2(\text{aq})$	-15.064
$\text{Magnetite} + 6\text{H}^+ \Leftrightarrow 3\text{Fe}^{2+} + 0.5\text{O}_2(\text{aq}) + 3\text{H}_2\text{O}$	-6.5076
$\text{Siderite} + \text{H}^+ \Leftrightarrow \text{Fe}^{2+} + \text{HCO}_3^-$	-0.1920
$\text{Goethite} + 2\text{H}^+ \Leftrightarrow \text{Fe}^{2+} + 1.5\text{H}_2\text{O} + 0.25\text{O}_2(\text{aq})$	-7.9555
$\text{Fe}(\text{OH})_2(\text{s}) + 2\text{H}^+ \Leftrightarrow \text{Fe}^{2+} + 2\text{H}_2\text{O}$	13.9045
$\text{Chukanovite} + 3\text{H}^+ \Leftrightarrow 2\text{Fe}^{2+} + \text{HCO}_3^- + 2\text{H}_2\text{O}$	12.32
$\text{Berthierine} + 10\text{H}^+ \Leftrightarrow 2\text{Fe}^{2+} + 2\text{Al}^{3+} + \text{SiO}_2(\text{aq}) + 7\text{H}_2\text{O}$	25.55
$\text{Cronstedtite} + 10\text{H}^+ \Leftrightarrow 2\text{Fe}^{2+} + 2\text{Fe}^{3+} + \text{SiO}_2(\text{aq}) + 7\text{H}_2\text{O}$	16.2603
$\text{Chlorite} + 16\text{H}^+ \Leftrightarrow 5\text{Fe}^{2+} + 2\text{Al}^{3+} + 3\text{SiO}_2(\text{aq}) + 12\text{H}_2\text{O}$	55.6554
<b>Ion exchange</b>	<b>K<sub>Na-cation</sub></b>
$\text{Na}^+ + \text{X-K} \Leftrightarrow \text{K}^+ + \text{X-Na}$	0.138
$\text{Na}^+ + 0.5\text{X}_2\text{-Ca} \Leftrightarrow 0.5\text{Ca}^{2+} + \text{X-Na}$	0.294
$\text{Na}^+ + 0.5\text{X}_2\text{-Mg} \Leftrightarrow 0.5\text{Mg}^{2+} + \text{X-Na}$	0.288
$\text{Na}^+ + 0.5 \text{X}_2\text{-Fe} \Leftrightarrow 0.5 \text{Fe}^{2+} + \text{X-Na}$	0.5
<b>Surface complexation</b>	<b>Log K<sub>int</sub></b>
$\equiv\text{S}^{\text{OH}}_2 \Leftrightarrow \equiv\text{S}^{\text{OH}} + \text{H}^+$	-4.5
$\equiv\text{S}^{\text{O}^-} + \text{H}^+ \Leftrightarrow \equiv\text{S}^{\text{OH}}$	7.9
$\equiv\text{S}^{\text{W}1}\text{OH}_2 \Leftrightarrow \equiv\text{S}^{\text{W}1}\text{OH} + \text{H}^+$	-4.5
$\equiv\text{S}^{\text{W}1}\text{O}^- + \text{H}^+ \Leftrightarrow \equiv\text{S}^{\text{W}1}\text{OH}$	7.9
$\equiv\text{S}^{\text{W}2}\text{OH}_2 \Leftrightarrow \equiv\text{S}^{\text{W}2}\text{OH} + \text{H}^+$	-6.0
$\equiv\text{S}^{\text{W}2}\text{O}^- + \text{H}^+ \Leftrightarrow \equiv\text{S}^{\text{W}2}\text{OH}$	10.5
$\equiv\text{S}^{\text{O}}\text{Fe}^+ + \text{H}^+ \Leftrightarrow \equiv\text{S}^{\text{OH}} + \text{Fe}^{2+}$	0.6
$\equiv\text{S}^{\text{O}}\text{FeOH} + 2\text{H}^+ \Leftrightarrow \equiv\text{S}^{\text{OH}} + \text{Fe}^{2+} + \text{H}_2\text{O}$	10.0
$\equiv\text{S}^{\text{O}}\text{Fe}(\text{OH})_2^- + 3\text{H}^+ \Leftrightarrow \equiv\text{S}^{\text{OH}} + \text{Fe}^{2+} + 2\text{H}_2\text{O}$	20.0
$\equiv\text{S}^{\text{W}1}\text{OFe}^+ + \text{H}^+ \Leftrightarrow \equiv\text{S}^{\text{W}1}\text{OH} + \text{Fe}^{2+}$	3.3

### 5.3.3 Important assumptions, simplifications, limitations

The revisited THMC model of the FEBEX in situ test of Samper et al. (2018b) does not account for steel corrosion and the interactions of corrosion products and compacted FEBEX bentonite. The model will be updated during the second year of the ACED WP by considering several assumptions for steel corrosion including a constant corrosion rate and a time-varying corrosion rate depending on ambient

conditions (T, pH, Eh). The model will include the inputs from the SOTA of ACED Task 1 and account for the conceptual model of Fe diffusion near the steel-bentonite interface proposed by Hadi et al. (2019).

Fe powder will be treated as a porous material made of 100% metallic iron, Fe(s). H<sub>2</sub>O will be assumed to be the corroding agent of Fe(s) under anaerobic conditions. A detailed description of this process is presented in Section 4.3.3. Additional corrosion products such as iron oxides and hydroxides, green-rust minerals and Fe-phyllsilicates will also be considered in the updated model.

### 5.3.4 Boundary Conditions

The temperature and the liquid pressure at the outer boundary (r= 50 m) are equal to 12 °C and 700 kPa, respectively. A constant temperature of 97 °C is prescribed at the internal boundary which coincides with the liner/bentonite interface (r = 0.465 m). The liner is not taken into account in the model. There was no flow at the heater/bentonite interface (r = 0.465 m).

The system is assumed open to the gas. Therefore, the gas pressure is equal to the atmospheric pressure.

### 5.3.5 Initial conditions / parameters

Bentonite has an initial porosity of 0.41, a volumetric water content of 24.5%, which corresponds to a gravimetric water content of around 14.5%, a liquid saturation degree of 59% and a suction of 1.1·10<sup>5</sup> kPa. This gravimetric water content is very similar to the mean value reported by Fuentes-Cantillana and García-Siñeriz (1998). Bentonite swelling is simulated with the state-surface approach of Nguyen et al. (2005). The granite has a porosity of 0.01 and is assumed to be always saturated. The deformation of the granite is disregarded. The gas pressure is set equal to 100 kPa. The initial temperature is uniform and equal to 12°C. The thermal, hydrodynamic and mechanical parameters of the bentonite and granite are listed in Table 5-2 and Table 5-3.

The initial concentration of the FEBEX bentonite pore water at a water content of 14% is taken from Fernández et al. (2001) while the initial composition of the granite groundwater is derived from experimental data (ENRESA, 2006a) as reported by Samper et al. (2008b). The initial compositions of the bentonite and the granite pore waters, the initial mineral volume fractions, the initial concentrations of exchanged ions and the total concentrations of surface complexation sites are listed in Table 5-4. The initial volume fraction of the carbon steel is assumed to be 100% Fe (Samper et al., 2016). The following Fe secondary minerals are allowed to precipitate: magnetite, goethite, siderite, Fe(OH)<sub>2</sub>(s), chukanovite, berthierine, cronstedtite and chlorite. The effective diffusion coefficients of chloride and sulphate for fully saturated bentonite are equal to 9.3·10<sup>-13</sup> m<sup>2</sup>/s and 1.1·10<sup>-13</sup> m<sup>2</sup>/s, respectively (García-Gutiérrez et al., 2004; 2006). The effective diffusion coefficients of the rest of the primary species were taken equal to 6.1·10<sup>-12</sup> m<sup>2</sup>/s (Table 5-5).

The dependence of the equilibrium constants for aqueous complexes and minerals on temperature is calculated with the following expression, which is valid for temperatures ranging from 0 to 300 °C (Wolery, 1992):

$$\log K(T) = \frac{b_1}{T^2} + \frac{b_2}{T} + b_3 \ln T + b_4 + b_5 T \quad (1)$$

where b<sub>1</sub> to b<sub>5</sub> are coefficients which were derived by fitting this equation to measured log K values at 0, 25, 60, 100, 150, 200, 250 and 300°C.

Table 5-2. Thermal, hydrodynamic and mechanical parameters of the bentonite and granite (Zheng and Samper 2008; Zheng et al., 2011, based on ENRESA 2006a).

Parameter	Bentonite	Granite
Intrinsic permeability for liquid flow, $k_{il}$ (m <sup>2</sup> )	$k_{il} = k_o \frac{\phi^3 (1 - \phi_o)^2}{(1 - \phi)^2 \phi_o^3}$ $k_o = 3.75 \cdot 10^{-21}$	$8 \cdot 10^{-18}$
Relative permeability to liquid, $k_{rl}$	$k_{rl} = S_l^3$	$k_{rl} = \sqrt{S_l} [1 - (1 - S_l^{0.5})^{0.5}]^2$
Retention curve	$S_l = \frac{(1 - 9.1 \cdot 10^{-7} \psi)^{1.1}}{[(1 + 5 \cdot 10^{-5} \psi)^{1.22}]^{0.18}}$	$S_l = \frac{1}{[(1 + (4.76 \cdot 10^{-4} \psi)^{1.3})]^{0.7}}$
Liquid viscosity (kg/m s)	$7 \cdot 10^{-5} (T - 44)^{-1.562}$	$661.2 \cdot 10^{-3} (T - 44)^{-1.562}$
Vapor tortuosity factor	0.09	1.0
Solid density (kg/m <sup>3</sup> )	$2780 e^{(-2 \cdot 10^{-6} (T - 12))}$	$2700 e^{(-2 \cdot 10^{-6} (T - 12))}$
Specific heat of the solid (J/kg °C)	835.5	1029
Thermal conductivity of the solid (W/m °C)	1.23	1.5

Table 5-3 – Thermal, hydrodynamic and mechanical parameters (Zheng and Samper, 2008, based on ENRESA, 2006a).

Parameter	Bentonite
Intrinsic permeability for gas flow (m <sup>2</sup> )	$5 \cdot 10^{-10}$
Relative permeability to gas, $k_{rg}$ (m <sup>2</sup> )	$k_{rg} = (1 - S_l)^3$
Thermo-osmosis permeability (m <sup>2</sup> /s °C)	$5.2 \cdot 10^{-12}$
Gas viscosity (kg/m s)	$1.76 \cdot 10^{-10}$
Specific heat of the liquid (J/kg °C)	4202
Specific heat of the air (J/kg °C)	1000
Specific heat of the vapor (J/kg °C)	1620
Thermal conductivity of the liquid (W/m °C)	0.6
Thermal conductivity of the air (W/m °C)	$2.6 \cdot 10^{-2}$
Thermal conductivity of the vapor (W/m °C)	$4.2 \cdot 10^{-2}$
Vaporization enthalpy (J/kg)	$2.45 \cdot 10^6$
Mechanical compressibility of the water (Pa <sup>-1</sup> )	$5 \cdot 10^{-7}$
Thermal compressibility of the water (°C <sup>-1</sup> )	$2.1 \cdot 10^{-4}$
Thermal compressibility of the solid (°C <sup>-1</sup> )	$2 \cdot 10^{-5}$

Table 5-4 – Initial pore water composition (Fernández et al., 2001; Samper et al., 2008a), initial mineral volume fractions (Samper et al., 2008a), initial concentrations of exchanged ions (Fernández et al., 2004) and total concentrations of surface complexation sites (Bradbury and Bayens, 1997, 2003).

	Bentonite	Granite
Initial pore water composition		
pH	7.72	8.35
O <sub>2</sub> (aq) (mol/L)	8.0·10 <sup>-60</sup>	2.0·10 <sup>-68</sup>
Na <sup>+</sup> (mol/L)	1.3·10 <sup>-2</sup>	3.8·10 <sup>-4</sup>
K <sup>+</sup> (mol/L)	1.7·10 <sup>-3</sup>	7.8·10 <sup>-6</sup>
Ca <sup>2+</sup> (mol/L)	2.2·10 <sup>-2</sup>	1.8·10 <sup>-4</sup>
Mg <sup>2+</sup> (mol/L)	2.3·10 <sup>-2</sup>	1.3·10 <sup>-6</sup>
Fe <sup>2+</sup> (mol/L)	6.58·10 <sup>-5</sup>	1.7·10 <sup>-8</sup>
HCO <sub>3</sub> <sup>-</sup> (mol/L)	4.1·10 <sup>-4</sup>	3.9·10 <sup>-4</sup>
SO <sub>4</sub> <sup>2-</sup> (mol/L)	3.2·10 <sup>-2</sup>	7.9·10 <sup>-5</sup>
Cl <sup>-</sup> (mol/L)	1.6·10 <sup>-1</sup>	1.3·10 <sup>-5</sup>
SiO <sub>2</sub> (aq) (mol/L)	1.1·10 <sup>-4</sup>	1.4·10 <sup>-4</sup>
Initial volume fractions of the minerals (%)		
Calcite	1	5
Chalcedony	4.5	20
Anhydrite	0	0
Gypsum	0.016	0
Halite	0	0
Smectite (sensitivity run)	53.48	0
Initial cation exchange concentrations (cmol(+)/kg)		
Na <sup>+</sup>	21.10	-
K <sup>+</sup>	1.94	-
Ca <sup>2+</sup>	31.31	-
Mg <sup>2+</sup>	41.41	-
Fe <sup>2+</sup>	0.896	-
Total concentration of surface complexation sites (mol/kg)		
=S <sup>s</sup> OH	2.0·10 <sup>-3</sup>	-
=S <sup>w1</sup> OH	4.0·10 <sup>-3</sup>	-
=S <sup>w2</sup> OH	4.0·10 <sup>-3</sup>	-

Table 5-5 – Effective diffusion coefficients in the bentonite and granite for the base run of the revisited model with and without solute back-diffusion from the bentonite into the granite.

	Bentonite (m <sup>2</sup> /s)		Granite (m <sup>2</sup> /s)	
	without back-diffusion	with back-diffusion	without back-diffusion	with back-diffusion
Cl <sup>-</sup> (García-Gutiérrez <i>et al.</i> , 2004)	9.3·10 <sup>-13</sup>	1.5·10 <sup>-11</sup>	6.7·10 <sup>-15</sup>	2·10 <sup>-11</sup>
SO <sub>4</sub> <sup>2-</sup> (García-Gutiérrez <i>et al.</i> , 2006)	1.1·10 <sup>-13</sup>	1.5·10 <sup>-11</sup>	7.8·10 <sup>-16</sup>	2·10 <sup>-11</sup>
Rest of the dissolved species (ENRESA, 2006a)	6.1·10 <sup>-12</sup>	10 <sup>-11</sup>	4.4·10 <sup>-14</sup>	1.4·10 <sup>-11</sup>

## 5.4 Numerical model

### 5.4.1 Spatial and temporal discretization

A 1D axisymmetric row of rectangular elements is used. The model domain includes the bentonite barrier, which extends from  $r = 0.465$  m to  $r = 1.135$  m, and the granitic rock which has a length of 48.865 m. The spatial discretization of the model has 616 nodes and 307 elements. The grid size in the granitic rock grows exponentially from 1 mm at the bentonite interface to 5 m at the external boundary.

The simulation time horizon covers the entire duration of the in situ test from February 1997 to 2015 (18 years). The numerical model accounts for the heating stages and the cooling phases after switching off the heaters at the end of the two operation periods (heater 1 after 5 years of operation, 1<sup>st</sup> operational phase, and heater 2 after 18 years of operation, 2<sup>nd</sup> operational phase).

### 5.4.2 Sensitivity analyses

The previous THMC models of the FEBEX in situ test performed by UDC (Samper *et al.*, 2018b) considered neither iron corrosion nor redox reactions. This section presents the methodology used to perform the sensitivity analyses on the previous THMC model of the FEBEX in situ test of Samper *et al.* (2018b). A similar sensitivity analysis will be performed with the updated model once steel corrosion, Fe species and redox reactions are included in the model.

Solute transfer from the bentonite pore water to the granite groundwater was not uniform along the FEBEX gallery due to the heterogeneity of the surrounding granitic rock. The revisited model of the FEBEX in situ test of Samper *et al.* (2018b) predicted no significant back-diffusion. The effective diffusion coefficients of the bentonite and the granite were adjusted to reproduce the solute back-diffusion experimental observations of Buil *et al.* (2010) and Garralón *et al.* (2018). The concentrations of dissolved Cl<sup>-</sup> and SO<sub>4</sub><sup>2-</sup> in the granite computed with the revisited model at a distance of 0.2 m from the bentonite interface were consistent with the experimental concentrations at the FU1-3 and FU1-4 intervals when the effective diffusion coefficients for Cl<sup>-</sup> and SO<sub>4</sub><sup>2-</sup> in the bentonite and granite were taken equal to 1.5·10<sup>-11</sup> m<sup>2</sup>/s and 2·10<sup>-11</sup> m<sup>2</sup>/s, respectively (Figure 5-6). The diffusion coefficients which reproduce the observed back-diffusion were larger than the diffusion coefficients of the revisited model. The back-diffusion of solutes from the bentonite into the granite led to a decrease of the dissolved concentrations in the bentonite. The concentrations of dissolved Ca<sup>2+</sup> in the bentonite at the end of the

1<sup>st</sup> operation period in the run with back-diffusion decreased noticeably near the heater and to a lesser extent, from  $r = 0.65$  m to  $r = 0.85$  m compared to the run without back-diffusion (

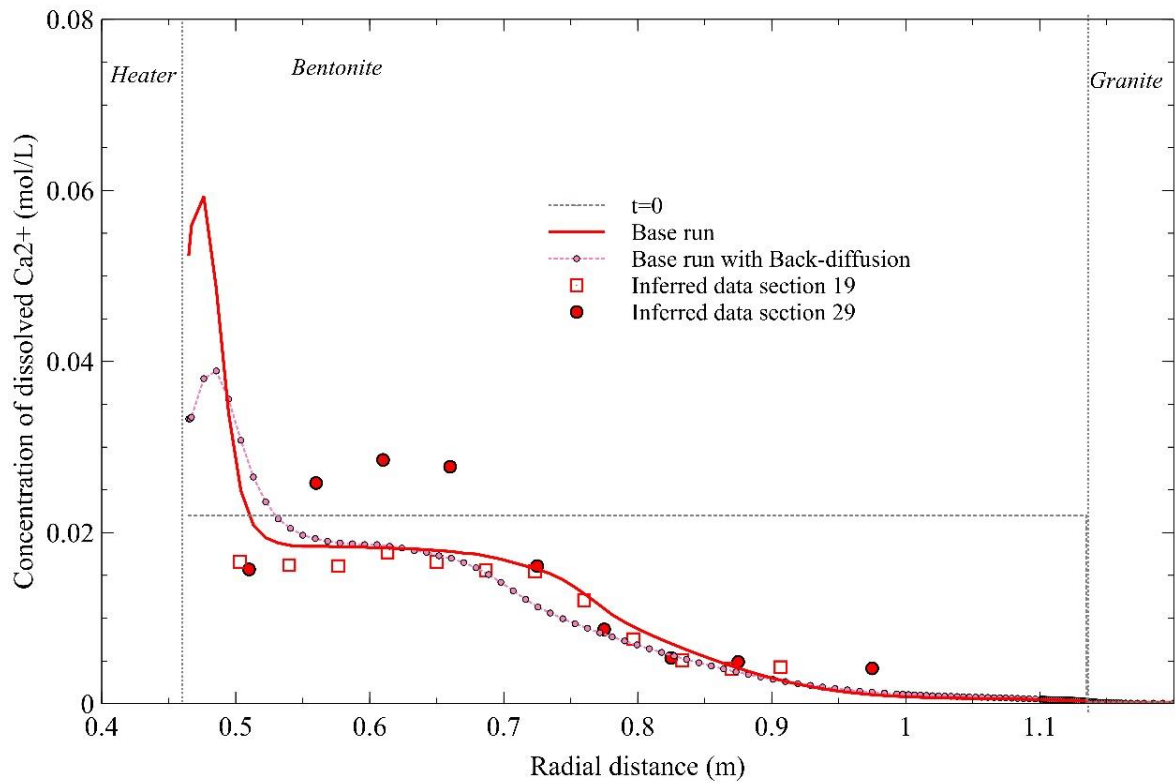


Figure 5-7). The effect of back-diffusion in the computed concentrations of dissolved  $\text{Ca}^{2+}$  in the bentonite was also important at the end of the 2<sup>nd</sup> operation period. The profile of the computed concentration of dissolved  $\text{Cl}^-$  at the end of the 2<sup>nd</sup> operation period with back-diffusion was flatter than the profile without back-diffusion. It can be concluded that solute back-diffusion from the bentonite into the granite affects the time evolution of the bentonite porewater composition, even near the steel-bentonite interface.

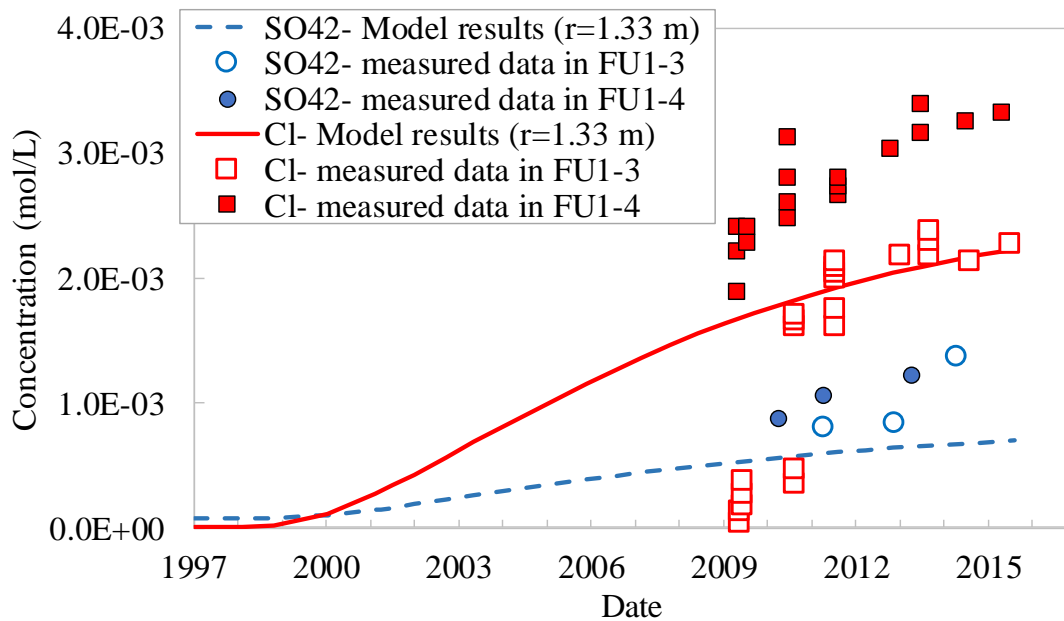


Figure 5-6 – Time evolution of the concentrations (lines) of dissolved  $\text{Cl}^-$  and  $\text{SO}_4^{2-}$  in the granite at a distance of 0.20 m from the bentonite/granite interface computed with revisited model with solute

back-diffusion. The measured concentrations of dissolved  $\text{Cl}^-$  and  $\text{SO}_4^{2-}$  in sections FU1-3 and FU1-4 of the FU1 borehole after 2009 (symbols) were taken from Buil et al. (2010) and Garralón et al. (2018).

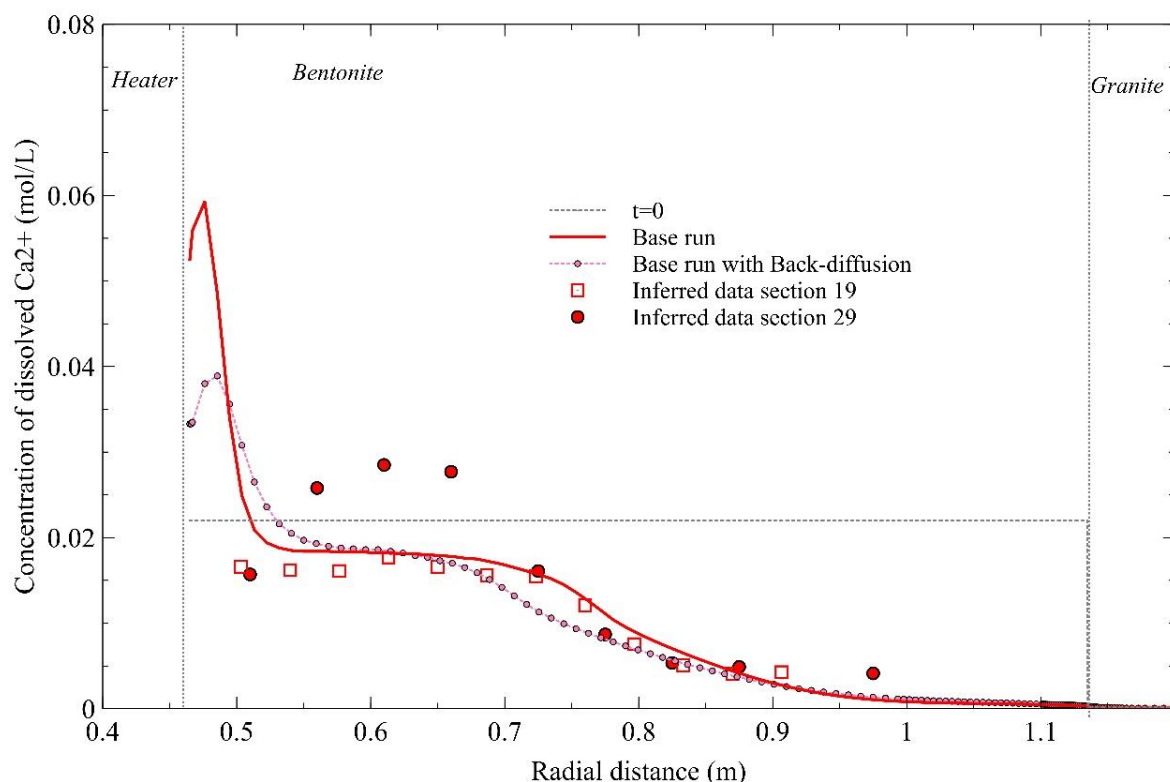


Figure 5-7 – Radial distribution of the computed concentration of dissolved  $\text{Ca}^{2+}$  at the end of the 1st operation period of the FEBEX in situ experiment for the base run of the model with and without solute back-diffusion. The pore water concentration data inferred from aqueous extracts in sections 29 and 19 were taken from Zheng et al. (2011).

Samper et al. (2018b) performed sensitivity analyses of the geochemical predictions of the state of the barrier at the end of the 1<sup>st</sup> operation period, i.e. after 5 years of operation and concluded that: 1) The computed concentrations of dissolved species are sensitive to an increase in the parameter  $\alpha$  of the van Genuchten retention curve of the bentonite (linked to the air-entry pressure). The increase in  $\alpha$  led to larger water evaporation rates and slightly larger solute concentrations; 2) The dissolved concentrations were less sensitive to smectite dissolution; 3) The computed concentrations of dissolved  $\text{Ca}^{2+}$ ,  $\text{K}^+$ ,  $\text{Mg}^{2+}$ ,  $\text{Na}^+$  and  $\text{Cl}^-$  near the heater increased when the vapour tortuosity decreased. The concentrations far from the heater, however, decreased when the vapour tortuosity decreased; and 4) The computed concentration profiles along the radius of the barrier for  $\text{Ca}^{2+}$ ,  $\text{K}^+$ ,  $\text{Mg}^{2+}$ ,  $\text{Na}^+$  and  $\text{HCO}_3^-$  became smoother when the diffusion coefficients of these ions in the bentonite were increased by a factor of 10. The pH and the dissolved concentrations of  $\text{Cl}^-$  and  $\text{SO}_4^{2-}$  were less sensitive to the change in the diffusion coefficients because their diffusion coefficients were smaller than those of the rest of the species. The results of this sensitivity run show that the diffusive transport is less relevant than other hydrodynamic and transport processes when  $D_e$  is smaller than a threshold diffusion coefficient, which was estimated to be within the interval  $(6.1 \cdot 10^{-12} - 6.1 \cdot 10^{-11}) \text{ m}^2/\text{s}$ .

### 5.4.3 Model calibration

The revisited THCM model of the FEBEX in situ test performed by Samper et al. (2018b) was tested with gravimetric water content data measured after dismantling heater 1 in 2002 and heater 2 in 2015 and on line data of temperature and volumetric water content in the bentonite and pore water pressure in the granitic rock collected from 2002 to 2015. The numerical model reproduced the main trends of the temperature data. The computed temperatures near the bentonite/granite interface were lower than the measured temperatures during the first 2000 days and higher than the measured temperatures after 2000 days. The computed temperature at the bentonite/granite interface at the end of the 2<sup>nd</sup> operation period was 3°C higher than the measured temperature. This discrepancy could be overcome by revising the formulation used in the model to relate the thermal conductivity of the bentonite with liquid water saturation. The computed volumetric water contents reproduced the general trends of the measured data. The predicted gravimetric water contents and dry densities at the end of the 1<sup>st</sup> (2002) and 2<sup>nd</sup> (2015) operation periods were within the range of the measured data and generally matched the trends of the measured data. The predicted dry densities were within the range of the measured data which show a large scatter in both operation periods.

When the corrosion processes will be implemented into the THCM model of the FEBEX in situ test, the model will be calibrated with the following measured data:

- 1) Aqueous extract data.
- 2) Cation exchange data.
- 3) Mineralogical observations.
- 4) Thickness and composition of the corrosion layer.
- 5) Thickness and composition of the red/orange and blue (Fe poor) zones.

## 5.5 First results and discussion

The previous THMC models of the FEBEX in situ test performed by UDC (Samper et al., 2018b) considered neither iron corrosion nor redox reactions. Work is in progress to extend the previous THCM model of Samper et al. (2018b) to account for redox processes, steel corrosion and the interactions of corrosion products and compacted FEBEX bentonite. No results are yet available. Here we report the main results of the THMC model of the FEBEX in situ test performed by Samper et al. (2018b).

The computed concentrations of dissolved Cl<sup>-</sup> at the end of the 2<sup>nd</sup> operation period (2015) with the revisited model of Samper et al. (2018b) are high near the heater due to the evaporation of the bentonite pore water and small at the granite/bentonite interface due to the hydration of the buffer with granite pore water, which has a smaller Cl concentration than the bentonite pore water and also to a net movement of the dissolved Cl<sup>-</sup> with the incoming water towards the internal part of the barrier. The predicted concentrations of dissolved Cl<sup>-</sup> at the end of the 2<sup>nd</sup> operation period (2015) showed a pattern similar to that of the computed concentrations at the end of the 1<sup>st</sup> operation period (2002), but were much smaller than those of 2002 (Figure 5-8). Model geochemical predictions at the end of the 2<sup>nd</sup> period were tested with measured Cl<sup>-</sup> data from Fernández et al. (2018). The concentrations of dissolved Cl<sup>-</sup> predicted with the revisited model reproduced the sharp increase of the measured Cl<sup>-</sup> data near the heater. The predicted concentrations matched the data measured in 5 out of 6 radial locations. The data at  $r = 0.6$  m were underestimated, possibly due to uncertainties in the diffusion coefficient (Figure 5-8).

The model predictions at the end of the 2<sup>nd</sup> period for other dissolved, precipitated and exchanged species will be tested in future studies.

Mineral dissolution/precipitation and cation exchange reactions affect the dissolved concentrations of the reactive species. The predicted concentrations of dissolved cations such as Na<sup>+</sup> and K<sup>+</sup> at the end of the 2<sup>nd</sup> operation period (2015) were also high near the heater and decreased towards the bentonite/granite interface (Figure 5-9 and Figure 5-10).

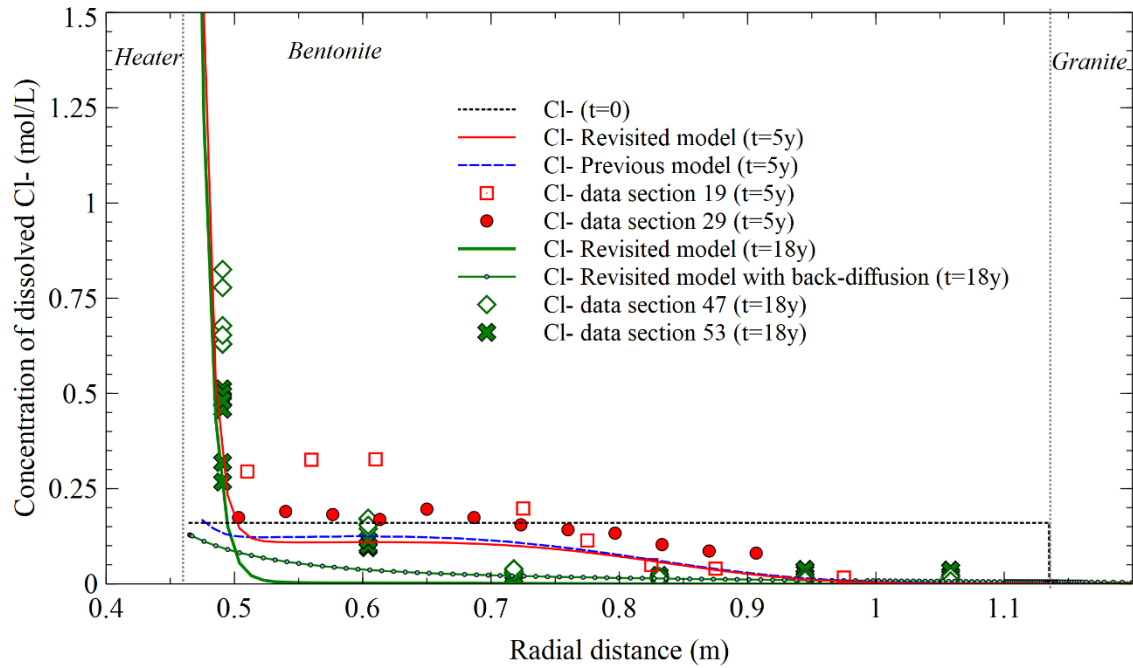


Figure 5-8 – Radial distribution of: 1) The concentrations of dissolved Cl<sup>-</sup> at the end of the 1<sup>st</sup> operation period (5 y) computed with the revisited model and the previous model of Zheng et al. (2011) and the pore water concentration data inferred from aqueous extracts in sections 19 (squares) and 29 (circles) from Zheng et al. (2011); and 2) The concentrations of dissolved Cl<sup>-</sup> at the end of the 2<sup>nd</sup> operation period (18 y) computed with the revisited model without and with solute back-diffusion and the pore water concentration data inferred from aqueous extracts in sections 47 (diamonds) and 53 (crosses) from Fernández et al. (2018).

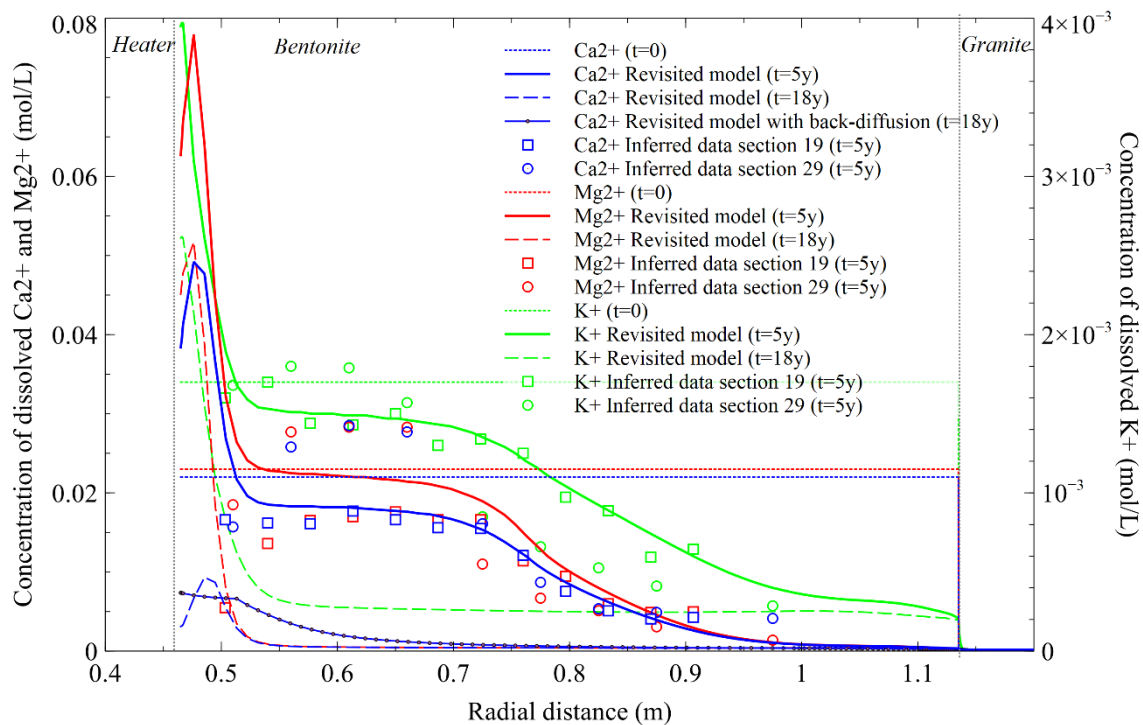


Figure 5-9 – Radial distribution of the computed concentrations of dissolved Ca<sup>2+</sup> and Mg<sup>2+</sup> (left axis) and K<sup>+</sup> (right axis) at the end of the 1<sup>st</sup> (2002) (continuous lines) and 2<sup>nd</sup> operation period (2015) (discontinuous lines). The pore water concentration data inferred from aqueous extracts in sections 19 (squares) and 29 (circles) were taken from Zheng et al. (2011). The concentrations of dissolved Ca<sup>2+</sup>

at the end of the 2<sup>nd</sup> operation period were computed with the revisited model without and with solute back-diffusion.

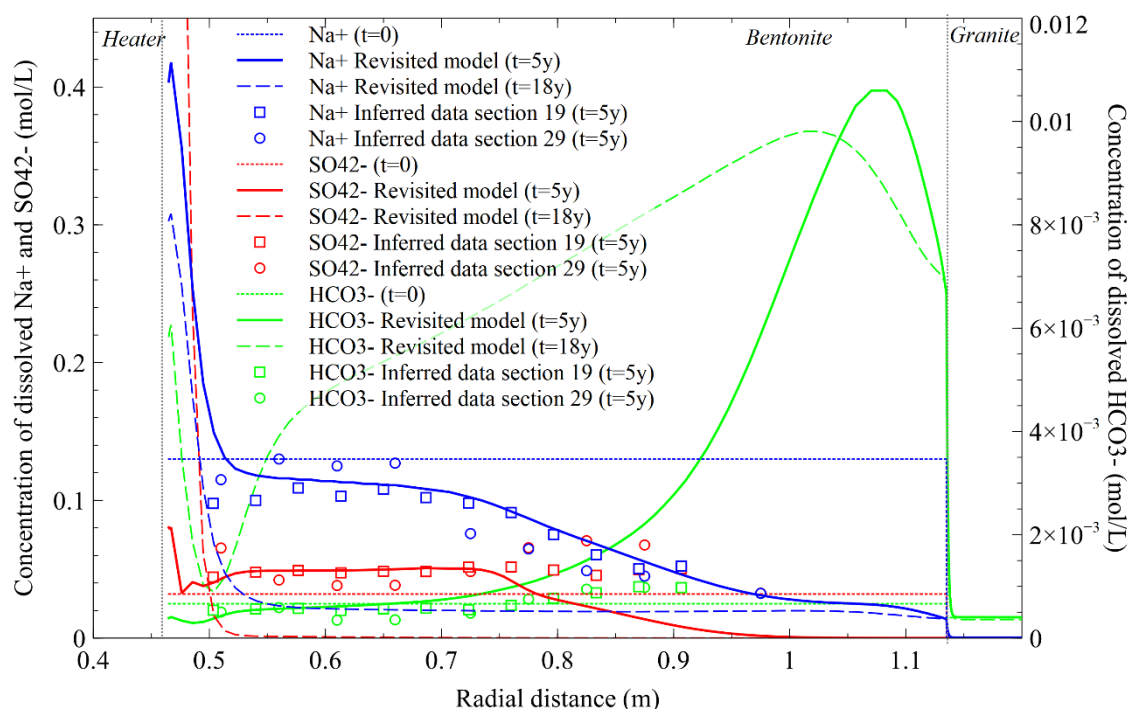


Figure 5-10 – Radial distribution of the computed concentrations of dissolved  $\text{Na}^+$  and  $\text{SO}_4^{2-}$  (left axis) and  $\text{HCO}_3^-$  (right axis), the end of the 1<sup>st</sup> (2002) (continuous lines) and 2<sup>nd</sup> operation periods (2015) (discontinuous lines). The pore water concentration data inferred from aqueous extracts in sections 19 (squares) and 29 (circles) were taken from Zheng et al. (2011).

The solubility of calcite decreases with increasing temperature. Therefore, calcite was expected to precipitate near the heater. Water evaporation also promoted calcite precipitation near the heater. However, model results showed that there was a thin band near the heater where calcite dissolved. This unexpected result was due to the precipitation of anhydrite. The large precipitation of anhydrite in the interval  $0.465 \text{ m} < r < 0.481 \text{ m}$  led to: 1) The dissolution of calcite (Figure 5-11); 2) The release of exchanged  $\text{Ca}^{2+}$  and  $\text{Mg}^{2+}$  which exchanged with dissolved  $\text{Na}^+$  and  $\text{K}^+$  (not shown here); and 3) The decrease of the dissolved concentrations of  $\text{Ca}^{2+}$  and  $\text{Mg}^{2+}$  (Figure 5-9). Model results showed also a second zone within the interval  $0.481 \text{ m} < r < 0.53 \text{ m}$  where calcite and gypsum precipitated instead of anhydrite. Exchanged  $\text{Ca}^{2+}$  in this zone was released from the cation exchange complex and exchanged mostly with dissolved  $\text{Mg}^{2+}$ . The largest concentrations of dissolved  $\text{Ca}^{2+}$  and  $\text{Mg}^{2+}$  in the bentonite occurred within this zone.

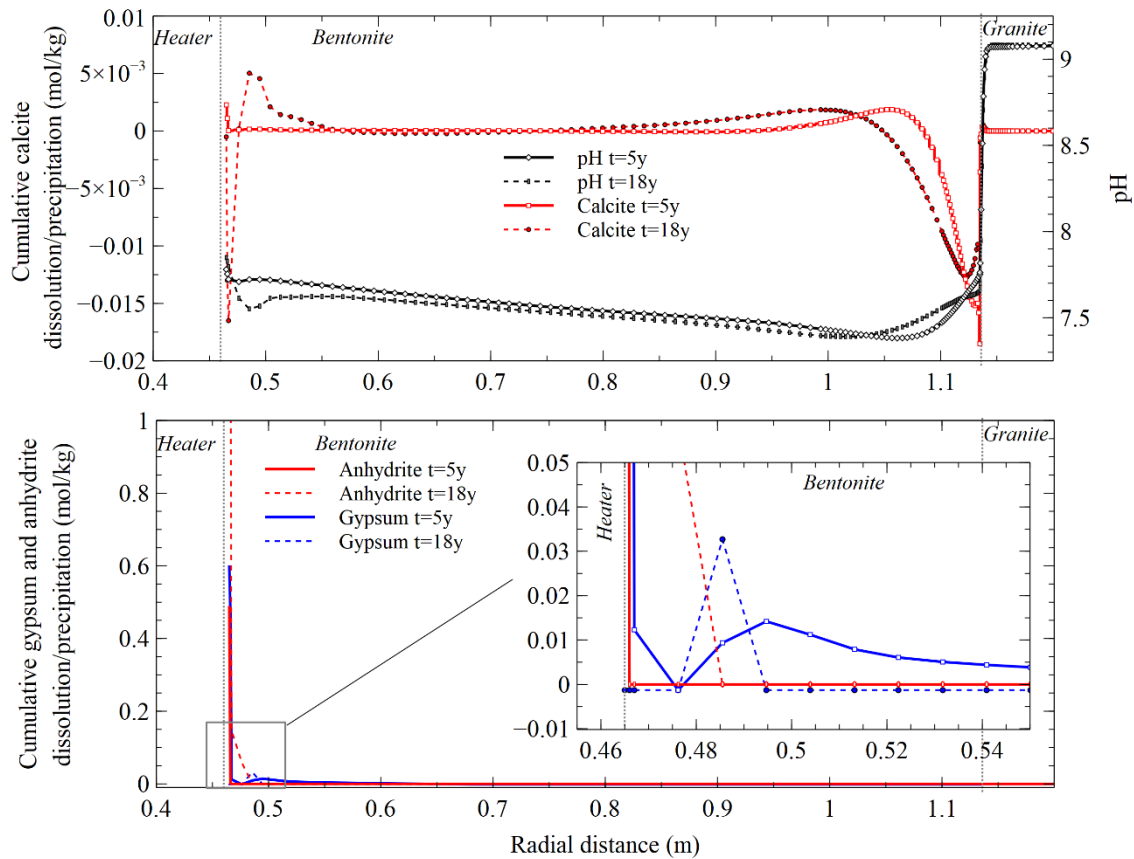


Figure 5-11 – Radial distribution of: 1) The computed cumulative dissolution/precipitation of calcite and pH at the end of the 1<sup>st</sup> (2002) and 2<sup>nd</sup> operation periods (2015) (top plot); and 2) The computed cumulative dissolution/precipitation of anhydrite and gypsum at the end of the 1<sup>st</sup> (2002) and 2<sup>nd</sup> operation periods (2015) (bottom plot). Positive for mineral precipitation and negative for mineral dissolution.

The model predictions showed that the concentrations of dissolved  $\text{SO}_4^{2-}$  in 2015 increased near the heater and decreased in the rest of the bentonite barrier compared to the computed concentration of dissolved  $\text{SO}_4^{2-}$  in 2002 (Figure 5-10).

The predicted concentrations of dissolved  $\text{HCO}_3^-$  were linked to the concentrations of dissolved  $\text{Ca}^{2+}$  and the dissolution/precipitation of calcite and sulphate minerals. The hydration of the bentonite with granite water induced the dissolution of calcite near the bentonite/granite interface. Consequently, the computed concentration of dissolved  $\text{HCO}_3^-$  increased near the bentonite/granite interface (Figure 5-10). There was a front of high concentrations of dissolved  $\text{HCO}_3^-$ , which diffused through the bentonite causing calcite precipitation and a decrease of pH. This was attested by the low pH computed near the granite/bentonite interface (Figure 5-11). Model predictions showed that the concentration of dissolved  $\text{HCO}_3^-$  in 2015 increased compared to the concentration in 2002 in most of the bentonite barrier due to the calcite dissolution front. The concentration of dissolved  $\text{HCO}_3^-$  increased in a thin band near the heater ( $0.465 \text{ m} < r < 0.481 \text{ m}$ ) where calcite dissolved and decreased within the interval  $0.481 \text{ m} < r < 0.53 \text{ m}$  where calcite precipitated (Figure 5-11).

The evolution of the computed pH in the bentonite was the result of the combined effect of several chemical reactions. The pH was mostly buffered by surface protonation reactions and calcite dissolution/precipitation. The results in Figure 5-11 attested the close linking between the computed pH and calcite dissolution/precipitation. The predicted pH at the end of the 2<sup>nd</sup> operation period (2015) changed slightly with respect to the pH computed at the end of the 1<sup>st</sup> operation period (2002). There are uncertainties in the prediction of the pH of bentonite pore water due to  $\text{CO}_2(\text{g})$  degassing from the

liquid phase which was not taken into account in the model. The  $\text{CO}_2(\text{g})$  released near the heater could migrate through the gas phase and redissolve in the condensation zone.  $\text{CO}_2(\text{g})$  degassing and dissolution could affect the pH, the concentration of dissolved  $\text{HCO}_3^-$  and calcite dissolution and precipitation.

Anhydrite, which was not initially present in the bentonite, precipitated near the heater because anhydrite is more stable (lower solubility) than gypsum for temperatures above a threshold temperature ranging from  $43^\circ$  to  $56^\circ$  C which depends on the chemical composition and salinity of the pore water (Blount and Dickson, 1973). Anhydrite precipitated near the heater in a 32 cm thick zone at the end of the 1<sup>st</sup> operation period. Most of the anhydrite previously precipitated transformed into gypsum after the switching off the heater. This transformation was quick because the model assumes chemical equilibrium for these two mineral phases. Some anhydrite remained precipitated near the heater only in a thin band of 1 mm thickness (Figure 5-11). The thickness of the band of the precipitated anhydrite was only 3 cm at the end of the 2<sup>nd</sup> operation period. Some of the precipitated anhydrite transformed into gypsum during the cooling stage of 2015. After cooling, anhydrite remained precipitated near the heater only in a 2 cm thick band (Figure 5-11). A small amount of gypsum dissolved initially in the bentonite because the initial bentonite pore water was not at equilibrium with this mineral. This mineral remained inactive during the heating stages of the experiment. Gypsum precipitated near the heater in a 17 cm thick zone after the cooling of the 1<sup>st</sup> operation period and precipitated within the interval  $0.475 \text{ m} < r < 0.495 \text{ m}$  after the cooling of the 2<sup>nd</sup> operation period (Figure 5-11).

## 6. Corrosion model of the steel bentonite interaction in the FEBEX in-situ experiment – UniBern approach

This chapter presents the progress made in the development of the steel-bentonite interaction model by University of Bern. As UDC, UniBern uses in a first step the findings from the FEBEX in-situ experiment, which provide a valuable dataset for model validation. The overall goal of this model development is to improve the modelling capabilities of complex coupled Fe corrosion and Fe-clay interaction within the numerical codes used already for reactive transport models within the context of safety analysis.

Chapters 6.2, 6.3 6.4 provide details on the modelling approach, conceptual model and numerical model, respectively for both, the general THC model for the FEBEX in-situ test and the specific implementation of the steel corrosion and interface processes. Chapter 6.5 presents some first preliminary results of the newly developed FEBEX-THC and corrosion model.

### 6.1 The FEBEX in-situ experiment

A description of the FEBEX in-situ experiment is provided in section 5.1.

### 6.2 Proposed modelling approach

A reactive transport model is under development, which includes chemical processes and their coupling to thermo-hydraulic processes. The model builds on our previous and current efforts in the development of a reactive transport model for clay barriers and their interaction with other material components. The powerful simulator PFLOTRAN ([www.pflotran.org](http://www.pflotran.org)), an open source, massively parallelised subsurface flow and reactive transport code, is used for numerical implementation. The ANDRA/Thermochemie Database v9.b (Giffaut et al., 2014; Grivé et al., 2015) is used for the calculation of aqueous reactions.

In a first step, the conceptual model is developed based on the recent phenomenological model for Fe corrosion and Fe-bentonite interaction in particular for the FEBEX case published by Hadi et al. (2019) (see Figure 5-4). In a second step, the model will be applied in an iterative way to the conditions encountered in the FEBEX experiment. The obtained profiles for Fe and other elements will be compared with the measured data. In a third step, the model will be refined based on this comparison as well as findings from the Fe(II) experiment (chapter 3).

### 6.3 Conceptual Model

#### 6.3.1 Objectives of the Model

The main objective of the Febex model under development is to improve the understanding of steel/bentonite interactions observed within the in-situ experiments. In this respect, the model should provide deeper insights in the process postulated by Hadi et al. (2019) and strive towards a quantitative description of those. The model once developed for FEBEX should also be adaptable for the description of other experiments, such as ABM1 and ABM2, the in-situ tests at Äspö Hard Rock Laboratory (S). An integral part of the model should be the evaluation of the initial oxic stage with its transition to anoxic conditions and of the coupled sorption and redox reaction of Fe (II) from the corrosion process and structural Fe in the clay.

Finally, the development of the experiment specific model should improve the capability to model coupled Fe corrosion and Fe–clay interaction and thus contribute to the current efforts to develop comprehensive reactive transport models for clay barriers in the near field of HLW repository settings.

#### 6.3.2 Processes to be modelled

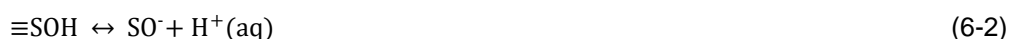
The conceptual model of Fe-release by corrosion and interaction with smectite is based on the phenomenological model developed by Hadi et al. (2019). Furthermore, chemical processes and their

coupling to thermo-hydraulic processes need to be included in order to allow for a realistic description of the total system in its temporal evolution. Thus, the key processes to be included in the model are:

- Saturation of the initially unsaturated bentonite with groundwater
- Development of a temperature gradient from the heater to the host rock
- Fe-release by aerobic corrosion of steel in the initial stages due to the presence of O<sub>2</sub> in the residual porewater and gas phase. Transition to anaerobic corrosion upon depletion of O<sub>2</sub>. The corrosion process in both stages is defined as:



- Aqueous chemistry of main solutes (Fe, Na, Ca, Mg, Cl, C<sub>inorg</sub>, sulfate) considering 46 primary and secondary aqueous species. Furthermore, the partitioning of H<sub>2</sub>(g), O<sub>2</sub>(g) and CO<sub>2</sub>(g) in the gas phase needs to be included. Chemistry of K is not yet implemented but will be added in a next stage of model refinement.
- Mineral dissolution and precipitation reactions of the most important corrosion products (goethite and magnetite), calcite, gypsum and hematite. Hematite and magnetite were selected to control the Eh of the granitic porewater as suggested by Wilson (2017).
- Diffusion of solutes in bentonite and rock porewater and diffusion of H<sub>2</sub>(g), O<sub>2</sub>(g) and CO<sub>2</sub>(g) in the gas phase
- Protonation and de-protonation reactions of the montmorillonite edge sites contributing to pH buffering, according to

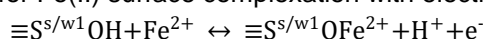


Where S indicates a generic surface sorption site (strong, weak1, weak2) on montmorillonite.

- Cation exchange involving Na, Fe, Ca, Mg. The Gaines-Thomas convention is used for the formulation of the cation-exchange reaction.
- Fe(II) surface complexation reactions on strong and weak1 sites of montmorillonite without electron transfer



- Sorption of Fe(II) on montmorillonite and transfer of an electron to the structural Fe(III) of montmorillonite. At the present stage of the modelling, the formulation of Soltermann et al. (2014) for Fe(II) surface complexation with electron release is adopted:



(6-5)

It should be noted that in the next model refinements, the experience gained from the experimental work (Chapter 3) and its modelling will be used to account explicitly for the alteration of montmorillonite.

### 6.3.3 Important assumptions, simplifications, limitations

Main assumptions and simplifications underlying the geochemical and transport model are:

- All aqueous reactions, exchange reactions, surface protonation/de-protonation and surface complexation reactions assume chemical equilibrium.
- Reaction constants in the Thermochemie database do not include temperature dependent data for all species, in such cases constants at standard temperature are applied over the whole temperature range.
- A simplified mineral composition of the Febex bentonite is assumed, including montmorillonite and traces of calcite and gypsum. Montmorillonite is considered inert, thus remaining constant in volume over time.
- Mineralogy of the granite is not specified explicitly, apart from the presence of calcite and of magnetite and hematite for redox-control.

- Calcite, gypsum, goethite, hematite and magnetite are allowed to precipitate in all compartments, but this does not induce a porosity change. At present, mineral kinetics are implemented based on mineral dissolution rates reported by Palandri and Kharaka (2004), thus porewaters are not necessarily in equilibrium with the above listed mineral phases.
- Saturation of the granite porespace does not go below 90%.
- Solute transport occurs in a single porosity, with all solutes exhibiting the same diffusion coefficient.
- A 1D cartesian grid is selected, thus ignoring the radial geometry of the experiment. No influx or outflow of atmospheric oxygen from the model domain is assumed.

Regarding the “Corrosion and Fe-montmorillonite interaction model”, the following simplifications were made:

- A 1 mm thick “steel\_reactive” compartment was defined, which exhibits a porosity of 50 % to allow for interaction of steel and porewater and represents corrosion at the steel surface.
- The aerobic corrosion follows first order kinetics with respect to  $O_2(aq)$ . Anaerobic corrosion is constant over the entire calculation period.

#### 6.3.4 Boundary Conditions

The left boundary of the 1-D system is placed at the interface (IF) from the reactive steel to inert steel. It is defined as a no-flow and zero-gradient boundary. A constant temperature of 97°C was prescribed for the entire calculation time.

The right boundary is set 50 m into the rock. It is defined as Dirichlet type boundary with a granite porewater composition, a constant temperature of 12°C and a liquid pressure of 700 kPa.

#### 6.3.5 Initial conditions / parameters

The initial composition of the FEBEX and granite porewaters, the considered mineral phases and the initial composition of the cation exchange are listed in Table 6-1. The initial composition of the porewater in the reactive steel is set identical to the FEBEX porewater, but devoid of any initial oxygen. The initial temperature in both, the bentonite and granite, is uniform and set to 12°C.

For the FEBEX bentonite, a dry density of 1600 kg/m<sup>3</sup> is used, which corresponds to a total porosity of 0.41. The initial liquid saturation degree is set to 0.59, which equals a volumetric and gravimetric water content of 24.2% and 15.1%, respectively. The retention curve of the bentonite is described by a van Genuchten function, using the parameters reported by Enresa (2000) for a FEBEX dry density of 1.6 to 1.65 g/cm<sup>3</sup>. Appendix B provides the parameterization and a visual comparison of the applied retention curve with the more recent experimental work of Lloret and Villar (2007) and Sánchez et al. (2010). The initial gas pressure is set to 100 MPa following (Samper et al., 2018b).

The granite has a porosity of 0.01 and is initially fully saturated. The liquid residual saturation is set to 0.9. Further hydrodynamic and thermal parameters of the steel, bentonite and granite are summarized in Table 6-2. Parameterization of cation exchange and sorption reactions are listed in Table 6-3.

Table 6-1 – Initial conditions of FEBEX and granite porewaters, mineralogy and exchanger composition as used in the model.

Parameter	Unit	FEBEX	Granite	Reference
<b>Initial porewater composition</b>				
pH		7.72	8.35	(Samper et al., 2018b; Zheng et al., 2011) based on (Enresa, 2000)
Na <sup>+</sup>	[mol/l]	1.3E-01	3.8E-04	
K <sup>+</sup>	[mol/l]	1.7E-03	7.8E-06	
Ca <sup>2+</sup>	[mol/l]	2.3E-02	1.8E-04	
Mg <sup>2+</sup>	[mol/l]	2.3E-02	1.3E-06	
Cl <sup>-</sup>	[mol/l]	1.6E-01	1.3E-05	
CO <sub>3</sub> <sup>2-</sup>	[mol/l]	4.1E-04	3.9E-04	
SO <sub>4</sub> <sup>2-</sup>	[mol/l]	4.4E-03	7.9E-05	
log pO <sub>2</sub>		-0.68	-72	Bentonite: atmospheric, Granite controlled by hematite/magnetite equilibrium
<b>Initial volume fractions of reactive minerals</b>				
Smectite	[% vol]	5.5E-01	0	FEBEX: corresponds to 92 wt%
Calcite	[% vol]	5.9E-03	1.0E-02	Corresponds to 1 wt% in both
Gypsum	[% vol]	9.7E-04	0	Corresponds to 0.14 wt%
Goethite	[% vol]	0	0	
Hematite	[% vol]	0	1.0E-03	Trace amount for redox control
Magnetite	[% vol]	0	1.0E-03	Trace amount for redox control
<b>Ion exchanger composition</b>				
Total CEC	[meq/kg]	959		(Fernández et al., 2004)
Na <sup>+</sup>	[meq/kg]	314		
Ca <sup>2+</sup>	[meq/kg]	287		
Mg <sup>2+</sup>	[meq/kg]	328		
K <sup>+</sup>	[meq/kg]	30		
<b>Surface site capacities</b>				
≡S <sup>s</sup> OH	[mol/kg]	1.84E-03		Based on (Bradbury and Baeyens, 1997) for montmorillonite
≡S <sup>w1</sup> OH	[mol/kg]	3.68E-02		
≡S <sup>w2</sup> OH	[mol/kg]	3.68E-02		

Table 6-2 – Hydrodynamic and thermal parameters of steel, bentonite and granite

Parameter	Unit	Reactive steel	FEBEX	Granite	Reference
Porosity	[-]	(0.5)*	0.41	0.01	(Samper et al., 2018; Zheng et al., 2011) based on (Enresa, 2000)
Solid density	[kg/m <sup>3</sup> ]	7860	2780	2700	
Permeability	[m <sup>2</sup> ]	3.75E-21	3.75E-21	8E-18	
Tortuosity	[-]	0.1	1.5E-2	4.4E-3	
D <sub>e</sub>	[m <sup>2</sup> /s]	5E-11 <sup>‡</sup>	6.1E-12	4.4E-14	
Specific heat of solid	[J/kg*°C]	502	835.5	768	Steel: Engineers Edge (2020a, b) FEBEX: Samper et al. (2018) Granite/ air: Kant et al. (2017) Liquid: Funabiki et al. (2014)
Thermal conductivity of solid	[W/K*m]	45	1.23	3.247	
Thermal conductivity air	[W/K*m]		2.7E-2		
Thermal conductivity liquid	[W/K*m]		0.6		
Thermal conductivity dry	[W/K*m]	45	0.257	3.095	Remark: Thermal conductivity of dry and saturated FEBEX bentonite calculated with the parameterization does not really fit experimental data and will be re-evaluated in the next steps of model development.
Thermal conductivity saturated	[W/K*m]	45	0.916	3.193	

\* porosity is a model requirement to allow for solid-aquous interaction and set arbitrarily to 0.5. It is not considered a physical parameter.

‡ Fast diffusion selected for rapid homogenization

Table 6-3 – Parameterization of site types, site capacities, protolysis constants and sorption parameters as considered in the Base Case

Surface complexation reaction	Log K	Reference
$\equiv S^{s/w1}OH \leftrightarrow S^{s/w1}O^- + H^+(aq)$	-7.9	Bradbury and Baeyens (1997)
$\equiv S^{s/w1}OH + H^+(aq) \leftrightarrow S^{s/w1}OH_2^+$	4.5	
$\equiv S^{w2}OH \leftrightarrow S^{w2}O^- + H^+(aq)$	-10.5	
$\equiv S^{w2}OH + H^+(aq) \leftrightarrow S^{w2}OH_2^+$	6.0	
$\equiv S^sOH + Fe^{2+} \leftrightarrow \equiv S^sOFe^+ + H^+$	1.9	Soltermann et al. (2014) for Fe rich montmorillonite (SWy-2)
$\equiv S^{w1}OH + Fe^{2+} \leftrightarrow \equiv S^{w1}OFe^+ + H^+$	-1.7	
$\equiv S^sOH + Fe^{2+} \leftrightarrow \equiv S^sOFe^{2+} + H^+ + e^-$	-1.4	
$\equiv S^{w1}OH + Fe^{2+} \leftrightarrow \equiv S^{w1}OFe^{2+} + H^+ + e^-$	-3.8	
Cation exchange reaction	Log $K_{sel-GT}$	
$K^+ + NaX \leftrightarrow KX + 2 Na^+$	0.86	Samper et al. (2018b)
$Ca^{2+} + 2 NaX \leftrightarrow CaX_2 + 2 Na^+$	0.53	
$Mg^{2+} + 2 NaX \leftrightarrow MgX_2 + 2 Na^+$	0.64	
$Fe^{2+} + 2 NaX \leftrightarrow FeX_2 + 2 Na^+$	0.80	Soltermann et al. (2014)

Steel corrosion is considered with two parallel running process:

- Aerobic corrosion, which is defined to be of first order kinetics with respect to  $O_2(aq)$ . In the Base Case, a rate constant of  $5E-4 \text{ mol}/(\text{m}^2 \cdot \text{sec})$  is selected. At atmospheric  $pO_2$  this equals approximately  $15 \mu\text{m}/\text{year}$ .
- Anaerobic corrosion with a constant rate of  $4.46E-9 \text{ mol}/(\text{m}^2 \cdot \text{sec})$ . This equals  $1 \mu\text{m}/\text{year}$ .

## 6.4 Numerical model

### 6.4.1 Spatial and temporal discretization

The model domain is a 1D structured cylindrical grid, with 1 cell in the yz dimension and 281 cells of variable size in the x dimension. Smaller cell sizes are selected for the interface regions, while cells of up to 1 m are selected for the granite (Table 6-4). The grid includes zones for the heater and inert steel, which are however inactive at the present stage of modelling. A separate EDZ zone is implemented, which has the same parameterization as the rock so far. The grid extends 50 m into the rock.

Table 6-4 – Spatial discretization of the FEBEX model. Thick black lines indicate the active model domain boundaries. The regions HEATER\_INERT and STEEL\_INERT are inactive, the EDZ has the same initial conditions and parameterization as the rock.

	Cells: n	cell size	total	total	distance from IF	distance from center
		[m]	[mm]	[m]	[m]	[m]
HEATER_INERT	1	0.47	470	0.470	-0.470	0.470
STEEL_INERT	14	1E-03	14	0.014	-0.014	0.484
STEEL_REACTIVE	10	1E-04	1	0.001	-0.001	0.485
FEBEX	20	1E-03	20	0.020	0.020	0.505
	10	2E-03	20	0.020	0.040	0.525
	20	5E-03	100	0.100	0.140	0.625
	100	5E-03	500	0.500	0.640	1.125
	10	1E-03	10	0.010	0.650	1.135
EDZ	10	1E-03	10	0.010	0.660	1.145
ROCK	4	1E-02	40	0.04	0.700	1.185
	9	5E-02	450	0.45	1.150	1.635
	15	1E-01	1500	1.5	2.650	3.135
	20	5E-01	10000	10	12.650	13.135
	38	1E+00	38000	38	50.650	51.135
<b>SUM</b>	<b>281</b>		<b>51135</b>	<b>51.135</b>		

### 6.4.2 Sensitivity analyses

In addition to the Base Case, the effect of a ten times slower anaerobic corrosion rate (Variant Case 1), a ten times slower aerobic corrosion rate (Variant case 2), and an increased goethite precipitation rate was tested. Further sensitivity analyses are foreseen for the future.

### 6.4.3 Model calibration

The corrosion model is still under development. No explicit model calibration has been performed so far. Some general geochemical, thermal and hydrodynamic results are crosschecked with reported data in literature however.

## 6.5 First results and discussion

First results regarding the hydrodynamic and thermal evolution of the FEBEX system as calculated with the present parameterization of the BASE CASE scenario are presented in Appendix B. Final calculated temperatures are 70-75°C in the centre of the bentonite and 59°C at the contact of FEBEX to the granite, thus in the range of temperatures reported for sections in the central part of heater 2 (Martinez et al., 2016). At a distance of 25 m into the granite, modelled temperatures drop below 20°C. Calculated final liquid saturation at the heater is 99%. This value is higher than the saturation of 85-90% measured by Villar et al. (2016) in sections of the central part of heater #2. In section 43 between heater #2 and the earlier dismantled heater #1, where temperatures remained below 88°C in the second operational phase, however full saturation was reached.

Figure 6-1 visualizes the evolution of Ca<sup>2+</sup> porewater concentrations with distance from the interface for different time steps. The same pattern is observed for most cations and anions (presented in Appendix B). The large concentration gradient between the initial saline residual porewater of the FEBEX bentonite and the dilute granite porewater saturating the bentonite results in a distinct concentration front moving into the bentonite upon progressing saturation. A significant alteration of the

granite porewater due to diffusion of solutes from bentonite into the granite however is predicted to be limited to the first few cm. This is because of the rapid mitigation of the concentration gradients at the interface between bentonite and rock upon advective inflow of groundwater in the unsaturated bentonite. At the steel-bentonite interface, computed solute concentrations show a distinct increase during the unsaturated phase, which however levels off upon saturation of the interface region. Calibration of computed concentration profiles with data inferred from the investigation of samples retrieved after dismantling of heater 1 (5 years) and heater 2 (18 years) is still pending. Comparison of our model results with the model and modelling results of UDC as presented in chapter 5 is foreseen once final calibration of thermal, hydraulic and transport parameters has been performed.

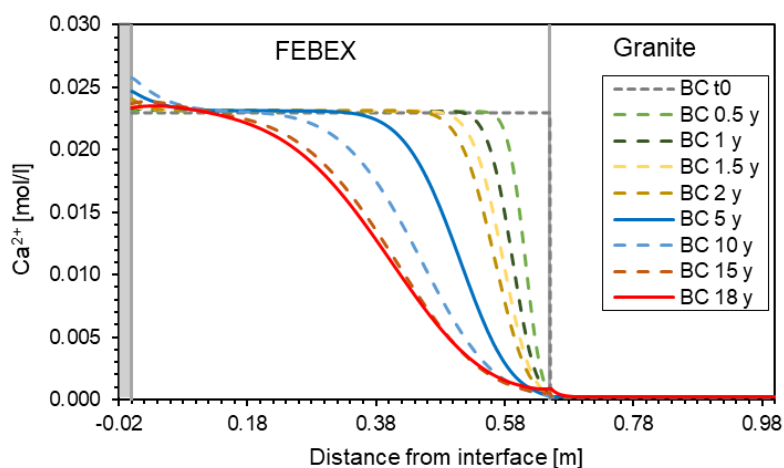


Figure 6-1 –  $Ca^{2+}$  concentration profiles in FEBEX and granite as computed for different times of the experiment (BASE CASE)

Figure 6-2 visualizes the computed evolution of the corrosion rate over time for the BASE CASE and the two variant cases with ten times slower anaerobic rate (Variant Case 1) and a ten times slower aerobic rate (Variant Case 2). The transition from aerobic to anaerobic corrosion is thus calculated to occur after 1.5 and 4 years for an initial corrosion rate of  $15 \mu\text{m/a}$  and  $2.5 \mu\text{m/a}$ , respectively. Note, that in the present model a 1D geometry is used, neglecting any increased  $O_2$  contribution due to the radial symmetry of the FEBEX packages or due to leakages in the experiment. In the present stage of the model development,  $H_2$  released during the anaerobic corrosion is included as a fully reactive species, thus leading to a rapid drop of  $p_e$  in the entire FEBEX bentonite due to the migration of  $H_2$  in the gas phase of the unsaturated bentonite.

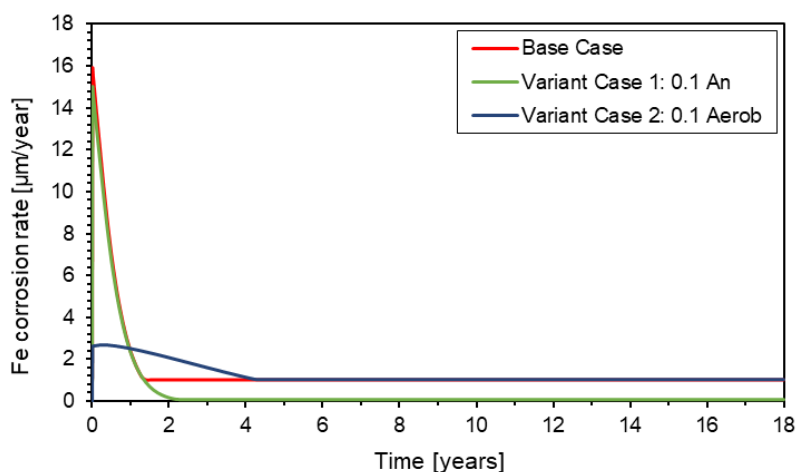


Figure 6-2 – Fe corrosion rates over time in the Base Case and Variant Case 1 and 2.

Figure 6-3 presents the different phases of steel corrosion and Fe migration as calculated with the Base Case model in its present stage of development. It also highlights some crucial points still under development. In the Base Case, goethite and magnetite mineral kinetics are constrained by the rate constants of Palandri and Kharaka (2004) for the mineral dissolution process. This rate is slow compared with the initial aerobic steel corrosion rate, thus allowing Fe to migrate several mm into the bentonite. A faster goethite precipitation rate or slower aerobic corrosion rate reduces the goethite precipitation front or entirely restricts it to the steel compartment (Figure 6-4). The high sensitivity Fe diffusion fronts due to the close interplay of Fe-corrosion and mineral precipitation rates is further illustrated in Figure 6-5, where total added Fe, goethite and Fe-sorption fronts of the three variant cases and the Base Case are compared. The slow magnetite precipitation kinetics considered at present restricts control of Fe concentrations by magnetite equilibrium in the anaerobic phase and thus results in high aqueous Fe concentrations in the steel porespace and a computed ongoing precipitation of goethite under anaerobic conditions. An instantaneous precipitation of magnetite until chemical equilibrium in the steel and clay porewater however would result in magnetite precipitation to become the dominant process in the anaerobic phase, rendering the Fe diffusion front rather short (data not shown). This would not be in line with the observations of Hadi et al. (2019), who did not detect significant amounts of magnetite. Thus, next steps in model development will focus on improving the description of goethite and magnetite precipitation kinetics and constraints, as one of the key controls on the Fe migration front.

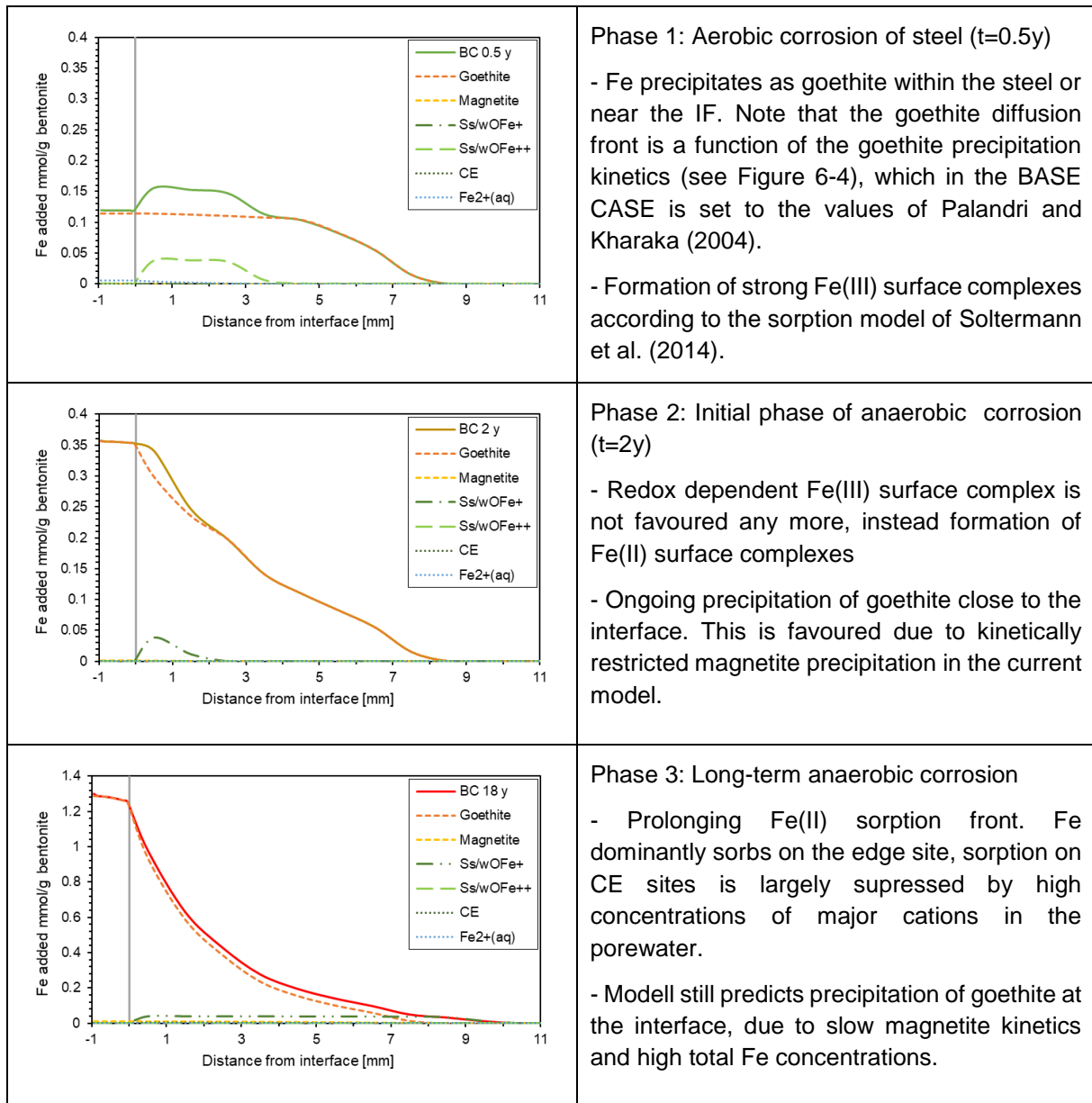


Figure 6-3 – Stages of steel corrosion and Fe diffusion as calculated for the present Base Case model. Note that the kinetics and control of goethite and magnetite precipitation are still under development.

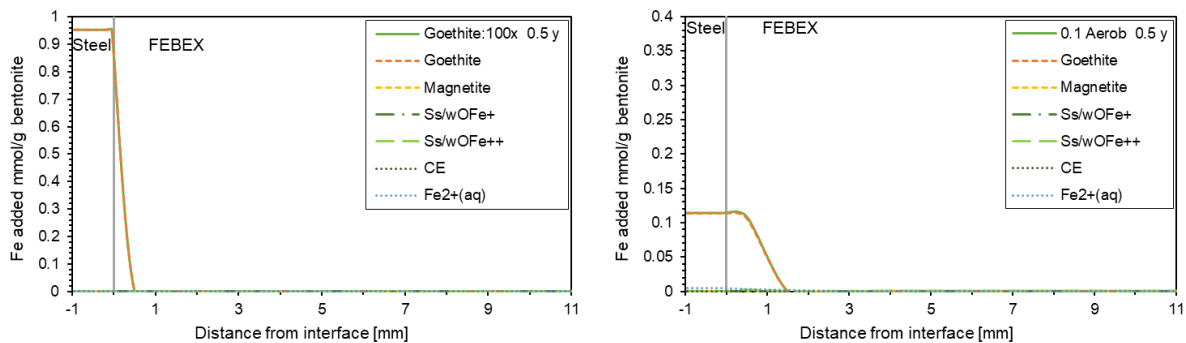


Figure 6-4 – Fe front after 0.5 years (aerobic corrosion phase) in case of a ~100 times faster goethite precipitation rate (left) or ten times slower aerobic corrosion rate (right) compared to the Base Case presented in Figure 6-3.

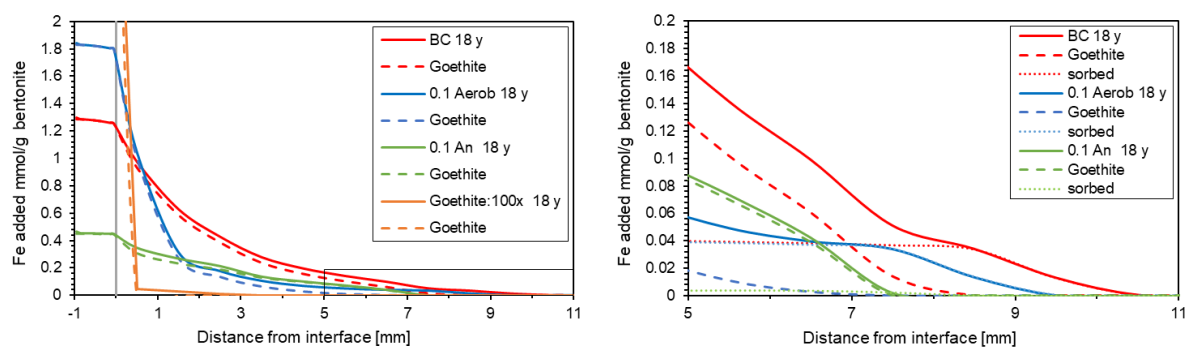


Figure 6-5 – Comparison of Fe fronts in the Base CASE and the three variant cases as calculated for  $t=18$  years. Solid lines indicate total Fe added for the cases indicated in the legend, dashed lines Fe in goethite only in the respective calculation case. The right figure is a blown up of the Fe-front marked by the rectangle in the left plot.

So far, no formulation of the redox transition of structural Fe in montmorillonite is included in the model. However, from the conceptual point of view this process is linked to Fe sorbing to edge and/or CE site. Thus, spatial extent and magnitude of montmorillonite alteration should be reflected by the Fe sorption front. This part of the model is directly linked to the experimental work on Fe(II)-bentonite interaction and its modelling (chapter 3) and will be implemented in the next stages. In this respect, it is also noted that Fe cation exchange parameterization is adopted from the work of Soltermann et al. (2014) determined for Na – Fe exchange on purified montmorillonite and thus not yet verified to be compatible with the FEBEX cation exchange parameterization for other cations implemented from Samper et al. (2018b). However, given the high concentrations of competing cations in the bentonite porewater in the interface region, cation exchange only plays a subordinate role for Fe sorption in the experiment and its parameterization is not expected to have a major impact on the calculated Fe diffusion front.

In summary, the first model results predict the development of a Fe front in the interface region dominated by goethite and to a minor extent magnetite close to the interface and Fe sorbed to clay minerals further into the bentonite. This general principal and the shape of the total accumulated Fe curve follows the observations of Hadi et al. (2019). Calculated distribution of Fe between mineral phases and sorption as well as the spatial extent of the diffusion front strongly varies depending on the selected kinetics of aerobic and anaerobic corrosion as well as mineral precipitation and dissolution kinetics. Elaboration of different variant cases with respect to these parameters as well as to saturation and redox evolution will thus help to understand different Fe profiles observed in the FEBEX experiment.

## 7. Steel – claystone interaction (MTA/SCK)

### 7.1 The MTA experiment

Boda Claystone Formation (BCF) is located in SW Hungary, to the west of the city of Pécs. The Permian, ca. 265 Ma old formation is known in an area larger than 150 km<sup>2</sup>. The recent 700–1000 m thick layers of BCF were settled in playa basin under extreme climatic inflow and geochemical conditions, and later they were buried to at least 3.5 to 4.5 km depth. The diagenesis of sediments occurred at high temperature (~150–200 °C) and at high pressure (120–150 MPa). The main lithology are albitic claystones and are highly indurated. It contains fractures and faults originating from a number of tectonic events.

Within this host rock, there is a formation ranging to 37 km<sup>2</sup> which has been identified as a potential disposal area in the depth of 500–900 m below the surface. In 2005, a preliminary safety assessment was carried out in order to judge the suitability of the host formation. This assessment was based on the data gathered on the exploration of the area before 2000. This assessment confirmed that low porosity, low permeability and high isotope retardation capability of BCF makes this candidate host rock suitable for the repository. However, it has to be stated that available information was not comprehensive and concepts behind the models were sometimes hypotheses.

The conceptual plan of the DGR was developed after the preliminary assessment. Assessments of inventory, heat load, packaging information, criticality and radiology were carried out to help designing DGR in the conceptual plan.

Hungarian final disposal concept was counting on copper overpack on the disposal casks and the layout of the disposal area where the final disposal of the casks would be placed into vertical disposal holes drilled on the bottom of the disposal tunnels, excavated in the Boda Claystone Formation. The concept of the encapsulation plant was based on the Swedish as well. The disposal tunnel system was planned 500–800 m below the surface, along with associated surface facilities. According the concept the surface and underground construction will be connected by vertical shafts. The disposal shafts will be connected to each other and the service area by ventilation ducts and utility piping. The development of the underground space will be performed by conventional drilling and cautious blasting methods. It is also assumed that for the large-section underground drifts, rock bolts and sprayed fibrous concrete lining with an average thickness of 10 cm, while for the small-section drifts (including the disposal drifts) rock bolts and a sprayed concrete lining 5 cm thick will be required.

Since there are numerous uncertainties such as lack of defined back-end strategy, thus inventory of the highly active residue of nuclear energy production, availability of suitable host rock formation, appropriate repository area, the main geometry and geological characteristics of the selected host area etc., the disposal concept is going to be revisited before each decision points. These revisions might result the changing of the original design, therefore we are fully committed to exploring new ideas, to improve suitable concept to serve our decision makers. We expect that results from the new experiments serve knowledge for a better understanding of the planned concept.

The STEEL-BCF experiment are focused on the steel/clay interaction, it comprises 1 new experiment with 3 units, which are planned to be taken out after 6, 9 and 12 months.

During the experiment an on line monitoring of the corrosion potential will be done. The post-mortem characterization will include:

- surface/morphology and elemental study by SEM/TEM
- mineralogy check by XRD and XRF methods
- water chemistry analysed by ICP
- porosity study using X, N-CT.

### 7.1.1 Experimental set up

The design of the experiment, the selected parameters of the BCF and the synthetic porewater are based on the following considerations:

Transport processes are anticipated to remain diffusion-dominated over geologic time frames (hundreds of thousands to millions of years)

- BCF has a self-healing capacity potential
- The weak sensitivity of hydraulic conductivity to changes in loading
- There are thick topset beds over the potential disposal zone and the uplift of W-Mecsek is low, so that no major changes in hydraulic gradient are expected
- Porosity and hydraulic conductivity of the intact rock matrix is very low (0.6–1.4 %; 10-15 m/s)
- A very small amount of swelling clays is fundamentally influencing rock behaviour. The flow of free water is limited as well by the size of capillaries. Mostly diffusion processes take place inside the rock even on the level of fractures.

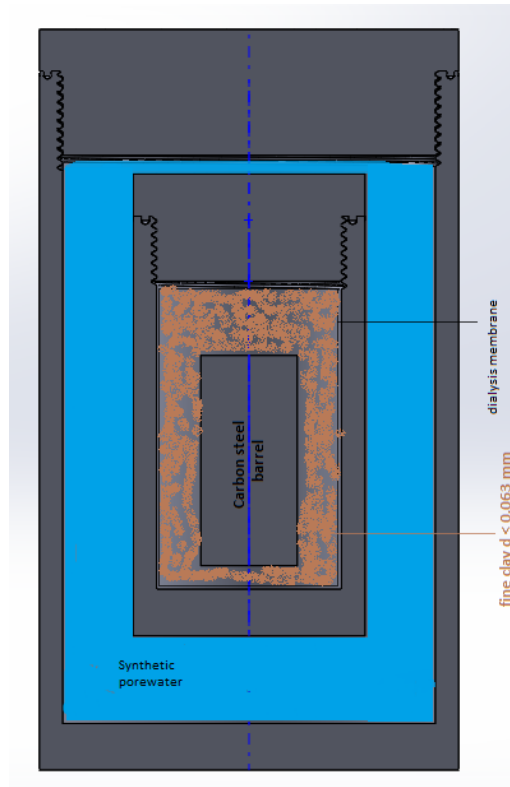
Geochemical stability of the groundwater-porewater system over geologic time frames

- The lack of organic material and pyrite helps to maintain the long-term geochemical stability of the formation.
- Intensive oxidation processes influencing the rock's mechanical status considerably are not expected to occur within the lifetime of the repository
- Due to the burial (thermal) history of BCF, the possible impact of heat production of HLW's (e.g. alteration of clay minerals, thermal softening) will be rather limited

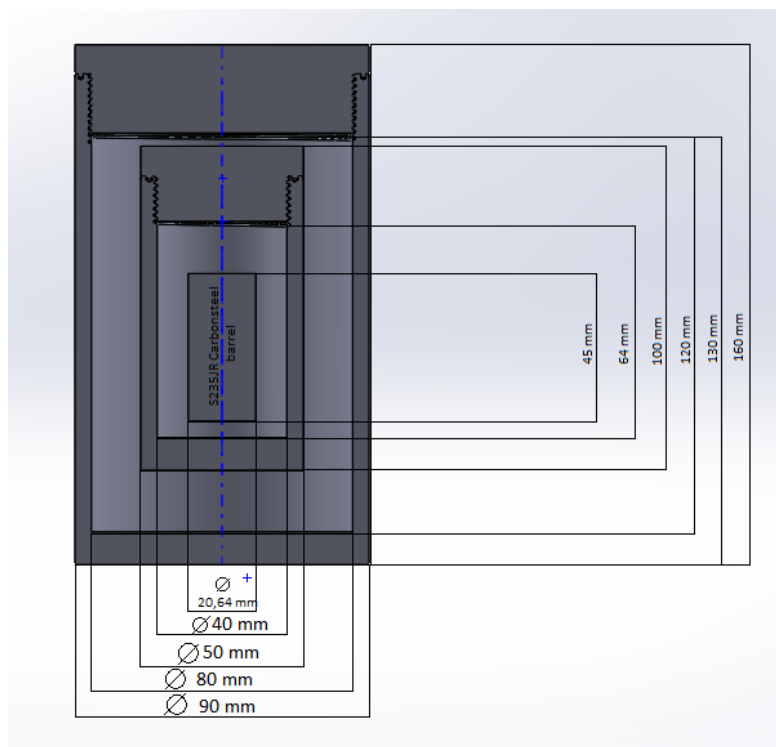
Geomechanical stability of the formations to natural perturbations

- The potential disposal zone is protected from the natural perturbations by the thick topset beds

General set-up and dimensions of the experimental cells are depicted in the following drawings.



cross-section view with sign of different materials



detailed drawing



...in reality.

Figure 7-1 – Cross-section view of experimental setup with sign of different materials (top), detailed drawing with dimensions (middle) and materials in reality (bottom) of the MTA experiment

### 7.1.2 Materials

The experimental set-up is shown in *Figure 7-1*. 2 Teflon Containers are built, to ensure the saturation during the experiments:

- 1 external Teflon container: height: 160 mm, diameter: 90 mm
- 1 internal Teflon container: h: 100mm, d: 50 mm

The inside is composed by a steel container from S235JR carbon steel, with h: 45 mm and d: 20.64 mm.

The Boda Claystone Formation (BCF) is used with following parameters:

- BCF porosity (%): min: 0.6-max: 1.4
- BCF hydraulic conductivity (m/s):  $1.0 \cdot 10^{-15}$
- BCF solid density ( $\text{kg/m}^3$ ): 2683.23
- BCF mineral fraction (%): analcime (13), calcite (12), dolomite (2), quartz (9), Na-plagioclase (11), K-feldspar (4), hematite (6), chlorite (5), muscovite/illite (29), illite/smectite (7).
- BCF cation exchange capacity (meq/100g): min: 11.2 best estimate: 12, max: 16.2

The Initial BCF porewater considered in the model is a synthetic groundwater with the following composition (mol/L):  $\text{Na}^+$ :  $1.7 \cdot 10^{-2}$ ,  $\text{Ca}^{2+}$ :  $3.1 \cdot 10^{-3}$ ,  $\text{Mg}^{2+}$ :  $2.3 \cdot 10^{-3}$ ,  $\text{K}^+$ :  $1.8 \cdot 10^{-4}$ ,  $\text{Cl}^-$ :  $2.3 \cdot 10^{-2}$ ,  $\text{HCO}_3^-$ :  $1.9 \cdot 10^{-3}$ , pH: 8.1, Eh=  $-300 \pm 10$  mV (measured at RT).

### 7.1.3 Conditions

After filling with the synthetic groundwater, the system will be closed. The clay will be saturated 100%. During the experiment, a constant temperature of  $80 \pm 2$  °C will be imposed.

## 7.2 Proposed modelling approach

The modelling applied to these tests will be carried out by SCK CEN after the acquisition of the first experimental results and the modelling approach defined in a later stage of the project.

## 8. Summary and Way forward

### 8.1 Summary

UJV Rez (Chapter 2) based their development of models for the interface of canister material (carbon steel) and bentonite on data from already existing experiments, both laboratory and in-situ (Grimsel test site), observing behaviour of the system under differing temperatures (starting from laboratory temperature up to 70°C). Data has been selected, sorted and categorised in each of considered experiments (CoPr, MaCoTe, UOS) in order to be used for development of the model in a PHREEQC environment. The very first modelling step, based on evaluation of available data has been made in order to characterize the bentonite pore solution, in contact with either iron powder or carbon steel powder.

With regard to the differences between the calculated bentonite pore waters (BPWs) and the initial solutions (SGW and GGW groundwaters), it can be observed that all the calculated BPWs contained more Na<sup>+</sup>, Mg<sup>2+</sup>, chlorides, and carbonates than the respective initial solutions. It can be clearly seen that, in general, the initial solution composition and temperature had rather minor effects on BPWs composition, whereas the initial bentonite composition has the dominant effect. This also explains the differences between the BaM- and MX-80-based BPWs that might be also reflected in resulting corrosion products in the system iron-bentonite-water.

UDC (Chapter 4) presents the first thermo-hydro-mechanical and chemical results of the reactive transport model of the FB corrosion tests. It is based on the reactive transport model for FB3 corrosion test (Mon, 2017) and has been extended to the timeframe of the FB4 corrosion test (7 years). However, data from FB4 corrosion test have not been available for model calibration yet. Corrosion relevant processes considered at the present stage include the steel corrosion at a kinetically controlled constant corrosion rate and precipitation of secondary minerals (magnetite, goethite, siderite and Fe(OH)<sub>2</sub>). Sensitivity runs with respect to steel corrosion rate and kinetic versus equilibrium magnetite precipitation are presented. The UDC corrosion model for the steel bentonite interaction in the FEBEX experiment (chapter 5) will be based on the well-developed revisited THMC model of the FEBEX in-situ test presented by Samper et al. (2018b). The implementation of corrosion and interaction of corrosion products with bentonite is foreseen for the second year of the project.

Development of the University of Bern model for corrosion and Fe-bentonite interaction in the FEBEX experiment (chapter 6) has started recently. A 1D model of the FEBEX experiment is presented, which describes the thermal, hydrodynamic and geochemical evolution in the 18 years of the FEBEX experiment. First processes relevant at the steel-bentonite interface are already implemented, such as aerobic and anaerobic corrosion, goethite and magnetite precipitation as well as an Fe sorption model. Some key parameters however, such as parameterization of mineral precipitation kinetics and limitation of H<sub>2</sub> reactivity require some further development. Furthermore, the implementation of the electron transfer between Fe(II) sorbed to montmorillonite and structural Fe(III) is still pending and awaits further progress from the experimental and modelling work of the Fe(II) diffusion experiment of University of Bern (chapter 3). This experiment is still in its preparation phase and modelling performed in this context is restricted to scoping calculations.

The MTA experiments (chapter 7) are still under development and modelling thus has not started yet.

### 8.2 Planned continuation, improvements

Owing to the early stage, models of experiments conducted within EURAD are still under development and continuous improvement, or have not yet started (MTA experiment).

Development of geochemical modelling of UJV experiments (chapter 2) is based on three-step approach. In the first step, a simple equilibrium model has been built, starting with the evaluation of bentonite pore water characterisation (finished).

The next step will represent a simple equilibrium model of for iron-bentonite interaction, however, without kinetic rate reactions or transport phenomena. The equilibrium modelling will represent a simplified approach, the sole purpose of which is to predict (i) the “direction” of the chemical processes from the initial to final (equilibrium) state; and (ii) the equilibrium state if the systems have infinite time to equilibrate. Influence of temperature will be also included.

Following that, a kinetic model will be developed, including kinetic effects and thereby time dependence of the geochemical processes. Finally, 1-D reactive transport model will complement the previous, in order to more realistically represent also spatial development of the system.

The further development of the Fe(II) – montmorillonite model of UniBern (chapter 3) will focus on the explicit description of the redox changes of structural Fe(III) in montmorillonite based on pre-experiments planned for the upcoming month and on the final results of the diffusion experiment, which are expected in 2021/2022. The implementation of a double porosity approach with explicit description of the Donnan space is considered in particular if experimental results cannot adequately be described by the present single-porosity diffusion model.

The reactive transport model of the FB corrosion tests (UDC) (chapter 4) will be updated during the ACED WP. The model will be improved by considering:

- 1) An early stage with aerobic corrosion and a late stage of anaerobic corrosion.
- 2) A time-varying corrosion rate for Fe powder. The rate will depend on ambient conditions (T, pH, Eh).
- 3) Steel corrosion and Fe diffusion with the conceptual model of Hadi et al. (2019). The precipitation of hematite and maghemite will be considered during the early stages of the test in which the Fe powder is not yet saturated. This will be consistent with Stage 1 of the conceptual model of Hadi et al. (2019).
- 4) A kinetically-controlled magnetite precipitation rate as reported by De Windt and Torres (2009), Samper et al. (2016) and Mon (2017). They considered a magnetite precipitation rate,  $r_m$ , with  $k_m = 9.53 \cdot 10^{-11} \text{ mol/m}^2 \cdot \text{s}$ ,  $\eta = 1$ ,  $\theta = 0.1$ , a specific surface of  $10^5 \text{ m}^2/\text{m}^3$  and an activation energy of 20 kJ/mol.
- 5) Additional corrosion products such as Fe-phyllsilicates (cronstedtite) and green rusts minerals in addition to magnetite, goethite, siderite and  $\text{Fe}(\text{OH})_2(\text{s})$ .
- 6) Kinetically-controlled smectite dissolution using different kinetic laws and parameters (kinetic rate constant, specific surface, activation energy and catalytic effect) proposed by Rozalen et al. (2008), Fernández et al. (2009) and Savage et al. (2011).
- 7)  $\text{Al}^{+3}$  as an additional aqueous primary species. The initial concentration of  $\text{Al}^{+3}$  in the bentonite porewater will be derived from ENRESA (2000) and Fernández et al. (2009).
- 8) Additional secondary clay minerals such as zeolites. The  $\text{Al}^{3+}$  released by smectite dissolution could precipitate as analcime (Marty et al., 2010; Savage, 2012).
- 9) Taking into account the changes in porosity, permeability and diffusion coefficients caused by mineral dissolution/precipitation reactions.
- 10) Revising the gas boundary condition. Previous models assumed that the gas phase was in equilibrium with atmospheric pressure.

The reactive transport modelling of the FEBEX in situ test by UCD (chapter 5) will be updated during the second year of the EURAD project. The steel liner will be included in the model to consider the steel-bentonite interactions. The planned continuation and improvements will be focused mostly on the geochemical model. ENRESA (UDC) will implement the following improvements:

- 1) Accounting for steel corrosion by using a constant corrosion rate and a time-varying corrosion rate depending on ambient conditions (T, pH, Eh).
- 2) Accounting for the conceptual geochemical model of steel corrosion and Fe diffusion mechanisms at the steel-bentonite interface of Hadi et al. (2019).
- 3) Accounting for corrosion products such as iron oxides and hydroxides, green-rust and Fe-phyllsilicates.

- 4) Accounting for kinetically-controlled Fe mineral precipitation.
- 5) Revising and updating the kinetic rate constant, specific surface, activation energy and catalytic effects of the kinetic rate law of smectite dissolution. The compiled data from Rozalen et al. (2008), Fernández et al. (2009 and Savage et al. (2011) will be used.
- 6) Extending the list of secondary minerals to include zeolites.
- 7) Taking into account the changes in porosity and other parameters caused by mineral dissolution/precipitation.
- 8) Revising the gas boundary condition of the THMC model. Previous models assumed that the gas phase was in equilibrium with atmospheric pressure.

A 1D axisymmetric THMC model will be performed at the location of Section 41. The computed temperatures and saturation degrees in this section at the end of the 1<sup>st</sup> and 2<sup>nd</sup> operation periods of the FEBEX in situ test are shown in Figure 8-1 and Figure 8-2, respectively.

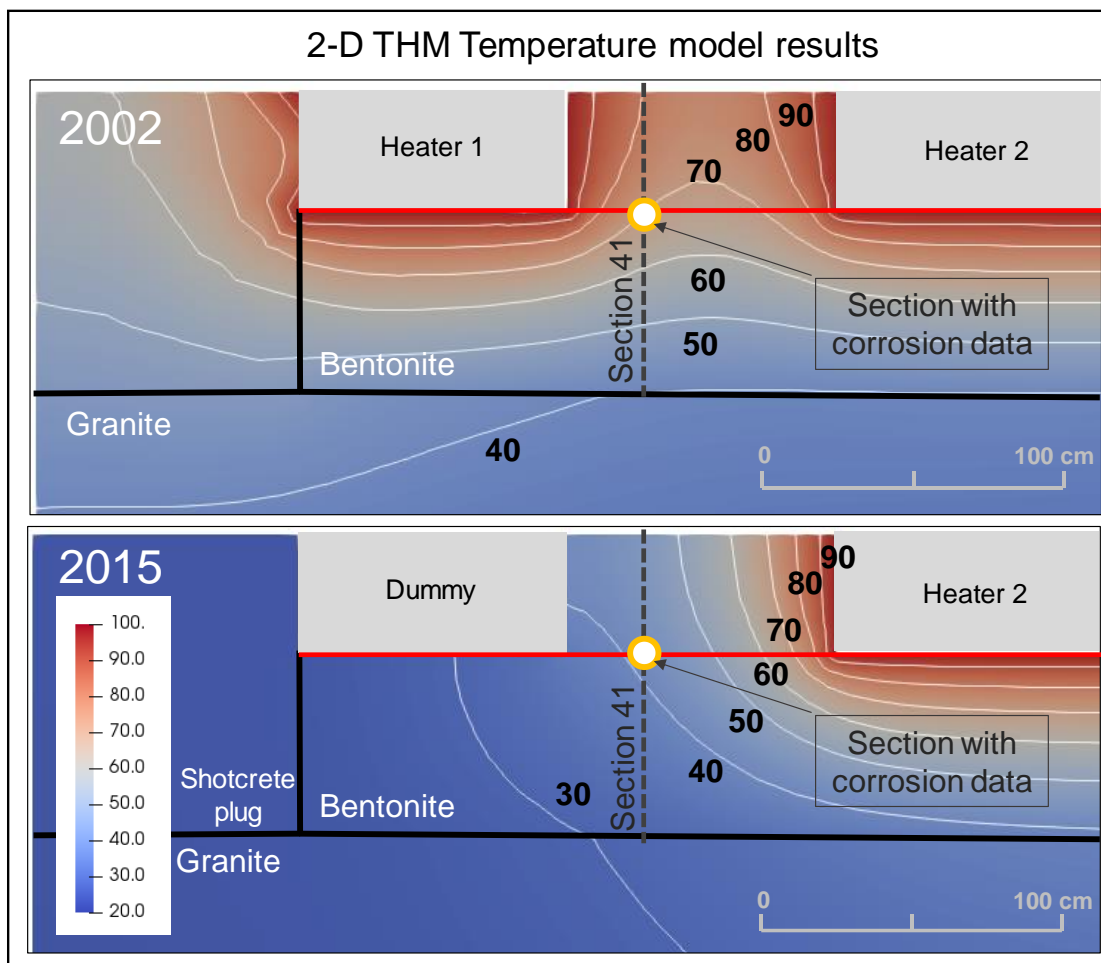


Figure 8-1 – Contour plots of computed temperatures at the end of the 1<sup>st</sup> and 2<sup>nd</sup> operation periods of the FEBEX in situ test in 2002 and 2015, respectively. Also shown the location of Section 41 where most of the corrosion data were collected.

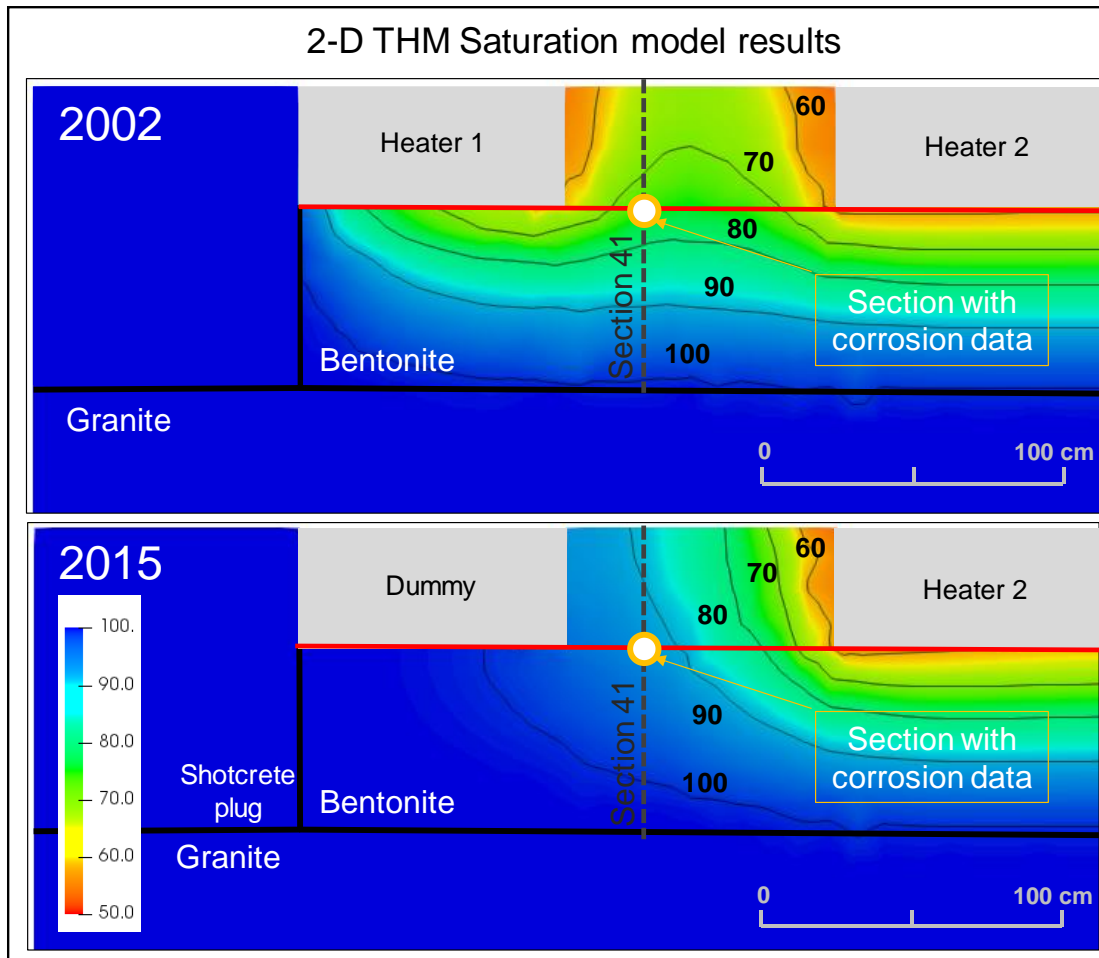


Figure 8-2 – Contour plots of computed saturation degrees at the end of the 1st and 2nd operation periods of the FEBEX in situ test in 2002 and 2015, respectively. Also shown the location of Section 41 where most of the corrosion data were collected.

Development of the FEBEX model by University of Bern (chapter 6) will be continued with a focus on the implementation of the conceptual model of Hadi et al. (2019). Thus, next steps include revised parameterization of kinetic mineral precipitation/dissolution rates, the control of  $H_2$  reactivity and the implementation of the electron-transfer process. Additional potential corrosion products such as e.g. green rust will be considered in subsequent steps. Adjustments of calculation convergence criteria will aim at an improved stability of the calculation, thus allowing for a later successful transfer of the model to different systems (i.e. ABM experiment, in-situ models) and corrosion rates. Different variant cases with respect to aerobic and anaerobic corrosion rates, secondary mineral kinetics as well as saturation and redox conditions will be elaborated to constrain and improve the understanding of the different corrosion profiles observed in the experiment.

### 8.3 Missing data validation

Results of the numerical models of the FB corrosion tests (chapter 4) indicate that the following additional data is required for model testing:

- 1) The reactive specific surface area of the Fe powder and the newly formed corrosion products such as magnetite. The specific surface area is defined as the surface area of a mineral phase per unit mass of mineral.
- 2) The corrosion rate of the Fe powder.
- 3) The kinetic rate constants of the newly formed corrosion products such as magnetite.

- 4) Detailed mineral phases characterization in the bentonite near the Fe powder.

As for the FB corrosion test the following data of the FEBEX in situ test may be missing for model testing

- 1) The corrosion rate of the steel liner and other metallic components of the FEBEX in situ test.
- 2) The kinetic rate constants of the newly formed corrosion products such as magnetite and goethite.

Data for validation of the Fe(II)-montmorillonite interaction model is still lacking but will be generated within EURAD. After validation for the well-constrained laboratory experiment, this model can be included in the model for the FEBEX-model.

The MTA experiments will just start and thus available and potentially missing data for the modelling still needs to be evaluated.

## 9. Conclusions

Modelling attempt, being focused on representation of steel – bentonite interface has been started within the first year of ACED WP. Several institutions underwent their attempt in order to either compile, evaluate and select data from already existing experiments (MaCoTe, FEBEX etc.), some modelling attempts would still await launching of experiments (MTA, Fe(II)-bentonite interaction experiment).

Even though just first steps in model construction has been made, it is clear that appropriate data and process evaluation are available and above mentioned models will strive to provide the base for up-scale to waste package (Task 3) and disposal cell scale (Task 4) by a significant reduction in the uncertainties of reactive transport models.

## Appendix A. Supporting Information to Chapter 2 – Interaction of Fe/steel with Ca-Mg bentonite

PhreeqC scripts, describing modelling effort in chapters 2.4- 2.7 are available in electronic form on request at UJV Rez

## Appendix B. Supporting Information to Chapter 6 – Corrosion model of the FEBEX in-situ experiment by UniBern

Retention curve for FEBEX bentonite

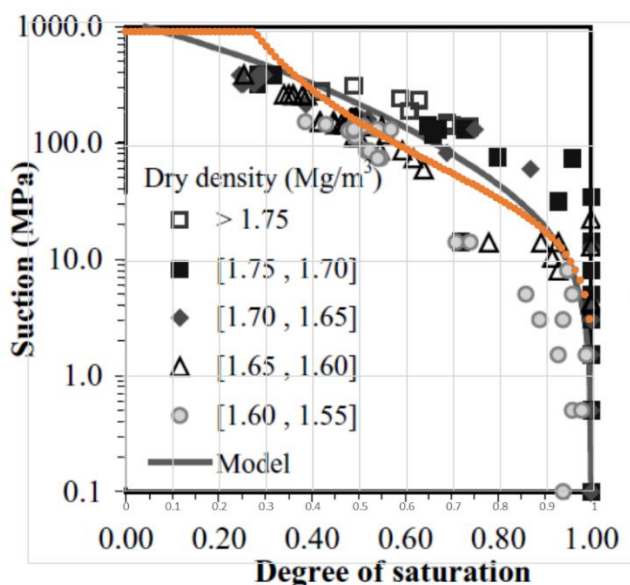
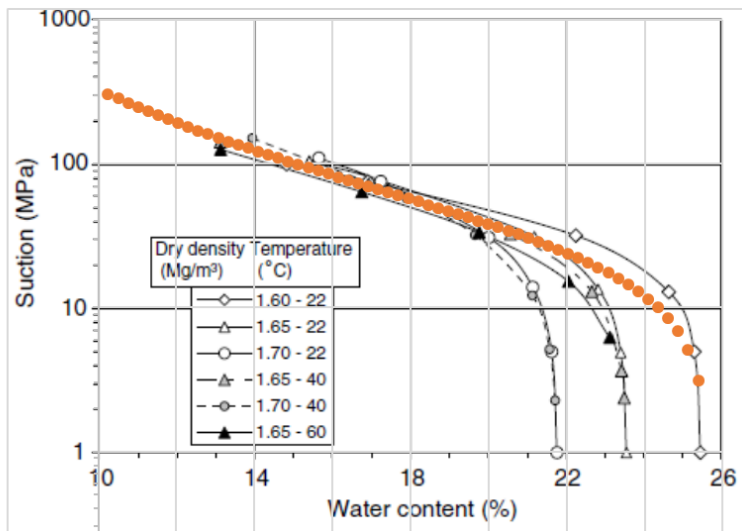
The suction curve of FEBEX bentonite is described by the van Genuchten expression

$$S_r = S_{r0} + (S_{max} - S_{r0}) \left[ 1 + \left( \frac{S}{P_0} \right)^{\frac{1}{1-\lambda}} \right]^{-\lambda}$$

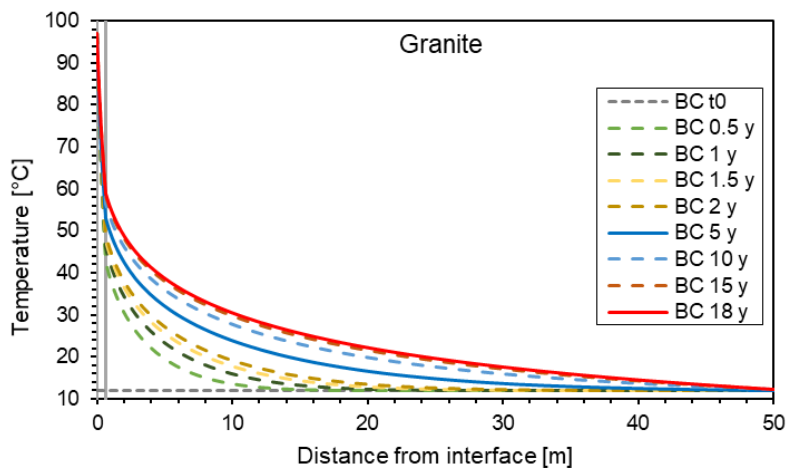
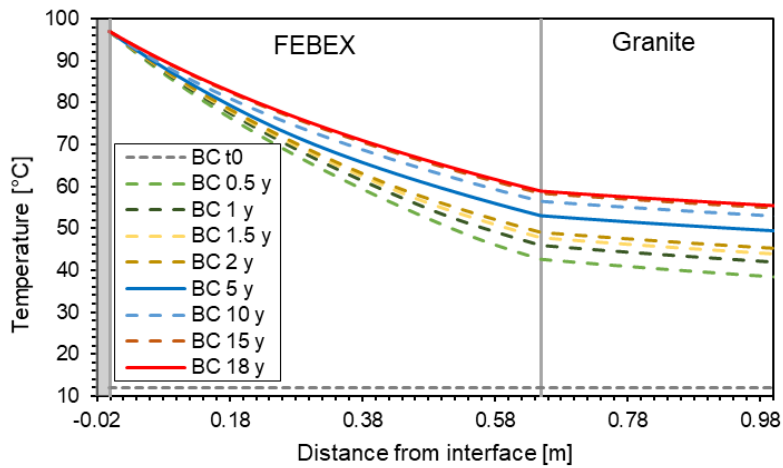
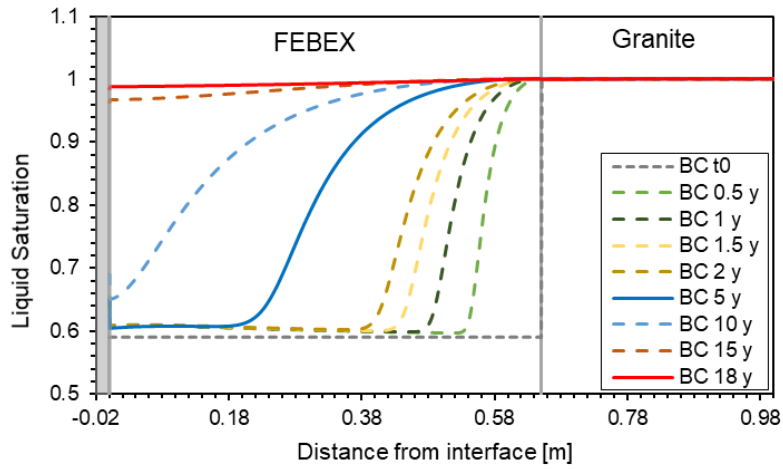
with the parameterization of (Enresa, 2000):

Residual saturation:  $S_{r0} = 0.1$ ; Maximum saturation  $S_{max} = 1$ ; air entry pressure  $P_0 = 30$  MPa, van Genuchten parameter  $\lambda = 0.32$ .

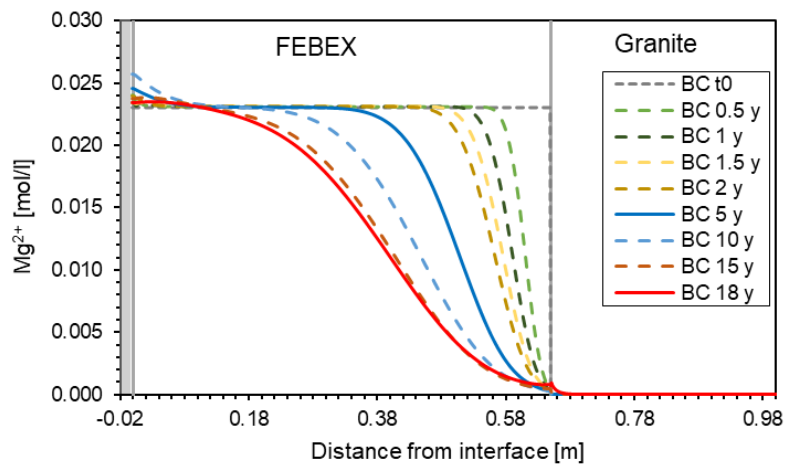
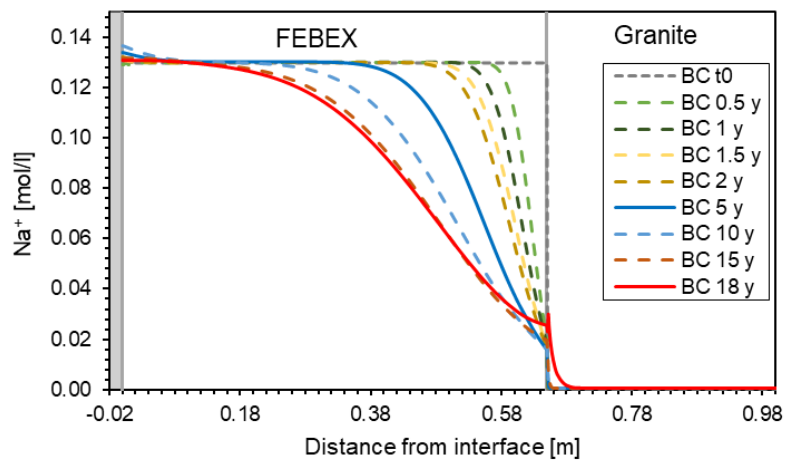
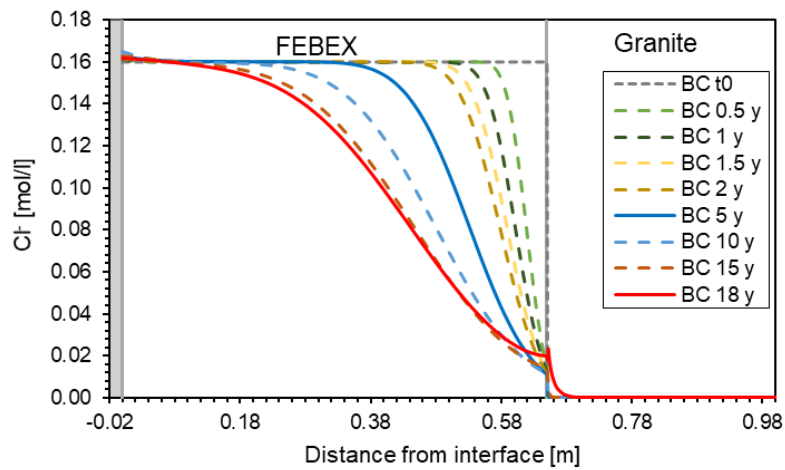
Below, the applied retention curve of the model (orange dots) is compared with experimental data by Lloret and Villar (2007) (top) and Sánchez et al. (2010) (bottom).

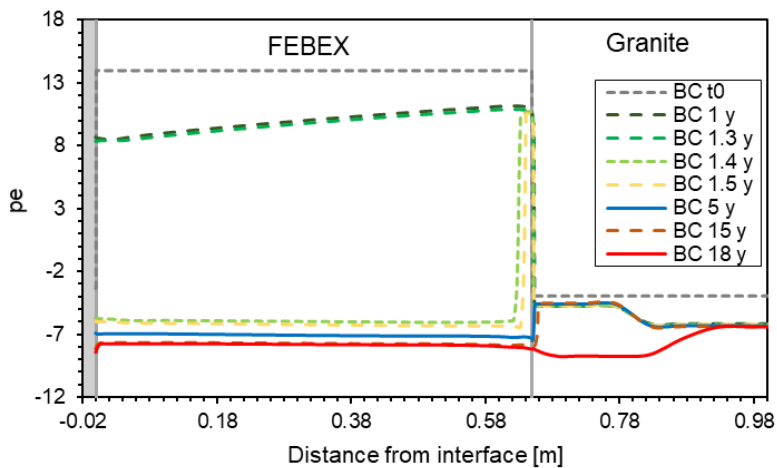
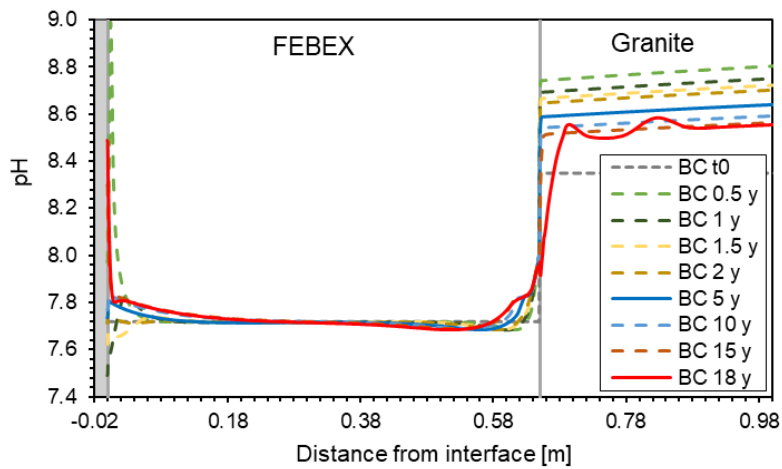
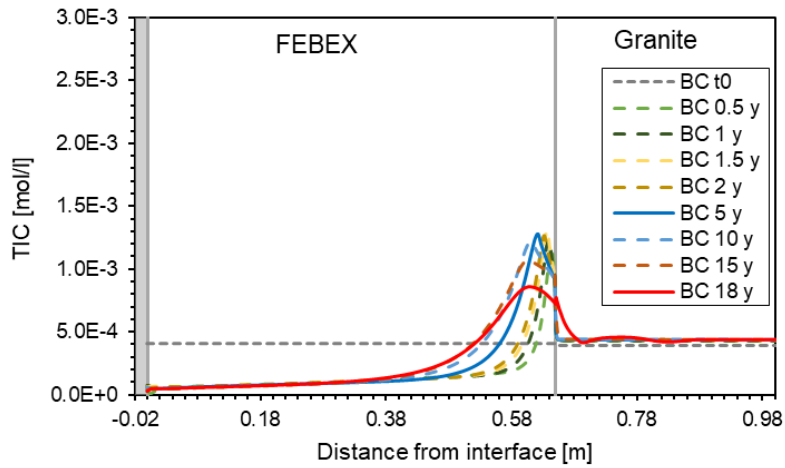


Hydrodynamic and thermal evolution as calculated for the Base Case scenario



Evolution of porewater chemistry in FEBEX and granite (Base Case)





## References

- Alonso, E., Ledesma, A. (2005) *Advances in Understanding Engineered Clay Barriers*, A. Balkema Pub., Leiden, 583 pp.
- Appelo, C. A. J., and D. Postma (1993) *Geochemistry, Groundwater and Pollution*, A. A. Balkema, Brookfield, Vt.
- Bestel, M., Glaus, M., Frick, S., Gimmi, T., Juranyi, F., Van Loon, L. and Diamond, L. (2018) Combined tracer through-diffusion of HTO and  $^{22}\text{Na}$  through Na-montmorillonite with different bulk dry densities. *Applied Geochemistry* 93.
- Birgersson, M. (2017) A general framework for ion equilibrium calculations in compacted bentonite, *Geochimica et Cosmochimica Acta*, 200: 186-200.
- Blanc, P., Lassin, A., Piantone, P., Azaroual, M., Jacquemet, N., Fabbri, A., Gaucher, E.C., (2012) Thermoddem: A geochemical database focused on low temperature water/rock interactions and waste materials. – *Appl. Geochem.*, 27, 2107–2116.
- Blount, C.W., and Dickson, F.W. (1973) Gypsum-anhydrite equilibria in systems  $\text{CaSO}_4\text{--H}_2\text{O}$  and  $\text{CaSO}_4\text{--NaCl--H}_2\text{O}$ . *American Mineralogist*, v. 58, p. 323–331.
- Bradbury, M.H. and Baeyens, B. (1997) A mechanistic description of Ni and Zn sorption on Na-montmorillonite. Part II: modelling. *J. Contam. Hydrol.* 27, 223–248.
- Bradbury, M.H. and Baeyens, B. (1998) A physicochemical characterisation and geochemical modelling approach for determining pore water chemistries in argillaceous rocks. *Geochim. Cosmochim. Acta* 62, 783–795.
- Bradbury, M. H., Baeyens, B. (2002) Porewater chemistry in compacted re-saturated MX-80 bentonite: Physicochemical characterisation and geochemical modelling. PSI report 02-10. – Paul Scherrer Institut (PSI). Switzerland.
- Bradbury, M.H. and Baeyens, B. (2003) Pore water chemistry in compacted resaturated MX-80 bentonite. *J. Contam. Hydrol.* 61, 329–338.
- Buil, B., Gómez, P., Peña, J., Garralón, A., Turrero, M.J., Escibano, A., Sánchez, L., Durán, J.M. (2010) Modelling of bentonite–granite solutes transfer from an in situ full-scale experiment to simulate a deep geological repository (Grimsel Test Site, Switzerland), *Applied Geochemistry* 25:1797–1804.
- Červinka, R., Hanuláková, D. (2013) Laboratorní výzkum tlumících, výplňových a konstrukčních materiálů. Geochemické modelování – bentonitová pórová voda (Závěrečná zpráva řešení podetapy 4.2 projektu TIP FR-TI1/362). – Report ÚJV Řež, a. s., TU Liberec, , Řež-Husinec..
- Červinka, R., Gondolli, J. (2015) Projekt UOS č. 14E1054 – Modelování pórové vody kompaktovaného bentonitu BaM. Revize 1. – Report ÚJV Řež, a. s., Husinec – Řež.
- Červinka, R., Gondolli, J., Klajmon M., Tomášová, Z., Rukavičková, L., Řihošek, J., Pacherová, P., Zeman, J., Vencelides, Z. (2017): Chování horninového prostředí/Příprava geochemického modelu úložiště – Definice vstupních dat a příprava modelů (průběžná zpráva). MS SURAO TZ 117/2017, Praha.
- Červinka, R.; Klajmon, M.; Zeman, J.; Vencelides, Z. (2018) The Geochemical Evolution of DGR: Preparation of Geochemical Model. *Geochemical Calculations and Reactive Transport Modelling*; report MS SURAO 271/2018/ENG; Praha.
- Curti, E. (2011) Comparison of Bentonite Pore Water calculations carried out with conventional and novel models (AN-44-11-18). – Paul Scherrer Institut (PSI). Switzerland.
- De Windt, L. and Torres, E. (2009) Modélisation d'expériences en cellule reproduisant les conditions THC d'une alvéole de déchets HAVL. Rapport Technique R201009LDEWI. Accord spécifique IRSN/ARMINES.

De Windt, L. and Torres, E. (2010) Interactions béton/argile sous gradient thermique et réhydratation: modélisation d'expérience en cellule. Rapport Technique R301110LDEWI. Accord spécifique IRSN/ARMINES.

Dobrev D., Gondolli J., Mendoza Miranda A. N., Steinová J., Zuna M. (2017a): Korozní zkouška v přírodním granitoidním prostředí. Zapojení v projektu Material Corrosion Test (MaCoTe), část zakázky č. 2 realizace a vyhodnocení MaCoTe experiment v Grimsel Test Site – MS SURAO, TZ 194/2017, Praha.

Dobrev D., Gondolli J., Kouřil M., Stoužil J., Straka M. (2017b) Korozní zkoušky s materiály navrženými pro konstrukci ukládacích obalových souborů – MS SURAO, Technical report, SÚRAO, Prague.

Dobrev D., Gondolli J., Mendoza Miranda A. N., Steinová J., Burkartová K., Zuna M. (2018): Korozní zkouška v přírodním granitoidním prostředí. Zapojení v projektu Material Corrosion Test (MaCoTe), část zakázky č. 2 realizace a vyhodnocení MaCoTe experiment v Grimsel Test Site – MS SURAO, Technical report No .194/2017 Rev. č. 1., Praha.

Dobrev D., Gondolli J., Mendoza Miranda A. N., Steinová J., Burkartová K., Zuna M. (2020): Korozní zkouška v přírodním granitoidním prostředí. Zapojení v projektu Material Corrosion Test (MaCoTe), část zakázky č. 2 realizace a vyhodnocení MaCoTe experiment v Grimsel Test Site – MS SURAO, Technical report No .194/2017 Rev. č. 2. Praha.

Duro, L., Grivé, M., Cera, E., Gaona, X., Doménech, C., Bruno, J. (2006) Determination and Assessment of the Concentration Limits to Be Used in SR-Can. SKB Technical Report TR-06-32. – SKB, Sweden.

Engineers Edge (2020a) Specific Heat Capacity of Metals Table Chart. Retrieved April 10, 2020 from [https://www.engineersedge.com/materials/specific\\_heat\\_capacity\\_of\\_metals\\_13259.htm](https://www.engineersedge.com/materials/specific_heat_capacity_of_metals_13259.htm).

Engineers Edge (2020b) Thermal Properties of Metals, Conductivity, Thermal Expansion, Specific Heat. Retrieved April 10, 2020 from [https://www.engineersedge.com/properties\\_of\\_metals.htm](https://www.engineersedge.com/properties_of_metals.htm).

ENRESA (2000) Full-scale engineered barriers experiment for a deep geological repository in crystalline host rock FEBEX Project. EUR 19147 EN, 403 pp.

ENRESA (2006a) FEBEX: Updated Final Report 1994-2004. ENRESA T Technical Publication PT 05-02/2006, 589 pp.

ENRESA (2006b) FEBEX: Final THG modelling report. ENRESA Technical Publication PT 05-3/2006, 155 pp.

Fernández, A.M., Cuevas, J., Rivas, P. (2001) Pore water chemistry of the FEBEX bentonite. Mat. Res. Soc. Symp. Proc. Vol. 603, 573-588.

Fernández, A.M., Baeyens, B., Bradbury, M., Rivas, P. (2004) Analysis of the pore water chemical composition of a Spanish compacted bentonite used in an engineered barrier. Physics and Chemistry of the Earth 29(1), 105-118.

Fernández, R., Cuevas, J., Mäder, U.K. (2009) Modelling concrete interaction with a bentonite barrier. Eur. J. Mineral. 21, 177-191.

Fernández, A.M., Sánchez-Ledesma, D.M., Melón, A., Robredo, L. M., Rey, J.J., Labajo, M., Clavero, M.A., Carretero, S., González, A.E. (2018) Thermo-hydro-geochemical behaviour of a Spanish bentonite after of the FEBEX in situ test at the Grimsel Test Site. Technical Report CIEMAT/DMA/2G216/03/16. Nagra Arbeitsbereich NAB16-025. Madrid, 270 pp.

Fuentes-Cantillana, J.L., García-Siñeriz, J.L. (1998) FEBEX. Final design and installation of the “in situ” test at Grimsel. Technical Publication ENRESA 12/98. Madrid, 184 pp.

Funabiki, A., Oguma, M., Yabuki, T. and Kakizaki, T. (2014) The Effects of Groundwater Flow on Vertical-Borehole Ground Source Heat Pump Systems. ASME 2014 12th Biennial Conference on Engineering Systems Design and Analysis, ESDA 2014 3.

Gaines, G.I., Thomas, H.C. (1953) Adsorption studies on clay minerals II. A formulation of the thermodynamics of exchange adsorption. *Journal of Chemical Physics* 21, 714–718.

García-Gutiérrez, M., Cormenzana, J.L., Missana, T., Mingarro, M. (2004) Diffusion coefficients and accessible porosity for HTO and <sup>36</sup>Cl in compacted FEBEX bentonite. *Applied Clay Science*, 26: 65-73.

García-Gutiérrez, M., Cormenzana, J.L., Missana, T., Mingarro, M., Molinero, J. (2006) Overview of laboratory methods employed for obtaining diffusion coefficients in FEBEX compacted bentonite. *Journal of Iberian Geology* 32 (1) 2006: 37-53.

Garralón, A., Gómez, P., Turrero, M.J., Torres, E., Buil, B., Sánchez L., Peña, J. (2018) Hydrogeochemical characterization of the groundwater in the FEBEX gallery. Technical Report NAGRA NAB 16-014.

Gens, A., Guimaraes, L. do N., Garcia-Molina, A., Alonso, E.E. (2002) Factors controlling rock–clay buffer interaction in a radioactive waste repository, *Engineering Geology* 64 (2002) 297–308.

Giffaut, E., Grivé, M., Blanc, P., Vieillard, P., Colàs, E., Gailhanou, H., Gaboreau, S., Marty, N., Madé, B. and Duro, L. (2014) Andra thermodynamic database for performance assessment: ThermoChimie. *Applied Geochemistry* 49, 225-236.

Gondolli J., Dobrev D., Klajmon M., Černoušek T., Kouřil M. (2018a) Chování UOS pro VJP a RAO/Korozní produkty. 3. Průběžná zpráva. – Technická zpráva číslo 217/2018, SÚRAO, Praha.

Gondolli J., Klajmon M., Kouřil M. (2018b) Chování UOS pro VJP a RAO/Korozní produkty. Závěrečná zpráva. – MS SURAO, Final report No 329/2018, SÚRAO, Praha.

Gondolli, J.; Dobrev, D.; Klajmon, M.; Mendoza, A.; Černoušek, T.; Kouřil, M.; Stouřil, J. (2018c) Behaviour of Waste Package for Spent Nuclear Fuel and High-Level Waste: Corrosion Products (final report); Technical report 329/2018/ENG; Praha.

Grivé, M., Duro, L., Colàs, E. and Giffaut, E. (2015) Thermodynamic data selection applied to radionuclides and chemotoxic elements: An overview of the ThermoChimie-TDB. *Applied Geochemistry* 55, 85-94.

Hadi, J., Wersin, P., Serneels, V., Greneche, J.-M., 2019. Eighteen years of steel-bentonite interaction in the FEBEX in situ test at the Grimsel Test Site in Switzerland. *Clays and Clay Minerals* 67(2), 111-131.

Hunter, Bate F., Heath T., Hoch A. (2007) Geochemical investigation of iron transport into bentonite as steel corrodes. – SKB Technical Report TR-07-09. Svensk Kärnbränslehantering AB, Stockholm, Sweden.

Idiart A, Pekala M. (2016) Models for Diffusion in Compacted Bentonite, SKB Technical Report TR-15-06, 52 pp.

Kant, M.A., Ammann, J., Rossi, E., Madonna, C., Höser, D. and Rudolf von Rohr, P. (2017) Thermal properties of Central Aare granite for temperatures up to 500°C: Irreversible changes due to thermal crack formation. *Geophysical Research Letters* 44, 771-776.

Kaufhold, S, Dohrmann, R, Ufer, K, Kober, F. (2019) Interactions of bentonite with metal and concrete from the FEBEX experiment: mineralogical and geochemical investigations of selected sampling sites. *Clay Miner.*, 1-19.

Kober, F., Giroud, N., Uyama, M., Hitomi, T., Hayagane, S., Kadota, N., Saito, H., Okamoto, S., Aoshima, K., Osawa, M., Hadi, J., Grenèche, J.M., Wersin, P., Svensson, D., Lundgren, C., Kaufhold, S., Dohrmann, R., Ufer, K., Torres, E., Turrero, M.J., Sánchez, L., Garralón, A., Gómez, P., Campos,

- R., Leal Olloqui, M., Scott, T.B., Madina, V. (2017) FEBEX-DP. Metal Corrosion and Iron-Bentonite Interaction Studies. Nagra Arbeitsbericht, NAB 16–16, Nagra, Wettingen, Switzerland, 300 pp.
- Lanyon, G.W. and Gaus, I. (2017) Main outcomes and review of the FEBEX In Situ Test (GTS) and Mock-up after 15 years of operation. Nagra Technischer Bericht, NTB 15–04, Nagra, Wettingen, Switzerland, 127 pp.
- Latta, D.E., Neumann, A., Premaratne, W.A.P.J. and Scherer, M.M. (2017) Fe(II)-Fe(III) Electron Transfer in a Clay Mineral with Low Fe Content. *Acs Earth Space Chem* 1, 197-208.
- Lloret, A. and Villar, M.V. (2007) Advances on the knowledge of the thermo-hydro-mechanical behaviour of heavily compacted "FEBEX" bentonite. *Phys Chem Earth* 32, 701-715.
- Lloret, A., Alonso, E.E. (1995) State surfaces for partially saturated soils, In: *Proceedings of the International Conference on Soils Mechanics and Foundation Engineering*, Balkema, pp. 557-562.
- Lu, C, J Samper, B. Fritz, A. Clement & L. Montenegro (2011) Interactions of corrosion products and bentonite: An extended multicomponent reactive transport model, *Physics and Chemistry of the Earth, Parts A/B/C*, Vol 36:1661–1668.
- Marques Fernandes M, Vér N, Baeyens B, (2015). Predicting the uptake of Cs, Ni, Co, Eu, Th and U on argillaceous rocks using sorption models for illite, *Applied Geochemistry* 59, 189-199.
- Martín, P.L., Barcala, J.M. (2005) Large scale buffer material test: Mock-up experiment at CIEMAT, *Engineering Geology* 81, 298– 316.
- Martinez, V., Abos, H. and Garcia-Sineriz, J.L. (2016) FEBEXe: Final Sensor Data Report, NAGRA Arbeitsbericht NAB 16-19.
- Marty, N., Claret, F., Gaboreau, S., Cochevin, B., Munier, I., Michau, N., Gaucher, E. C., Burnol, A. (2010) Dual alteration of bentonite by iron corrosion and concrete interaction under high temperature conditions. In *Clays in Natural and Engineered Barriers for Radioactive Waste Confinement*, Nantes, France, pp. 473-474.
- Mendoza, A.; Havlová, V. (ÚJV Řež, a. s.), personal communication, 2020.
- Mon, A (2017) Coupled thermo-hydro-chemical-mechanical models for the bentonite barrier in a radioactive waste repository. Ph. D. Dissertation. Universidad de A Coruña, Spain.
- Mon, A., Samper, J., Montenegro, L., Naves, A., Fernández, J. (2017) Reactive transport model of compacted bentonite, concrete and corrosion products in a HLW repository in clay. *Journal of Contaminant Hydrology* 197, 1-16.
- Nguyen, T.S., Selvadurai, A.P.S., Armand, G. (2005) Modelling the FEBEX THM experiment using a state surface approach. *Int. J. Rock Mech. Min. Sci.* 42 (5–6), 639–651.
- Palandri, J. and Kharaka, Y. (2004) A Compilation of Rate Parameters of Water-Mineral Interaction Kinetics for Application to Geochemical Modeling. 1068, 71.
- Parkhurst D. L., Appelo C. A. J. (2013): Description of input and examples for PHREEQC version 3-A computer program for speciation, batch-reaction, one-dimensional transport, and inverse geochemical calculations. – U.S. Geological Survey Techniques and Methods, book 6, chapter A43, 497 p., dostupné na <http://pubs.usgs.gov/tm/06/a43/>.
- Quintessa (2013) QPAC: Quintessa's General-Purpose Modelling Software. Quintessa Report QRS-QPAC-11. Henley-on-Thames, UK.
- Samper, J., Lu, C., Montenegro, L. (2008a) Reactive transport model of interactions of corrosion products and bentonite, *Physics and Chemistry of the Earth*, Vol. 33, Supplement 1, S306-S316. doi:10.1016/j.pce.2008.10.009.

- Samper, J., Zheng, L., Montenegro, L., Fernández, A. M., Rivas, P. (2008b) Coupled thermo-hydro-chemical models of compacted bentonite after FEBEX in situ test, *Applied Geochemistry* vol. 23, pp. 1186-1201.
- Samper, J., Zheng, L., Fernández, A.M., Montenegro, L. (2008c) Inverse modelling of multicomponent reactive transport through single and dual porosity media. *Journal of Contaminant Hydrology* 98,115-127.
- Samper J., Naves A., Montegro L., Mon A. (2016) Reactive transport modelling of the long-term interactions of corrosion products and compacted bentonite in a HLW repository in granite: Uncertainties and relevance for performance assessment. – *Applied Geochemistry*, 67, 42–51.
- Samper J., A. Mon, L. Montenegro, J. Cuevas, M.J. Turrero, A. Naves, R. Fernández, E. Torres (2018a) Coupled THCM model of a heating and hydration concrete-bentonite column test. *Applied Geochemistry* 94 67–81.
- Samper, J., Mon, A., Montenegro, L. (2018b) A revisited thermal, hydrodynamic, chemical and mechanical model of compacted bentonite for the entire duration of the FEBEX in situ test. *Appl. Clay Sci.* 160, 58–70.
- Sánchez, M., Gens, A. and Olivella, S. (2010) Effect of thermo-coupled processes on the behaviour of a clay barrier submitted to heating and hydration. *Anais da Academia Brasileira de Ciências* 82, 153-168.
- Savage, D. (2012) Prospects for coupled modelling. STUK-TR 13. Radiation and Nuclear Safety Authority.
- Savage, D., Arthur, R., Watson, C., Wilson, J., Strömberg, B. (2011) Testing geochemical models of bentonite pore water evolution against laboratory experimental data. *Physics and Chemistry of the Earth* 36, 1817-1829.
- Savage, D., Watson, C., Benbow, S., Wilson, J. (2010) Modelling iron/bentonite interactions. *Applied Clay Science* 47, 91-98.
- Soltermann, D., Baeyens, B., Bradbury, M.H. and Marques Fernandes, M. (2014) Fe(II) Uptake on Natural Montmorillonites. II. Surface Complexation Modeling. *Environmental Science & Technology* 48, 8698-8705.
- Torres, E., Turrero, M. J., Peña, J., Martín, P.L., Escribano, A., Alonso, U. and Villar, M.V. (2008) Deliverable 2.3.2 of component 2 NF-PRO project. Interaction iron-compactated bentonite: corrosion products and changes in the properties of the bentonite. CIEMAT.
- Torres, E., Turrero, M.J., Escribano, A. (2013) Synthesis of corrosion phenomena at the iron/bentonite interface under unsaturated conditions. CIEMAT Technical Note CIEMAT/DMA/2G210/02/2013. PEBS Project.
- Turrero, M. J., Villar, M. V., Torres, E., Escribano, A., Cuevas, J., Fernández, R., Ruiz, A. I., Vigil de la Villa, R. and del Soto, I. (2011) Deliverable 2.3-3-1 of PEBS Project. Laboratory tests at the interfaces, Final results of the dismantling of the tests FB3 and HB4, 2011. CIEMAT.
- Villar M. V., A. Lloret (2007) Dismantling of the first section of the FEBEX in situ test: THM laboratory tests on the bentonite blocks retrieved. *Physics and Chemistry of the Earth* 32, 716–729.
- Villar, M.V., Iglesias, R.J., Abós, H., Martínez, V., de la Rosa, C., Manchón, M.A. (2016) FEBEX-DP on-site analyses report. Nagra Arbeitsbericht, NAB 16–12, Nagra, Wettingen, Switzerland, 115 pp.
- Villar, M.V.; García-Siñeriz, J.L., Bárcena I. and Lloret, A. (2005) State of the bentonite barrier after five years operation of an in situ test simulating a high level radioactive waste repository. *Engineering Geology* 80(3-4): 175-198.

- Wersin P. (2003) Geochemical modelling of bentonite porewater in high-level waste repositories. – J. Contam. Hydrol. 61, 405-422.
- Wersin P., Curti E., Appelo C.A.J. (2004) Modelling bentonite–water interactions at high solid/liquid ratios: swelling and diffuse double layer effects. – Appl. Clay Sci. 26, 249-257.
- Wilkin, R.T., Barnes, H.L. (1998) Solubility and stability of zeolites in aqueous solution: I. Analcime, Na- and K-clinoptilolite. American Mineralogist 83, 746-761.
- Wilson, J.C. (2017) FEBEX-DP: Geochemical modelling of iron-bentonite interactions. Quintessa's contribution on behalf of RWM. Quintessa Report QRS-1713A-R3 v1.3.
- Wilson, J.C., Benbow, S., Watson, C., Sasamoto, H., Savage, D. (2015) Fully-coupled reactive transport models of the iron-bentonite interface. Applied Geochemistry 61, 10-28.
- Zheng, L., Samper, J. (2008) A coupled THMC model of FEBEX mock-up test. Physics and Chemistry of the Earth 33, S486-S498.
- Zheng, L., Samper, J., Montenegro, L., Fernández, A.M. (2010) A coupled THMC model of a heating and hydration laboratory experiment in unsaturated compacted FEBEX bentonite. Journal of Hydrology 386, 80-94.
- Zheng, L., Samper, J., Montenegro, L. (2011) A coupled THMC model of the FEBEX in situ test with bentonite swelling and chemical and thermal osmosis, J of Contaminant Hydrology 126:45–60.